Nutrient Homeostasis in *Acinetobacter baumannii*

By

Zachery Ryan Lonergan

Dissertation

Submitted to the Faculty of the

Graduate School of Vanderbilt University

in partial fulfillment of the requirements

for the degree of

DOCTOR OF PHILOSOPHY

in

Microbiology and Immunology

March 31, 2020

Nashville, Tennessee

Approved:

Richard M. Peek, Jr, M.D.

Tina M. Iverson, Ph.D.

Timothy L. Cover, M.D.

Maria Hadjifrangiskou, Ph.D.

Eric P. Skaar, Ph.D, M.P.H.

ACKNOWLEDGEMENTS

I would like to start by thanking my thesis mentor, Eric Skaar. You have given me the intellectual space and freedom to ask exciting questions and think critically about my projects. Even when I stubbornly chose to focus on research questions that were probably (definitely) too ambitious for a single graduate student, you consistently provided sound advice and reason to help me advance through graduate school. Thank you for the feedback on countless presentations, posters, abstracts, and manuscripts that I sent to you and for numerous recommendation letters that you have written and will hopefully continue to write. You taught me to approach science with curiosity, excitement, and rigor, and I have learned to never be afraid of asking questions. Perhaps most importantly, thank you for creating a community in the lab full of equally curious and engaging scientists with whom I have forged lifelong friendships.

To the members of the Skaar laboratory, thank you for the years of engaging scientific discussions, experimental assistance, challenging questions, and thoughtful feedback. Each of you have contributed to this Thesis in some way, and I would not be the scientist that I am without the conversations I have had with you. Thank you Nichole Lobdell and Nichole Maloney for your organization and leadership in keeping the lab on track, and thank you to the research staff Valeria Garcia, Sydney Drury, Anderson Miller Amber Petoletti, and those who came before you, for your contributions to keeping science moving. To my Acinetobesties Lauren Palmer, Erin Green, Jessica Sheldon, Laura Hesse, Ben Fowler, and Jeanette Miller – thank you for the immense intellectual contributions you have given me over the years, and for always being willing to grab a coffee or a Diet Coke. To all the other amazing postdocs in the laboratory Will Beavers, Chris Lopez, Andrew Monteith, Hualiang Pi, Aaron Wexler, Andy Weiss, Valeria Reyes Ruiz, and Cait

Murdoch – you are all some of the smartest, hardest working, and kindest people I have ever had the privilege of working with, and I am so excited to see where your science goes in the next few years. To my fellow graduate students not already mentioned – Reece Knippel, Clare Laut, and Catherine Leasure, thank you for the years of comradery, laughter, scientific discussions, and occasional struggles that come from being a student in a sea of postdocs. To former lab members Brittany Nairn, Joe Zackular, Jacob Choby, and Lillian Juttukonda – thank you for your mentorship during my early years in the lab and for your ongoing friendship and support.

I would also like to acknowledge and thank the numerous collaborators I worked with in the lab. Walter Chazin's lab provided recombinant calprotectin for numerous experiments presented in this Thesis. I am indebted to David Giedroc and Jiefei Wang from Indiana University who contributed resources, time, and mental energy into almost every aspect of this Thesis, and I am fortunate to have shared co-first authorship with Jiefei on the manuscript presented in Chapter II. Other contributors for Chapter II include Giovanni Gonzalez-Gutierrez, who was instrumental in solving the crystal structure of RibBX, Yixiang Zhang, who aided in the proteomics experiment under the supervision of Jonathan Trinidad, and Claudia Andreini, who performed the *A. baumannii* zinc proteome predictions. In Chapter III, special thanks to Jiefei Wang in David Giedroc's laboratory who worked to perform peptidoglycan mass spectrometry under the supervision of Jonathan Trinidad, and she also performed metal binding analyses. I was also fortunate to travel to Indiana University and work with Yen-Pang Hsu under the mentorship of Michael VanNieuwenhze to perform the very first fluorescent amino acid labeling of *A. baumannii*. Thanks to Brittany Nairn who generated the *zrlA* mutant, Will Beavers who performed ICP-MS analyses, and Laura Hesse who aided with protein expression and fractionation experiments. In Chapter V, I would like to thank Allegra Aron and Marie Heffern from Chris

Chang's lab, with whom I shared co-first authorship on our investigation into iron homeostasis during *A. baumannii* infection. This was a truly collaborative project and one of the most fun I had during my time in graduate school. Other contributors for Chapter V include Yaofang Zhang, who performed the LA-ICP-MS, as well as Mark Vander Wal, Brian Blank, Benjamin Spangler, Hyo Min Park, Andreas Stahl, and Adam Renslo, all of whom directly contributed to research design, experimentation, or reagent contributions.

I would like to thank the Vanderbilt Office of Biomedical Research Education & Training for the constant support, program management, and career development opportunities. Within the PMI department, I would like to thank Lorie Franklin and Chris Aiken for their management of the former Microbiology and Immunology training program, and now Microbe-Host Interactions training program. I would also like to thank the administrative staff of the Molecular Pathogenesis Division and VI4, who continue to provide critical support to graduate student and postdoc education in the department.

I would also like to thank my Ph.D. thesis Committee, which includes Committee Chair Richard Peek, Tina Iverson, Maria Hadjifrangiskou, and Tim Cover. You have been an incredible resource during my graduate school tenure and provided valuable feedback and critical questions at each committee meeting. I also appreciate the time you have taken to meet with me individually, attend my presentations, and provide letters of support.

I would like to acknowledge the funding sources that supported work presented in this dissertation. I received funding from the National Institutes of Health (NIH) training program in environmental toxicology T32 ES007028 and from an NIH Ruth L. Kirschstein National Research Service Award F31 AI136255. Eric Skaar, Walter Chazin, and David Giedroc were supported by R01 AI101171. Eric Skaar was also supported by R01 AI069233, R01 AI073843, and R01

AI138581. David Giedroc was also supported by R35 GM118157. Yen-Pang Hsu and Michael VanNieuwenhze were supported by R01 GM113172. Brittany Nairn was supported by F32 AI108192 and T32 AI095202. Laura Hesse was supported by T32 GM065086. Will Beavers was supported by T32 HL069765. Chris Chang was supported by GM79645 and is an Investigator with the Howard Hughes Medical Institute and a Canadian Institute for Advanced Research Senior Fellow. Allegra Aron was supported by a National Science Foundation graduate fellowship and T32 GM 066698. Marie Heffern was supported by the University of California President's Postdoctoral Program. Benjamin Spangler was supported by T32 GM064337.

Finally, I would like to thank my family and friends. To Brittany, along with Maya and Caesar, thank you for your unwavering love and support. To my parents and siblings, thank you for always welcoming me home with open arms. To my lifelong friends – Chad, Jima, Cassie, Justin, Mark, and Michael, I thank you for many years of encouragement, adventures, and memories. To all of you, thank you for everything.

TABLE OF CONTENTS

Page

Chapter

Appendix

LIST OF TABLES

Table Page

LIST OF FIGURES

Figure Page

CHAPTER I

INTRODUCTION

A portion of the following section was previously published in *Trends in Biochemical Sciences* (July 2019) doi: 10.1016/j.tibs.2019.06.010.

The discovery of penicillin in the early 20th century ushered in a new area of medical treatments that revolutionized bacterial infection management. Over several decades, a variety of antibiotics with distinct modes of action were discovered that increased life expectancy considerably (Adedeji, 2016). As quickly as these therapies became commonplace, so did the discovery of bacteria resistant to antibiotics. Antibiotic-resistant bacterial infections now represent a major public health crisis, and estimates project that antibiotic-resistant infections will become the main cause of mortality in the United States within a few decades (O'Neill, 2014). Importantly, the rise of these antibiotic-resistant infections hastens the arrival of a post-antibiotic era, where therapies that were commonplace for half a century will no longer be sufficient to prevent or eliminate bacterial infections. This Dissertation focuses on *Acinetobacter baumannii,* which is a bacterial species that has emerged as a major concern for antibiotic-resistant infections. Multi-drug and pan-drug resistant *A. baumannii* infections have become so difficult to treat that the World Health Organization has listed *A. baumannii* as its most critical pathogen for which new therapeutics are needed to treat infections (WHO, 2017). It has also been listed by the CDC as an "urgent threat" to public health, which is its highest threat level (CDC, 2019).

A. baumannii is a Gram-negative obligate aerobe and a frequent cause of nosocomial infections. While the genus *Acinetobacter* possesses many environmental species located globally, the natural reservoir for *A. baumannii* is unknown, but it is likely in human-associated locations (Peleg et al., 2008). As an opportunistic pathogen, infections resulting from *A. baumannii* usually occur in immunocompromised patients and manifest themselves in several ways, including wound and burn infections, urinary tract infections, and sepsis (Peleg et al., 2008). Notably, *A. baumannii* is one of the most common causes of ventilator-associated pneumonia. Despite the alarming increase in multi-drug resistant *A. baumannii* infections, mechanistic studies of the organism's basic physiology and virulence are limited (Harding et al., 2018). These facts highlight the importance of understanding how *A. baumannii* causes disease to inform new antimicrobial therapy design.

Like all bacterial pathogens, *A. baumannii* must acquire nutrients from the host to replicate. Specifically, nutrient metals are required for life and serve in a variety of structural and enzymatic contexts in all domains of life. In this Dissertation, I present research focused on how the struggle for nutrients shapes the host-*Acinetobacter* interactions and physiology, which a major focus on nutrient zinc (Zn). Chapter I (Introduction) summarizes mechanisms used by the vertebrate host to buffer against changes in Zn availability and provides a literature review of diverse bacterial pathogen Zn homeostasis systems. I also address unanswered questions regarding how nutrient starvation impacts *A. baumannii* physiology, especially since key metabolic steps are metal-dependent. Chapter II presents evidence that host-mediated metal starvation stresses the metal-dependent process of riboflavin biosynthesis in *A. baumannii*, and the bacterium responds to this metal limitation by employing a multi-step regulatory network to maintain sufficient flavin levels. This regulatory network provides a new framework for how flavin regulation likely occurs throughout Proteobacteria. Additionally, enzymes involved in bacterial cell envelope biogenesis are metal-dependent, but whether bacteria alter the cell wall in response to nutrient limitation was unknown. In Chapter III, I demonstrate that *A. baumannii* responds to nutrient Zn starvation by upregulating a cell wall-modifying enzyme that promotes maintenance of an effective cellular envelope during nutrient starvation I also found that this enzyme is crucial for survival within the host and synergizes with a clinically-relevant antibiotic to limit *A. baumannii* pathogenesis. In Chapter IV, I describe how the amino acid histidine serves as a nutrient source for *A. baumannii*. This utilization is critical for the ability of *A. baumannii* to cause disease in a mouse model of pneumonia, but it may be driven by histidine serving as a nitrogen source instead of a carbon source. Chapter V focuses instead on how the host responds to *A. baumannii* infection and provides insight into dynamics of metal withholding from bacterial pathogens by utilizing a bioluminescent iron reporter. Together, this Thesis underscores the struggle for nutrients at the host-pathogen interface and highlights important metabolic requirements that *A. baumannii* possesses to cause disease.

Zinc is required for life

Transition metals are essential micronutrients required to carry out biological processes in all domains of life (Andreini et al., 2006b). Their requirement stems from unique biochemical properties attributed to late *d*-block elements that selected for their incorporation into catalytic and structural components of proteins during evolution. The essential metal zinc (Zn) is unique among the first row *d*-block elements in that it possesses a filled *d*-orbital and does not undergo redox cycling. Zn is ubiquitous in life and is required for the structure or function of thousands of metalloproteins (Andreini et al., 2006a). Zn is an essential micronutrient for the survival and proliferation of bacteria, including pathogens that are major causes of morbidity and mortality worldwide (Hood and Skaar, 2012). Given this essentiality, both vertebrate hosts and pathogens evolved processes to maintain Zn homeostasis. While mechanisms of maintenance and storage of Zn within vertebrates have been well described in recent decades (King et al., 2000), the diverse array of systems that pathogens possess to compete for this essential nutrient during infections has only recently been appreciated (Hood and Skaar, 2012). In this review, we discuss vertebrate Zn homeostasis and mobilization during infections, followed by a summary of our current understanding of bacterial Zn uptake and utilization systems.

Vertebrate zinc homeostasis is a highly regulated and dynamic process

As the second most abundant trace metal in humans, around 2 to 4 grams of Zn are distributed throughout the body in various tissue sites (Eggleton, 1940). In vertebrates, the gastrointestinal tract serves as a major regulator of Zn homeostasis by tuning absorption and excretion via metal transporter proteins (King et al., 2000) (**Figure 1**). While the range of total Zn within the body is relatively stable for most humans, changes in dietary Zn availability are associated with poor health (King et al., 2000). Human genetic deficiencies in Zrt/Irt-like Protein (ZIP) family members, which are the primary Zn importers in eukaryotes, cause severe Zn deficiency (Kury et al., 2002). Additionally, dietary Zn deficiency is a major public health burden, with at least 25% of the global population being at risk of inadequate dietary Zn (Maret and Sandstead, 2006; Wessells and Brown, 2012). Consequences of Zn deficiency include impaired immune function, delayed wound healing, diarrhea, and increased susceptibility to infection (Hambidge, 2000). Conversely, Zn toxicity occurs in acute and chronic forms and is linked to several sources, including Zn supplements and parenteral nutrition, among others (Broun et al., 1990; Potter, 1981). Acute symptoms of Zn intoxication include symptoms like nausea and vomiting (McKinney et al., 1994), while chronic intoxication may result in reduced immune function and altered copper (Cu) and iron (Fe) levels, demonstrating the interconnectedness between nutrient metals within the body (Trumbo et al., 2001).

Host tissues and circulating cells evolved mechanisms to control Zn levels to mitigate against the adverse effects of Zn deficiency and toxicity on human health. In circulation, serum Zn is mostly bound by albumin, transferrin, and α_2-macroglobulin but remains accessible to transporters to balance Zn levels within cells (Rink and Haase, 2007). The primary regulators of mammalian Zn transport are the ZIP Zn importers and the Zn-transport (ZNT) exporters (**Figure 1**). There are 14 isoforms of mammalian ZIP transporters that share many structural and functional properties, where they facilitate the import of Zn, and sometimes other cations, into the cytoplasm from the extracellular space or from intracellular vesicles and organelles (Kimura and Kambe, 2016). However, aside from ZIP1 which is found on all cells, expression of the other ZIPs varies depending on the cell type (Bonaventura et al., 2015). Likewise, the ZNT family includes 10 isoforms, some of which are expressed ubiquitously, while others are cell-type specific (Bonaventura et al., 2015). ZNTs generally function in reverse of ZIPs, where they export Zn out of the cytoplasm into circulation or cellular vesicles and organelles. Expression of a subset of ZIPs and ZNTs is controlled by the Metal response element-binding Transcription Factor-1 (MTF-1) (Giedroc et al., 2001). MTF-1 is a cytoplasmic transcription factor that undergoes nuclear translocation following Zn binding, where it regulates certain ZIPs and ZNTs to maintain Zn homeostasis (Kimura and Kambe, 2016). However, not all Zn transporters are MTF-1-regulated, and the diversity of expression and localization of ZIPs and ZNTs highlights the importance of fine-tuning Zn levels depending on the tissue and cell type.

Aside from direct import and export of Zn, intracellular Zn sequestration also must occur to prevent toxicity. A major component of Zn chelation within eukaryotic cells occurs through the action of metallothionein and glutathione. Metallothionein and glutathione are cysteine-containing molecules that link reversible Zn binding with the cellular redox state (Jiang et al., 1998; Maret, 2000). This reversible Zn binding allows these molecules to serve as a component of the intracellular Zn buffering system that includes the potential delivery of Zn to apoforms of metalloenzymes (Jacob et al., 1998). Metallothionien is synthesized in several organs, including the liver and kidneys, and can be found in circulation (Rahman et al., 2017). *In vitro* estimates demonstrate that sulfur-containing molecules like metallothionein control approximately 30% of a cell's Zn buffering capacity (Krezel et al., 2007). However, the exact dynamics of Zn buffering are likely dependent on cell type and environmental conditions.

Alterations in nutrient Zn availability affect many biological processes, and mechanistic studies have identified how immune system function changes in response to Zn fluctuations (Rink and Haase, 2007). The impact of Zn deficiency on immune system function has been reviewed in-depth previously (Bonaventura et al., 2015; Rink and Haase, 2007). Importantly, altered Zn concentrations affect both innate and adaptive branches of the immune system. Within innate immunity, excess Zn can induce chemotaxis of neutrophils, which are one of the primary cell types responsible for innate immune-mediated pathogen clearance (Hujanen et al., 1995). Zn deficiency impedes the antimicrobial activity of neutrophils and macrophages by altering the oxidative burst and inhibiting phagocytosis (Hasegawa et al., 2000; Sheikh et al., 2010). The maturation of dendritic cells (DCs), which connect the innate and adaptive immune system through antigen presentation, is also modulated by Zn availability. DCs experiencing Zn deficiency increase expression of major histocompatibility complexes and costimulatory molecules, while Zn excess inhibits this upregulation (Kitamura et al., 2006). In the adaptive immune system, T cells and various T cells subsets are susceptible to alterations in Zn availability; insufficient Zn decreases T cell maturation while increasing apoptosis (King et al., 2005). Changes in Zn homeostasis alter the balance of T_H1, T_H2 and T_H17 subsets, and Zn supplementation promotes regulatory T cell induction and T_H9 differentiation (Kitabayashi et al., 2010; Maywald et al., 2018; Prasad, 2000; Rosenkranz et al., 2016). B cells appear to be impacted less by Zn deprivation, but they too experience a reduction in total cell numbers as well as alterations in development and antibody production (DePasquale-Jardieu and Fraker, 1984; Stefanidou et al., 2006). Collectively, these studies establish Zn homeostasis as a critical determinant of vertebrate survival and immune cell function.

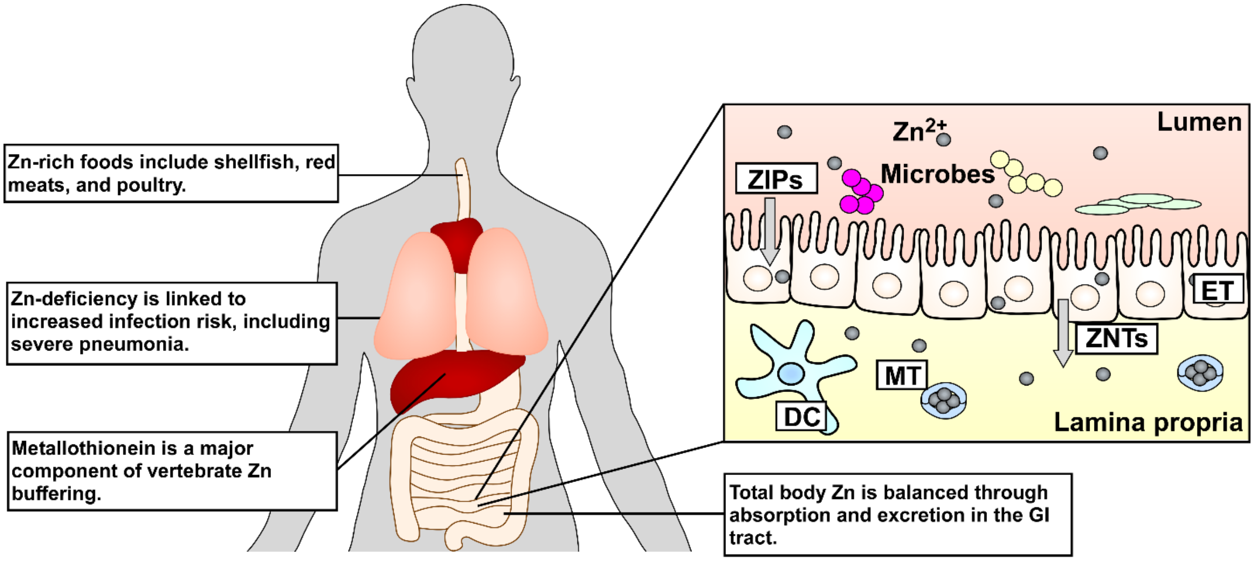

Figure 1. Vertebrate Zn homeostasis systems. Changes in dietary Zn (grey) can be associated with adverse clinical outcomes and diarrheal disease. Zn buffering is regulated by changes in epithelial cell (ET) Zn uptake/efflux associated with the gastrointestinal (GI) tract primarily by the action of ZIP Zn importers and ZNT Zn exporters. ZIP activity results in Zn uptake from the intestinal lumen into ETs, and ZNT activity results in efflux of Zn from the ETs via the lamina propria into circulation and the extracellular space. Small molecule Zn chelators such as metallothioneins (MTs) that are produced in high abundance by the liver and kidneys also contribute to Zn buffering (King et al., 2000). Immune cells such as dendritic cells (DCs) may respond differentially depending on nutrient Zn availability.

Zinc is mobilized during microbial infections

In addition to altered immune function in response to changes in dietary Zn, Zn availability can also modulate the response of the vertebrate host to infection and inflammation. During the acute phase of inflammation, serum Zn drops substantially due to proinflammatory cytokines altering Zn transporter expression, which results in the accumulation of Zn-bound metallothioneins by hepatocytes that capture incoming Zn (Aydemir et al., 2012) (**Figure 2**). This decrease in bioavailable Zn is part of an immune response known as nutritional immunity, which was first described for sequestration of Fe from invading microbes (Weinberg, 1974). However, our understanding of nutritional immunity has expanded in recent years to include other nutrients, such as manganese (Mn) and Zn (Palmer and Skaar, 2016). Nutritional immunity is implicated as a critical host defense mechanism for many types of pathogens, and the role of nutrient metal withholding during fungal infections has been reviewed previously (Crawford and Wilson, 2015). Host strategies to limit Zn availability from bacterial pathogens include both cell-mediated Zn restriction and extracellular Zn sequestration. Cell-mediated Zn restriction occurs mainly through the activity of Zn transporters. For example, the ZIP8 Zn transporter is expressed by immune cells, where it associates with the lysosomal transmembrane glycoprotein Lamp1 and decreases lysosomal Zn levels (Pyle et al., 2017) (**Figure 2**). These findings suggest that Zn is actively removed from the lysosome as a strategy to limit nutrient Zn from pathogens trapped within this cellular compartment.

Extracellular Zn sequestration mechanisms implicate members of the S100 protein family as being critical for Zn limitation during infections (**Figure 2**). S100 proteins are EF-hand calcium-binding proteins found in vertebrates that serve important functions in basic physiology and in the host inflammatory response (Zackular et al., 2015). A unifying feature among S100 proteins is that they form dimers and may form transition metal binding sites at the dimer interface (Zackular et al., 2015). S100A8 and S100A9 are unique among S100 proteins in that they preferentially form heterodimers (Hunter and Chazin, 1998). The heterodimeric S100A8/S100A9 protein complex is called calprotectin (also known as calgranulin A/B or myeloid-related protein 8/14). Calprotectin (Vokaty et al.) is involved in many biological processes, including serving as a damage-associated molecular pattern (DAMP) and as ligands for Toll-like receptor 4 (TLR4), the receptor for advanced glycation end products (Falagas et al.), and CD33 (Eksioglu et al., 2017; Leclerc et al., 2009; Vogl et al., 2007). CP is readily detected at infectious foci during infections (Corbin et al., 2008) and accounts for more than 40% of the cytoplasmic protein content of neutrophils (Yui et al., 2003), underscoring CP's importance during an immune response.

Part of CP's immunological importance is due to the protein's ability to chelate nutrient metals. At the dimer interface between S100A8 and S100A9, two metal binding sites are formed that are termed Site I and Site II. Site I possess broad metal-binding capabilities, including ability to bind Zn, manganese (Mn), Fe, Cu, and nickel (Ni) (Besold et al., 2017; Corbin et al., 2008; Damo et al., 2013; Kehl-Fie et al., 2011; Nakashige et al., 2015; Nakashige et al., 2017). Site II only coordinates Zn with high affinity (Brophy et al., 2012; Damo et al., 2013; Korndorfer et al., 2007). The two metal binding sites are important for CP's antimicrobial activity, as demonstrated by numerous microbial pathogens displaying growth inhibition *in vitro* in the presence of CP (Besold et al., 2017; Clark et al., 2016; Clohessy and Golden, 1995; Corbin et al., 2008; Gaddy et al., 2014; Hood et al., 2012; Zygiel et al., 2019). Importantly, addition of exogenous Zn and Mn is generally sufficient to reverse CP-mediated growth inhibition, which demonstrates that metal-binding by CP is adequate to limit microbial growth (Zackular et al., 2015). However, other nutrient metals have been implicated in binding by CP, including Ni and Fe, among others. While the relative contribution of CP to Ni withholding is not yet known, Fe is increasingly recognized as a metal restricted by CP (Wang et al., 2019; Zygiel et al., 2019). Further, mice deficient in producing the CP heterodimer (*S100A9*$^{-/-}$) have altered infection susceptibility, demonstrating that CP is critical to infection outcome (Achouiti et al., 2012; Corbin et al., 2008; Gaddy et al., 2014; Hood et al., 2012; Kehl-Fie et al., 2011; Urban et al., 2009; Wakeman et al., 2016; Zackular et al., 2016).

Other S100 proteins are also implicated in Zn withholding at the host-pathogen interface, including S100A7 and S100A12 (**Figure 2**). S100A7, also called psoriasin, functions as a homodimer and is constitutively expressed in the skin and at mucosal surfaces. S100A7 binds two Zn ions across the dimer interface (Brodersen et al., 1999). Similar to CP, Zn withholding by S100A7 may contribute to limiting metal availability from bacteria (Glaser et al., 2005). S100A12, also known as calgranulin C, also functions as a homodimer and binds Zn and Cu at its dimer interface (Moroz et al., 2003). Recombinant S100A12 can inhibit microbial growth through Zn chelation (Haley et al., 2015; Shank et al., 2018), but its broader contribution to immunity has been difficult to define due to its absence in mice (Zackular et al., 2015). Additionally, the contribution of S100A12 to Cu withholding during bacterial infections is largely unexplored.

Zn mobilization occurs during infections not only to sequester the metal from invading pathogens, but perhaps to be trafficked within immune cells to impart toxicity (**Figure 2**). While Zn is redox-inactive, the Irving-Williams series predicts that the high affinity of Zn for metal binding sites promotes aberrant loading of Zn to non-Zn proteins, which leads to toxic effects through mismetallation or other indirect mechanisms (Braymer and Giedroc, 2014). Macrophages infected with *Mycobacterium tuberculosis* accumulate Zn within the cell that is sufficient to induce bacterial Zn intoxication (Botella et al., 2011). Additionally, internalization of *Streptococcus* *pyogenes* by human neutrophils results in Zn mobilization that may induce bacterial Zn poisoning (Ong et al., 2014). Conversely, macrophages infected with the fungal pathogen *Histoplasma capsulatum* also accumulate Zn, but this Zn is shuttled from the phagosome to the Golgi apparatus in a granulocyte macrophage-colony stimulating factor (GM-CSF)-dependent manner (Subramanian Vignesh et al., 2013a). Downstream consequences of this Zn shuttling include generation of reactive oxygen species (ROS) to inhibit *H. capsulatum* growth, presumably by preventing appropriate metalation of Zn/Cu superoxide dismutase enzymes (Subramanian Vignesh et al., 2013b). These results imply that Zn accumulation within immune cells, mediated by shuttling of Zn out of the phagosome, indirectly diminishes pathogen viability (Subramanian Vignesh et al., 2013b). These findings suggest that both Zn starvation and toxicity are employed by the host to limit microbial survival, but precise situations in which starvation or toxicity may be utilized is not well-defined.

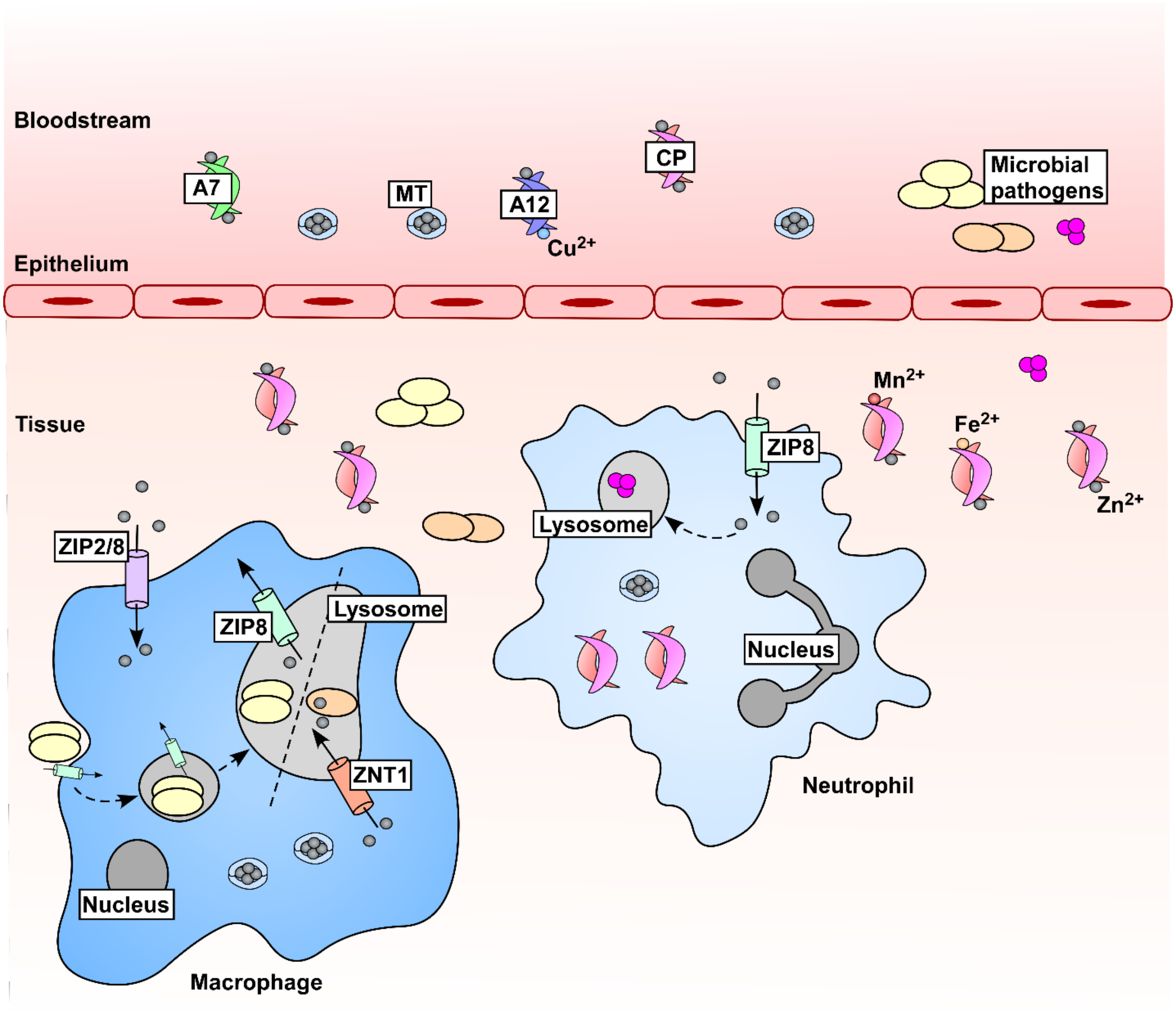

Figure 2. Zn is mobilized in hosts during microbial infections and inflammation. In response to microbial challenge, serum Zn drops through increased expression of zinc transporters (not depicted) and mobilization and uptake of Zn-binding metallothioneins (MTs). Immune cells contribute to changes in Zn availability, where expression of ZIP Zn importers drives accumulation of Zn within these cells. Zn is also mobilized within immune cells; *Mycobacterium tuberculosis* (orange ovals) experiences Zn intoxication within macrophages in a ZNT1-dependent manner, and *Streptococcus pyogenes* (pink spheres) is poisoned by Zn within the neutrophil lysosome (Botella et al., 2011; Ong et al., 2014). Conversely, the fungal pathogen *Histoplasma capsulatum* (yellow ovals) has been shown to be Zn-starved within the macrophage lysosome (Subramanian Vignesh et al., 2013a). These two mechanisms within the lysosome are denoted by a dashed line. Additionally, metal-chelating proteins are produced as part of the inflammatory response to further reduce Zn availability for pathogens, including those within the S100 protein family. S100A7 binds Zn and is produced in high abundance by keratinocytes, and S100A12 binds both Zn and Cu. The heterodimer of S100A8/S100A9, known as calprotectin (Vokaty et al.), binds Zn with high affinity, as well as other divalent cations. CP is a major component of the neutrophil cytoplasmic protein content and is abundant at sites of infection and inflammation within vertebrates.

Metalloregulators control bacterial zinc homeostasis

In response to metal restriction by the host, microbes have evolved mechanisms to subvert nutritional immunity during infections. The bacterial response to changes in metal availability is primarily mediated by metalloregulatory proteins, although metabolite-sensing and riboswitch-mediated sensing systems are also described (Chandrangsu et al., 2017). Generally, these metalloregulators sense changes in cellular metal concentrations and alter gene expression of metal homeostatic systems. These metalloregulators are widely distributed in bacteria, and they respond to metal limitation, metal intoxication, or both conditions. The diversity in bacterial metalloregulators has been reviewed previously (Capdevila et al., 2017), therefore will focus here specifically on mechanisms of bacterial Zn homeostasis.

As a bacterial cell experiences Zn starvation, transcriptional changes must occur to counterbalance these conditions. Many diverse Zn-responsive transcriptional regulators have been identified and reviewed previously (Choi and Bird, 2014). In many bacterial pathogens, the primary regulator for Zn homeostasis is the Zn uptake regulator (Zur) (Gaballa and Helmann, 1998; Patzer and Hantke, 1998). Zur is a member of the ferric uptake regulator (Fur) family of metallosensing DNA-binding proteins. Metal-sensing by Fur family members is directly mediated by metal binding to the metalloregulator, which induces conformational changes and alters the regulator's affinity for DNA (Lee and Helmann, 2007). Zur is exquisitely sensitive to Zn fluctuations and senses changes to Zn concentrations in the femtomolar (10^{-15}) range to regulate transcription (Outten and O'Halloran, 2001). In Zn-replete conditions, the metal binding sites of Zur are predicted to be occupied. The increased affinity of Zn-bound Zur for DNA permits the metalloregulator to recognize and bind to conserved palindromic inverted repeat regions, termed Zur boxes, in the DNA promoter region of its regulon (Lee and Helmann, 2007). The Zur box location generally overlaps with motifs required for effective RNA polymerase recruitment, thereby inhibiting gene transcription. Upon Zn starvation, an increasing proportion of Zur is no longer bound by Zn, which diminishes the affinity of Zur binding to DNA and results in derepression of the Zur regulon (Gilston et al., 2014). Derepression of the Zur regulon induces several physiological changes, and general themes will be explored for Gram-positive and Gram-negative bacteria.

Zinc sensing in Gram-positive bacteria

Mechanistic studies into the response of Gram-positive bacteria to Zn starvation have been conducted in several organisms (Chandrangsu et al., 2017). In *Bacillus subtilis*, Zn starvation is sensed by the metalloregulator Zur (Gaballa and Helmann, 1998). However, non-Fur family Zn metalloregulators have been identified as well; for example, *Streptomyces pneumoniae* controls Zn uptake through the MarR family member AdcR (Reyes-Caballero et al., 2010). Precise investigations into Zn sensing by *B. subtilis* Zur revealed that the regulator possesses differential activity, corresponding to varying DNA affinity, depending on the number of Zn-binding sites occupied (Ma et al., 2011)(**Figure 3**). This differential activity permits a fine-tuned response to Zn starvation that occurs in a step-wise fashion with three distinct stages (Shin and Helmann, 2016). First, non-Zn utilizing ribosomal proteins L31* and L33* are expressed, which replace Zn-requiring isoforms to effectively decrease the total cellular requirement of Zn and promote Zn mobilization. Second, the high affinity Zn uptake ABC transport system genes, *znuABC*, are derepressed to promote Zn acquisition. The ZnuABC system is widely conserved across many species and therefore represents a major metal acquisition system, although other transporters also promote Zn uptake (**Table 1**). Along with *znuABC*, the predicted Zn metallochaperone gene *zagA* (formerly *yciC*) is also derepressed (Chandrangsu et al., 2019; Gabriel et al., 2008). Finally, further Zn starvation leads to induction of an additional alternative ribosomal protein S14* to sustain protein synthesis and the Zn-independent GTP cyclohydrolase I FolE2, which permits the continuation of *de novo* folate biosynthesis, which is a critical metabolite for life (Shin and Helmann, 2016). While the extent to which this graded response occurs in other bacteria is not well-defined, the Gram-negative pathogen *Salmonella enterica* serovar Typhimurium has some features of a graded transcriptional response (Osman et al., 2019). Additionally, these same general transcriptional changes occur in other Gram-positive organisms during Zn limitation. These responses include expression of the Zur-regulated Zn uptake systems in *Listeria monocytogenes, Bacillus anthracis, Staphylococcus aureus,* and *Streptococcus pyogenes* (Dalet et al., 1999; Grim et al., 2017; Kandari et al., 2018; Makthal et al., 2017) and Zn mobilization via induction of non-Zn requiring ribosomal proteins in *Streptomyces coelicolor* (Shin et al., 2007).

Bacteria also respond to Zn toxicity through metal-sensing transcriptional regulators. While some metalloregulators can function as both repressors and activators (Huang et al., 2017), others are functionally divided. In *B. subtilis*, excess Zn is sensed by the ArsR family of metalloregulators, CzrA (Moore et al., 2005), which effectively functions in reverse of Zur (**Figure 3**). When CzrA is not metallated, the protein represses its regulon. Upon metalation, CzrA undergoes a conformational change that lowers its DNA binding affinity and leads to derepression of metal efflux genes that encode a P-type ATPase named CadA and a cation diffusion facilitator type transporter named CzcD (Moore et al., 2005). Analogous proteins are involved in detoxification of other divalent cations (Nies, 2003), demonstrating that metal efflux is a broadly conserved bacterial strategy to overcome metal intoxication.

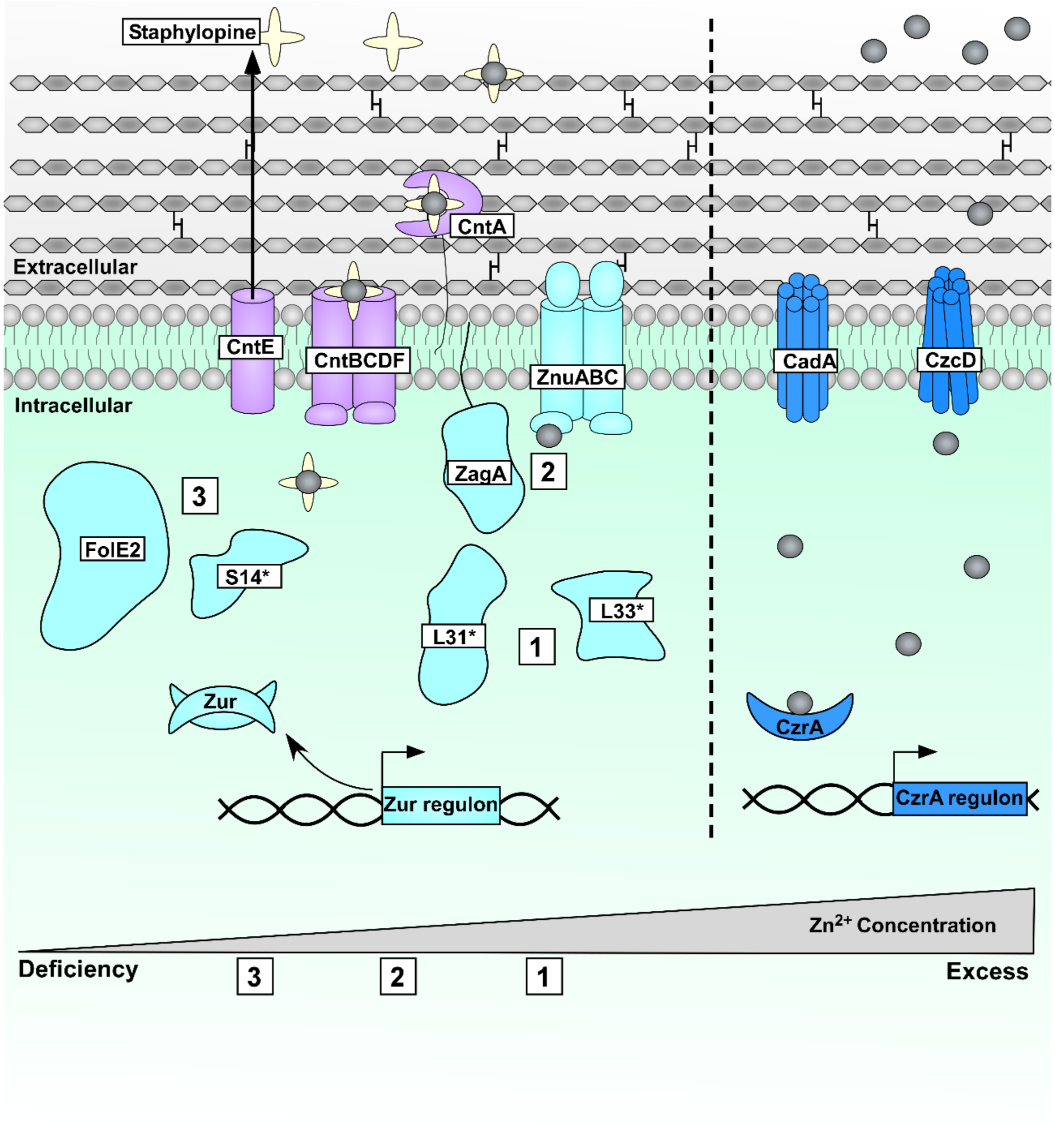

Figure 3. Zn sensing in Gram-positive bacteria. In response to Zn starvation, the *Bacillus subtilis* Zur regulon experiences derepression in three distinct waves. **1)** The non-Zn binding ribosomal proteins L31* and L33* are synthesized to displace the Zn-binding L31/L33 ribosomal proteins, followed by **2)** upregulation of the ZnuABC high affinity Zn transport system and the putative metallochaperone ZagA (Chandrangsu et al., 2019). Lastly, **3)** the Zn-independent GTP cyclohydrolase I enzyme FolE2 and the non-zinc requiring S14* ribosomal protein are expressed. Some Gram-positive organisms also produce metal-binding small molecules to capture Zn from the extracellular space. For example, *Staphylococcus aureus* produces the metal-binding small molecule staphylopine that aids in Zn acquisition (Ghssein et al., 2016; Grim et al., 2017). Staphylopine is secreted via CntE, captured by CntA, and imported by the CntBCDF system. Gram-positive bacteria also experience transcriptional changes in response to Zn excess; in *B. subtilis*, CzrA-regulated genes are expressed during Zn intoxication and includes the P-type ATPase CadA and the cation diffusion family (CDF) transporter CzcD (Moore et al., 2005). Expression of these proteins results in Zn efflux from the bacterial cell.

Zinc sensing in Gram-negative bacteria

Consistent with findings in Gram-positive bacteria, Gram-negative organisms primarily sense Zn starvation through the metalloregulator Zur (**Figure 4**). Structural insights into *Escherichia coli* Zur-DNA interactions have provided important details about protein conformational changes that occur during Zn binding by Zur. High sequence similarity among Zur homologs from different species suggests these mechanisms are conserved (Gilston et al., 2014). As is the case with Gram-positive Zur homologs, Zur-regulated derepression in Gram-negative organisms includes induction of genes encoding the high affinity ZnuABC Zn transporters, and these transporters are important for virulence of important human pathogens (Hood et al., 2012; Liu et al., 2012) (**Table 1**). Additionally, the Zur regulon has been defined for several Gram-negative bacteria, including *Yersinia pestis* (Li et al., 2009), *Neisseria meningitidis* (Pawlik et al., 2012), and *Acinetobacter baumannii* (Mortensen et al., 2014); in addition to the highly conserved ZnuABC transporters, non Zn-binding ribosomal proteins are also typically increased in expression in response to Zn limitation (Capdevila et al., 2017). Further, Zn starvation induces expression of an outer membrane TonB-dependent Zn transporter named ZnuD in *N. meningitidis* (Stork et al., 2010) (**Figure 4**). Structural studies into *N. meningitidis* ZnuD demonstrate that large extracellular loops directly interact with Zn ions and suggest active uptake of free Zn from the extracellular space. Interestingly, ZnuD possesses structural homology to bacterial heme transporters but does not bind heme (Calmettes et al., 2015); these findings demonstrate that ZnuD is capable of binding free Zn but does not exclude the possibility that ZnuD may bind Zn in some chelated form. *A. baumannii* also encodes ZnuD homologues that are directly regulated by Zur (Mortensen et al., 2014). In addition to the ZnuD with high homology to the *N. meningitidis* ZnuD, certain *A. baumannii* strains encode an additional candidate *znuD*, denoted *znuD2* (Mortensen et al., 2014). However, the relative contribution of each of these ZnuD transporters to *A. baumannii* Zn homeostasis is unknown.

Similar to *B. subtilis* CzrA, *E. coli* possesses a separate metalloregulator named ZntR to respond to Zn excess (Brocklehurst et al., 1999) (**Figure 4**). ZntR is a member of the MerR family of transcriptional regulators. ZntR recognizes conserved inverted repeat sequences in the promoter region of the gene encoding a P-type ATPase named ZntA (Brocklehurst et al., 1999). Apo-ZntR binds this inverted repeat and causes DNA distortions that prevent gene transcription (Outten et al., 1999). Following Zn binding, Zn-ZntR induces DNA untwisting and unkinking that promotes efficient RNA polymerase recruitment and *zntA* expression (Outten et al., 1999). Induction of P-type ATPases and cation diffusion family (CDF) transporters during Zn intoxication have been shown in other Gram-negative organisms as well. In *A. baumannii*, Zn intoxication leads to significant induction of a wide array of P-type ATPases and CDF transporters that also deplete cellular copper levels (Hassan et al., 2017). While the transcriptional regulator responsible for these changes is undefined, an *A. baumannii* strain lacking Zur has increased expression of predicted cation efflux systems and other transporters, which suggesting Zur plays a regulatory role in Zn efflux (Mortensen et al., 2014).

Bacterial zinc homeostasis beyond transporters

More recently, our understanding of bacterial Zn uptake has been expanded to include additional systems other than the ZnuABCD transporters. One strategy that has become increasingly appreciated for Zn acquisition is the production and secretion of Zn-binding small molecules (**Figures 3 & 4**). This strategy is well-defined for Fe, where Fe-binding molecules termed siderophores are produced that facilitate Fe acquisition in diverse environments (Sheldon et al., 2016). However, some siderophores are capable of binding other nutrient metals, including Zn. The Gram-negative bacterium *Pseudomonas putida* produces the siderophore pyridine-2,6-bis(thiocarboxylic acid) (PDTC) that is capable of binding both ferric Fe and Zn (Cortese et al., 2002; Leach et al., 2007). Other siderophores including pyochelin, micacocidin, and yersiniabactin have been shown to bind Fe, Zn, and potentially other metals (Braud et al., 2010; Braud et al., 2009; Chaturvedi et al., 2012; Kobayashi et al., 1998; Kreutzer et al., 2011). Mechanistic studies into the role of yersiniabactin in Zn uptake revealed that the Gram-negative pathogen *Yersinia pestis* uses a dedicated Zn-yersiniabactin importer named YbtX to acquire Zn from the molecule; further, genetic inactivation of the *znu* system and yersiniabactin biosynthetic genes reduces *Y. pestis* virulence in a septicemic plague model (Bobrov et al., 2014). Zn-binding metallophores have also been implicated in Gram-positive Zn acquisition. For example, *Streptomyces coelicolor* produces a small molecule termed coelibactin which may bind Zn (Zhao et al., 2012), and *S. aureus* produces the metallophore staphylopine with broad metal-chelating abilities that affect Zn homeostasis (Ghssein et al., 2016; Grim et al., 2017).

Type VI secretion systems (T6SSs) are multiprotein machines used by many Gram-negative bacterial species to translocate effectors into neighboring cells and have been implicated in Zn acquisition (**Figure 4**). *Burkholderia thailandensis* produces a Zn-scavenging molecule named TseZ that is secreted through a specific T6SS, termed T6SS4. Zn-bound TseZ is then imported into the bacterial cell using the heme transporter HmuR specifically during conditions of oxidative stress, where Zn may be used to populate Cu/Zn superoxide dismutase enzymes and ameliorate potential damage from reactive oxygen species (Si et al., 2017). A similar model also occurs in *Y. pseudotuberculosis*, where the oxidative stress regulator OxyR induces expression of T6SS4 (Wang et al., 2015). Additionally, ZntR was recently identified as a transcriptional activator of the *Y. pseudotuberculosis* T6SS4 (Wang et al., 2017), which is consistent with the observation that Zn deficiency promotes increased oxidative damage (Eide, 2011). This T6SS4 can translocate a Zn-binding molecule named YezP that aids in Zn uptake. While a dedicated importer for YezP is not known, there likely exists an energy-dependent transporter that facilitates YezP uptake, as is the case for other metal-binding small molecules (Sheldon et al., 2016; Wang et al., 2015).

Cell wall modifications are necessary to construct complex secretion systems and other macromolecular structures. Given the induction of T6SSs and Zn uptake machinery during Zn limitation, there may be changes to the bacterial cell envelope that occur specifically during nutrient starvation. Indeed, members of the genus *Acinetobacter* are morphologically-constricted to shortened, rounded cells during nutrient limitation and significantly alter the abundance of major peptidoglycan muropeptides (James et al., 1995; Lonergan et al., 2019). Further, the M15 family Zn-binding peptidase ZrlA contributes to these muropeptide changes and promotes efficient Zn uptake and cell envelope barrier function (Lonergan et al., 2019). In *Vibrio cholerae* the M23 family Zn-binding endopeptidase ShyB is implicated in cell wall maintenance during Zn limitation (Murphy et al., 2019). Importantly, both ZrlA and ShyB are directly regulated by Zur and collectively demonstrate that bacterial pathogens encode peptidoglycan-modifying enzymes that are important for surviving Zn limitation (**Figure 4**).

In addition to the production of metal-chelating molecules by bacterial pathogens, some bacteria can utilize host-derived molecules as a metal source. For example, *S. aureus* can use human hemoglobin as its sole Fe source through deployment of the iron-regulated surface determinant (Isd) system (Mazmanian et al., 2003). As the second most abundant trace metal in humans, Zn scavenging within the vertebrate host may be an effective strategy to subvert nutritional immunity. Consistent with this prediction, the *N. meningitidis* TonB-dependent outer membrane receptor protein CpbA is expressed during Zn starvation (Stork et al., 2010) (**Figure 4**). CpbA is capable of binding human CP, and the presence of CpbA permits *N. meningitidis* to use CP as its sole Zn source. Additionally, the CpbA homolog in *Neisseria gonorrhoeae* named TdfH also binds CP and permits Zn acquisition from the protein (Jean et al., 2016). These "Zn piracy" mechanisms (Stork et al., 2013) represent an exciting new area of future investigation towards understanding bacterial Zn acquisition during vertebrate colonization.

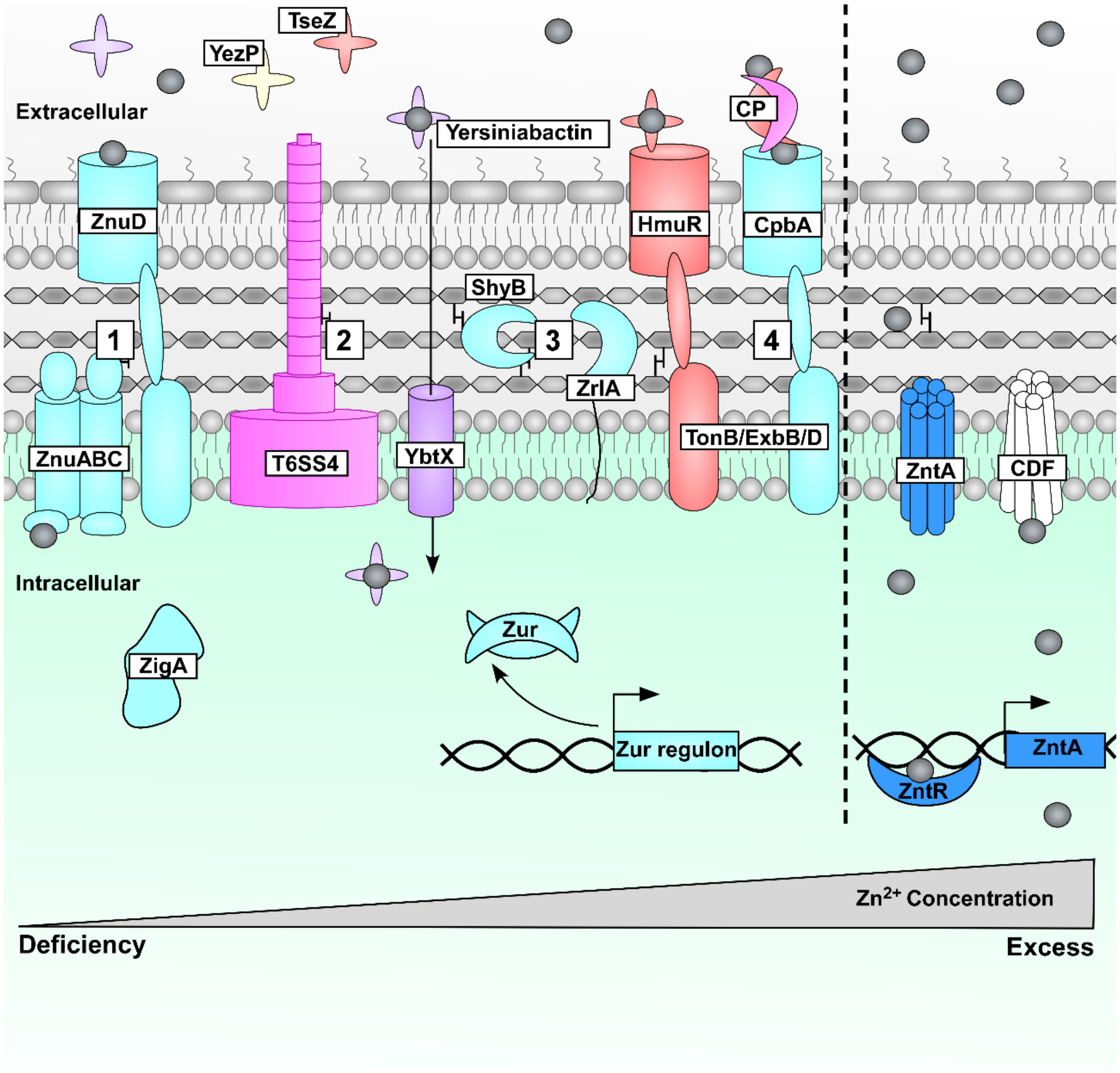

Figure 4. Zn sensing in Gram-negative bacteria. Zn starvation in Gram-negative bacteria leads to a number of physiological changes. **1)** Zur-derepression leads to expression of genes encoding the Zn uptake ZnuABCD system, as well as the predicted Zn metallochaperone ZigA in *Acinetobacter baumannii* (Nairn et al., 2016). **2)** Zn-binding molecules are produced such as YezP and TseZ, which are secreted by T6SS4, and yersiniabactin, which is captured by YbtX (Bobrov et al., 2014; Si et al., 2017; Wang et al., 2015). **3)** Enzymes implicated in cell wall homeostasis are induced, including *Vibrio cholerae* ShyB (Murphy et al., 2019) and *A. baumannii* ZrlA (Lonergan et al., 2019). **4)** TonB-dependent transporters aid in the uptake of Zn-bound molecules; *Burkholderia thailandensis* HmuR captures the TSS64-secreted TseZ (Si et al., 2017) , and *Neisseria meningititis* and *Neisseria gonorrhoeae* use CpbA/TdfH to bind calprotectin (Vokaty et al.) for Zn acquisition as a form of Zn piracy (Jean et al., 2016; Stork et al., 2013). During Zn intoxication, *Escherichia coli* Zn-ZntR causes DNA conformational changes leading to expression of the P-type ATPase ZntA to alleviate the metal toxicity (Brocklehurst et al., 1999). Many Gram-negative organisms also encode cation diffusion family (CDF) transporters that contribute to overcoming Zn intoxication.

Bacterial zinc buffering and allocation

Metal availability varies widely across environments and niches. Therefore, bacterial survival is largely dependent on systems to maintain cellular metabolism despite fluctuations in available nutrients. Considering there is essentially no free Zn within a bacterial cell despite the relatively high total Zn level, Zn must exist in chelated forms that is accessible during Zn starvation (Outten and O'Halloran, 2001). In *B. subtilis*, Zn limitation induces expression of non-Zn binding ribosomal proteins and the Zn-independent folate biosynthesis enzyme FolE2 (Nanamiya et al., 2004; Shin and Helmann, 2016)(**Figure 5**). In a system analogous to eukaryotic metallothionein, *B. subtilis* uses the low-molecular weight molecule bacillithiol to maintain an intracellular labile Zn pool (Ma et al., 2014). Similarly, *E. coli* uses glutathione to buffer Zn and other divalent cations (Helbig et al., 2008). *A. baumannii* utilizes the amino acid L-histidine as a component of its labile pool (Nairn et al., 2016); during conditions of Zn starvation, *A. baumannii* upregulates the histidine utilization (Hut) system, thereby catabolizing cellular Zn-histidine complexes and increasing levels of bioavailable Zn (Nairn et al., 2016) (**Figure 5**). However, the complete inventory of molecules capable of aiding in Zn buffering is not well-defined and warrants further investigation.

The requirement of Zn for many cellular processes suggests that a mechanism exists to ensure appropriate metalation of cognate metalloproteins, particularly during times of Zn starvation. For metalloregulators, differences in standard free energies for metal complex formation compared to relative metal-binding affinities dictates regulator-metal specificity (Osman et al., 2019). However, the process of appropriate metallation is likely more complex for diverse metalloenzymes. To aid in proper metal allocation, members of the G3E GTPase superfamily have been identified as metallochaperones and/or metal insertases (Haas et al., 2009). Four subfamilies exist within the G3E superfamily. Two of the subfamilies, represented by the metallochaperones UreG and HypB, are involved in Ni incorporation into the Ni metalloenzymes urease and hydrogenase, respectively (Maier et al., 1995; Mehta et al., 2003). A third family is represented by MeaB, which is involved in methylmalonyl-CoA mutase activation (Hubbard et al., 2007). The fourth subfamily, denoted the COG0523 subfamily, is less defined but is conserved in all domains of life (Haas et al., 2009). Genomic analyses suggest that a subset of COG0523 members are Zur-regulated and may therefore serve as Zn metallochaperones (Haas et al., 2009). Representative members include *E. coli* YjiA and YeiR, *B. subtilis* ZagA, and *A. baumannii* ZigA. Each of these proteins bind Zn and possess GTPase activity (Blaby-Haas et al., 2012; Khil et al., 2004; Nairn et al., 2016; Sydor et al., 2013) (**Figure 5**). Since Zn is required for many essential cellular processes, COG0523 members may aid in the prioritization of Zn to core metabolic processes when the metal is limited (Wang et al., 2019). Consistent with this prediction, analyses of the response of *B. subtilis* and *A. baumannii* to Zn starvation revealed that folate and riboflavin biosynthesis are hindered, respectively (Chandrangsu et al., 2019; Wang et al., 2019). In *B. subtilis*, ZagA interacts with the Zn-dependent FolE enzyme and aids in folate biosynthesis during Zn starvation, and this interaction is dependent on the Z nucleotide ZTP (Chandrangsu et al., 2019). In *A. baumannii*, severe Zn restriction hinders *de novo* flavin biosynthesis (Wang et al., 2019). This flavin deficiency is exacerbated in a strain lacking *zigA* (Wang et al., 2019), which suggests that ZigA impacts flavin biosynthesis. These studies position Zn metallochaperones at important metabolic hubs, and uncovering other processes altered by COG0523 members represents an exciting area of future research.

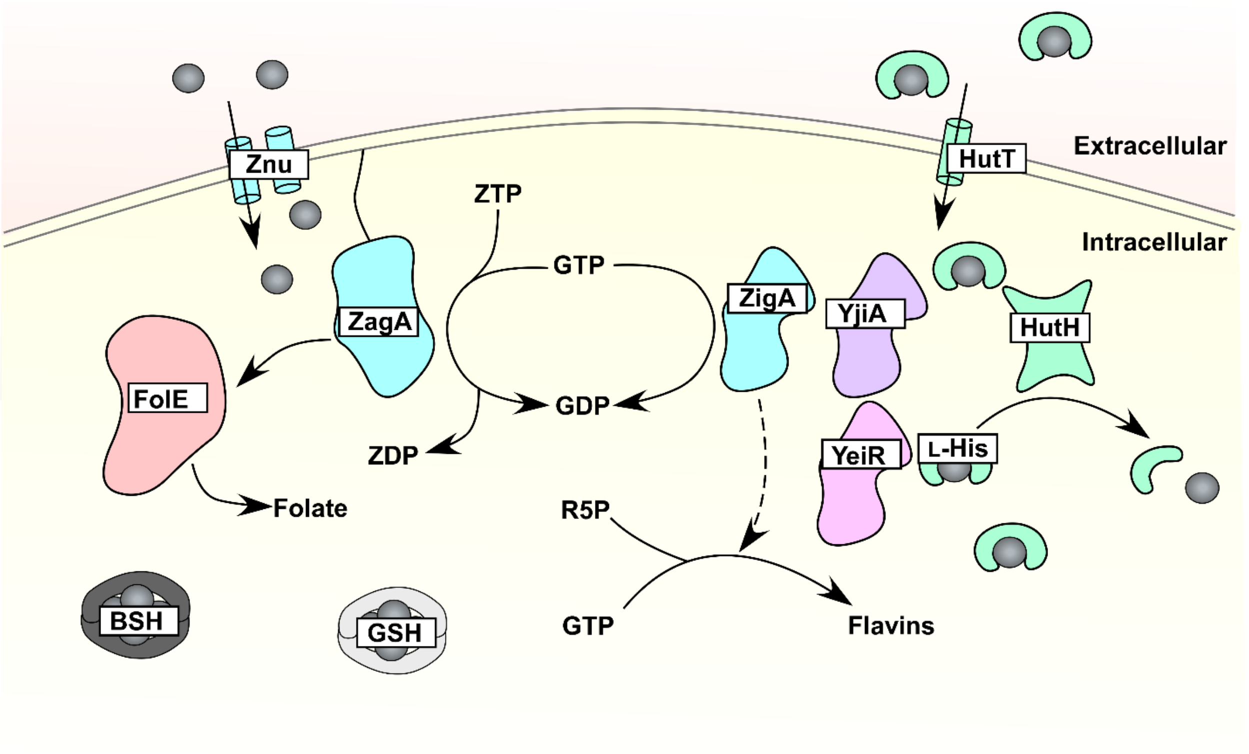

Figure 5. Bacterial systems for Zn buffering. In order to buffer cellular changes to Zn availability, bacteria employ small molecules to bind excess Zn that can be accessed during zinc limitation. Bacillithiol (BSH) in *Bacillus subtilis*, glutathione (GSH) in *Escherichia coli,* and L-histidine in *Acinetobacter baumannii* serve as components of the labile Zn pool (Helbig et al., 2008; Ma et al., 2014; Nairn et al., 2016). In *A. baumannii*, the histidine transporter HutT captures Zn-L-His, and its subsequent HutH-mediated degradation is hypothesized to liberate Zn (Nairn et al., 2016). The delivery of Zn to metalloenzymes remains an area of active investigation, but the mobilization of enzymes involved in essential cofactor biosynthesis implicates these pathways targets for Zn metallochaperone activity. Consistent with this prediction, *B. subtilis* folate biosynthesis and *A. baumannii* riboflavin biosynthesis are stressed during Zn limitation. In *B. subtilis*, the metallochaperone ZagA responds to Zn limitation and the purine alarmone ZTP to interact with, and possibly metallate, the Zn-dependent folate biosynthetic enzyme FolE (Chandrangsu et al., 2019). In *A. baumannii*, the predicted metallochaperone ZigA contributes to maintenance of cellular flavin levels during Zn limitation through an undefined mechanism (Wang et al., 2019). Possible metallochaperone interactions are denoted with arrows in the figure.

Conclusions

Zn is required for life, which necessitates that both bacterial pathogens and vertebrate hosts have evolved strategies to acquire and maintain appropriate Zn levels. Members of the S100 protein family such as CP are capable of withholding Zn from invading pathogens; however, the extent to which Zn starvation occurs in diverse sites within the host is unexplored, but it is likely niche- and pathogen-specific. For example, *S. aureus* microcolonies experience heterogeneous Fe starvation even within a single tissue (Cassat et al., 2018), which suggests a complex interplay in metallostasis between host and pathogen that that has yet to be defined.

Within a bacterial cell, Zn starvation upregulates Zn uptake machinery, but it also has major consequences for Zn-dependent metabolic processes. Zn starvation has been shown to change ribosome composition, alter bacterial cell wall dynamics, and impact labile Zn pools within the cell. Additionally, representative COG0523 members ZigA and ZagA have been implicated in Zn allocation to metalloenzymes but further exploration is required to determine their precise mechanisms of action as well as the identity of their client proteins. Interestingly, COG0523 members are also present in humans (Haas et al., 2009), which suggests that understanding their functionality within bacteria may inform metal homeostasis more broadly. Interrogating systems used by both vertebrates and microbes to balance nutrient metals has the potential to improve human health while simultaneously broadening our understanding of metal biology.

Table 1. Bacterial pathogen zinc uptake systems.

Transporter	**Pathogen**	**Role in Pathogenesis**	**Reference**
ZnuABC	*Acinetobacter baumannii*	Lung colonization	(Hood et al., 2012)
	Brucella abortus	Macrophage survival and systemic infection	(Yang et al., 2006)
	Campylobacter jejuni	Cecal colonization	(Davis et al., 2009)
	Escherichia coli	Epithelial cell interactions and urinary tract infections	(Gabbianelli et al., 2011; Patzer and Hantke, 1998; Sabri et al., 2009)
	Francisella tularensis	Macrophage survival	(Moreau et al., 2018)
	Moraxella catarrhalis	Intracellular invasion and lung colonization	(Murphy et al., 2013)
	Neisseria gonorrhoeae	Not defined	(Chen and Morse, 2001)
	Pasturella multocida	Systemic infection	(Garrido et al., 2003)
	Proteus mirabilis	Urinary tract infections	(Nielubowicz et al., 2010)
	Pseudomonas aeruginosa	Not defined	(Pederick et al., 2015)
	Salmonella enterica serovar Typhimurium	Systemic infection and cecal inflammation	(Ammendola et al., 2007; Campoy et al., 2002; Liu et al., 2012)
	Treponema pallidum	Not defined	(Desrosiers et al., 2007)
	Vibrio cholerae	Gut colonization	(Sheng et al., 2015)
	Vibrio parahaemolyticus	Systemic infection	(Liu et al., 2013)
	Yersinia pestis	Systemic infection when yersiniabactin production is inactivated	(Bobrov et al., 2014)
ZnuD	*Neisseria meningitis*	Complement resistance	(Hubert et al., 2013; Stork et al., 2013)
AdcABC	*Streptococcus agalactiae*	Survival in human biological fluids	(Moulin et al., 2016)
	Streptococcus pneumoniae	Survival in biological fluids	(Bayle et al., 2011)
	Streptococcus pyogenes	Systemic infection	(Makthal et al., 2017)
ZupT	*Escherichia coli*	Urinary tract infection	(Sabri et al., 2009)
	Francisella tularensis	Macrophage survival	(Moreau et al., 2018)

	Salmonella enterica serovar Typhimurium	Systemic infection	(Cerasi et al., 2014)
ZinT	*Escherichia coli*	Epithelial cell adherence	(Gabbianelli et al., 2011)
	Salmonella enterica serovar Typhimurium	Systemic infection when *znuA* is inactivated	(Petrarca et al., 2010)
ZinABC/ZurA	*Listeria monocytogenes*	Lethality following oral infection	(Corbett et al., 2012)
ZevAB	*Haemophilus influenzae*	Lung colonization	(Rosadini et al., 2011)
TroABCD	*Treponema pallidum*	Not defined	(Desrosiers et al., 2007)

References

Achouiti, A., Vogl, T., Urban, C.F., Rohm, M., Hommes, T.J., van Zoelen, M.A., Florquin, S., Roth, J., van 't Veer, C., de Vos, A.F., *et al.* (2012). Myeloid-related protein-14 contributes to protective immunity in gram-negative pneumonia derived sepsis. *PLoS pathogens 8,* e1002987.

Adedeji, W.A. (2016). The Treasure Called Antibiotics. *Ann Ib Postgrad Med 14,* 56-57.

Ammendola, S., Pasquali, P., Pistoia, C., Petrucci, P., Petrarca, P., Rotilio, G., and Battistoni, A. (2007). High-affinity Zn2+ uptake system ZnuABC is required for bacterial zinc homeostasis in intracellular environments and contributes to the virulence of Salmonella enterica. *Infection and immunity 75*, 5867-5876.

Andreini, C., Banci, L., Bertini, I., and Rosato, A. (2006a). Counting the zinc-proteins encoded in the human genome. *Journal of proteome research 5,* 196-201.

Andreini, C., Banci, L., Bertini, I., and Rosato, A. (2006b). Zinc through the three domains of life. *Journal of proteome research 5,* 3173-3178.

Aydemir, T.B., Chang, S.M., Guthrie, G.J., Maki, A.B., Ryu, M.S., Karabiyik, A., and Cousins, R.J. (2012). Zinc transporter ZIP14 functions in hepatic zinc, iron and glucose homeostasis during the innate immune response (endotoxemia). *PloS one 7,* e48679.

Bayle, L., Chimalapati, S., Schoehn, G., Brown, J., Vernet, T., and Durmort, C. (2011). Zinc uptake by *Streptococcus pneumoniae* depends on both AdcA and AdcAII and is essential for normal bacterial morphology and virulence. *Molecular microbiology 82,* 904-916.

Besold, A.N., Gilston, B.A., Radin, J.N., Ramsoomair, C., Culbertson, E.M., Li, C.X., Cormack, B.P., Chazin, W.J., Kehl-Fie, T.E., and Culotta, V.C. (2017). The role of calprotectin in withholding zinc and copper from *Candida albicans*. *Infection and immunity*.

Blaby-Haas, C.E., Flood, J.A., Crecy-Lagard, V., and Zamble, D.B. (2012). YeiR: a metal-binding GTPase from *Escherichia coli* involved in metal homeostasis. *Metallomics : integrated biometal science 4,* 488-497.

Bobrov, A.G., Kirillina, O., Fetherston, J.D., Miller, M.C., Burlison, J.A., and Perry, R.D. (2014). The *Yersinia pestis* siderophore, yersiniabactin, and the ZnuABC system both contribute to zinc acquisition and the development of lethal septicaemic plague in mice. *Molecular microbiology 93,* 759-775.

Bonaventura, P., Benedetti, G., Albarede, F., and Miossec, P. (2015). Zinc and its role in immunity and inflammation. *Autoimmun Rev 14,* 277-285.

Botella, H., Peyron, P., Levillain, F., Poincloux, R., Poquet, Y., Brandli, I., Wang, C., Tailleux, L., Tilleul, S., Charriere, G.M., *et al.* (2011). Mycobacterial p(1)-type ATPases mediate resistance to zinc poisoning in human macrophages. *Cell Host Microbe 10*, 248-259.

Braud, A., Geoffroy, V., Hoegy, F., Mislin, G.L., and Schalk, I.J. (2010). Presence of the siderophores pyoverdine and pyochelin in the extracellular medium reduces toxic metal accumulation in *Pseudomonas aeruginosa* and increases bacterial metal tolerance. *Environ Microbiol Rep 2*, 419-425.

Braud, A., Hoegy, F., Jezequel, K., Lebeau, T., and Schalk, I.J. (2009). New insights into the metal specificity of the *Pseudomonas aeruginosa* pyoverdine-iron uptake pathway. *Environmental microbiology 11*, 1079-1091.

Braymer, J.J., and Giedroc, D.P. (2014). Recent developments in copper and zinc homeostasis in bacterial pathogens. *Curr Opin Chem Biol 19*, 59-66.

Brocklehurst, K.R., Hobman, J.L., Lawley, B., Blank, L., Marshall, S.J., Brown, N.L., and Morby, A.P. (1999). ZntR is a Zn(II)-responsive MerR-like transcriptional regulator of zntA in *Escherichia coli*. *Molecular microbiology 31*, 893-902.

Brodersen, D.E., Nyborg, J., and Kjeldgaard, M. (1999). Zinc-binding site of an S100 protein revealed. Two crystal structures of Ca2+-bound human psoriasin (S100A7) in the Zn2+-loaded and Zn2+-free states. *Biochemistry 38*, 1695-1704.

Brophy, M.B., Hayden, J.A., and Nolan, E.M. (2012). Calcium ion gradients modulate the zinc affinity and antibacterial activity of human calprotectin. *Journal of the American Chemical Society 134*, 18089-18100.

Broun, E.R., Greist, A., Tricot, G., and Hoffman, R. (1990). Excessive zinc ingestion. A reversible cause of sideroblastic anemia and bone marrow depression. *JAMA 264*, 1441-1443.

Calmettes, C., Ing, C., Buckwalter, C.M., El Bakkouri, M., Chieh-Lin Lai, C., Pogoutse, A., Gray-Owen, S.D., Pomes, R., and Moraes, T.F. (2015). The molecular mechanism of Zinc acquisition by the neisserial outer-membrane transporter ZnuD. *Nature communications 6*, 7996.

Campoy, S., Jara, M., Busquets, N., Perez De Rozas, A.M., Badiola, I., and Barbe, J. (2002). Role of the high-affinity zinc uptake znuABC system in *Salmonella enterica* serovar Typhimurium virulence. *Infection and immunity 70*, 4721-4725.

Capdevila, D.A., Edmonds, K.A., and Giedroc, D.P. (2017). Metallochaperones and metalloregulation in bacteria. Essays Biochem *61*, 177-200.

Cassat, J.E., Moore, J.L., Wilson, K.J., Stark, Z., Prentice, B.M., Van de Plas, R., Perry, W.J., Zhang, Y., Virostko, J., Colvin, D.C., *et al.* (2018). Integrated molecular imaging reveals tissue heterogeneity driving host-pathogen interactions. Sci Transl Med *10*.

CDC (2019). Antibiotic resistance threats in the United States.

Cerasi, M., Liu, J.Z., Ammendola, S., Poe, A.J., Petrarca, P., Pesciaroli, M., Pasquali, P., Raffatellu, M., and Battistoni, A. (2014). The ZupT transporter plays an important role in zinc homeostasis and contributes to *Salmonella enterica* virulence. *Metallomics : integrated biometal science 6*, 845-853.

Chandrangsu, P., Huang, X., Gaballa, A., and Helmann, J.D. (2019). *Bacillus subtilis* FolE is sustained by the ZagA zinc metallochaperone and the alarmone ZTP under conditions of zinc deficiency. *Molecular microbiology*.

Chandrangsu, P., Rensing, C., and Helmann, J.D. (2017). Metal homeostasis and resistance in bacteria. *Nat Rev Microbiol 15*, 338-350.

Chaturvedi, K.S., Hung, C.S., Crowley, J.R., Stapleton, A.E., and Henderson, J.P. (2012). The siderophore yersiniabactin binds copper to protect pathogens during infection. *Nature chemical biology 8*, 731-736.

Chen, C.Y., and Morse, S.A. (2001). Identification and characterization of a high-affinity zinc uptake system in *Neisseria gonorrhoeae*. *FEMS Microbiol Lett 202*, 67-71.

Choi, S., and Bird, A.J. (2014). Zinc'ing sensibly: controlling zinc homeostasis at the transcriptional level. *Metallomics : integrated biometal science 6*, 1198-1215.

Clark, H.L., Jhingran, A., Sun, Y., Vareechon, C., de Jesus Carrion, S., Skaar, E.P., Chazin, W.J., Calera, J.A., Hohl, T.M., and Pearlman, E. (2016). Zinc and Manganese Chelation by Neutrophil S100A8/A9 (Calprotectin) Limits Extracellular Aspergillus fumigatus Hyphal Growth and Corneal Infection. *Journal of immunology 196*, 336-344.

Clohessy, P.A., and Golden, B.E. (1995). Calprotectin-mediated zinc chelation as a biostatic mechanism in host defence. *Scand J Immunol 42*, 551-556.

Corbett, D., Wang, J., Schuler, S., Lopez-Castejon, G., Glenn, S., Brough, D., Andrew, P.W., Cavet, J.S., and Roberts, I.S. (2012). Two zinc uptake systems contribute to the full virulence of *Listeria monocytogenes* during growth in vitro and in vivo. *Infection and immunity 80*, 14-21.

Corbin, B.D., Seeley, E.H., Raab, A., Feldmann, J., Miller, M.R., Torres, V.J., Anderson, K.L., Dattilo, B.M., Dunman, P.M., Gerads, R., *et al.* (2008). Metal chelation and inhibition of bacterial growth in tissue abscesses. *Science 319*, 962-965.

Cortese, M.S., Paszczynski, A., Lewis, T.A., Sebat, J.L., Borek, V., and Crawford, R.L. (2002). Metal chelating properties of pyridine-2,6-bis(thiocarboxylic acid) produced by *Pseudomonas* spp. and the biological activities of the formed complexes. *Biometals 15*, 103-120.

Crawford, A., and Wilson, D. (2015). Essential metals at the host-pathogen interface: nutritional immunity and micronutrient assimilation by human fungal pathogens. *FEMS Yeast Res 15*.

Dalet, K., Gouin, E., Cenatiempo, Y., Cossart, P., and Hechard, Y. (1999). Characterisation of a new operon encoding a Zur-like protein and an associated ABC zinc permease in *Listeria monocytogenes*. *FEMS Microbiol Lett 174*, 111-116.

Damo, S.M., Kehl-Fie, T.E., Sugitani, N., Holt, M.E., Rathi, S., Murphy, W.J., Zhang, Y., Betz, C., Hench, L., Fritz, G., *et al.* (2013). Molecular basis for manganese sequestration by calprotectin and roles in the innate immune response to invading bacterial pathogens. *Proceedings of the National Academy of Sciences of the United States of America 110*, 3841-3846.

Davis, L.M., Kakuda, T., and DiRita, V.J. (2009). A *Campylobacter jejuni* znuA orthologue is essential for growth in low-zinc environments and chick colonization. *Journal of bacteriology 191*, 1631-1640.

DePasquale-Jardieu, P., and Fraker, P.J. (1984). Interference in the development of a secondary immune response in mice by zinc deprivation: persistence of effects. *The Journal of nutrition 114*, 1762-1769.

Desrosiers, D.C., Sun, Y.C., Zaidi, A.A., Eggers, C.H., Cox, D.L., and Radolf, J.D. (2007). The general transition metal (Tro) and Zn^{2+} (Znu) transporters in *Treponema pallidum*: analysis of metal specificities and expression profiles. *Molecular microbiology 65*, 137-152.

Eggleton, W.G. (1940). The zinc and copper contents of the organs and tissues of Chinese subjects. *Biochem J 34*, 991-997.

Eide, D.J. (2011). The oxidative stress of zinc deficiency. *Metallomics : integrated biometal science 3*, 1124-1129.

Eksioglu, E.A., Chen, X., Heider, K.H., Rueter, B., McGraw, K.L., Basiorka, A.A., Wei, M., Burnette, A., Cheng, P., Lancet, J., *et al.* (2017). Novel therapeutic approach to improve hematopoiesis in low risk MDS by targeting MDSCs with the Fc-engineered CD33 antibody BI 836858. *Leukemia 31*, 2172-2180.

Falagas, M.E., Roussos, N., Gkegkes, I.D., Rafailidis, P.I., and Karageorgopoulos, D.E. (2009). Fosfomycin for the treatment of infections caused by Gram-positive cocci with advanced antimicrobial drug resistance: a review of microbiological, animal and clinical studies. Expert *Opin Investig Drugs 18*, 921-944.

Gaballa, A., and Helmann, J.D. (1998). Identification of a zinc-specific metalloregulatory protein, Zur, controlling zinc transport operons in Bacillus subtilis. *Journal of bacteriology 180*, 5815-5821.

Gabbianelli, R., Scotti, R., Ammendola, S., Petrarca, P., Nicolini, L., and Battistoni, A. (2011). Role of ZnuABC and ZinT in *Escherichia coli* O157:H7 zinc acquisition and interaction with epithelial cells. *BMC microbiology 11*, 36.

Gabriel, S.E., Miyagi, F., Gaballa, A., and Helmann, J.D. (2008). Regulation of the *Bacillus subtilis* yciC gene and insights into the DNA-binding specificity of the zinc-sensing metalloregulator Zur. *Journal of bacteriology*, pp. 3482-3488.

Gaddy, J.A., Radin, J.N., Loh, J.T., Piazuelo, M.B., Kehl-Fie, T.E., Delgado, A.G., Ilca, F.T., Peek, R.M., Cover, T.L., Chazin, W.J., *et al.* (2014). The host protein calprotectin modulates the *Helicobacter pylori* cag type IV secretion system via zinc sequestration. *PLoS pathogens 10*, e1004450.

Garrido, M.E., Bosch, M., Medina, R., Llagostera, M., Perez de Rozas, A.M., Badiola, I., and Barbe, J. (2003). The high-affinity zinc-uptake system znuACB is under control of the iron-uptake regulator (fur) gene in the animal pathogen *Pasteurella multocida*. *FEMS Microbiol Lett 221*, 31-37.

Ghssein, G., Brutesco, C., Ouerdane, L., Fojcik, C., Izaute, A., Wang, S., Hajjar, C., Lobinski, R., Lemaire, D., Richaud, P., *et al.* (2016). Biosynthesis of a broad-spectrum nicotianamine-like metallophore in *Staphylococcus aureus*. *Science 352*, 1105-1109.

Giedroc, D.P., Chen, X., and Apuy, J.L. (2001). Metal response element (MRE)-binding transcription factor-1 (MTF-1): structure, function, and regulation. *Antioxidants & redox signaling 3*, 577-596.

Gilston, B.A., Wang, S., Marcus, M.D., Canalizo-Hernandez, M.A., Swindell, E.P., Xue, Y., Mondragon, A., and O'Halloran, T.V. (2014). Structural and mechanistic basis of zinc regulation across the *E. coli* Zur regulon. *PLoS biology 12*, e1001987.

Glaser, R., Harder, J., Lange, H., Bartels, J., Christophers, E., and Schroder, J.M. (2005). Antimicrobial psoriasin (S100A7) protects human skin from *Escherichia coli* infection. *Nat Immunol 6*, 57-64.

Grim, K.P., San Francisco, B., Radin, J.N., Brazel, E.B., Kelliher, J.L., Parraga Solorzano, P.K., Kim, P.C., McDevitt, C.A., and Kehl-Fie, T.E. (2017). The Metallophore Staphylopine Enables *Staphylococcus aureus* To Compete with the Host for Zinc and Overcome Nutritional Immunity. *mBio 8*.

Haas, C.E., Rodionov, D.A., Kropat, J., Malasarn, D., Merchant, S.S., and de Crecy-Lagard, V. (2009). A subset of the diverse COG0523 family of putative metal chaperones is linked to zinc homeostasis in all kingdoms of life. *BMC genomics 10*, 470.

Haley, K.P., Delgado, A.G., Piazuelo, M.B., Mortensen, B.L., Correa, P., Damo, S.M., Chazin, W.J., Skaar, E.P., and Gaddy, J.A. (2015). The Human Antimicrobial Protein Calgranulin C Participates in Control of *Helicobacter pylori* Growth and Regulation of Virulence. *Infection and immunity 83*, 2944-2956.

Hambidge, M. (2000). Human zinc deficiency. *The Journal of nutrition 130*, 1344S-1349S.

Harding, C.M., Hennon, S.W., and Feldman, M.F. (2018). Uncovering the mechanisms of *Acinetobacter baumannii* virulence. *Nat Rev Microbiol 16*, 91-102.

Hasegawa, H., Suzuki, K., Suzuki, K., Nakaji, S., and Sugawara, K. (2000). Effects of zinc on the reactive oxygen species generating capacity of human neutrophils and on the serum opsonic activity in vitro. *Luminescence 15*, 321-327.

Hassan, K.A., Pederick, V.G., Elbourne, L.D., Paulsen, I.T., Paton, J.C., McDevitt, C.A., and Eijkelkamp, B.A. (2017). Zinc stress induces copper depletion in *Acinetobacter baumannii*. *BMC microbiology 17*, 59.

Helbig, K., Bleuel, C., Krauss, G.J., and Nies, D.H. (2008). Glutathione and transition-metal homeostasis in *Escherichia coli*. *Journal of bacteriology 190*, 5431-5438.

Hood, M.I., Mortensen, B.L., Moore, J.L., Zhang, Y., Kehl-Fie, T.E., Sugitani, N., Chazin, W.J., Caprioli, R.M., and Skaar, E.P. (2012). Identification of an *Acinetobacter baumannii* zinc acquisition system that facilitates resistance to calprotectin-mediated zinc sequestration. *PLoS pathogens 8*, e1003068.

Hood, M.I., and Skaar, E.P. (2012). Nutritional immunity: transition metals at the pathogen-host interface. *Nat Rev Microbiol 10*, 525-537.

Huang, X., Shin, J.H., Pinochet-Barros, A., Su, T.T., and Helmann, J.D. (2017). *Bacillus subtilis* MntR coordinates the transcriptional regulation of manganese uptake and efflux systems. *Molecular microbiology 103*, 253-268.

Hubbard, P.A., Padovani, D., Labunska, T., Mahlstedt, S.A., Banerjee, R., and Drennan, C.L. (2007). Crystal structure and mutagenesis of the metallochaperone MeaB: insight into the causes of methylmalonic aciduria. *The Journal of biological chemistry 282*, 31308-31316.

Hubert, K., Devos, N., Mordhorst, I., Tans, C., Baudoux, G., Feron, C., Goraj, K., Tommassen, J., Vogel, U., Poolman, J.T., *et al.* (2013). ZnuD, a potential candidate for a simple and universal *Neisseria meningitidis* vaccine. *Infection and immunity 81*, 1915-1927.

Hujanen, E.S., Seppa, S.T., and Virtanen, K. (1995). Polymorphonuclear leukocyte chemotaxis induced by zinc, copper and nickel in vitro. *Biochim Biophys Acta 1245*, 145-152.

Hunter, M.J., and Chazin, W.J. (1998). High level expression and dimer characterization of the S100 EF-hand proteins, migration inhibitory factor-related proteins 8 and 14. *The Journal of biological chemistry 273*, 12427-12435.

Jacob, C., Maret, W., and Vallee, B.L. (1998). Control of zinc transfer between thionein, metallothionein, and zinc proteins. *Proceedings of the National Academy of Sciences of the United States of America 95*, 3489-3494.

James, G.A., Korber, D.R., Caldwell, D.E., and Costerton, J.W. (1995). Digital image analysis of growth and starvation responses of a surface-colonizing *Acinetobacter* sp. *Journal of bacteriology 177*, 907-915.

Jean, S., Juneau, R.A., Criss, A.K., and Cornelissen, C.N. (2016). *Neisseria gonorrhoeae* Evades Calprotectin-Mediated Nutritional Immunity and Survives Neutrophil Extracellular Traps by Production of TdfH. *Infection and immunity 84*, 2982-2994.

Jiang, L.J., Maret, W., and Vallee, B.L. (1998). The glutathione redox couple modulates zinc transfer from metallothionein to zinc-depleted sorbitol dehydrogenase. *Proceedings of the National Academy of Sciences of the United States of America 95*, 3483-3488.

Kandari, D., Gopalani, M., Gupta, M., Joshi, H., Bhatnagar, S., and Bhatnagar, R. (2018). Identification, Functional Characterization, and Regulon Prediction of the Zinc Uptake Regulator (zur) of *Bacillus anthracis* - An Insight Into the Zinc Homeostasis of the Pathogen. *Front Microbiol 9*, 3314.

Kehl-Fie, T.E., Chitayat, S., Hood, M.I., Damo, S., Restrepo, N., Garcia, C., Munro, K.A., Chazin, W.J., and Skaar, E.P. (2011). Nutrient metal sequestration by calprotectin inhibits bacterial superoxide defense, enhancing neutrophil killing of *Staphylococcus aureus*. *Cell Host Microbe 10*, 158-164.

Khil, P.P., Obmolova, G., Teplyakov, A., Howard, A.J., Gilliland, G.L., and Camerini-Otero, R.D. (2004). Crystal structure of the *Escherichia coli* YjiA protein suggests a GTP-dependent regulatory function. *Proteins 54*, 371-374.

Kimura, T., and Kambe, T. (2016). The Functions of Metallothionein and ZIP and ZnT Transporters: An Overview and Perspective. *Int J Mol Sci 17*, 336.

King, J.C., Shames, D.M., and Woodhouse, L.R. (2000). Zinc homeostasis in humans. *The Journal of nutrition 130*, 1360S-1366S.

King, L.E., Frentzel, J.W., Mann, J.J., and Fraker, P.J. (2005). Chronic zinc deficiency in mice disrupted T cell lymphopoiesis and erythropoiesis while B cell lymphopoiesis and myelopoiesis were maintained. *J Am Coll Nutr 24*, 494-502.

Kitabayashi, C., Fukada, T., Kanamoto, M., Ohashi, W., Hojyo, S., Atsumi, T., Ueda, N., Azuma, I., Hirota, H., Murakami, M., *et al.* (2010). Zinc suppresses Th17 development via inhibition of STAT3 activation. *Int Immunol 22*, 375-386.

Kitamura, H., Morikawa, H., Kamon, H., Iguchi, M., Hojyo, S., Fukada, T., Yamashita, S., Kaisho, T., Akira, S., Murakami, M., *et al.* (2006). Toll-like receptor-mediated regulation of zinc homeostasis influences dendritic cell function. *Nat Immunol 7*, 971-977.

Kobayashi, S., Nakai, H., Ikenishi, Y., Sun, W.Y., Ozaki, M., Hayase, Y., and Takeda, R. (1998). Micacocidin A, B and C, novel antimycoplasma agents from *Pseudomonas* sp. II. Structure elucidation. *J Antibiot* (Tokyo) *51*, 328-332.

Korndorfer, I.P., Brueckner, F., and Skerra, A. (2007). The crystal structure of the human (S100A8/S100A9)2 heterotetramer, calprotectin, illustrates how conformational changes of interacting alpha-helices can determine specific association of two EF-hand proteins. *J Mol Biol 370*, 887-898.

Kreutzer, M.F., Kage, H., Gebhardt, P., Wackler, B., Saluz, H.P., Hoffmeister, D., and Nett, M. (2011). Biosynthesis of a complex yersiniabactin-like natural product via the mic locus in phytopathogen *Ralstonia solanacearum*. *Applied and environmental microbiology 77*, 6117-6124.

Krezel, A., Hao, Q., and Maret, W. (2007). The zinc/thiolate redox biochemistry of metallothionein and the control of zinc ion fluctuations in cell signaling. *Arch Biochem Biophys 463*, 188-200.

Kury, S., Dreno, B., Bezieau, S., Giraudet, S., Kharfi, M., Kamoun, R., and Moisan, J.P. (2002). Identification of SLC39A4, a gene involved in acrodermatitis enteropathica. *Nat Genet 31*, 239-240.

Leach, L.H., Morris, J.C., and Lewis, T.A. (2007). The role of the siderophore pyridine-2,6-bis (thiocarboxylic acid) (PDTC) in zinc utilization by Pseudomonas putida DSM 3601. *Biometals 20*, 717-726.

Leclerc, E., Fritz, G., Vetter, S.W., and Heizmann, C.W. (2009). Binding of S100 proteins to RAGE: an update. *Biochim Biophys Acta 1793*, 993-1007.

Lee, J.W., and Helmann, J.D. (2007). Functional specialization within the Fur family of metalloregulators. *Biometals 20*, 485-499.

Li, Y., Qiu, Y., Gao, H., Guo, Z., Han, Y., Song, Y., Du, Z., Wang, X., Zhou, D., and Yang, R. (2009). Characterization of Zur-dependent genes and direct Zur targets in *Yersinia pestis*. *BMC microbiology 9*, 128.

Liu, J.Z., Jellbauer, S., Poe, A.J., Ton, V., Pesciaroli, M., Kehl-Fie, T.E., Restrepo, N.A., Hosking, M.P., Edwards, R.A., Battistoni, A., *et al.* (2012). Zinc sequestration by the neutrophil protein calprotectin enhances *Salmonella* growth in the inflamed gut. *Cell Host Microbe 11*, 227-239.

Liu, M., Yan, M., Liu, L., and Chen, S. (2013). Characterization of a novel zinc transporter ZnuA acquired by *Vibrio parahaemolyticus* through horizontal gene transfer. *Front Cell Infect Microbiol 3*, 61.

Lonergan, Z.R., Nairn, B.L., Wang, J., Hsu, Y.P., Hesse, L.E., Beavers, W.N., Chazin, W.J., Trinidad, J.C., VanNieuwenhze, M.S., Giedroc, D.P., *et al.* (2019). An *Acinetobacter baumannii*, Zinc-Regulated Peptidase Maintains Cell Wall Integrity during Immune-Mediated Nutrient Sequestration. *Cell Rep 26*, 2009-2018 e2006.

Ma, Z., Chandrangsu, P., Helmann, T.C., Romsang, A., Gaballa, A., and Helmann, J.D. (2014). Bacillithiol is a major buffer of the labile zinc pool in *Bacillus subtilis*. *Molecular microbiology 94*, 756-770.

Ma, Z., Gabriel, S.E., and Helmann, J.D. (2011). Sequential binding and sensing of Zn(II) by *Bacillus subtilis* Zur. *Nucleic acids research 39*, 9130-9138.

Maier, T., Lottspeich, F., and Bock, A. (1995). GTP hydrolysis by HypB is essential for nickel insertion into hydrogenases of *Escherichia coli*. *Eur J Biochem 230*, 133-138.

Makthal, N., Nguyen, K., Do, H., Gavagan, M., Chandrangsu, P., Helmann, J.D., Olsen, R.J., and Kumaraswami, M. (2017). A Critical Role of Zinc Importer AdcABC in Group A *Streptococcus*-Host Interactions During Infection and Its Implications for Vaccine Development. *EBioMedicine 21*, 131-141.

Maret, W. (2000). The function of zinc metallothionein: a link between cellular zinc and redox state. *The Journal of nutrition 130*, 1455S-1458S.

Maret, W., and Sandstead, H.H. (2006). Zinc requirements and the risks and benefits of zinc supplementation. *J Trace Elem Med Biol 20*, 3-18.

Maywald, M., Wang, F., and Rink, L. (2018). Zinc supplementation plays a crucial role in T helper 9 differentiation in allogeneic immune reactions and non-activated T cells. *J Trace Elem Med Biol 50*, 482-488.

Mazmanian, S.K., Skaar, E.P., Gaspar, A.H., Humayun, M., Gornicki, P., Jelenska, J., Joachmiak, A., Missiakas, D.M., and Schneewind, O. (2003). Passage of heme-iron across the envelope of *Staphylococcus aureus*. *Science 299*, 906-909.

McKinney, P.E., Brent, J., and Kulig, K. (1994). Acute zinc chloride ingestion in a child: local and systemic effects. *Ann Emerg Med 23*, 1383-1387.

Mehta, N., Benoit, S., and Maier, R.J. (2003). Roles of conserved nucleotide-binding domains in accessory proteins, HypB and UreG, in the maturation of nickel-enzymes required for efficient *Helicobacter pylori* colonization. *Microb Pathog 35*, 229-234.

Moore, C.M., Gaballa, A., Hui, M., Ye, R.W., and Helmann, J.D. (2005). Genetic and physiological responses of *Bacillus subtilis* to metal ion stress. *Molecular microbiology 57*, 27-40.

Moreau, G.B., Qin, A., and Mann, B.J. (2018). Zinc Acquisition Mechanisms Differ between Environmental and Virulent *Francisella* Species. *Journal of bacteriology 200*.

Moroz, O.V., Antson, A.A., Grist, S.J., Maitland, N.J., Dodson, G.G., Wilson, K.S., Lukanidin, E., and Bronstein, I.B. (2003). Structure of the human S100A12-copper complex: implications for host-parasite defence. *Acta Crystallogr D Biol Crystallogr 59*, 859-867.

Mortensen, B.L., Rathi, S., Chazin, W.J., and Skaar, E.P. (2014). *Acinetobacter baumannii* response to host-mediated zinc limitation requires the transcriptional regulator Zur. *Journal of bacteriology 196*, 2616-2626.

Moulin, P., Patron, K., Cano, C., Zorgani, M.A., Camiade, E., Borezee-Durant, E., Rosenau, A., Mereghetti, L., and Hiron, A. (2016). The Adc/Lmb System Mediates Zinc Acquisition in *Streptococcus agalactiae* and Contributes to Bacterial Growth and Survival. *Journal of bacteriology 198*, 3265-3277.

Murphy, S.G., Alvarez, L., Adams, M.C., Liu, S., Chappie, J.S., Cava, F., and Dorr, T. (2019). Endopeptidase Regulation as a Novel Function of the Zur-Dependent Zinc Starvation Response. *mBio 10*.

Murphy, T.F., Brauer, A.L., Kirkham, C., Johnson, A., Koszelak-Rosenblum, M., and Malkowski, M.G. (2013). Role of the zinc uptake ABC transporter of *Moraxella catarrhalis* in persistence in the respiratory tract. *Infection and immunity 81*, 3406-3413.

Nairn, B.L., Lonergan, Z.R., Wang, J., Braymer, J.J., Zhang, Y., Calcutt, M.W., Lisher, J.P., Gilston, B.A., Chazin, W.J., de Crecy-Lagard, V., *et al.* (2016). *The Response of Acinetobacter baumannii to Zinc Starvation*. *Cell Host Microbe 19*, 826-836.

Nakashige, T.G., Zhang, B., Krebs, C., and Nolan, E.M. (2015). Human calprotectin is an iron-sequestering host-defense protein. *Nature chemical biology 11*, 765-771.

Nakashige, T.G., Zygiel, E.M., Drennan, C.L., and Nolan, E.M. (2017). Nickel Sequestration by the Host-Defense Protein Human Calprotectin. *Journal of the American Chemical Society 139*, 8828-8836.

Nanamiya, H., Akanuma, G., Natori, Y., Murayama, R., Kosono, S., Kudo, T., Kobayashi, K., Ogasawara, N., Park, S.M., Ochi, K., *et al.* (2004). Zinc is a key factor in controlling alternation of two types of L31 protein in the *Bacillus subtilis* ribosome. *Molecular microbiology 52*, 273-283.

Nielubowicz, G.R., Smith, S.N., and Mobley, H.L. (2010). Zinc uptake contributes to motility and provides a competitive advantage to *Proteus mirabilis* during experimental urinary tract infection. *Infection and immunity 78*, 2823-2833.

Nies, D.H. (2003). Efflux-mediated heavy metal resistance in prokaryotes. *FEMS Microbiol Rev 27*, 313-339.

O'Neill, J. (2014). Antimicrobial Resistance: Tackling a crisis for the health and wealth of nations. *Review on Antimicrobial Resistance*.

Ong, C.L., Gillen, C.M., Barnett, T.C., Walker, M.J., and McEwan, A.G. (2014). An antimicrobial role for zinc in innate immune defense against group A streptococcus. *J Infect Dis 209*, 1500-1508.

Osman, D., Martini, M.A., Foster, A.W., Chen, J., Scott, A.J.P., Morton, R.J., Steed, J.W., Lurie-Luke, E., Huggins, T.G., Lawrence, A.D., *et al.* (2019). Bacterial sensors define intracellular free energies for correct enzyme metalation. *Nature chemical biology 15*, 241-249.

Outten, C.E., and O'Halloran, T.V. (2001). Femtomolar sensitivity of metalloregulatory proteins controlling zinc homeostasis. *Science 292*, 2488-2492.

Outten, C.E., Outten, F.W., and O'Halloran, T.V. (1999). DNA distortion mechanism for transcriptional activation by ZntR, a Zn(II)-responsive MerR homologue in *Escherichia coli*. The *Journal of biological chemistry 274*, 37517-37524.

Palmer, L.D., and Skaar, E.P. (2016). Transition Metals and Virulence in Bacteria. *Annu Rev Genet 50*, 67-91.

Patzer, S.I., and Hantke, K. (1998). The ZnuABC high-affinity zinc uptake system and its regulator Zur in *Escherichia coli*. *Molecular microbiology 28*, 1199-1210.

Pawlik, M.C., Hubert, K., Joseph, B., Claus, H., Schoen, C., and Vogel, U. (2012). The zinc-responsive regulon of *Neisseria meningitidis* comprises 17 genes under control of a Zur element. *Journal of bacteriology 194*, 6594-6603.

Pederick, V.G., Eijkelkamp, B.A., Begg, S.L., Ween, M.P., McAllister, L.J., Paton, J.C., and McDevitt, C.A. (2015). ZnuA and zinc homeostasis in *Pseudomonas aeruginosa*. *Scientific reports 5*, 13139.

Peleg, A.Y., Seifert, H., and Paterson, D.L. (2008). *Acinetobacter baumannii*: emergence of a successful pathogen. *Clin Microbiol Rev 21*, 538-582.

Petrarca, P., Ammendola, S., Pasquali, P., and Battistoni, A. (2010). The Zur-regulated ZinT protein is an auxiliary component of the high-affinity ZnuABC zinc transporter that facilitates metal recruitment during severe zinc shortage. *Journal of bacteriology 192*, 1553-1564.

Potter, J.L. (1981). Acute zinc chloride ingestion in a young child. Ann Emerg Med *10*, 267-269.
Prasad, A.S. (2000). Effects of zinc deficiency on Th1 and Th2 cytokine shifts. *J Infect Dis 182 Suppl 1*, S62-68.

Pyle, C.J., Azad, A.K., Papp, A.C., Sadee, W., Knoell, D.L., and Schlesinger, L.S. (2017). Elemental Ingredients in the Macrophage Cocktail: Role of ZIP8 in Host Response to *Mycobacterium tuberculosis*. *Int J Mol Sci 18*.

Rahman, M.T., Haque, N., Abu Kasim, N.H., and De Ley, M. (2017). Origin, Function, and Fate of Metallothionein in Human Blood. *Rev Physiol Biochem Pharmacol 173*, 41-62.

Reyes-Caballero, H., Guerra, A.J., Jacobsen, F.E., Kazmierczak, K.M., Cowart, D., Koppolu, U.M., Scott, R.A., Winkler, M.E., and Giedroc, D.P. (2010). The metalloregulatory zinc site in *Streptococcus pneumoniae* AdcR, a zinc-activated MarR family repressor. *J Mol Biol 403*, 197-216.

Rink, L., and Haase, H. (2007). Zinc homeostasis and immunity. *Trends Immunol 28*, 1-4.

Rosadini, C.V., Gawronski, J.D., Raimunda, D., Arguello, J.M., and Akerley, B.J. (2011). A novel zinc binding system, ZevAB, is critical for survival of nontypeable *Haemophilus influenzae* in a murine lung infection model. *Infection and immunity 79*, 3366-3376.

Rosenkranz, E., Metz, C.H., Maywald, M., Hilgers, R.D., Wessels, I., Senff, T., Haase, H., Jager, M., Ott, M., Aspinall, R., *et al.* (2016). Zinc supplementation induces regulatory T cells by inhibition of Sirt-1 deacetylase in mixed lymphocyte cultures. *Mol Nutr Food Res 60*, 661-671.

Sabri, M., Houle, S., and Dozois, C.M. (2009). Roles of the extraintestinal pathogenic *Escherichia coli* ZnuACB and ZupT zinc transporters during urinary tract infection. *Infection and immunity 77*, 1155-1164.

Shank, J.M., Kelley, B.R., Jackson, J.W., Tweedie, J.L., Franklin, D., Damo, S.M., Gaddy, J.A., Murphy, C.N., and Johnson, J.G. (2018). The Host Antimicrobial Protein Calgranulin C Participates in the Control of C*ampylobacter jejuni* Growth via Zinc Sequestration. *Infection and immunity 86*.

Sheikh, A., Shamsuzzaman, S., Ahmad, S.M., Nasrin, D., Nahar, S., Alam, M.M., Al Tarique, A., Begum, Y.A., Qadri, S.S., Chowdhury, M.I., *et al.* (2010). Zinc influences innate immune responses in children with enterotoxigenic *Escherichia coli*-induced diarrhea. *The Journal of nutrition 140*, 1049-1056.

Sheldon, J.R., Laakso, H.A., and Heinrichs, D.E. (2016). Iron Acquisition Strategies of Bacterial Pathogens. *Microbiol Spectr 4*.

Sheng, Y., Fan, F., Jensen, O., Zhong, Z., Kan, B., Wang, H., and Zhu, J. (2015). Dual Zinc Transporter Systems in *Vibrio cholerae* Promote Competitive Advantages over Gut Microbiome. *Infection and immunity 83*, 3902-3908.

Shin, J.H., and Helmann, J.D. (2016). Molecular logic of the Zur-regulated zinc deprivation response in *Bacillus subtilis*. *Nature communications 7*, 12612.

Shin, J.H., Oh, S.Y., Kim, S.J., and Roe, J.H. (2007). The zinc-responsive regulator Zur controls a zinc uptake system and some ribosomal proteins in *Streptomyces coelicolor* A3(2). *Journal of bacteriology 189*, 4070-4077.

Si, M., Wang, Y., Zhang, B., Zhao, C., Kang, Y., Bai, H., Wei, D., Zhu, L., Zhang, L., Dong, T.G., *et al.* (2017). The Type VI Secretion System Engages a Redox-Regulated Dual-Functional Heme Transporter for Zinc Acquisition. *Cell Rep 20*, 949-959.

Stefanidou, M., Maravelias, C., Dona, A., and Spiliopoulou, C. (2006). Zinc: a multipurpose trace element. *Arch Toxicol 80*, 1-9.

Stork, M., Bos, M.P., Jongerius, I., de Kok, N., Schilders, I., Weynants, V.E., Poolman, J.T., and Tommassen, J. (2010). An outer membrane receptor of *Neisseria meningitidis* involved in zinc acquisition with vaccine potential. *PLoS pathogens 6*, e1000969.

Stork, M., Grijpstra, J., Bos, M.P., Manas Torres, C., Devos, N., Poolman, J.T., Chazin, W.J., and Tommassen, J. (2013). Zinc piracy as a mechanism of *Neisseria meningitidis* for evasion of nutritional immunity. *PLoS pathogens 9*, e1003733.

Subramanian Vignesh, K., Landero Figueroa, J.A., Porollo, A., Caruso, J.A., and Deepe, G.S., Jr. (2013a). Granulocyte macrophage-colony stimulating factor induced Zn sequestration enhances macrophage superoxide and limits intracellular pathogen survival. *Immunity 39*, 697-710.

Subramanian Vignesh, K., Landero Figueroa, J.A., Porollo, A., Caruso, J.A., and Deepe, G.S., Jr. (2013b). Zinc sequestration: arming phagocyte defense against fungal attack. *PLoS pathogens 9*, e1003815.

Sydor, A.M., Jost, M., Ryan, K.S., Turo, K.E., Douglas, C.D., Drennan, C.L., and Zamble, D.B. (2013). Metal binding properties of *Escherichia coli* YjiA, a member of the metal homeostasis-associated COG0523 family of GTPases. *Biochemistry 52*, 1788-1801.

Trumbo, P., Yates, A.A., Schlicker, S., and Poos, M. (2001). Dietary reference intakes: vitamin A, vitamin K, arsenic, boron, chromium, copper, iodine, iron, manganese, molybdenum, nickel, silicon, vanadium, and zinc. *J Am Diet Assoc 101*, 294-301.

Urban, C.F., Ermert, D., Schmid, M., Abu-Abed, U., Goosmann, C., Nacken, W., Brinkmann, V., Jungblut, P.R., and Zychlinsky, A. (2009). Neutrophil extracellular traps contain calprotectin, a cytosolic protein complex involved in host defense against *Candida albicans*. *PLoS pathogens 5*, e1000639.

Vogl, T., Tenbrock, K., Ludwig, S., Leukert, N., Ehrhardt, C., van Zoelen, M.A., Nacken, W., Foell, D., van der Poll, T., Sorg, C., *et al.* (2007). Mrp8 and Mrp14 are endogenous activators of Toll-like receptor 4, promoting lethal, endotoxin-induced shock. *Nat Med 13*, 1042-1049.

Vokaty, S., McPherson, V.O., Camus, E., and Applewhaite, L. (1993). Ovine trypanosomosis: a seroepidemiological survey in coastal Guyana. *Rev Elev Med Vet Pays Trop 46*, 57-59.

Wakeman, C.A., Moore, J.L., Noto, M.J., Zhang, Y., Singleton, M.D., Prentice, B.M., Gilston, B.A., Doster, R.S., Gaddy, J.A., Chazin, W.J., *et al.* (2016). The innate immune protein calprotectin promotes *Pseudomonas aeruginosa* and *Staphylococcus aureus* interaction. *Nature communications 7*, 11951.

Wang, J., Lonergan, Z.R., Gonzalez-Gutierrez, G., Nairn, B.L., Maxwell, C.N., Zhang, Y., Andreini, C., Karty, J.A., Chazin, W.J., Trinidad, J.C., *et al.* (2019). Multi-metal Restriction by Calprotectin Impacts De Novo Flavin Biosynthesis in *Acinetobacter baumannii*. *Cell Chem Biol*.

Wang, T., Chen, K., Gao, F., Kang, Y., Chaudhry, M.T., Wang, Z., Wang, Y., and Shen, X. (2017). ZntR positively regulates T6SS4 expression in *Yersinia pseudotuberculosis*. *J Microbiol 55*, 448-456.

Wang, T., Si, M., Song, Y., Zhu, W., Gao, F., Wang, Y., Zhang, L., Zhang, W., Wei, G., Luo, Z.Q., *et al.* (2015). Type VI Secretion System Transports Zn2+ to Combat Multiple Stresses and Host Immunity. *PLoS pathogens 11*, e1005020.

Weinberg, E.D. (1974). Iron and susceptibility to infectious disease. *Science 184*, 952-956.

Wessells, K.R., and Brown, K.H. (2012). Estimating the global prevalence of zinc deficiency: results based on zinc availability in national food supplies and the prevalence of stunting. *PloS one 7*, e50568.

WHO (2017). Guidelines for the prevention and control of carbapenem-resistant Enterobacteriaceae, *Acinetobacter baumannii* and *Pseudomonas aeruginosa* in health care facilities. World Health Organization.

Yang, X., Becker, T., Walters, N., and Pascual, D.W. (2006). Deletion of znuA virulence factor attenuates *Brucella abortus* and confers protection against wild-type challenge. *Infection and immunity 74*, 3874-3879.

Yui, S., Nakatani, Y., and Mikami, M. (2003). Calprotectin (S100A8/S100A9), an inflammatory protein complex from neutrophils with a broad apoptosis-inducing activity. *Biol Pharm Bull 26*, 753-760.

Zackular, J.P., Chazin, W.J., and Skaar, E.P. (2015). Nutritional Immunity: S100 Proteins at the Host-Pathogen Interface. *The Journal of biological chemistry 290*, 18991-18998.

Zackular, J.P., Moore, J.L., Jordan, A.T., Juttukonda, L.J., Noto, M.J., Nicholson, M.R., Crews, J.D., Semler, M.W., Zhang, Y., Ware, L.B., *et al.* (2016). Dietary zinc alters the microbiota and decreases resistance to *Clostridium difficile* infection. *Nat Med*.

Zhao, B., Moody, S.C., Hider, R.C., Lei, L., Kelly, S.L., Waterman, M.R., and Lamb, D.C. (2012). Structural analysis of cytochrome P450 105N1 involved in the biosynthesis of the zincophore, coelibactin. *Int J Mol Sci 13*, 8500-8513.

Zygiel, E.M., Nelson, C.E., Brewer, L.K., Oglesby-Sherrouse, A.G., and Nolan, E.M. (2019). The human innate immune protein calprotectin induces iron starvation responses in *Pseudomonas aeruginosa*. *The Journal of biological chemistry*.

CHAPTER II

MULTI-METAL RESTRICTION BY CALPROTECTIN IMPACTS *DE NOVO* FLAVIN BIOSYNTHESIS IN *ACINETOBACTER BAUMANNII*

A version of the following section was previously published in *Cell Chemical Biology* 26 (5) 745-755.E7 (May 2019) doi: 10.1016/j.chembiol.2019.02.011.

Introduction

Transition metals are important to microbial physiology and execute key catalytic, structural, and regulatory functions that broadly impact all phases of cellular physiology. The mammalian host takes advantage of this essentiality by restricting growth of invading bacteria through a process termed nutritional immunity, in which transition metals are withheld from microbial invaders by mammalian metal-binding proteins (Damo, et al., 2013; Hood and Skaar, 2012; Weinberg, 1975). Host neutrophils and other immune cells secrete a number of metal-chelating innate immune proteins at sites of infection, including S100-family proteins. One such protein is calprotectin (CP, S100A8/A9 oligomer), which is a versatile extracellular metal-sequestering protein that forms high thermodynamic and/or kinetic stability coordination complexes with Zn^{II}, Mn^{II}, Fe^{II} and Ni^{II} (Damo, et al., 2013; Nakashige, et al., 2015; Nakashige, et al., 2017). CP-dependent metal-binding restricts the availability of these metals and inhibits the growth of pathogens (Corbin, et al., 2008; Zygiel and Nolan, 2018). While the physiological impact of CP is expected to be niche- and pathogen-dependent, little is known about how CP induced stress impacts metabolism in different pathogens (Besold, et al., 2017; Wakeman, et al., 2016).

Acinetobacter baumannii is a Gram-negative bacterial pathogen commonly associated with hospital-acquired infections and is a leading cause of ventilator-associated pneumonia (Doyle, et al., 2011). Increasing reports of community-acquired and multidrug resistant *Acinetobacter* infections has attracted considerable public attention (Harding, et al., 2018). Calprotectin (CP) inhibits *A. baumannii* growth and protects against *A. baumannii* infection in a mouse model of pneumonia (Hood, et al., 2012). A transposon mutagenesis screen identified a strain lacking the Zn uptake transporter *znuB*, which is regulated by the Zn uptake repressor Zur, as being defective for growth in the presence of CP and is consistent with the finding that CP induces Zn but not Mn starvation (Hood, et al., 2012). Subsequent transcriptomic experiments with the Δ*zur* strain identified the Zur regulon as well as other Zn-responsive genes, which included the putative $\mathrm{Zn^{II}}$ chaperone, ZigA (Zur-induced GTPase A) (Mortensen, et al., 2014); follow-up work revealed that the Δ*zigA* strain is sensitive to CP stress (Mortensen, et al., 2014; Nairn, et al., 2016). While the importance of Zur and the induction of known Zur-regulated genes in response to CP has been defined (Mortensen, et al., 2014; Nairn, et al., 2016), it is not yet known how other metal homeostasis and metabolism systems are perturbed by CP stress.

Elucidating a global understanding of CP-induced perturbations in bacterial transition metal distribution network(s) and downstream physiological changes in cellular metabolism is important but remains largely understudied (Zygiel and Nolan, 2018). Cells must alter their metabolism when they are metal-starved. A number of essential metabolic pathways are *initiated* with a $\mathrm{Zn^{II}}$ metalloenzyme, including the biosynthesis of folate, queuosine-tRNA, riboflavin, and in some organisms, tetrahydrobiopterin (Phillips, et al., 2012). Given that enzymes that require

Zn^{II} or another transition metal for activity are positioned at critical hubs in cellular physiology, it is unclear how bacterial cells balance cellular metabolism under CP-induced metal-deficient conditions. In addition, while studies of how cells regulate metal transport are widespread, these studies have tended to underestimate how intermediary metabolism adapts to host-induced metal starvation. In *A. baumannii*, CP moderately induces the genes required for *L*-histidine catabolism (*hut*), which are proposed to contribute to the release of Zn^{II} from Zn-His_2 complexes, thus increasing access by Zn^{II}-dependent processes under extreme Zn limitation (Nairn, et al., 2016). Additionally, iron starvation has been linked to induction of flavin biosynthesis in bacteria and eukaryotes where substitution of flavodoxins for ferredoxins as cellular reductants was proposed (LaRoche, et al., 1996; Tognetti, et al., 2007). A global, systems-level view of how CP impacts metabolic processes is clearly needed.

The studies presented here describe the metabolic impact of nutritional immunity in *A. baumannii*. Using *A. baumannii* Δ*zigA* as a tool to exacerbate multi-metal (Zn and Fe) starvation induced by CP, we observe an incrementally increased abundance of two related enzymes of the flavin biosynthesis pathway, RibBX and RibB, consistent with cellular efforts to ensure sufficient flavin supply under conditions of extreme metal limitation or mis-allocation, predicted of the basis of global changes in Zn^{II} proteome. These observations are consistent with our discovery that Δ*zigA* is unable to maintain appropriate flavin abundance during metal starvation and that *ribBX* contributes to the ability of *A. baumannii* to synthesize flavins and overcome nutrient metal limitation. Our findings support a dual regulatory model explaining how *A. baumannii* maintains cellular flavin sufficiency required for central metabolic processes in an effort to overcome CP-induced metal starvation. Our studies also validate ongoing efforts to develop pharmacological strategies against *A. baumannii* by identifying flavin biosynthetic enzymes as required to survive nutrient limitation. Notably, these enzymes are established antimicrobial targets in other bacterial pathogens, underscoring the general significance of these findings (Islam, et al., 2015).

Materials and Methods

Bacterial strains and reagents

Experiments were performed on *A. baumannii* ATCC 17978 and mutant derivatives of this strain, including the Δ*zigA* mutant generated previously (Nairn, et al., 2016) and the Δ*ribBX* mutant generated as described below. Cloning was performed in *E. coli* DH5α and protein expression in *E. coli* BL21 (DE3). Strains were cultured in Luria Broth (LB) at 37 °C with aeration unless otherwise noted, and OD_{600} was used to measure bacterial growth as previously described (Nairn, et al., 2016). Kanamycin (Sigma) was used at 40 µg/mL. Ampicillin (Sigma) was used at 100 µg/mL for *E. coli* and 500 µg/mL for *A. baumannii*. Recombinant human CP were expressed and purified as previously described (Corbin, et al., 2008). S100A8 and S100A9 cloned into pET1120 were transformed separately into *E. coli* C41 (DE3) cells for expression. Cells were induced at 37 °C at OD_{600} between 0.6 and 0.8 with the addition of 1 mM isopropyl thio-β-D-galactoside (IPTG) and allowed to grow 4 h post-induction. Cells were harvested by centrifugation (6500 rpm, 20 min, 4 °C), and re-suspended in Lysis Buffer (50 mM Tris pH 8.0, 100 mM NaCl, 1 mM EDTA, 1 mM phenylmethane sulfonyl fluoride (PMSF), 0.5 % Triton X-100). Once homogenized, sample was sonicated (10 min, 50 watts, 5 s on/10 s off), and centrifuged (20,000 rpm, 20 min). The supernatant was filtered and loaded onto a SourceQ column (General Electric) with flow rate at 1 mL/min. After loading, the column was washed with three column volume (CV) Buffer A (20 mM Tris, pH 8.0) and eluted with a gradient from 0 to 100% Buffer B (20 mM Tris, pH 8.0, 1 M NaCl) over 10 CV. S100A8/A9 containing fractions were pooled according to SDS-

PAGE, concentrated, and loaded onto S75 column (General Electric). The column was washed with 1 CV S75 Buffer (20 mM Tris, pH 8.0, 100 mM NaCl), S100A8/A9 containing fractions pooled according to SDS-PAGE, flash frozen, and stored at –80°C.

A. baumannii mutant generation

To generate in-frame the Δ*ribBX* strain, approximately 1000 base pairs of DNA in both the 5' and 3' flanking regions surrounding the open reading frame, leaving the N-terminal ~200 nucleotides of *ribBX* intact to limit polarity, were amplified from *A. baumannii* genomic DNA using primers listed in **Table 4**, and the kanamycin resistance gene *aph* was amplified by PCR from the pUCK1 plasmid using primers listed in **Table 4** (Menard, et al., 1993). The 3 PCR products and pFLP2 vector were assembled together using Gibson assembly (New England Biolabs) and sequence verified (Hoang, et al., 1998). pFLP2 was then electroporated into *A. baumannii*, plated onto LB Km 40 agar, and grown overnight at 37 °C. Transformants were patched to LB Km40 or LB agar with 10 % sucrose to isolate Km^R and sucrose^S merodiploids. Merodiploid strains were grown in LB supplemented with 10 μg/mL riboflavin overnight at 37 °C to resolve the plasmid. Cultures were serially diluted, plated on LB agar with 10 % sucrose, and incubated at 37 °C overnight. The resulting Km^R sucrose^R strains were screened for loss of *ribBX* and replacement with *aph* by multiple PCR reactions.

A. baumannii expression construct generation

The *ribBX* gene was amplified from WT *A. baumannii* genomic DNA using primers listed in **Table 4** and incorporated a C-terminal cMyc tag. The amplified gene product was ligated into digested pWH1266 containing the constitutive *r01* promoter, which was generated as previously described (Mortensen, et al., 2014): the 16s gene *r01* was amplified from *A. baumannii* genomic DNA and ligated into the pWH1266 expression vector. The integrity of the *r01* promoter and *ribBX* was confirmed by sequencing. The empty vector and the *ribBX* expression vector were transformed into WT and *∆zigA* by electroporation.

Growth in calprotectin or metal chelators

Overnight *A. baumannii* cultures started from independent colonies as replicates were subcultured 1:50 in LB for 1 h. Back-diluted cultures were then inoculated 1:100 into LB containing various concentrations of tetrakis-(2-pyridylmethyl)ethylenediamine (TPEN) as indicated, and growth was monitored over time. For growth in medium containing recombinant human WT CP, back-diluted cultures were inoculated 1:100 into LB containing 40% CP buffer (20 mM Tris-HCl pH 7.5, 100 mM NaCl, 5 mM □-mercaptoethanol, 3 mM $CaCl_2$) supplemented with CP, and growth was monitored over time. To assess growth during Fe limitation, back-diluted cultures were inoculated 1:100 into M9 minimal media supplemented with 0.5% sodium succinate dibasic hexahydrate and 10 µM ethylenediamine-di(*o*-hydroxyphenylacetic acid) (EDDHA, LGC Standards), and growth was monitored over time.

ICP-MS quantification of total metals

The quantification of total metal content of the growth media used here (LB + 40 % CP buffer) and total cell-associated metal was carried out largely as described before on a Perkin-Elmer Elan DRCII ICP-MS (Nairn, et al., 2016). Briefly, the growth media was incubated with 200 µg/mL calprotectin (CP) at 37 °C for 2 h. CP was then removed via filtration with a pre-washed and pre-equilibrated 3 or 10 kDa filter with the flow-through eluent analyzed for total metal content and compared with the same media prior to filtration, essentially as described (Nakashige, et al., 2015). The CP used for these studies contained 0.11 protomer mol•equiv Zn, 0.08 protomer mol•equiv Cu, 0.01 protomer mol•equiv Mn, 0.03 protomer mol•equiv Ni and 0.04 protomer mol•equiv Fe and is thus 85% metal-free (2 metal sites per protomer); quantitation of the total metal chelated by CP in replicate experiments was found to be 95 ±7% of expected value based on the concentration of CP-binding sites (site 1 + site 2, per protomer). For bacterial lysates, strains were grown in the presence of the 200 µg/mL CP as described above. Cells were normalized to the same OD_{600} and pelleted at 4 °C, then washed 3 times with ice-cold, chelexed PBS buffer. Cell pellets were stored at –80 °C before measurements. Samples were incubated with 30% nitric acid at 95° for 10 min and 65 °C for 1 h. The volumes were then adjusted to 3 mL with 2.5% nitric acid and subjected to elemental quantification on a Perkin-Elmer Elan DRCII ICP-MS equipped with AS-93 autosampler run alongside elemental standards. Cellular metal content was normalized to protein amount which was measured using a standard Bradford assay, as described previously (Jacobsen, et al., 2011).

RNA Sequencing

WT *A. baumannii* was grown overnight in 3 mL LB. Cultures were reseeded 1:50 in LB and grown for 1 h at 37 °C with shaking. These cultures were reseeded 1:100 in 40 % LB, 60 % CP buffer plus or minus 250 µg/ml CP and grown for 7 h at 37 °C with shaking. Cultures were pelleted at 4 °C with 2,500 x *g* for 8 min and then air dried on ice. Each pellet was suspended in 1 mL TRIzol and transferred to tubes containing lysing matrix B (MP Biomedicals). Bacteria were lysed using a FastPrep-24 (MP Biomedicals) bead beater for 45 s at 6 m/s. Two hundred µL chloroform then was added to each tube. After brief vortexing, the tubes were centrifuged for 15 min at 4 °C and the upper layer was transferred to another new tube. RNA was purified using the RNeasy preparation kit (Qiagen) according to the RNeasy lipid tissue directions. DNA contamination was removed by adding 8 μL RQ1 (Promega), 12 μL 10x RQ1 buffer, and 2 μL RNase inhibitor (Promega) to each sample and incubating at 37 °C for 2 h. Samples were then cleaned up using the RNeasy miniprep RNA cleanup protocol (Qiagen). To ensure purity of the RNA from DNA contamination, an aliquot of RNA was removed for reverse transcription (RT), including no-RT controls, and assessed by PCR. Prior to sequencing, RNA was quantified on the Synergy 2 with Gen5 2.00 software (BioTek).

Vanderbilt Technologies for Advanced Genomics Core Facility (VANTAGE) prepared RNA-seq libraries from 1.5 μg of *A. baumannii* total RNA using the following protocol. The integrity of the total RNA was evaluated using the Agilent Bioanalyzer Nano RNA chip. The Ribo-Zero rRNA removal kit for Gram-negative bacteria (Epicentre) was used to remove rRNA by following the manufacturer's protocol. The rRNA-reduced RNA was used as an input to the TruSeq stranded mRNA sample preparation kit (Illumina), skipping the mRNA selection step and going directly into the RNA fragmentation and random hexamer priming step. The RNA was converted into double-stranded cDNA, adapter ligated, and enriched with PCR, replacing the enzyme from the kit with KAPA HiFi DNA polymerase to create the final cDNA sequencing library. The cDNA library underwent quality control (QC) by running on an Agilent Bioanalyzer HS DNA assay to confirm the final library size and on an Agilent Mx3005P quantitative PCR (qPCR) machine using the KAPA Illumina library quantification kit to determine concentration. A 2 nM stock was created, and samples were pooled by molarity for multiplexing. From the pool, a 10.5 pM concentration was loaded into each well for the flow cell on the Illumina cBot for cluster generation. The flow cell was then loaded onto an Illumina HiSeq 2500, utilizing v3 chemistry and

HTA 1.8 for a paired-end 50-bp run. The raw sequencing reads in BCL format were processed through CASAVA-1.8.2 for FASTQ conversion and demultiplexing. The RTA chastity filter was used, and only the PF (pass filter) reads were retained for further analysis.

Transcriptomic analysis

The Illumina HiSeq 2500-generated FASTQ reads were processed by using the Bayesian adapter trimmer Scythe (version 0.992; http://github.com/vsbuffalo/scythe) to trim 3= adaptor sequence contaminants from the reads. EDGE-pro v1.3 (Estimated Degree of Gene Expression in Prokaryotes) software (Magoc, et al., 2013) then was used to align the reads with Bowtie2 v2.1.0 (Langmead and Salzberg, 2012) and estimate gene expression directly from the alignment output. The FASTA of the reference genome sequence (.fna), protein translation table with coordinates of protein coding genes (.ptt), and a table containing coordinates of tRNA and rRNA genes were downloaded from NCBI (ftp://ftp.ncbi.nih.gov/GenBank/genomes/Bacteria/Acinetobacter_ baumannii_ATCC_17978_ uid17477). The .fna, .ptt, and .rnt files were concatenated from the main genome and two native plasmids into single input files, and they were used as inputs into EDGE-pro. EDGE-pro was run with default parameters, except for defining the read length as 50 bp (-l 50) and using 16 threads (-t 16) on a 64-core Linux server. On average, more than 96% of the reads were uniquely aligned. Alignment statistics and other QC metrics were calculated from the aligned BAM file using the RSeQC program suite (Wang, et al., 2012). The output of EDGE-pro was an RPKM value table for the genome and plasmids. A script provided with EDGE-pro called edgeToDeseq.perl was used to concatenate the output of the various samples into a single count table for input into DESeq. The expression level of each gene was determined using DESeq (Anders and Huber, 2010) in the statistical programming package R-3.0.0 (http://www.r-project.org). Differences in expression comparing untreated WT *A. baumannii* to CP-treated *A. baumannii* were considered significant based on a *P* value less than or equal to 0.01.

Quantitative RT-PCR

Overnight cultures of *A. baumannii* were diluted 1:50 in LB and grown for 1 h at 37°C. Cultures were then diluted 1:100 into LB plus or minus 250 μg/ml CP and grown for 8 h. Cultures were pelleted at 4°C and resuspended in 1:1 acetone : ethanol prior to storage at -80°C until processing. For RNA extraction, cells were pelleted and resuspended in LETS buffer and lysed using Lysis Matrix B tubes (MP Biologicals) and a FastPrep-24 (MP) bead beater. Samples were heated to 55°C for 5 min and pelleted at 15,000 rpm for 10 min. The top phase was combined with TRIzol and incubated at room temperature for 5 min. Chloroform was mixed with each sample, incubated for 3 min, and centrifuged for 15 min at 4°C at 15,000 rpm. Following centrifugation, the upper aqueous phase was transferred to a new tube and incubated with isopropyl alcohol for 10 min at room temperature to precipitate the RNA. Samples were centrifuged at 4°C for 10 min at 15,000 rpm. Supernatant was removed, and the pellet was washed twice with 70% ethanol and dissolved in water. DNA contamination was removed by adding RQ1 and RQ1 buffer (Promega), and RNAse inhibitor (Thermo), and the samples were incubated at 37°C for 2 h. Following DNAse treatment, RNA was purified using RNease mini kit (Qiagen) following manufacturer's recommendation. RNA was quantified, and 2 μg of RNA was used for cDNA synthesis. cDNA synthesis and qRT-PCR was performed as previously described using the $2^{\Delta\Delta CT}$ method (Mortensen, et al., 2014; Nairn, et al., 2016). Primers used for qRT-PCR are listed in **Table 4**.

LC-MS/MS proteomic analysis

Protein samples were denatured in 8 M urea, 100 mM ammonium bicarbonate solution, then incubated for 45 min at 56 °C with 10 mM dithiothreitol (DTT) to reduce cysteine residues. The free cysteine residue side chains were then alkylated with 40 mM iodoacetamide for 1 h in the dark at room temperature. The solution was diluted to 1 M urea and 1:100 (w:w) ratio of trypsin was added and the samples were digested at 37 °C overnight. Peptides were desalted by Zip-tip and injected into an Easy-nLC HPLC system coupled to an Orbitrap Fusion Lumos mass spectrometer (Thermo Scientific, Bremen, Germany). Peptide samples were loaded onto a home-made C18 trap column (75 μm × 20 mm, 3 μm) in 0.1% formic acid. The peptides were separated using an Acclaim PepMapTM RSLC C18 analytical column (75 μm × 150 mm, 2 μm) using an acetonitrile-based gradient (Solvent A: 0% acetonitrile, 0.1% formic acid; Solvent B: 80% acetonitrile, 0.1% formic acid) at a flow rate of 400 nL/min. A 30 min gradient was implemented as follows: 0-0.5 min, 2-9% B; 0.5-24 min, 9-26% B; 24-26 min, 26-100% B; 26-30 min, 100% B followed by re-equilibration to 2% B. The electrospray ionization was carried out with a nanoESI source at a 260 °C capillary temperature and 1.8 kV spray voltage. The mass spectrometer was operated in data-dependent acquisition mode with mass range 400 to 1600 m/z. The precursor ions were selected for tandem mass (MS/MS) analysis in Orbitrap with 3 sec cycle time using HCD at 35% collision energy. Intensity threshold was set at 5e3. The dynamic exclusion was set with a repeat count of 1 and exclusion duration of 30 s. The resulting data were searched against an *Acinetobacter baumannii* database (Uniprot UP000094982, 3,780 entries, with the database downloaded on 07/06/2017 from Uniprot) in Proteome Discoverer 2.1. Carbamidomethylation of cysteine residues was set as a fixed modification. Protein N-terminal acetylation, oxidation of methionine, protein N-terminal methionine loss, protein N-terminal methionine loss and acetylation, and pyroglutamine formation were set as variable modifications. A total of 3 variable modifications were allowed. Trypsin digestion specificity with two missed cleavage was allowed. The mass tolerance for precursor and fragment ions was set to 10 ppm and 0.6 Da respectively.

Statistical rationale and bioinformatics analysis

Data analysis was performed as previously described (Kentache, et al., 2017; Park, et al., 2014). Proteins detected fewer than 3 times in 4 replicate lysates were excluded from our statistical analysis. The statistical analysis of these data was completed using unpaired, two-tailed student's *t* test with Welch's correction. Functional information for the selected proteins were gathered from the National Center for Biotechnology Information (NCBI, https://www.ncbi.nlm.nih.gov/) and the SEED database (http://pubseed.theseed.org/?page= Minimal) (Overbeek, et al., 2005). Metabolism pathway information for the selected proteins were obtained from the Kyoto Encyclopedia of Genes and Genomes (KEGG) database (https://www.genome.jp/kegg/pathway.html).

Siderophore quantification

Siderophore production was quantified using a Chrome Azurol S (CAS) assay as described previously (Alexander and Zuberer, 1991; Schwyn and Neilands, 1987). Briefly, *A. baumannii* was grown for 36 h in the presence of 250 μg/mL CP or buffer as described above. Supernatants were collected and filtered through a 0.22 μm filter (Millipore). Supernatants were mixed 1:1 with the chrome azurol S shuttle solution(Alexander and Zuberer, 1991), and OD_{630} was determined after a 30 min incubation at room temperature. Values were normalized to starting cell density as determined by OD_{600}.

Zinc Proteome prediction of *A. baumannii*

Using a previously published approach (Valasatava, et al., 2016), we created two libraries of Hidden Markov Model profiles (Eddy, 1998)**:** a library of Zn-binding Pfam domains (Finn, et al., 2014), and a library of Zn-binding structural motifs. The Pfam domain library was created by merging two lists: 1). a list of Pfam domains with known 3-dimensional structure that contain a Zn-binding site extracted from MetalPDB (Putignano, et al., 2018) in which each of these domains could be associated with the residues responsible for Zn-binding and with their positions within the domain sequence and 2). a list of Pfam domains without a known 3D structure but annotated as Zn-binding, obtained by text mining of the annotations in the Pfam database. The procedure resulted in a set of 573 Pfam domains: 541 with an associated Zn-containing 3D structure, and an additional 32 annotated as Zn-binding domains. The library of Zn-binding structural motifs was created by splitting into fragments the Zn-binding sites stored in MetalPDB as of June 2017, as previously described (Rosato, et al., 2016). Only one representative was kept for Zn-binding sites that, though found in different PDB structures, fall in the same position of the same protein domain. Sites that are not physiologically relevant based on literature inspection, *e.g.,* Zn-substituted structures, spurious sites, were manually removed from the dataset. This procedure resulted in a set of 6450 zinc-binding motifs derived from 2651 Zn-binding sites.

The Zn proteome of *Acinetobacter baumannii* was obtained by using the hmmscan tool (Eddy, 1998) to search each bacterial sequence for the profiles contained in the two libraries. A bacterial sequence was identified as containing a potential Zn-binding site if at least one of the following conditions was verified: A) The profiles of all the fragments of a given site matched the sequence with an e-value lower than 10^{-3} and the corresponding ligands are conserved in the sequence. B) The profile of a domain with associated ligands matched the sequence with an e-value lower than 10^{-5} and the ligands are conserved in the sequence. C) The profile of a domain with no associated ligands matched the sequence with an e-value lower than 10^{-7}. These predictions were integrated by adding the proteins annotated as Zn-binding in the UniProt database (UniProt Consortium, 2018). In total, 213 proteins of *Acinetobacter baumannii* were identified as Zn-binding proteins.

FAD quantification

Overnight *A. baumannii* cultures were back-diluted 1:50 into LB for 1 h. Cultures were then inoculated 1:100 into LB containing 40% CP buffer (20 mM Tris-HCl pH 7.5, 100 mM NaCl, 5 mM β-mercaptoethanol, 3 mM $CaCl_2$) supplemented with 200 μg/ml CP and grown for 6 h. Optical densities were normalized across strains, and cells were pelleted and washed with PBS. Total cellular FAD was quantified using the FAD assay kit (Abcam). Pellets were resuspended in FAD assay buffer and lysed twice using Lysis Matrix B tubes (MP Biologicals) and a FastPrep-24 (MP) bead beater. Supernatants were collected, and protein concentration was determined by BCA assay (Thermo Scientific). Samples were deproteinized by adding ice-cold 4 M perchloric acid and incubated on ice for 5 min. Samples were centrifuged for 2 min at 4°C at 13,000 x g, and supernatants were transferred to a new Eppendorf tube. Ice-cold 2 M potassium hydroxide was added until the pH was 6.5-8. Samples were centrifuged for 15 min at 4°C at 13,000 x g, and supernatants were collected. To quantify FAD, 50 μL reaction mixtures were prepared by combining 46 μL of 1:50 dilution of sample with 2 μL OxiRad probe and 2 μL enzyme mixture (Abcam). OD_{570} was monitored over 30 min, and values were plotted against an FAD standard curve and normalized to total protein. Data are averaged from 3 independent experiments.

Purification of *A. baumannii* proteins

Oligonucleotide primers used for cloning are listed in **Table 4**. The gene sequences of *ribA*, *ribB* and *ribBX* from *Acinetobacter baumannii ATCC 17978* (locus tags A1S_3107, A1S_0823 and A1S_3388, respectively) were obtained from the SEED database. The gene *ribBX* encodes a 373 amino acid protein that is 41% identical and 56% similar to the homolog encoded by *Mycobacterium tuberculosis* H37Rv (locus tag Rv1415; NP_215931; PDB: 4I14) over their entire length (**Figure 13B**) (Singh, et al., 2013). The calculated molecular mass and theoretical isoelectric point (pI) value for the *A. baumannii* RibBX are 40,899 Da and 5.62, respectively (https://web.expasy.org/protparam/). Full length proteins were cloned into a pHIS plasmid at the *Nco*I site using an isothermal assembly method and was expressed with an N-terminal His-tag (Gibson, et al., 2009).

These resulting plasmids were transformed into *E. coli* BL21(DE3) for expression. Cells were grown in lysogeny broth (LB) medium supplemented with 100 µg/mL ampicillin and shaking at 37 °C to OD_{600} of 0.6, at which time ITPG was added to final 0.5 mM. The cells were allowed to induce at 16 °C overnight. For each 0.8 L cell pellet, cells were suspended in 40 mL lysis buffer (25 mM Tris, 500 mM NaCl, 2 mM TCEP, pH 8) and sonicated at 60 % power (3 s on; 9 s off, on ice), for total 15 min/L cells. This solution was centrifuged at 10,000 g (20 min, 4 °C). The supernatant was filtered with 0.22 µm for loading onto a 5 mL HisTrap column (GE Healthcare). The Ni-NTA column was run at 3 mL/min, and protein was eluted with a 4-40% buffer B (25 mM Tris, 500 mM NaCl, 2 mM TCEP, pH 8) gradient over 20 column volumes. The protein-containing fractions were pooled, cleaved with TEV protease and dialyzed again buffer (25 mM Tris, 500 mM NaCl, 2 mM TCEP, pH 8) at 4 °C overnight. Solutions were filtered with 0.22 µm and run through Ni-NTA column. Non-tagged protein factions are pooled and concentrated to ~3 mL for loading on Hi LoadTM 16/600 SuperdexTM 200 or 75 (GE Healthcare). Running buffer was (25 mM Tris, 200 mM NaCl, 2 mM TCEP, pH 8), and protein was eluted at a flow-rate of 1 mL/min. Protein-containing fractions were pooled, concentrated and flash-frozen in liquid nitrogen, stored at –80 °C, and buffer exchanged prior to use. Protein mass was confirmed by LC-ESI-MS or trypsin digested MALDI-MS and was judged to be 90% pure by overloaded SDS-PAGE gels. For RibBX, the residual FMN bound to RibBX during purification was confirmed by LC-MS/MS and UV-Vis spectroscopy.

GCHII activity assay

The GTP cyclohydrolase II (GCHII) activities of RibA and RibBX were measured essentially as previously described (Singh, et al., 2013). Briefly, reaction mixtures were prepared in a buffer containing 50 mM Tris, 100 mM NaCl, 10 mM $MgCl_2$, 2 mM TCEP, 10 µM $ZnSO_4$, pH 8.0 in a total volume of 200 µL, with reactions initiated by the addition of enzyme to a final concentration of 2 µM with 0~1 mM GTP. To monitor the formation of 2,5-diamino-6-ribosylamino-4(3*H*)-pyrimidinone 5'-phosphate (DARP), the absorbance at 310 nm was monitored at 37 °C for 20 min and the concentration of DARP was calculated using an extinction coefficient of Abs_{310} = 7.43 $mM^{-1}cm^{-1}$. The linear range of these kinetic traces was used to calculate the initial rate and these rates were used to fit to the Michaelis-Menten steady-state model.

DHBPS activity assay

The 3,4-dihydroxy-2-butanone 4-phosphate synthase (DHBPS) activities of RibB and RibBX were measured by a colorimetric method as described (Singh, et al., 2013). Briefly, reaction mixtures contained 50 mM Tris, 150 mM NaCl, 10 mM $MgCl_2$, pH 7.5 in a total volume of 60 µL. Reactions were initiated by the addition of enzyme to final 1 µM with final 0~1 mM ribulose-5-phosphate (Cayman). After incubation at 37 °C for 15 min, 48 µL of a saturated creatine (Fisher Scientific) solution was added, followed immediately by 24 µL 1-naphthol (Fisher Scientific) (dissolved at 35 mg/mL in 1 M NaOH). The absorbance at 525 nm was measured after 45 min using plate reader (BioTek, Synergy Neo2). The standard curve was constructed with 0~500 µM 2,3-butadione (Sigma-Aldrich) for calculating product (DHBP) formation. Initial rates were calculated for Michaelis-Menten fit. Inhibition of FMN was measured in the presence of 0~1 mM FMN (Cayman).

FMN binding by ITC

All ITC titrations were carried out as described before (Grossoehme and Giedroc, 2009) using a MicroCal VP-ITC calorimeter. 300 µM FMN was placed into the syringe with ~30 µM RibBX protomer in the reaction cell. Injections (2~8 µL) were made at a rate of 2 µL s^{-1}, with 180~240 s allowed for equilibration of the mixture between injections. All reactions were conducted in at least triplicate in 50 mM Tris, 150 mM NaCl, 10 mM $MgCl_2$, pH 7.5 at 25.0 °C. The Origin 7.0 Software package provided by MicroCal was used and data were fitted as single-site binding model with the n and K_a values optimized during the fit.

Crystal structure of RibBX

RibBX expressed and purified as described above was subjected to polishing on a Superdex 200 10/300 GL column (GE Healthcare) running in 25 mM Tris, 200 mM NaCl, 2 mM TCEP, pH 8.0 at a flow-rate of 0.5 mL/min. Peak fractions were concentrated to 8~12 mg/mL using an Amicon centrifugal concentrator with a 30 kDa cutoff membrane (Millipore) and used for crystallization by vapor-diffusion in 96-well sitting-drop plates. Initial crystallization screening was carried out using commercial kits from MemGold2^{TM} (Molecular Dimensions) by mixing 0.15 µL reservoir buffer and 0.15 µL protein solution and equilibrating against 30 µL reservoir buffer at 293 K. Small crystals appeared after 1 day when RibBX was equilibrated against a reservoir solution containing 10 mM MES, 100 mM NaCl, 150 mM ammonia sulfate, 19% (w/v) PEG 1000. The crystallization conditions were optimized over 19~24% (w/v) PEG1000 over 10~15 mg/mL RibBX while changing the protein:buffer ratio to 2:1 by hanging drop vapor diffusion. The plates were incubated at 20 °C for 1-2 weeks, with crystals appearing before that time.

Crystals were harvested after 4-7 days, cryo-protected in the reservoir solution supplemented with 25% glycerol and flash frozen in liquid nitrogen. Diffraction data were collected at 100 K at the Beamline station 4.2.2 at the Advanced Light Source (Berkeley National Laboratory, CA) and were indexed, integrated, and scaled using XDS (Kabsch, 2010). The structure was solved by molecular replacement using PHASER the PDB 4I14 as search model. The Autobuild function was used to generate a model that was improved by iterative cycles of manual building in Coot (Emsley, et al., 2010) and refinement using PHENIX (Adams, et al., 2010). Torsion-angle non-crystallographic symmetry restraints and secondary structure restraints were used during refinement. MolProbity software (Chen, et al., 2010) was used to assess the geometric quality of the models. PyMOL (PyMOL Molecular Graphics System, Version 1.2r3pre, Schrödinger, LLC.) was used to generate molecular images. Data collection and refinement statistics are indicated in **Table 3**.

Analytical gel filtration chromatography

A Superdex 200 10/300 GL column (GE Healthcare) was equilibrated and chromatographed in 50 mM Tris, 150 mM NaCl, 10 mM $MgCl_2$, 2 mM TCEP, pH 7.5 at a flow-rate of 0.5 mL/min and calibrated with the Gel Filtration Calibration Kit HMW (GE Healthcare). A linear fit a plot of K_{av} vs. log M_r gave R^2= 0.90. 100 µM RibBX was pre-incubated with 1.25 eq. FMN at 4 °C for 1 h. 100 µL samples were injected for each chromatography run.

A. baumannii growth with riboflavin

Overnight cultures of *A. baumannii* were subcultured 1:50 in LB for 1 h. Cultures were then inoculated 1:100 into M9 minimal media supplemented with Vishniac's trace metal mix with or without $ZnCl_2$ as previously described (Nairn, et al., 2016). M9 minimal media supplemented with full Vishniac's trace metal mix contained 36 µM Fe, 5.2 µM Mn, 3.2 µM Cu, 1.8 µM Mo, 13.4 µM Co and 27.2 µM Zn. Sodium succinate dibasic hexahydrate (Sigma) or sodium fumarate dibasic (Sigma) were used as the sole carbon source at 0.5 % (w/v). Riboflavin (Sigma) was supplemented with a final concentration of 10 µg/mL, and OD_{600} was monitored over time. Data are representative of at least 3 independent experiments.

Quantification and Statistical Analysis

Bioassays were performed with at least 3 biological replicates (*n*=3) as indicated. The averages and standard deviation of the separate replicates and Student's *t* test were then calculated using Graphpad Prism and Microsoft Excel. The structure of RibBX was refined with internal statistical analysis as reported in the deposition in the PDB. Detailed quantification and statistical analysis are fully described in the manuscript Figure legend and Methods sections of the manuscript.

Data and software availability

The coordinates for the RibBX crystal structure have been deposited in the Protein Data Bank PDB: 6MNZ. Software used to analyze RNA sequencing results are fully described in the manuscript Methods section with appropriate citations, and data have been uploaded to the National Institutes of Health Gene Expression Omnibus with accession number GSE125491 (https://www.ncbi.nlm.nih.gov/geo/query/acc.cgi?acc=GSE125491). Briefly, raw sequencing reads were processed using CASAVA-1.8.2 for FASTQ conversion. FASTQ reads were processed using the Bayesian adapter trimmer Scythe version 0.992. EDGE-pro version 1.3 was used to align reads with Bowtie2 version 2.1.0. The expression level of each gene was determined using DESeq in the statistical programming package R-3.0.0. Software used for diffraction data are fully described in the manuscript Methods section with appropriate citations. Briefly, diffraction data were collected at 100 K at the Beamline station 4.2.2 at the Advanced Light Source (Berkeley National Laboratory, CA) and were indexed, integrated, and scaled using XDS (Kabsch, 2010). Software used for LC-MS/MS data is xcaliber v4.0. All software used in this study are reported in Method Details.

Table 3. RibBX data collection and refinement statistics.

	A.baumannii RibBX
PDB ID	6MNZ
Data collection	
Wavelength (Å)	1.00003
Space group	C2
Cell dimensions	
a, b, c (Å)	116.71, 136.86, 51.86
α, β, γ (°)	90.00, 98.53, 90.00
Resolution (Å)	68.43 – 2.66
R_{sym}	0.131 (1.122)
R_{meas}	0.153 (1.309)
R_{pim}	0.079 (0.672)
CC1/2	0.993 (0.557)
$I/\sigma(I)$	7.4 (1.2)
Completeness (%)	99.1 (99.7)
Multiplicity	3.7 (3.8)
Refinement	
Resolution (Å)	44.12 –2.66 (2.75 – 2.66)
No. unique reflections	22952 (2298)
R_{work}	0.2778 (0.4011)
R_{free}	0.3030 (0.4528)
R.m.s.d values	
Bond lengths (Å)	0.002
Bond angles (°)	0.539
No. atoms	
Protein	5170
Ligand	47
B-factors (Å^2)	
Protein/ligand/solvent	52.64
Ramachandran statistics	
Favored (%)	93.30
Allowed (%)	6.55
MolProbity score	1.73
Rotamer outliers (%)	0.37

[*] Highest-resolution shell values are shown in parentheses.

Table 4. Oligonucleotides used in Chapter II.

Name	**Sequence (5' to 3')**	**Description**
RibBX_Nhis_F	CAG GGC GCC ATG GAT CCG CTG AGT CGT GTT GA	CloningRibBX into pHIS, forward
RibBX_Nhis_R	CCT TTG AAT TCC GGA TCC ATG GTT ATT TCG TTG TGA TTT GAT CAG CAG T	CloningRibBX into pHIS, reverse
RibA_Nhis_F	CAG GGC GCC ATG GAT CCT ATA GAG TTC ATT GCA ACA TCA AAA CT	CloningRibA into pHIS, forward
RibA_Nhis_R	CCT TTG AAT TCC GGA TCC ATG GTT AAA AAT CAT CTT TTT GGT AAA GGT GAT CCA	CloningRibA into pHIS, reverse
RibB_Nhis_F	CAG GGC GCC ATG GAT TCT AGT TTA ATT CAA CCA GAA CTT TTT TTC TCA	CloningRibB into pHIS, forward
RibB_Nhis_R	CCT TTG AAT TCC GGA TCC ATG GTT AAA TAC CGT GTT GTT GAC GAT ATT GTA	CloningRibB into pHIS, reverse
A1S_3388_F	GGA TCC ATG CCG CTG AGT CGT	Cloning ribBX into pWH1266, foward
A1S_3388_myc_R	GTC GAC TTA TAG ATC TTC TTC AGA TAT CAG TTT CTG TTC GAT TTT CGT TGT GAT TTG	Cloning ribBX into pWH1266, reverse
A1S_3388_FL1_F_KO2	TGA TGG GTT AAA AAG GAT CGA TCC TCT AGA AAG AGT TAA CTC AAG CTC TCG CG	Cloning ribBX 5' flanking region into pFLP2, forward
A1S_3388_FL1_R_KO2	TCC TAG TTA GTC ACA TAT GTC GCT TTC ACC TTT TTT TG	Cloning ribBX 5' flanking region into pFLP2, reverse
A1S_3388_Kan_F_KO2	AAA GCG ACA TAT GTG ACT AAC TAG GAG GAA TAA ATG	Cloning Kn cassette into pFLP2; forward
A1S_3388_Kan_R_KO2	TCC CAA GCA TAT GTC ATT ATT CCC TCC AGG TAC	Cloning Kn cassette into pFLP2; reverse
A1S_3388_FL2_F_KO2	GAG GGA ATA ATG ACA TAT GCT TGG GAC CAG C	Cloning ribBX 3' flanking region into pFLP2, forward
A1S_3388_FL2_R_KO2	TTC CGA AGT TCC TAT TCT CTA GGG GGA TCC ACG TAA CTC GTA AGC ACC TAA AC	Cloning ribBX 3' flanking region into pFLP2, reverse
Ab0092RTFor	GGA GCA TAC CGC GCC TAT TAA C	*A1S_0092* qRT-PCR, forward
Ab0092RTRev	GTC GAG TTG CGT TTG GTC TGA A	*A1S_0092* qRT-PCR, reverse
Ab0170RTFor	GTG GAA TGC TGA TGT AGC GCT TG	*A1S_0170* qRT-PCR, forward

Ab0170RTRev	ACT TTC ACG CGC AAA CTG AGA AC	*A1S_0170* qRT-PCR, reverse
Ab0242RTFor	GGC GAC CAT CAC CAA AGT GAA	*A1S_0242* qRT-PCR, forward
Ab0242RTRev	TGG TAA TCA CTT CCA CTC GCG T	*A1S_0242* qRT-PCR, reverse
Ab0652RTFor	GGG CTA TCG TAA CGA AAG TTC AAG C	*A1S_0652* qRT-PCR, forward
Ab0652RTRev	AAC GAG AAT AGG GTC ACC ACC A	*A1S_0652* qRT-PCR, reverse
Ab1214RTFor	AAC CGA ACG CTC TTC TGC AAC	*A1S_1214* qRT-PCR, forward
Ab1214RTRev	AAG CGA ACA GTG ACT TTG TCG C	*A1S_1214* qRT-PCR, reverse
Ab1647RTFor	GCC ACT ACA TCC TTG GCA AGC	*A1S_1647* qRT-PCR, forward
Ab1647RTRev	AGG TCC GAA TTG ATG TAG TCG GTG	*A1S_1647* qRT-PCR, reverse
Ab1844RTFor	GAT ATG CCA GCC GAC AAA GCA AAT	*A1S_1844* qRT-PCR, forward
Ab1844RTRev	CGC CAG ATA TGA CGC CAT TTA CC	*A1S_1844* qRT-PCR, reverse
Ab1868RTFor	TCA ATA CGC CGT GCG CTT AAG	*A1S_1868* qRT-PCR, forward
Ab1868RTRev	CCT AGC TTT AAA GTC GCG CCG	*A1S_1868* qRT-PCR, reverse
Ab2382RTFor	GTG GGC TTC TGT ACA GGC G	*A1S_2382* qRT-PCR, forward
Ab2382RTRev	TTG CAT GGT GAC CAC AGG C	*A1S_2382* qRT-PCR, reverse
Ab2580RTFor	ACG GCA CAA CCC GTA AAA CAA	*A1S_2580* qRT-PCR, forward
Ab2580RTRev	CAT CGT GTT GTG TTG GCG C	*A1S_2580* qRT-PCR, reverse
3411RTf	GATCAGGCTCAGCAAGACCAG	*A1S_3411* qRT-PCR, forward
3411RTr	GTGCTTGGACAGCTTCATCA	*A1S_3411* qRT-PCR, reverse
r01RTf	CTGTAGCGGGTCTGAGAGGAT	*r01* qRT-PCR, forward
r01RTr	CCATAAGGCCTTCTTCACAC	*r01* qRT-PCR, reverse

Results

Calprotectin induces multi-metal restriction in *A. baumannii*

Although calprotectin is known to induce a Zn^{II} starvation in *A. baumannii* (Hood, et al., 2012), the extent to which other metal homeostasis systems are impacted by CP is not known. To address the question, a global transcriptomic analysis (RNAseq) (**Figure 6**) and a proteomic analysis (**Figure 8**) were performed on a *wild-type* (WT) strain grown in the presence or absence of physiologically relevant concentrations of CP (Clohessy and Golden, 1995). We first measured the metal concentration in the culture media (60% LB + CP buffer) with or without 200 µg/mL CP (**Figure 6A; Figure 7**). CP notably depletes the culture medium of major metals Zn and Fe, with no effect on Cu. Mn and Co are also significantly decreased by CP.

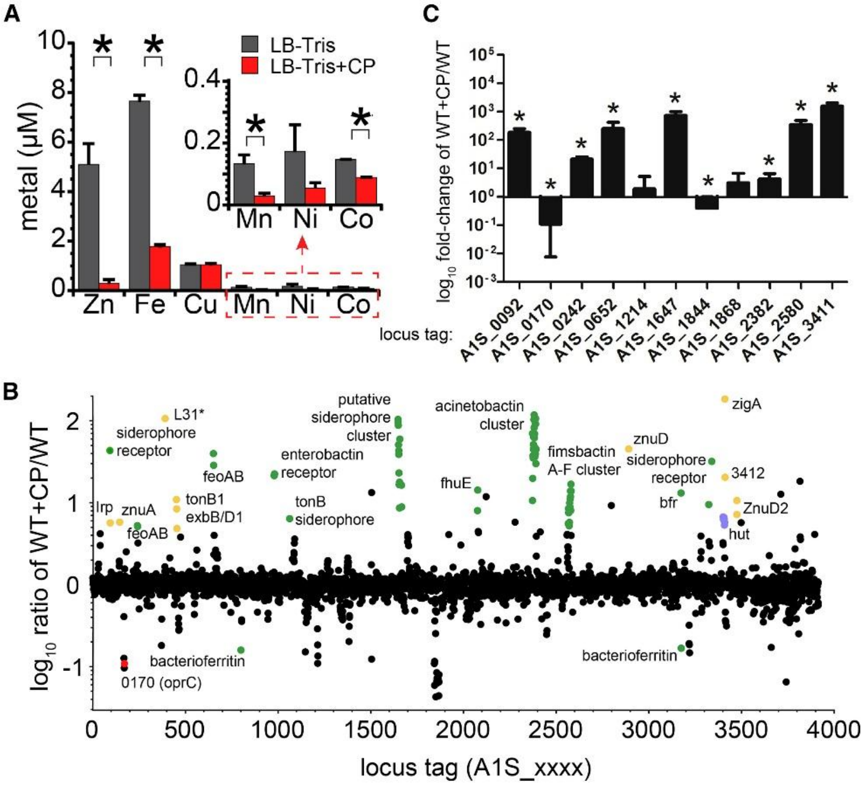

Figure 6. Transcriptomic analysis of WT and WT+CP *A. baumannii*. A) Metal content in the LB-Tris buffer growth media treated with 0 (*grey)* or 200 µg/mL CP (*red*). B) RNAseq analysis of untreated WT vs. 200 µg/mL calprotectin treated WT (WT+CP) *A. baumannii* cells from 4 biological replicates. The fold-change in expression for each locus tag is indicated (see **Table 2, Appendix A**). Gene names are indicated according to the NCBI annotation; otherwise, the locus tag (A1S_xxxx where 'xxxx' represents the locus tag number) is indicated. Genes regulated by the Zn uptake regulator (Zur) (*yellow* symbols), involved in Fe homeostasis (*green* symbols), involved in Cu uptake (*red* symbols) and associated with the histidine utilization (*hut*) operon (*purple* circles) (Nairn, et al., 2016) are highlighted. C) qRT-PCR validation of selected genes identified by RNA-seq. *A1S_0092*, putative ferric siderophore uptake protein; *A1S_0170*, OprC outer membrane copper receptor; *A1S_0242*, FeoA; *A1S_0652*, FeoA; *A1S_1214*, benzoate 1,2-dioxygenase β subunit; *A1S_1647*, siderophore biosynthesis protein; *A1S_1844*, CatC3, muconolactone δ-isomerase; *A1S_1868*, porin for benzoate transport; *A1S_2382*, BasD; *A1S_2580*, siderophore biosynthesis protein. . $*p < 0.05$ as determined by Student's *t* test with hypothetical value of 1. Data are the mean combined from 3 independent experiments ± S.D.

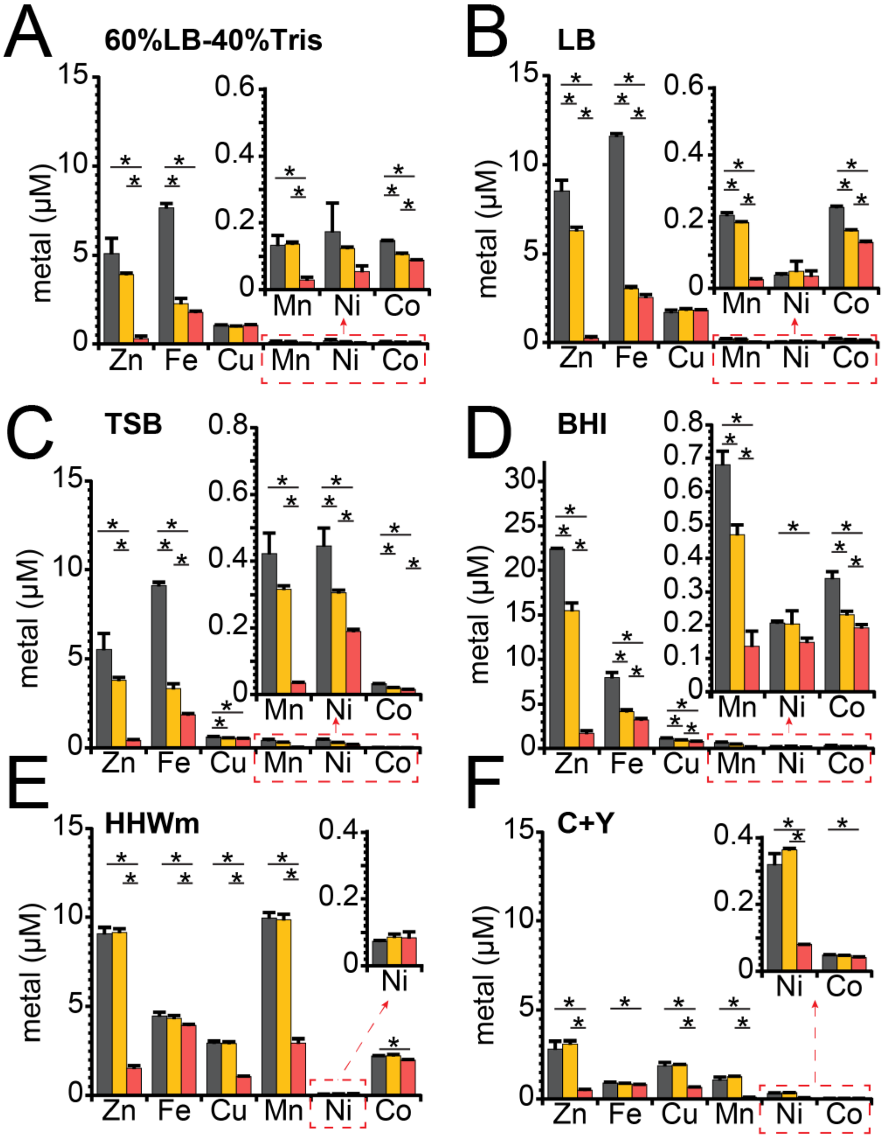

Figure 7. Calprotectin (CP) induces metal starvation. Total transition metal analysis of various standard growth media, including the 60% LB/40% Tris-buffer used to culture *A. baumannii* in this study (A-F). All measurements were made in triplicate by ICP-MS on freshly prepared media dissolved in chelexed Milli-Q water (*gray* bars) and on the effluent of the same media spun through a 10 kD MWCO filter in the absence (*orange* bars) or presence (*red* bars) of 200 µg/mL (16.6 µM transition metal binding sites) CP, following incubation for 2 h, 37 ºC (see Methods for further details). A) 60% LB/40% Tris buffer; B) LB; C) Tryptic soy broth (TSB); D) brain-heart infusion (BHI); E) a chemically defined Hussein-Hastings-White-methionine medium often used to culture *S. aureus*; and F) C+Y media, a more optically transparent media used to culture *S. pneumoniae*. Note that the all rich growth media contain higher molecular weight metal complexes that can be filtered in the absence of CP; given the sub-picomolar affinity of CP for Fe^{II}, it seems likely that at least some fraction of these complexes are bound to CP (Nakashige et al., 2015). The mean of three independent replicates ± S.D. is shown and *, $p < 0.05$ in Student *t*-test as indicated.

We next performed a transcriptomic analysis (**Figure 6B; Table 2, Appendix A**) and an LC-MS/MS, label-free proteomic analysis, in which we detected up to 1094 proteins in these cytoplasmic lysates, which corresponds to 28.9% of the *A.baumannii* proteome (**Figure 8; Figure 9A-D)**. Of the 67 genes that are significantly increased in CP-treated relative to untreated WT cells, 14 also displayed increased transcription in a strain lacking the Zn^{II}-responsive transcriptional regulator *zur* (*Δzur*) (Mortensen et al., 2014) (**Figure 6B**). Furthermore, among the most up-regulated genes are Zur-regulated targets including genes involved in cellular Zn uptake and *zigA* (Mortensen, et al., 2014); increased abundance of ZigA is further confirmed in the proteomic analysis (**Figure 8D**).

Both experiments reveal that CP induces both Zn^{II} and Fe starvation. Relative to Fe starvation, the RNAseq (**Figure 6B**) reveals a dramatically decreased transcription of genes encoding bacterioferritins, but increased transcription of genes involved in the global Fe limitation response, including *feoAB*, which brings Fe^{II} into the cell, and Fe^{III}-siderophore receptors, as confirmed by quantitative RT-PCR (**Figure 6C**). Consistently, putative achromobactin and acinetobactin siderophore biosynthesis/utilization proteins become more cell-abundant with CP stress, some at a level approaching that of ZigA (**Figure 8D**). The upregulation of siderophore uptake systems was further confirmed by robust siderophore production following CP exposure (**Figure 9E-F**). In addition, changes were observed in cellular abundances of Fe-proteins, including those involved in Fe-S cluster biogenesis (IscS and IscR), and the fumarase (FumA) (**Figure 8C-D**) characterized as part of the Fe-sparing response (Lee and Helmann, 2007). These results are consistent with a significant CP-mediated impact on Fe homeostasis and suggest a strong perturbation of Fe metabolism in *A. baumannii.*

These findings also revealed an unexpected intersection of CP-induced Zn and Fe starvation with Cu homeostasis. We observed a transcriptomic down-regulation of a putative Cu importer *oprC* (outer membrane porin, A1S_0170) (Yoneyama and Nakae, 1996) (**Figure 6**) coupled with detection of a previously unannotated protein V5VEM0, a putative copper storage protein (Csp) (Straw, et al., 2018) only in CP-treated cells (**Figure 8D**). These findings suggest that Zn- and Fe-starved *A. baumannii* may decrease bioavailability of Cu under these CP-treatment conditions.

Cell-abundant metalloproteins induced by CP stress are established therapeutic targets

We also found 26 proteins significantly increased in normalized cellular abundance in CP-treated lysates including two known Zn^{II} metalloenzymes (**Figure 8C**), β-carbonic anhydrase, MtcA2, which may be important for survival, invasion, and pathogenicity (Aspatwar, et al., 2018) and succinyl-diaminopimelate desuccinylase, DapE, which is involved synthesis of *meso*-diaminopimelate (*m*-Dap), a component of the peptidoglycan of all Gram-negative bacteria. Fifteen proteins were detected only in CP-treated cells at high cellular levels (**Figure 8D**), including Zn metalloenzyme QueD, which is involved in queuosine-tRNA biosynthesis (Vinayak and Pathak, 2010), and ZigA, which is required for bacterial growth under Zn-limiting conditions and disseminated infections in mice (Nairn, et al., 2016).

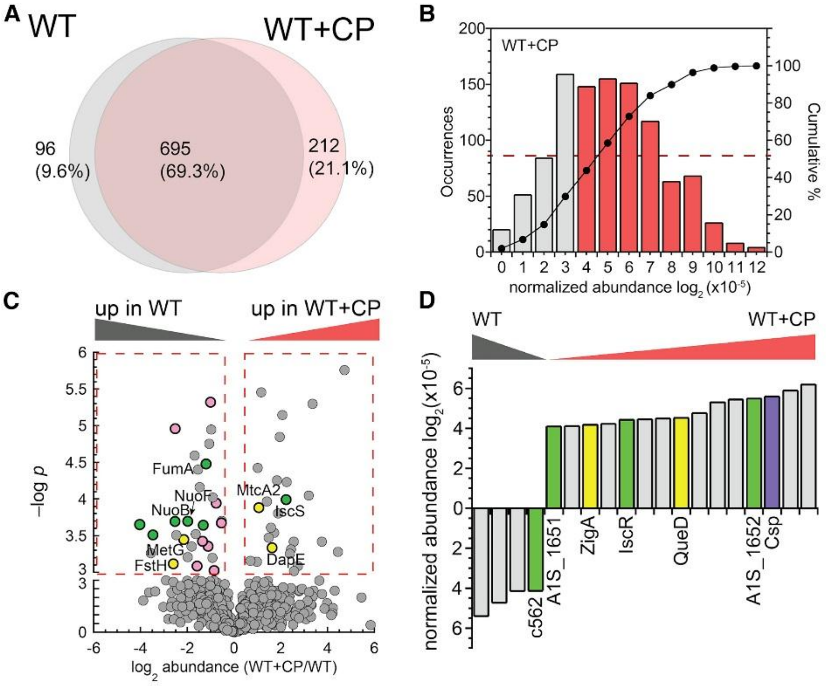

Figure 8. LC-MS/MS proteomic analysis for WT and WT+CP *A. baumannii***.** Protein profiles of untreated WT vs. 200 µg/mL calprotectin treated WT (WT+CP) *A. baumannii* cells from 4 biological replicates. A) Venn diagram for proteins detected at least 3 times in 4 replicates. B) Histogram plot of the distribution of normalized abundance for all proteins detected in the untreated WT strain, as representative of all 4 growth conditions (see **Figure 9A-D**). The top-most 50% abundant proteins are indicated with *red dash line* with the bars shaded *red.* C) Volcano plot for proteins detected at least 3 times for each condition among 4 biological replicates. The significance threshold was set at $p \leq 0.001$ and fold-change in protein abundance at >1.3 as shown in *red dash box* for proteins are up (right top) and down (left top) in WT+CP. Filled circles are shaded *yellow* for Zn-binding proteins, *green* for proteins involved in iron homeostasis, *purple* for Cu-binding proteins and *pink* for proteins involved in transcription or translation. D) Proteins that are strongly changed in WT+CP conditions. Normalized abundance for proteins that was detected only in WT or WT+CP in all 4 replicates with the significance threshold set at the top-most 50% abundance (see **Figure 8B**).

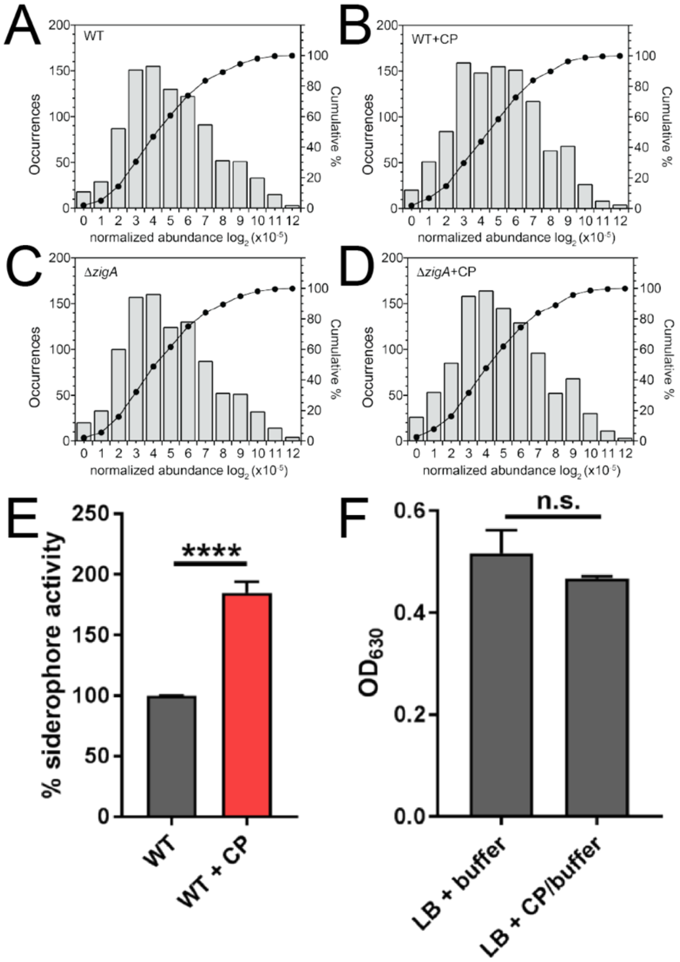

Figure 9. Proteomics analysis for WT and WT+CP. Histogram plot of the distribution of normalized protein abundance or all proteins detected in three of four biological replicates of the A) untreated wild-type strain (WT); B) the wild-type strain treated with 200 µg/mL of CP; C) the Δ*zigA* strain; and D) the Δ*zigA* strain treated with 200 µg/mL of CP. Normalized abundances are binned in units of $\log_2$ x10^{-5} units, plotted as a function of frequency (bar height) and the cumulative %, from low to high abundance (filled circles). Panel A is reproduced in the main text as **Figure 8B** and is shown here to facilitate comparison to other strains and conditions. These distributions are very similar to one another, with only the top-most 50% abundant proteins considered when found only in one strain (see **Figure 8D** and **12C**). Treatment of wild-type *A. baumannii* with 200 µg/mL CP results in increased siderophore production. E) Siderophore content in the spent (filtered) medium was detected by the Chrome Azurol S (CAS) assays, which monitors the mobilization of the Fe from CAS to extracellular Fe chelators, *e.g.,* siderophores, giving rise to increased absorption at λ=630 nm. The mean of three independent replicates ± S.D. is shown and ****, $p < 0.0001$ in a Student *t*-test as indicated. F) CP is unable to compete with CAS for CAS-bound Fe as revealed by no significant change in Abs$_{630}$.

A. baumannii Δ*zigA* is more susceptible to CP-induced metal starvation

As the candidate metallochaperone ZigA (Nairn, et al., 2016) is among the most abundant metalloproteins that is detected *only* in CP-treated WT cells (*vide infra*), investigation of how the Δ*zigA* strain adapts to CP stress relative to the WT strain may identify crippled ZigA-dependent processes. The addition of CP gave rise to a significant decrease in growth yield of exponentially growing cells (*t*=4 h), but only in the Δ*zigA* strain (**Figure 10A**; **Figure 11A-B**). CP induces a measurable decrease in total cell-associated Zn and Fe, but only in the WT strain (**Figure 10B**), a finding consistent with transcriptomic and proteomic analysis (**Figures 6 & 8**). In addition, the *ΔzigA* strain exhibits increased expression of the Zn uptake genes (Nairn, et al., 2016), which may account for these findings. Total cell-associated Cu is also lower only in the WT strain (**Figure 10C**), consistent with the down regulation of *oprC* (**Figure 6**). The Δ*zigA* strain, in contrast, takes up slightly more Mn and Ni when treated with CP (**Figure 10C**). These CP-induced trends in growth yield and in cellular metal content largely persist at 6 and 8 h of growth (**Figure 11C-F**). These results reveal that CP restricts Zn and Fe availability and the loss of ZigA has little further impact on total cell-associated metal, but with a perturbation in metal allocation to cellular targets. This is representative of "adaptive" physiology, since metallation can increase the stability of metalloproteins (**Figure 10D**).

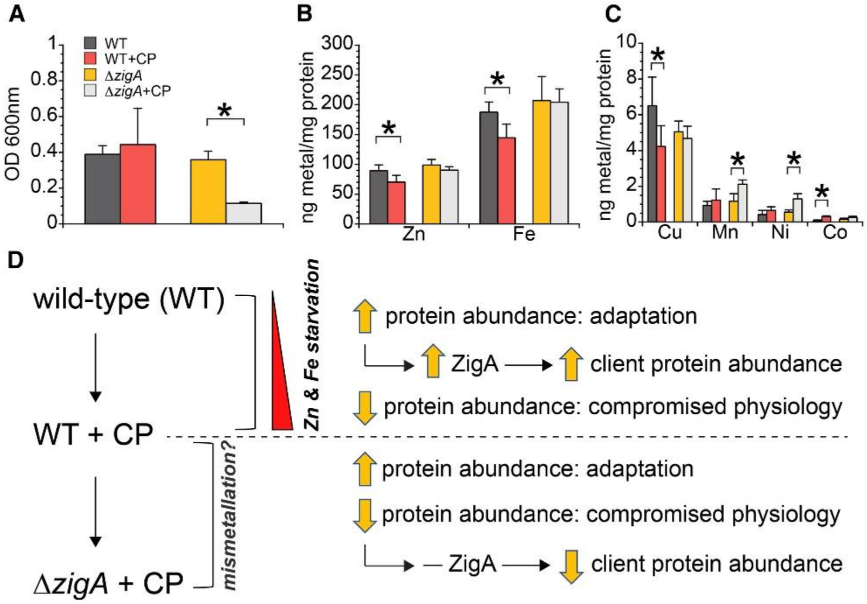

Figure 10. Calprotectin (CP) induces metal starvation in *A. baumannii***.** Growth yield at 4 h (OD 600 nm) A) of cell cultures treated with 0 or 200 µg/mL CP when cell samples were collected for determination of total cell-associated metal by ICP-MS (panels B, C). Total cell-associated metal of WT and Δ*zigA* cells are shown in B) for zinc (Zn) and iron (Fe) and C) for other transition metals. The results shown reflect the mean of 3 independent replicates ± S.D. *$p \leq 0.05$ as determined by Student's *t* test. D) Rationale and design of this study using *ΔzigA* as a tool to study the effects of extreme metal limitation.

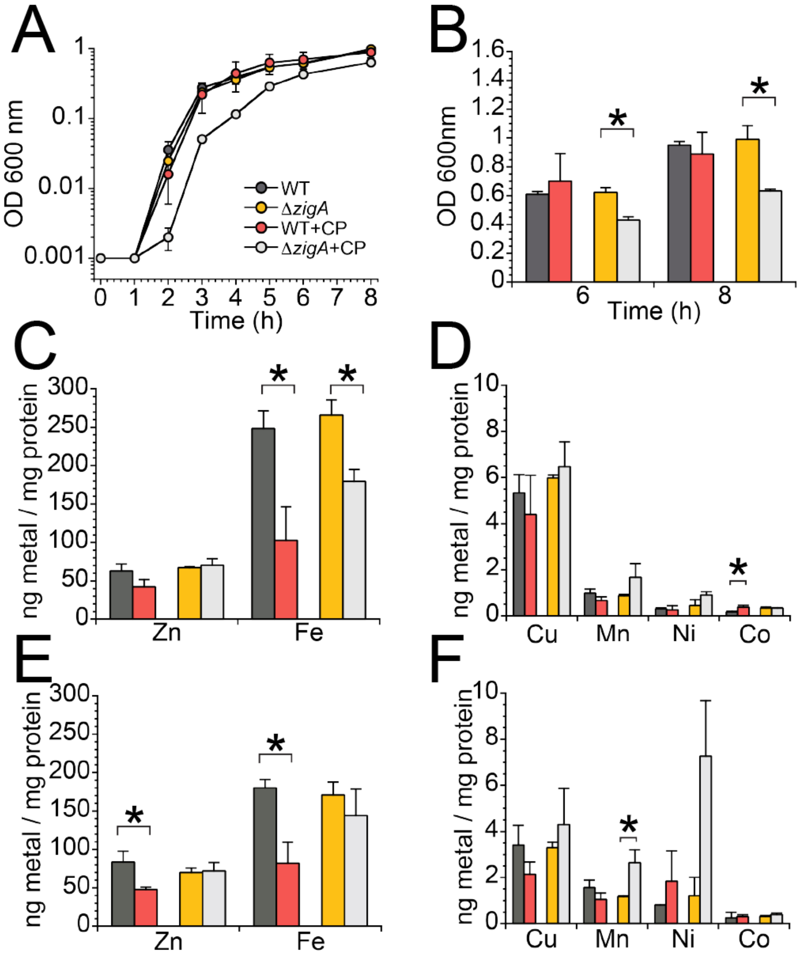

Figure 11. Calprotectin (CP) induces metal starvation on *A. baumannii*. Exponentially growing cells were diluted into pre-warmed LB broth containing 0 or 200 µg/mL CP at time zero and allowed to grow. Growth curves are shown in A) and growth yields at 6 h and 8 h are shown in B). Total cell-associated metal of wild-type (WT) and *ΔzigA* cells collected at 6 h are shown in C) for zinc (Zn) and iron (Fe) and in panel D) for other transition metals. Total cell-associated metal of wild-type (WT) and Δ*zigA* cells collected at 8 h is shown in E) for zinc (Zn) and iron (Fe) and in panel F) for other transition metals. Color code in panels B-F is the same as panel (A). The mean of three independent replicates ± S.D. is shown and *, $p<0.05$ in Student *t*-test as indicated.

As an effort to monitor a perturbation in metal allocation, we found the proteomic profiles of unstressed WT and *ΔzigA* cells are extremely similar but show marked differences in the presence of CP (**Figure 12A-C**; **Figure 13A-B**). In order to understand these differences, a bioinformatics approach was employed to predict the entire Zn proteome of *A. baumannii*. We predicted 213 Zn-proteins corresponding to ≈5% of the proteome, similar to predictions for *E. coli* (Andreini, et al., 2006), and these proteins are anticipated to impact a considerable range of cellular metabolism (**Figure 13C**), with 84 high-probability Zn-proteins were detected in at least three replicates in the proteomic analysis (**Figure 13D**). Overall, zinc-proteins are modestly more abundant (by protein count) in the WT relative to the Δ*zigA* strain in the presence of CP, including MtcA2 (**Figure 12B**) and the global Fe uptake regulator (Fur) (**Figure 11E**), with the striking exception of tRNA-guanosine transglycosylase (Tgt), involved in queuosine-tRNA biosynthesis (Vinayak and Pathak, 2010), which is detected only in CP-treated *ΔzigA* cells at high abundance (**Figure 12C**)

A dual regulatory model of flavin biosynthesis in *A. baumannii* in response to CP

We found RibB is detected only in CP-stressed Δ*zigA* but is undetectable in the WT strain in both conditions (**Figure 12C-D**). Like many bacteria, *A. baumannii* synthesizes riboflavin, flavin mononucleotide (FMN), and flavin adenine dinucleotide (FAD) from guanosine 5'-triphosphate (GTP) via the combined actions of the Zn^{II}-dependent GTP cyclohydrolase II (GCHII), encoded by *ribA*, and from ribulose-5'-phosphate (Ru5P), a product of the pentose phosphate pathway, via the activity of 3,4-dihydroxy-2-butanone 4-phosphate synthase (DHBPS), encoded by *ribB* (**Figure 12E**). In addition to an impact of CP of Zn-protein abundance (*vide infra*), while RibA abundance is unchanged by CP treatment, an uncharacterized RibB-domain containing fusion protein that we designate RibBX is more abundant in the WT strain in the presence of CP ($p \leq 0.05$) (**Figure 12D** and **Figure 13F**), indicating the two RibB- enzymes associated with riboflavin biosynthesis (*rib)*, also play a role in the response to CP.

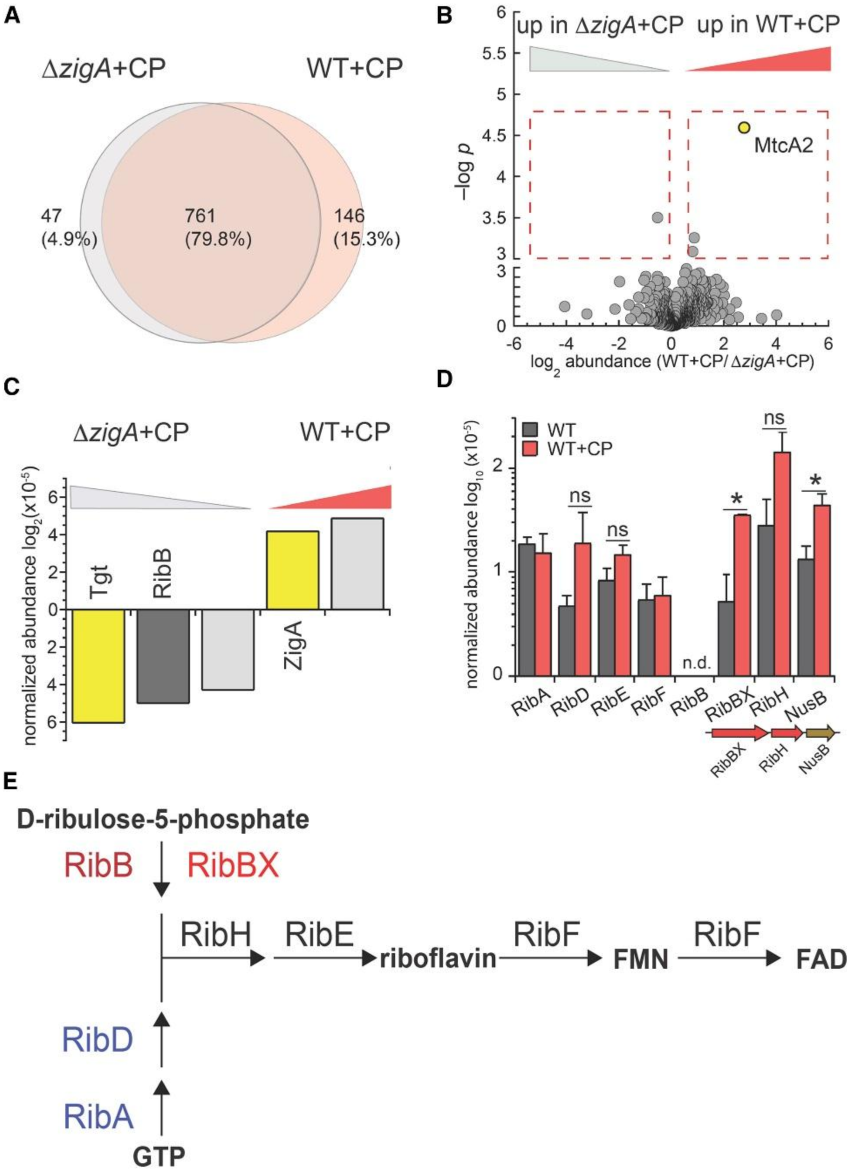

Figure 12. LC-MS/MS proteomic analysis for WT and Δ*zigA* *A. baumannii*. Protein profiles of WT (WT+CP) vs. Δ*zigA* (Δ*zigA*+CP) *A. baumannii* cells treated with 200 μg/mL calprotectin from 4 biological replicates. A) Venn diagram and B) Volcano plot for proteins detected at least 3 times under each condition in 4 replicates. The significance threshold was set at $p \leq 0.001$ and fold-change in protein abundance at >1.3 as shown in *red dash box*. *Yellow*, Zn-binding proteins. C) Proteins that are strongly changed in WT+CP and Δ*zigA*+CP cells. Normalized protein abundance for proteins that were only detected in WT+CP or Δ*zigA*+CP for in all 4 replicates with the significance threshold was set at the top-most 50% abundance. D) Normalized protein abundances of enzymes of the flavin biosynthetic (*rib*) pathway (compare to **Figure 13F**) in the WT (*grey*) or WT+CP (*red*) cells. * $p \leq 0.05$ as determined by Student's *t* test. Except for the RibF, which was only detected twice out of 4 replicates in WT, all proteins shown were detected in at least 3 of the 4 biological replicates. The mean of independent replicates ± S.D. is shown. E) Riboflavin biosynthesis pathway in *A. baumannii*. Metabolites are indicated in *bold* and Zn^{II} metalloenzymes are highlighted in blue.

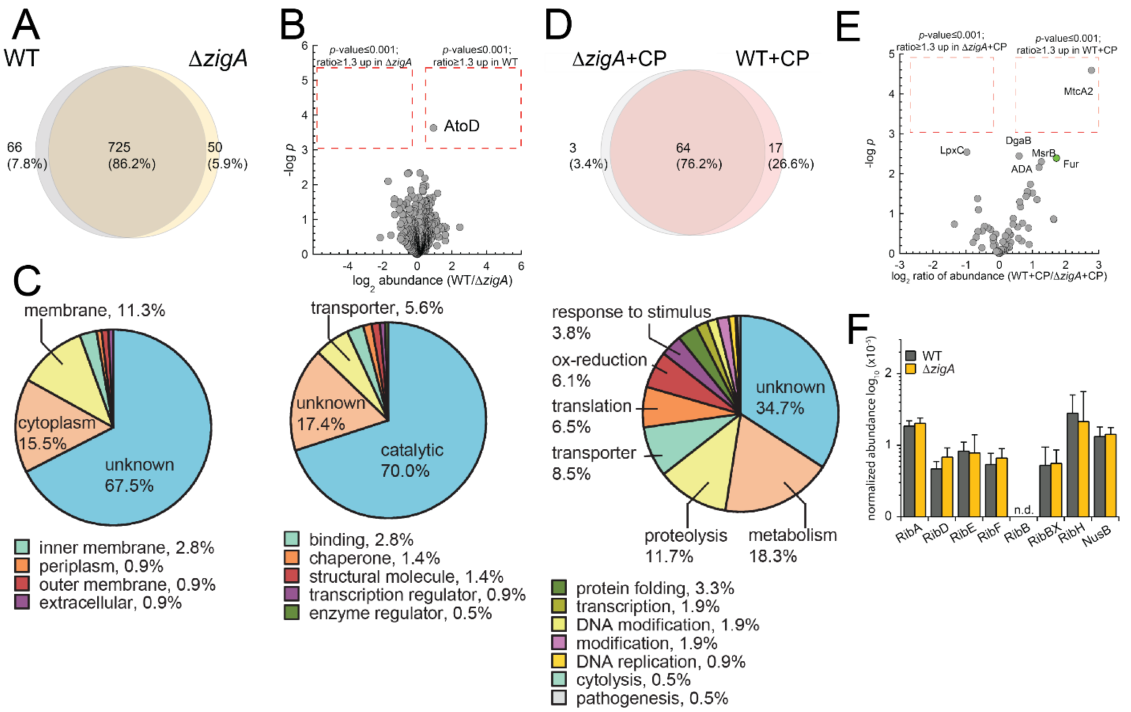

Figure 13. Proteomics analysis of untreated wild-type (WT) vs. Δ*zigA* *A. baumannii* derived from four biological replicates. Those proteins derived from the three of the four replicates are compared in each strain. A)Venn diagram of the all proteins detected at least 3 times in all four replicates shown. B) V-plot for proteins detected at least three times among four biological replicates. The significance threshold was set at $p<0.001$ and fold-change in protein abundance at >1.3. Only one protein, acyl-CoA:acetate CoA-transferase, α-subunit (AtoD; A1S_1732), meets this criterion. C) Predicted subcellular localization (*left panel*), functional role *(middle panel*) and predicted biological functions (*right panel*) of the 213 high-confidence Zn metalloproteins in *A. baumannii.* Proteomics analysis of the wild-type (WT) vs. the Δ*zigA* *A. baumannii* strain each treated with 200 µg/mL calprotectin (CP) with only the candidate Zn metalloproteins. 84 of the 213 maximum predicted cytoplasmic Zn metalloproteins were detected (39.4%). D) Venn diagram for all Zn metalloproteins detected in at least three biological replicates from four total replicates. Zn metalloproteins unique to the Δ*zigA*+CP condition (3) and the WT + CP condition (17) are shown. E) V-plot for proteins detected in at least three biological replicates from four total replicates, with the β-carbonic anhydrase, MtcA2 (Supuran and Capasso, 2017), most similar to the *M. tuberculosis* Rv3588c, the only zinc metalloenzyme meeting the statistical criteria chosen ($p<0.001$; abundance changes by >1.3). Other Zn-metalloproteins with $0.01<p<0.001$ are also highlighted as well, and include the Fe-uptake repressor, Fur (A1S_0895), which harbors a structural Zn-coordination site. Other proteins are methionine sulfoxide reductase subunit B (MsrB; A1S_1469), UDP-2-acetamido-3-amino-2,3-dideoxy-D-glucuronic acid acetyltransferase (DgaB; A1S_0054), adenosine deaminase (ADA; A1S_0718) and UDP-3-O-[3-hydroxymyristoyl] *N*-acetylglucosamine deacetylase (LpxC; A1S_3330). F) Normalized protein abundances of proteins of the flavin biosynthetic (*rib*) pathway (compare to **Figure 12D**) in the wild-type (*black*) or the Δ*zigA* strain (*orange*). The proteomic differences between these two strains are not statistically significant, as anticipated. Proteomics analysis of the Zn metalloproteome in *A. baumannii* (D-F).

The increased cell abundance of RibBX induced by CP stress implies a functional role that is compensatory to RibB under CP stress **(Figure 12E)**, although the function of the RibBX is unknown. This is particularly true for the C-terminal RibX domain that is homologous to RibA, but appears to lack Zn^{II} coordinating residues of authentic RibA. We measured the DHBPS and GCHII activity of RibBX (**Figure 14**) and find that RibBX possesses robust DHBPS activity that is comparable to that of authentic DHBPS (RibB) (**Figure 14A**), but is completely devoid of GCHII activity, consistent with the loss of all three cysteine ligands to the Zn (Singh, et al., 2013) (**Figure 14B**). We then noted that purified RibBX solution is yellow, which suggests the presence of a bound flavin (**Figure 15A**); indeed, LC-MS/MS analysis reveals sub-stoichiometric FMN (**Figure 15B**). We then used FMN-stripped RibBX to show that FMN binds reversibly to RibBX, with a K_a of 1.4 ± 0.5 μM^{-1} and a subunit binding stoichiometry near 1:1 by isothermal titration calorimetry (**Figure 14C**). We then reasoned that FMN might regulate the DHBPS activity of RibBX because in some organisms FMN regulates flavin biosynthesis through a canonical FMN-sensing riboswitch (Baird, et al., 2010), which is predicted to fold upstream of *ribB* in *A. baumannii*, but not upstream of *ribBX*. To test this hypothesis, we measured the DHBPS activity of both RibBX and RibB in the presence of increasing FMN (**Figure 14D**; **Figure 15C**), and only RibBX is inhibited by FMN but with a K_i value of 7.8 µM (comparable to K_a). We note that this K_i is 3-4 orders of magnitude higher than observed for FMN riboswitch-mediated regulation of *ribB* in other bacteria.

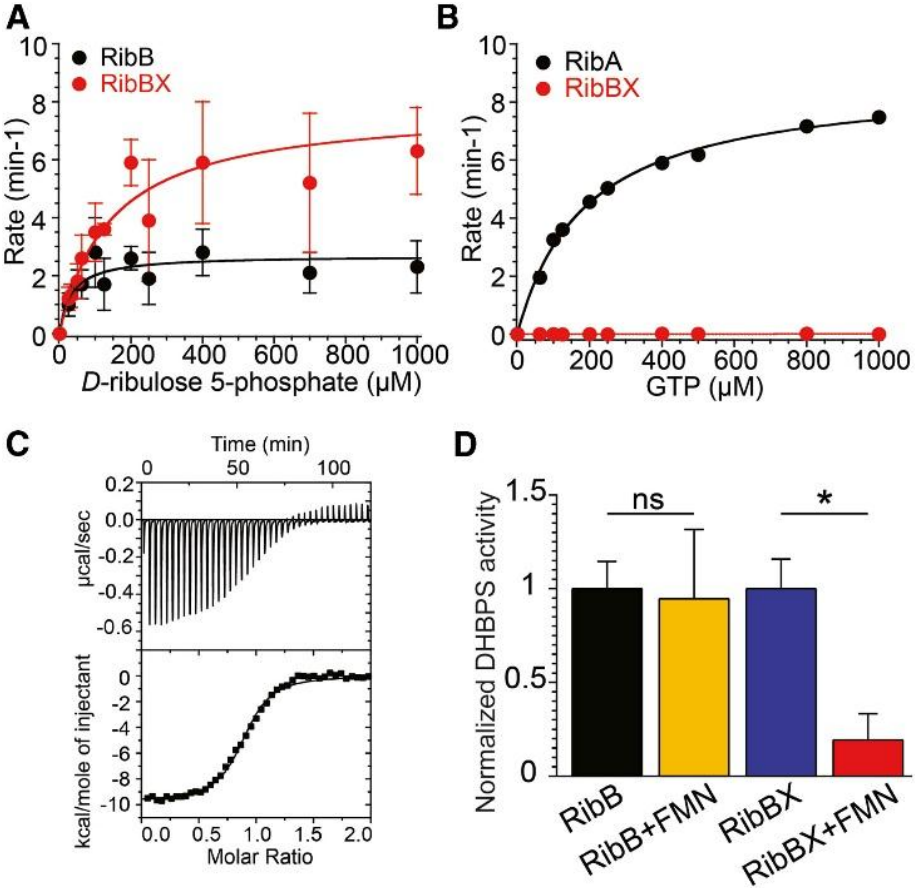

Figure 14. Biochemical characterization of RibBX**.** A) Michaelis-Menten plot for DHBPS activity with various substrate Ru5P concentrations. Error bars represent S.D. from 3 replicates. RibBX is in *red*. RibB (*blank)* is the authentic DHBPS in *A. baumannii*. B) Michaelis-Menten plot for GCHII activity with various substrate GTP concentrations. Error bars represent S.D. from 3 replicates. RibBX is in *red*. RibA (*blank)* is the authentic GCHII in *A. baumannii*. C) ITC titration of FMN to RibBX. The panel is shown as a representative fitting of 3 replicates. D) Inhibition of DHBPS activity with 200 µM FMN. Reaction rate is normalized to the value with 0 µM FMN. * $p \leq 0.05$ using Student's *t*-test. The mean of 3 independent replicates ± S.D. is shown.

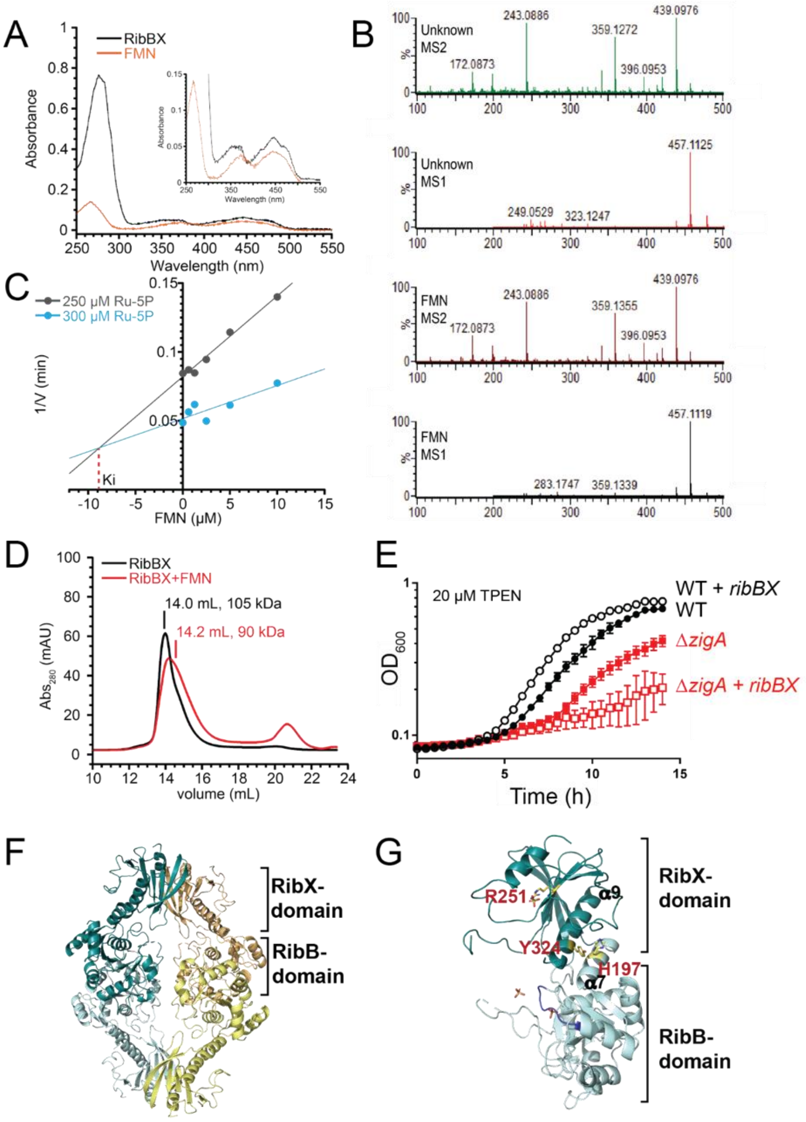

Figure 15. Inhibition of *Ab* RibBX RibB activity by FMN. A) UV-vis spectrum of purified RibBX compared with FMN alone. B) The yellow color associated with purified *Ab* RibBX (labeled Unknown) is identified as authentic FMN (labeled FMN) as determined by tandem LC-MS/MS. Both MS1 (primary) and MS2 (fragmentation spectra) are shown. C) Dixon plot of the inhibition of *Ab* RibBX by added FMN to FMN-stripped RibBX. D) Size exclusion chromatography of *Ab* RibBX alone or RibBX incubated with 1.25 eq. FMN. The molecular weight of the RibBX protomer is 40.9 kDa. The elution time is consistent with a homodimer in both the absence and presence of bound FMN. E) 6 h growth yields relative to untreated (100% growth) in the presence of 250 µg/mL CP. All data are representative of at least three independent replicates and depict the mean ± S.D., where **** $p < 0.0001$ as determined by one-way ANOVA with Tukey multiple comparisons test. F) A ribbon representation of *A. baumannii* RibBX, with each of 4 protomers shaded differently, with the *teal* and *bright orange* protomers defining a crystallographic unit. G) Structure of RibBX protomer. N-terminal RibB-domain is indicated in *pale cyan* with *blue* marking the substrate binding loop. The C-terminal RibX-domain is indicated in *teal*. Missing residues are indicated by the dashed line.

To gain additional insight into the FMN-mediated inhibition of RibBX activity, we determined its structure by x-ray crystallography using molecular replacement with *Mtb* RibBA (Singh, et al., 2013) (see **Table 3** for structure statistics). *A. baumannii* RibBX crystallizes as a pseudo-D_2 symmetric homotetramer (**Figure 15F**). In solution, however, RibBX is a dimer and the oligomerization state is not significantly affected by the presence of bound FMN (**Figure 15D**). As anticipated, the overall architecture of RibBX is similar to that of *Mtb* RibBA, with a canonical RibB-domain (Islam, et al., 2015) (**Figure 16A**). The RibX-domain adopts a topology highly similar to the GCHII (RibA) domain of *Mtb* RibBA, but with no Zn^{II} site present (**Figure 16B**). We hypothesized that FMN binds in RibX-domain and allosterically regulates RibB-domain activity (see **Figure 15G**). These structural and functional findings suggest a dual regulatory model of flavin biosynthesis that is employed by cells experiencing transition metal perturbation (**Figure 16C**).

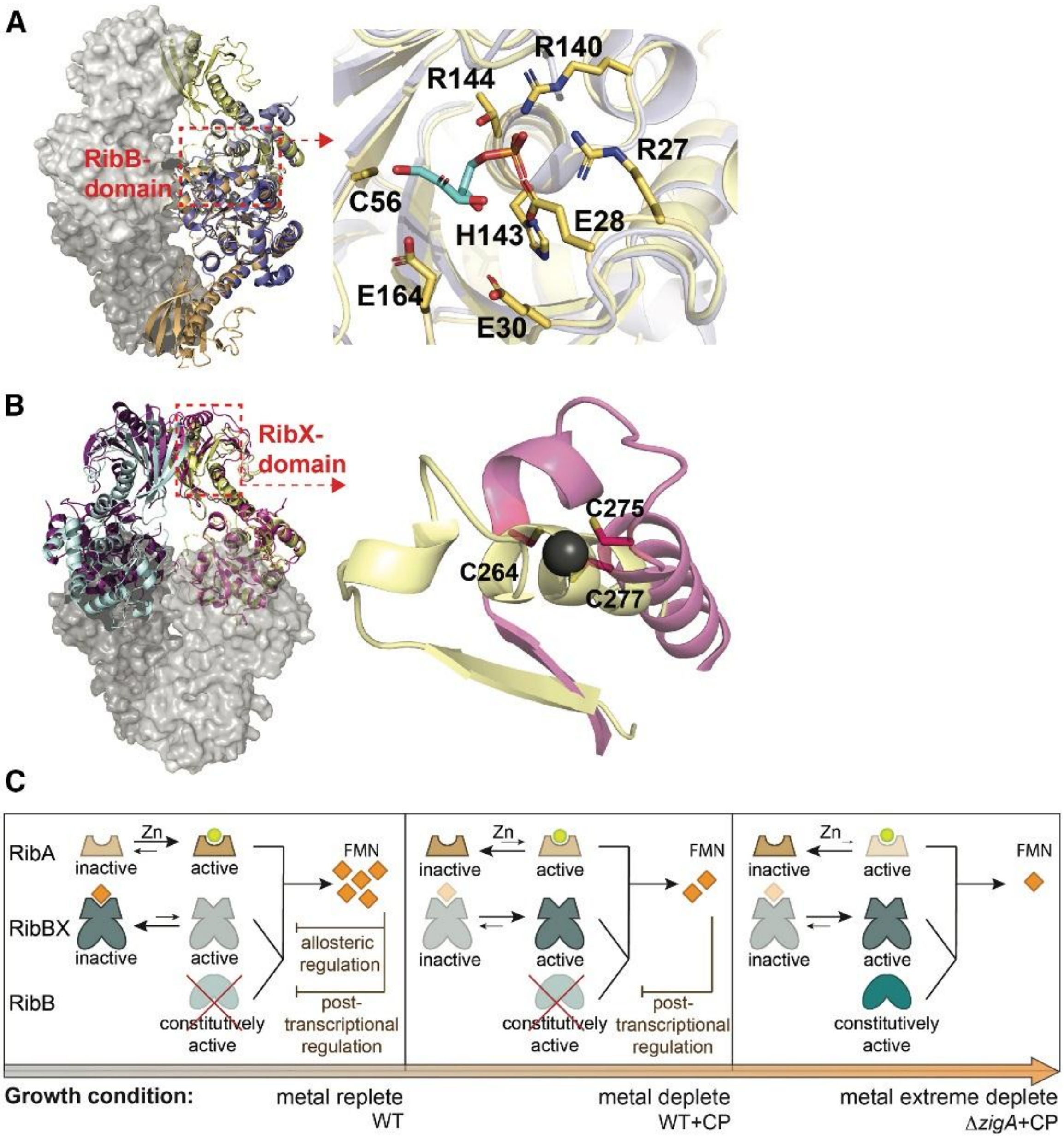

Figure 16. Crystal structure of *A. baumannii* RibBX**.** A) Superposition of structure of RibBX (*bright orange* and *pale yellow*) and *Vibrio cholerae* RibB (Islam et al., 2015) (*Vc*RibB) in the *D*-ribulose 5-phosphate-bound form (*blue*). Substrate binding residues are indicated for RibBX (*bold*). B) Superposition of structure of RibBX (*pale cyan* and *pale yellow)* and *Mycobacterium tuberculosis* RibBA (Singh, et al., 2013) (*Mt*RibBA; Rv1415) in the apo form (*magenta*). Zinc (Zn) binding residues in *Mt*RibBA (*stick* representation). C) Proposed dual regulatory model of the riboflavin biosynthesis pathway that becomes operative under extreme metal limitation mediated by CP.

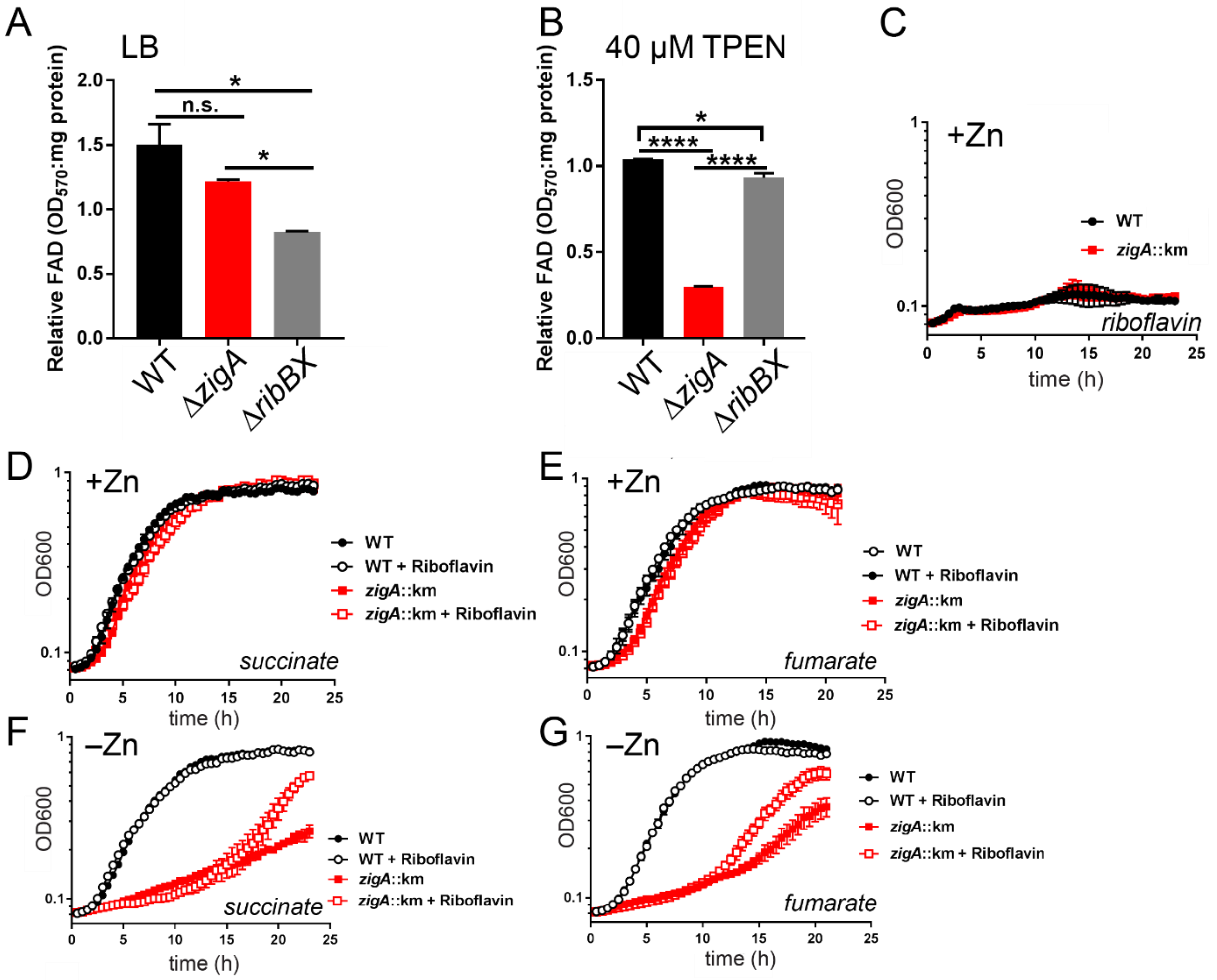

Figure 17. Relative FAD levels and growth yields of the wild-type (WT) (*black*) Δ*ribBX* (*gray*) and Δ*zigA* (*red*) *Ab* strains in the absence (LB or M9, as indicated) and presence (TPEN, CP or EDDHA, as indicated) of chelator-induced metal starvation. A) Relative FAD levels in LB media or in B) LB media supplemented with 40 µM TPEN. All data are representative of at least three independent experiments and depict the mean ± S.D., where * $p < 0.05$, **** $p < 0.0001$ as determined by one-way ANOVA with Tukey multiple comparisons test. Growth monitored over time by OD_{600} in WT and the Δ*zigA* strain (C-G). C) Growth of WT and Δ*zigA* using riboflavin as the sole carbon source. Growth curves are representative of at least three independent experiments, and the mean ± S.D. is shown. Riboflavin cannot be used as a carbon source by *A. baumannii*. Riboflavin can partially rescue the growth of the Δ*zigA* strain. WT and Δ*zigA* strains can use succinate D) or fumarate E) as the sole carbon source, and the addition of riboflavin has no impact on cell growth in Zn-replete conditions. Riboflavin partially rescues the growth phenotype of Δ*zigA* with succinate F) or fumarate G) as sole carbon source in Zn-deplete conditions.

Flavin supplementation complements the Δ*zigA* growth phenotype

We hypothesized in the dual regulatory model that the cellular flavin supply is tightly regulated by balancing the activities and cell abundance of RibA, RibB and RibBX. To elucidate the importance of *ribBX*, we found that a Δ*ribBX* strain has a significant growth defect during Zn starvation (**Figure 18A**). Given the differential abundance of RibBX in the WT and Δ*zigA* strains, the contribution of RibBX to the *A. baumannii* response to Zn limitation was interrogated in a system uncoupled from any transcriptional regulation that may exist for *ribBX*. *ribBX* was expressed under a constitutive promoter in WT and *ΔzigA A. baumannii*, and these strains were grown in Zn limitation induced by TPEN. Constitutive expression of *ribBX* did not alter growth of WT or *ΔzigA* in Zn-replete conditions. However, in Zn-starved conditions, the *ΔzigA* strain experienced growth inhibition upon expression of *ribBX* whereas *ribBX* expression improved growth in WT *A. baumannii* during Zn limitation (**Figure 18B**; **Figure 15E**). These data revealed that RibBX helps overcome nutrient Zn limitation in *A. baumannii*.

Cellular flavin levels are markedly lower in Δ*zigA* under CP stress

The proteomics data suggest an impact on cellular flavin levels mediated by CP stress and/or ZigA (**Figure 12D**) as summarized in our dual regulatory model (**Figure 16C**). To test this, we quantified FAD levels as a proxy of flux through the riboflavin biosynthesis pathway. The *ΔzigA* strain has notably reduced total cellular FAD levels, but only under CP stress (**Figure 18C**), a finding consistent with the detection of RibB only in these cells, whose levels are predicted to be strongly repressed by a canonical FMN-sensing riboswitch under unstressed conditions (Serganov, et al., 2009) (**Figure 12C**). Both CP-stressed (**Figure 18C**) and TPEN-treated (**Figure 17A-B**) Δ*zigA* cells show reduced flavin supply and induce a growth yield phenotype (**Figure 10A**;

Figure 15E); indeed, the Δ*ribBX* strain has lower levels of FAD even in Zn-replete conditions (**Figure 17A**).

Exogenous flavin partially rescues the growth deficiency of Δ*zigA* under CP stress

Our dual regulatory model predicts that supplementation of the Δ*zigA* strain with riboflavin might rescue this growth phenotype observed during CP- or TPEN-mediated metal limitation. To test this prediction, we employed a minimal growth medium with a carbon source(s) that would increase the cellular demand for both flavins and Fe, and supplement with riboflavin, as riboflavin is the precursor to FMN and FAD (**Figure 12E**) (Nwugo, et al., 2011). We used succinate and fumarate, two TCA cycle intermediates, for this purpose. Succinate dehydrogenase is a 4Fe-4S, flavin and heme-requiring enzyme that interconverts succinate and fumarate, while fumarase (FumA) is a 4Fe-4S cluster-containing enzyme, that converts fumarate to malate and whose cellular levels are decreased in CP-stressed cells (**Figure 8C**). Both WT and the *ΔzigA* strain have similar growth kinetics in Zn-replete minimal media with either succinate or fumarate as the sole carbon source but not riboflavin in Zn-replete conditions (**Figure 17C-E**). Strikingly, in Zn-deplete conditions, the *ΔzigA* strain has a dramatic growth defect, which can be partially rescued by supplementation with low levels of riboflavin (**Figure 18D**; **Figure 17F-G**), but not by folate, the biosynthesis of which is also initiated from a Zn enzyme, GTP cyclohydrolase I (FolE) (**Figure 19A-B**). Neither WT or Δ*zigA A. baumannii* is able to utilize riboflavin as a carbon source, revealing that this growth rescue is not from additional carbon source supplementation (**Figure 17C**). Growth of Δ*zigA* and the effect of riboflavin supplementation under Zn-deplete conditions is not observed in a rich growth medium, revealing that increasing the cellular Fe requirement via the use of fumarate or succinate as the sole carbon source also exacerbates the demand for flavins

(**Figure 19C-D**). Consistent with this prediction, both the Δ*zigA* and Δ*ribBX* strains have significant growth defects compared to the WT strain when succinate is provided as the sole carbon source and Fe is restricted by the Fe chelator EDDHA (**Figure 19E-F**).

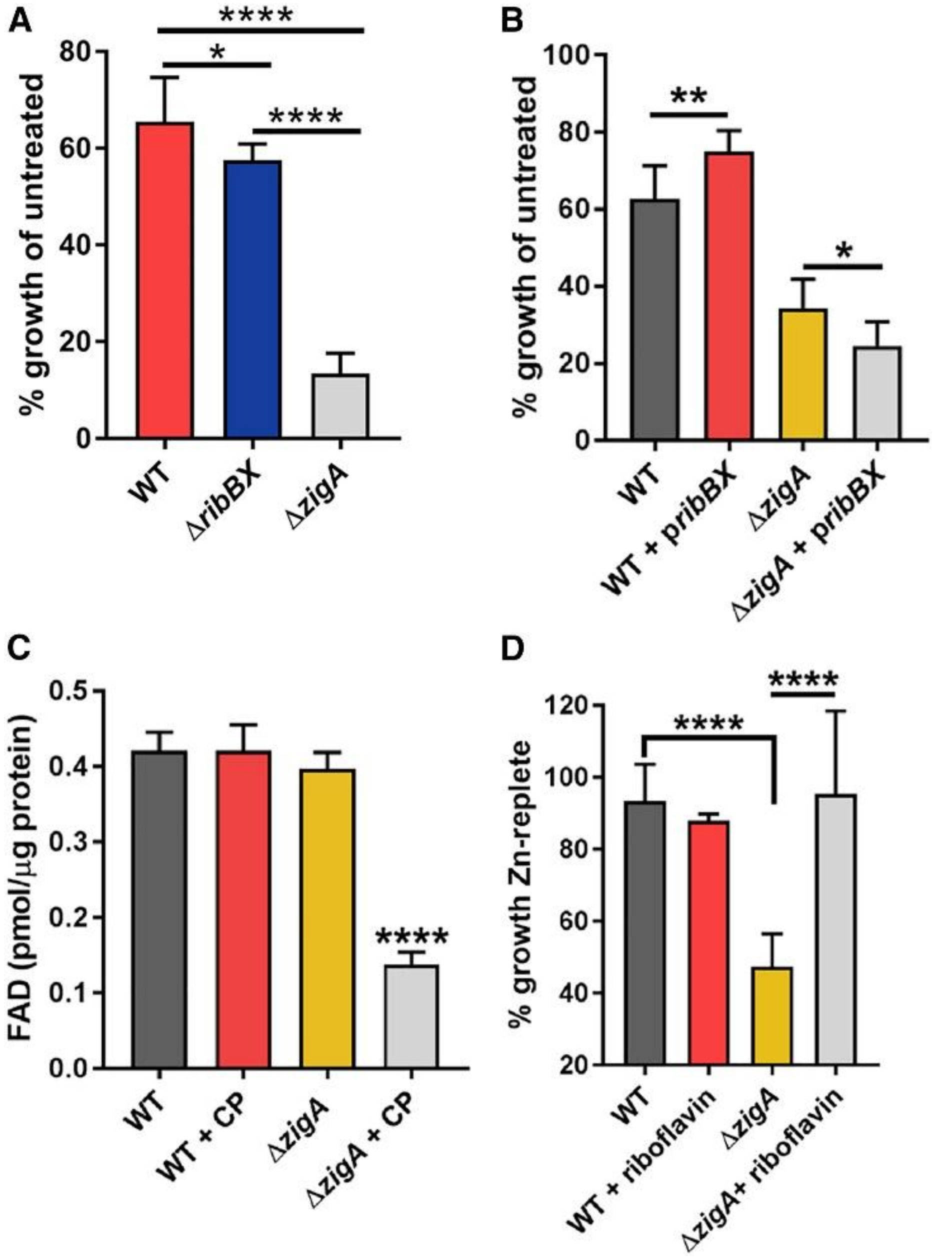

Figure 18. Riboflavin can rescue the growth of Δ*zigA***.** A) Growth of *ΔribBX* and *ΔzigA* is impaired with 40 µM TPENThe mean of at least 3 independent replicates ± S.D. is shown. B) Constitutive expression of *ribBX* in the presence of 20 µM TPEN improves growth of WT *A. baumannii* but impairs growth of *ΔzigA*. C) Cellular FAD levels are notably decreased only in the *ΔzigA* strain in the presence of CP. D) Riboflavin partially rescues the growth phenotype of *ΔzigA* with fumarate as sole carbon source in Zn-deplete conditions. See text for additional details. * $p \leq 0.05$, * $p \leq 0.01$ and **** $p < 0.0001$ as determined by one-way ANOVA with Tukey multiple comparisons test. The mean of at least 3 independent replicates ± S.D. is shown.

.

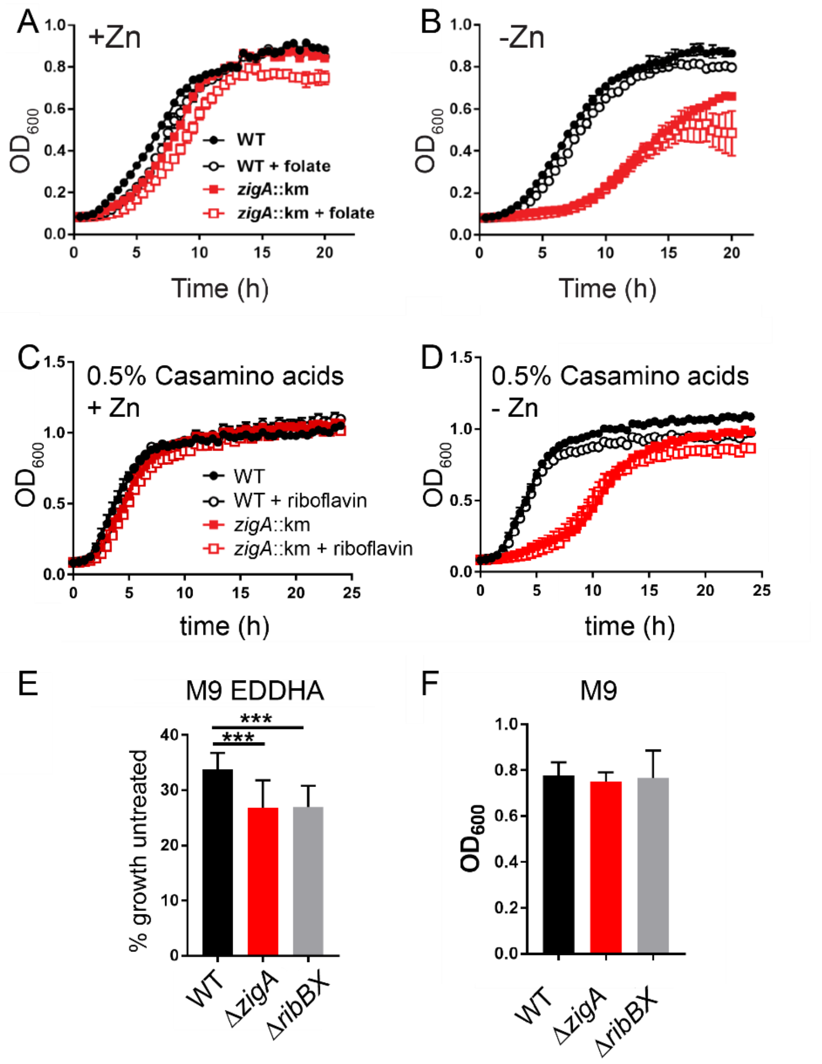

Figure 19. Growth of wild-type and Δ*zigA* strains monitored over time by OD_{600}. A) Growth of wild-type and Δ*zigA* strains supplemented with folate when Zn is replete in an M9 succinate growth media. B) Growth of wild-type and Δ*zigA* strains supplemented with folate when Zn is depleted (20 µM TPEN) in M9 succinate. Folate fails to rescue the Δ*zigA* growth phenotype when these cells are stressed with 20 µM TPEN, in contrast to that which occurs with the addition of riboflavin. C) Full growth curves of the WT (*black*) and the Δ*zigA* (*red*) strains on 0.5% Chelex-treated casamino acids as the sole carbon source under Zn-replete or Zn-deplete D) conditions, in the absence (*closed* symbols) or presence (*open* symbols) of riboflavin. Zn-deplete conditions induce a dramatic growth phenotype in the Δ*zigA* strain that is not rescued by riboflavin supplementation on this growth medium when casamino acids are the sole carbon source. End-point growth yields (OD_{600}) for each strain in the E) presence or F) absence of 10 µM ethylenediamine-*N,N′*-bis(2-hydroxyphenylacetic acid), EDDHA in M9 succinate. All data are representative of at least three independent experiments and depict the mean ± S.D., where * $p < 0.05$, **** $p < 0.0001$ as determined by one-way ANOVA with Tukey multiple comparisons test.

Discussion

The findings presented here reveal a CP-induced multi-metal (Fe and Zn) perturbation of transition metal bioavailability that is exacerbated by the loss of ZigA in a way that impacts central metabolic processes in an important human pathogen. These processes include *de novo* flavin biosynthesis, the product of which functions as an essential cofactor involved in many aspects of cellular redox and energy metabolism (Bacher, et al., 2000), and potentially other Zn-requiring enzymes including the β-carbonic anhydrase (MtcA2) (Supuran and Capasso, 2017) and enzymes (QueD and Tgt) of the queuosine-tRNA biosynthesis pathway (McCarty and Bandarian, 2012). We describe a dual regulation model of flavin biosynthesis that is orchestrated by the DHBPS RibB and a unique, structurally characterized RibBX which functions in an effort to maintain cellular flavin sufficiency under conditions of CP-induced metal starvation and the loss of ZigA. The fact that RibBX homologs are widespread in Proteobacteria (Brutinel, et al., 2013) underscores the importance of this dual regulation model of flavin biosynthesis in other bacteria.

It is now well established that CP is a broad-spectrum chelator capable of inducing microenvironmental niche- and pathogen-dependent transition metal starvation (Zygiel, et al., 2019; Zygiel and Nolan, 2018). The niche-dependence is likely due to the spectrum of total metals defined by the site of infection (Cassat, et al., 2018). However, it is often not clear how much of this total metal is bioavailable at infection sites, since the metal speciation in complex environments is not typically known (Juttukonda, et al., 2017). As proxy for this, and from the perspective of comparing data obtained under different culture conditions, we have surveyed a sampling of typical growth media and found that the total metal composition and the ability of CP to deplete metals from these media varies dramatically (**Figure 7**). We conclude that although CP is clearly capable of depleting divalent metals, what metals CP depletes from the growth medium appears strongly influenced by the relative concentrations of total metal and total CP-binding sites. The coupling between the niche-dependent metal depletion by CP and intrinsic metal requirements in different bacteria (Lisher and Giedroc, 2013) potentially unifies previously conflicting responses to CP in various organisms.

Here, using a standard growth medium, we confirmed an adaptive response to Zn starvation regulated by Zur (Mortensen, et al., 2014), but also revealed a strong Fe limitation response, in that siderophore biosynthesis and utilization genes are found to be notably upregulated at both the transcriptome and proteome levels in *A. baumannii.* These findings are fully consistent with our metal analysis (**Figure 7**), and the previous observation that CP reduces Fe uptake in multiple bacteria (Zygiel, et al., 2019). On the one hand, Zn^{II} starvation may affect the functional integrity of the global Fe regulator Fur, since Fur contains a structural Zn^{II} site. On the other hand, CP-induced a Zur-regulatd putative stand-alone siderophore receptor protein (A1S_0092), which may have a unique role in transition metal acquisition and/or represent regulatory overlap between Zur and Fe limitation. Our findings also provide further evidence that transition metal homeostasis systems are interconnected (Hassan, et al., 2017). Genes detected in RNAseq involved in Fe metabolism are not differentially expressed in the *Δzur* strain, demonstrating that their upregulation is mediated through a Zur-independent mechanism (Mortensen, et al., 2014). The detection of a candidate cell-abundant Csp3 suggests that cytoplasmic Csp3 traps Cu^{I} (Dennison, et al., 2018) and thus potentially allows *A. baumannii* to cope with the restricted bioavailability of Zn and Fe (**Figure 10D)**; further, *A. baumannii* have an as-yet unknown nutritional need for Cu.

ZigA is a key player in response to Zn starvation and infection in mice, but how ZigA functions at the molecular level is unclear. ZigA exhibits weak GTPase activity and binds Zn^{II}

with high affinity, and is therefore proposed to be a Zn metallochaperone from the COG0523 family (Nairn, et al., 2016). As a result, the loss of ZigA may exacerbate cellular metal deficiency due to a failure to mobilize or allocate cellular Zn from metal complexes to high priority protein targets that emerge under conditions of extreme metal limitation, with little or no impact on total metal. Regardless of the mechanism, we employed the Δ*zigA* strain as a tool to assess changes in the proteome that could be reporting on perturbations in metabolism that result from the loss of ZigA under these Zn/Fe-starved conditions. We identified two cellular processes, *de novo* flavin biosynthesis and queuosine-tRNA biosynthesis, that appear strongly impacted by extreme CP-induced metal depletion.

It is known that in bacteria and plants, flavodoxins are required as non-metal substitutes for ferredoxins, thus prioritizing (ribo)flavin biosynthesis under these conditions (Pi and Helmann, 2017; Sepulveda Cisternas, et al., 2018; Tognetti, et al., 2007). In *H. pylori*, riboflavin is reported to be secreted from cells and is thought to participate in Fe reduction to $\mathrm{Fe^{II}}$ and acquisition potentially through FeoAB (**Figure 6B**), with the flavin biosynthesis pathway found to be upregulated under Fe deficiency (Worst, et al., 1998); this is true in other bacteria as well (da Silva Neto, et al., 2013; Vasileva, et al., 2012). Recent work reveals that riboflavin and Fe levels are reciprocally regulated in *Vibrio cholerae* (Sepulveda-Cisternas, et al., 2018), and we observe elements of this in *A. baumannii,* since the Δ*ribBX* strain, like the Δ*zigA* strain, is sensitive to Fe starvation (**Figure 19E-F**). Although in *B. subtilis*, *ribBA* expression is reported to be Fur-regulated (Worst, et al., 1998), it is unknown how the transcription of the *ribBX* operon is regulated in *A. baumannii*. We showed here that while RibBX has WT-like DHBPS activity under conditions where authentic RibB is not detected in cells, RibBX is subjected to product inhibition by cellular FMN, but only at very high concentrations, and thus can be used in CP-treated cells to bypass the regulatory control of the FMN-sensing riboswitch upstream of *ribB* under these conditions (**Figure 16C**) (Serganov, et al., 2009). We also found that two enzymes, QueD and Tgt, also become more cell-abundant in CP-stressed cells thus suggesting that queuosine-tRNA biosynthesis, a second pathway downstream of FolE, is prioritized under these conditions. The cellular logic for this is unknown but strongly implicates this tRNA modification as involved in response to CP-induced metal starvation in *A. baumannii*.

In summary, we show here that CP treatment of *A. baumannii* under these growth conditions strongly restricts the availability of Zn and Fe. The bacteria respond by inducing an acute cellular response to Zn and Fe deficiency while limiting the bioavailability of Cu. CP stress impacts flavin biosynthesis, and it is plausible that Fe homeostasis and flavin biosynthesis are reciprocally regulated in *A. baumannii*. Taken together, these results outline significant crosstalk between metal homeostasis systems and a key intersection with flavin, and perhaps queuosine, biosynthetic pathways. These results also identify cell-abundant antimicrobial targets, including MtcA2 (Aspatwar, et al., 2018; Supuran and Capasso, 2017), DapE (Gillner, et al., 2013; Starus, et al., 2015), ZigA and RibBX, for the development of antibacterial strategies for the treatment of *A. baumannii* infection while this multi-drug resistant organism is actively subjected to nutritional immunity in the infected host.

References

Adams, P.D., Afonine, P.V., Bunkoczi, G., Chen, V.B., Davis, I.W., Echols, N., Headd, J.J., Hung, L.W., Kapral, G.J., Grosse-Kunstleve, R.W., et al. (2010). PHENIX: a comprehensive Python-based system for macromolecular structure solution. *Acta Crystallogr D Biol Crystallogr* 66, 213-221.

Alexander, D.B., and Zuberer, D.A. (1991). Use of chrome azurol-S reagents to evaluate siderophore production by Rhizosphere bacteria. *Biol Fert Soils* 12, 39-45.

Anders, S., and Huber, W. (2010). Differential expression analysis for sequence count data. *Genome Biol* 11, R106.

Andreini, C., Banci, L., Bertini, I., and Rosato, A. (2006). Zinc through the three domains of life. *J Proteome Res* 5, 3173-3178.

Aspatwar, A., Winum, J.Y., Carta, F., Supuran, C.T., Hammaren, M., Parikka, M., and Parkkila, S. (2018). Carbonic anhydrase inhibitors as novel drugs against mycobacterial beta-carbonic anhydrases: an update on *in vitro* and *in vivo* Studies. *Molecules* 23, 2911.

Bacher, A., Eberhardt, S., Fischer, M., Kis, K., and Richter, G. (2000). Biosynthesis of vitamin B2 (riboflavin). *Annu Rev Nutr* 20, 153-167.

Baird, N.J., Kulshina, N., and Ferre-D'Amare, A.R. (2010). Riboswitch function: flipping the switch or tuning the dimmer? *RNA biology* 7, 328-332.

Besold, A.N., Gilston, B.A., Radin, J.N., Ramsoomair, C., Culbertson, E.M., Li, C.X., Cormack, B.P., Chazin, W.J., Kehl-Fie, T.E., and Culotta, V.C. (2017). The role of calprotectin in withholding zinc and copper from *Candida albicans*. *Infect Immun* 82, e00779-00717.

Brutinel, E.D., Dean, A.M., and Gralnick, J.A. (2013). Description of a riboflavin biosynthetic gene variant prevalent in the phylum Proteobacteria. *J Bacteriol* 195, 5479-5486.

Cassat, J.E., Moore, J.L., Wilson, K.J., Stark, Z., Prentice, B.M., Van de Plas, R., Perry, W.J., Zhang, Y., Virostko, J., Colvin, D.C., et al. (2018). Integrated molecular imaging reveals tissue heterogeneity driving host-pathogen interactions. *Sci Transl Med* 10, eaan6361.

Chen, V.B., Arendall, W.B., 3rd, Headd, J.J., Keedy, D.A., Immormino, R.M., Kapral, G.J., Murray, L.W., Richardson, J.S., and Richardson, D.C. (2010). MolProbity: all-atom structure validation for macromolecular crystallography. *Acta Crystallogr D Biol Crystallogr* 66, 12-21.

Clohessy, P.A., and Golden, B.E. (1995). Calprotectin-mediated zinc chelation as a biostatic mechanism in host defence. *Scand J Immunol* 42, 551-556.

Corbin, B.D., Seeley, E.H., Raab, A., Feldmann, J., Miller, M.R., Torres, V.J., Anderson, K.L., Dattilo, B.M., Dunman, P.M., Gerads, R., et al. (2008). Metal chelation and inhibition of bacterial growth in tissue abscesses. *Science* 319, 962-965.

da Silva Neto, J.F., Lourenco, R.F., and Marques, M.V. (2013). Global transcriptional response of *Caulobacter crescentus* to iron availability. *BMC Genomics* 14, 549.

Damo, S.M., Kehl-Fie, T.E., Sugitani, N., Holt, M.E., Rathi, S., Murphy, W.J., Zhang, Y.F., Betz, C., Hench, L., Fritz, G., et al. (2013). Molecular basis for manganese sequestration by calprotectin and roles in the innate immune response to invading bacterial pathogens. *Proc Natl Acad Sci* 110, 3841-3846.

Dennison, C., David, S., and Lee, J. (2018). Bacterial copper storage proteins. *J. Biol. Chem*. 293, 4616-4627.

Doyle, J.S., Buising, K.L., Thursky, K.A., Worth, L.J., and Richards, M.J. (2011). Epidemiology of infections acquired in intensive care units. *Semin Respir Crit Care Med* 32, 115-138.

Eddy, S.R. (1998). Profile hidden Markov models. *Bioinformatics* 14, 755-763.

Emsley, P., Lohkamp, B., Scott, W.G., and Cowtan, K. (2010). Features and development of Coot. *Acta Crystallogr D Biol Crystallogr* 66, 486-501.

Finn, R.D., Bateman, A., Clements, J., Coggill, P., Eberhardt, R.Y., Eddy, S.R., Heger, A., Hetherington, K., Holm, L., Mistry, J., et al. (2014). Pfam: the protein families database. *Nucleic Acids Res* 42, D222-230.

Gibson, D.G., Young, L., Chuang, R.Y., Venter, J.C., Hutchison, C.A., 3rd, and Smith, H.O. (2009). Enzymatic assembly of DNA molecules up to several hundred kilobases. *Nat Methods* 6, 343-345.

Gillner, D.M., Becker, D.P., and Holz, R.C. (2013). Lysine biosynthesis in bacteria: a metallodesuccinylase as a potential antimicrobial target. *J Biol Inorg Chem* 18, 155-163.

Grossoehme, N.E., and Giedroc, D.P. (2009). Energetics of allosteric negative coupling in the zinc sensor *S. aureus* CzrA. *J Am Chem Soc* 131, 17860-17870.

Harding, C.M., Hennon, S.W., and Feldman, M.F. (2018). Uncovering the mechanisms of *Acinetobacter baumannii* virulence. *Nat Rev Microbiol* 16, 91-102.

Hassan, K.A., Pederick, V.G., Elbourne, L.D., Paulsen, I.T., Paton, J.C., McDevitt, C.A., and Eijkelkamp, B.A. (2017). Zinc stress induces copper depletion in *Acinetobacter baumannii*. *BMC Microbiol* 17, 59.

Hoang, T.T., Karkhoff-Schweizer, R.R., Kutchma, A.J., and Schweizer, H.P. (1998). A broad-host-range Flp-FRT recombination system for site-specific excision of chromosomally-located

DNA sequences: application for isolation of unmarked *Pseudomonas aeruginosa* mutants. *Gene* 212, 77-86.

Hood, M.I., Mortensen, B.L., Moore, J.L., Zhang, Y., Kehl-Fie, T.E., Sugitani, N., Chazin, W.J., Caprioli, R.M., and Skaar, E.P. (2012). Identification of an *Acinetobacter baumannii* zinc acquisition system that facilitates resistance to calprotectin-mediated zinc sequestration. *PLoS Pathog* 8, e1003068.

Hood, M.I., and Skaar, E.P. (2012). Nutritional immunity: transition metals at the pathogen-host interface. *Nat Rev Microbiol* 10, 525-537.

Islam, Z., Kumar, A., Singh, S., Salmon, L., and Karthikeyan, S. (2015). Structural basis for competitive inhibition of 3,4-dihydroxy-2-butanone-4-phosphate synthase from *Vibrio cholerae*. *J Biol Chem* 290, 11293-11308.

Jacobsen, F.E., Kazmierczak, K.M., Lisher, J.P., Winkler, M.E., and Giedroc, D.P. (2011). Interplay between manganese and zinc homeostasis in the human pathogen *Streptococcus pneumoniae*. *Metallomics* 3, 38-41.

Juttukonda, L.J., Berends, E.T.M., Zackular, J.P., Moore, J.L., Stier, M.T., Zhang, Y., Schmitz, J.E., Beavers, W.N., Wijers, C.D., Gilston, B.A., et al. (2017). Dietary manganese promotes Staphylococcal infection of the heart. *Cell Host Microbe* 22, 531-542 e538.

Kabsch, W. (2010). Integration, scaling, space-group assignment and post-refinement. *Acta Crystallogr D Biol Crystallogr* 66, 133-144.

Kentache, T., Ben Abdelkrim, A., Jouenne, T., De, E., and Hardouin, J. (2017). Global dynamic rroteome study of a pellicle-forming *Acinetobacter baumanni*i strain. *Mol Cell Proteomic*s 16, 100-112.

Langmead, B., and Salzberg, S.L. (2012). Fast gapped-read alignment with Bowtie 2. *Nat Methods* 9, 357-359.

LaRoche, J., Boyd, P.W., McKay, R.M.L., and Geider, R.J. (1996). Flavodoxin as an *in situ* marker for iron stress in phytoplankton. *Nature* 382, 802-805.

Lee, J.W., and Helmann, J.D. (2007). Functional specialization within the Fur family of metalloregulators. *Biometals* 20, 485-499.

Lisher, J.P., and Giedroc, D.P. (2013). Manganese acquisition and homeostasis at the host-pathogen interface. *Front Cell Infect Microbiol* 3, 91.

Magoc, T., Wood, D., and Salzberg, S.L. (2013). EDGE-pro: estimated degree of gene expression in prokaryotic genomes. *Evol Bioinform Online* 9, 127-136.

McCarty, R.M., and Bandarian, V. (2012). Biosynthesis of pyrrolopyrimidines. *Bioorganic Chem* 43, 15-25.

Menard, R., Sansonetti, P.J., and Parsot, C. (1993). Nonpolar mutagenesis of the *Ipa* genes defines Ipab, Ipac, and Ipad as effectors of *Shigella-Flexneri* entry into epithelial-cells. *J. Bacteriol*. 175, 5899-5906.

Mortensen, B.L., Rathi, S., Chazin, W.J., and Skaar, E.P. (2014). *Acinetobacter baumannii* response to host-mediated zinc limitation requires the transcriptional regulator Zur. *J Bacteriol* 196, 2616-2626.

Nairn, B.L., Lonergan, Z.R., Wang, J., Braymer, J.J., Zhang, Y., Calcutt, M.W., Lisher, J.P., Gilston, B.A., Chazin, W.J., de Crecy-Lagard, V., et al. (2016). The Response of *Acinetobacter baumannii* to zinc starvation. *Cell Host Microbe* 19, 826-836.

Nakashige, T.G., Zhang, B., Krebs, C., and Nolan, E.M. (2015). Human calprotectin is an iron-sequestering host-defense protein. *Nat Chem Biol* 11, 765-771.

Nakashige, T.G., Zygiel, E.M., Drennan, C.L., and Nolan, E.M. (2017). Nickel sequestration by the host-defense protein human calprotectin. *J Am Chem Soc* 139, 8828-8836.

Nwugo, C.C., Gaddy, J.A., Zimbler, D.L., and Actis, L.A. (2011). Deciphering the iron response in *Acinetobacter baumannii*: A proteomics approach. *J Proteomics* 74, 44-58.

Overbeek, R., Begley, T., Butler, R.M., Choudhuri, J.V., Chuang, H.Y., Cohoon, M., de Crecy-Lagard, V., Diaz, N., Disz, T., Edwards, R., et al. (2005). The subsystems approach to genome annotation and its use in the project to annotate 1000 genomes. *Nucleic Acids Res* 33, 5691-5702.

Park, A.J., Murphy, K., Krieger, J.R., Brewer, D., Taylor, P., Habash, M., and Khursigara, C.M. (2014). A temporal examination of the planktonic and biofilm proteome of whole cell *Pseudomonas aeruginosa* PAO1 using quantitative mass spectrometry. *Mol Cell Proteomics* 13, 1095-1105.

Phillips, G., Grochowski, L.L., Bonnett, S., Xu, H., Bailly, M., Blaby-Haas, C., El Yacoubi, B., Iwata-Reuyl, D., White, R.H., and de Crecy-Lagard, V. (2012). Functional promiscuity of the COG0720 family. *ACS Chem Biol* 7, 197-209.

Pi, H., and Helmann, J.D. (2017). Sequential induction of Fur-regulated genes in response to iron limitation in *Bacillus subtilis*. *Proc Natl Acad Sci* 114, 12785-12790.

Putignano, V., Rosato, A., Banci, L., and Andreini, C. (2018). MetalPDB in 2018: a database of metal sites in biological macromolecular structures. *Nucleic Acids Res* 46, D459-D464.

Rosato, A., Valasatava, Y., and Andreini, C. (2016). Minimal functional sites in metalloproteins and their usage in structural bioinformatics. *Int J Mol Sci* 17.671

Schwyn, B., and Neilands, J.B. (1987). Universal chemical assay for the detection and determination of siderophores. *Anal Biochem* 160, 47-56.

Sepulveda Cisternas, I., Salazar, J.C., and Garcia-Angulo, V.A. (2018). Overview on the bacterial iron-riboflavin metabolic axis. *Frontiers in microbiology* 9, 1478.

Sepulveda-Cisternas, I., Lozano Aguirre, L., Fuentes Flores, A., Vasquez Solis de Ovando, I., and Garcia-Angulo, V.A. (2018). Transcriptomics reveals a cross-modulatory effect between riboflavin and iron and outlines responses to riboflavin biosynthesis and uptake in *Vibrio cholerae*. *Sci Rep* 8, 3149.

Serganov, A., Huang, L., and Patel, D.J. (2009). Coenzyme recognition and gene regulation by a flavin mononucleotide riboswitch. *Nature* 458, 233-237.

Sheffield, P., Garrard, S., and Derewenda, Z. (1999). Overcoming expression and purification problems of RhoGDI using a family of "parallel" expression vectors. *Protein Expres Purif* 15, 34-39.

Singh, M., Kumar, P., Yadav, S., Gautam, R., Sharma, N., and Karthikeyan, S. (2013). The crystal structure reveals the molecular mechanism of bifunctional 3,4-dihydroxy-2-butanone 4-phosphate synthase/GTP cyclohydrolase II (Rv1415) from *Mycobacterium tuberculosis*. *Acta Crystallogr D Biol Crystallogr* 69, 1633-1644.

Starus, A., Nocek, B., Bennett, B., Larrabee, J.A., Shaw, D.L., Sae-Lee, W., Russo, M.T., Gillner, D.M., Makowska-Grzyska, M., Joachimiak, A., et al. (2015). Inhibition of the *dapE*-encoded N-succinyl-L,L-diaminopimelic acid desuccinylase from *Neisseria meningitidis* by L-Captopril. *Biochemistry* 54, 4834-4844.

Straw, M.L., Chaplin, A.K., Hough, M.A., Paps, J., Bavro, V.N., Wilson, M.T., Vijgenboom, E., and Worrall, J.A.R. (2018). A cytosolic copper storage protein provides a second level of copper tolerance in *Streptomyces lividans*. *Metallomics* 10, 180-193.

Supuran, C.T., and Capasso, C. (2017). An overview of the bacterial carbonic anhydrases. *Metabolites* 7, 56.

Tognetti, V.B., Zurbriggen, M.D., Morandi, E.N., Fillat, M.F., Valle, E.M., Hajirezaei, M.R., and Carrillo, N. (2007). Enhanced plant tolerance to iron starvation by functional substitution of chloroplast ferredoxin with a bacterial flavodoxin. *Proc Natl Acad Sci* 104, 11495-11500.

UniProt Consortium, T. (2018). UniProt: the universal protein knowledgebase. *Nucleic Acids Res* 46, 2699.

Valasatava, Y., Rosato, A., Banci, L., and Andreini, C. (2016). MetalPredator: a web server to predict iron-sulfur cluster binding proteomes. *Bioinformatics* 32, 2850-2852.

Vasileva, D., Janssen, H., Honicke, D., Ehrenreich, A., and Bahl, H. (2012). Effect of iron limitation and *fur* gene inactivation on the transcriptional profile of the strict anaerobe *Clostridium acetobutylicum*. *Microbiology* 158, 1918-1929.

Vinayak, M., and Pathak, C. (2010). Queuosine modification of tRNA: its divergent role in cellular machinery. *Biosci Rep* 30, 135-148.

Wakeman, C.A., Moore, J.L., Noto, M.J., Zhang, Y., Singleton, M.D., Prentice, B.M., Gilston, B.A., Doster, R.S., Gaddy, J.A., Chazin, W.J., et al. (2016). The innate immune protein calprotectin promotes *Pseudomonas aeruginosa* and *Staphylococcus aureus* interaction. *Nat Commun* 7, 11951.

Wang, L., Wang, S., and Li, W. (2012). RSeQC: quality control of RNA-seq experiments. *Bioinformatics* 28, 2184-2185.

Weinberg, E.D. (1975). Nutritional immunity. Host's attempt to withold iron from microbial invaders. *JAMA* 231, 39-41.

Worst, D.J., Gerrits, M.M., Vandenbroucke-Grauls, C.M., and Kusters, J.G. (1998). *Helicobacter pylori* ribBA-mediated riboflavin production is involved in iron acquisition. *J Bacteriol* 180, 1473-1479.

Yoneyama, H., and Nakae, T. (1996). Protein C (OprC) of the outer membrane of *Pseudomonas aeruginosa* is a copper-regulated channel protein. *Microbiology* 142, 2137-2144.

Zygiel, E.M., Nelson, C.E., Brewer, L.K., Oglesby-Sherrouse, A.G., and Nolan, E.M. (2019). The human innate immune protein calprotectin induces iron starvation responses in *Pseudomonas aeruginosa*. *J Biol Chem,* Accepted January 8, 2019, doi: 10.1074, online.

Zygiel, E.M., and Nolan, E.M. (2018). Transition metal sequestration by the host-defense protein calprotectin. *Annu Rev Biochem* 87, 621-643.

CHAPTER III

AN *ACINETOBACTER BAUMANNII*, ZINC REGULATED PEPTIDASE MAINTAINS CELL WALL INTEGRITY DURING IMMUNE-MEDIATED NUTRIENT SEQUESTRATION

A version of the following section was previously published in *Cell Reports* 26 (8) P2009-2018.E6 (February 2019) doi: 10.1016/j.celrep.2019.01.089.

Introduction

In Gram-negative bacteria, the cell envelope is comprised of two membranes and a peptidoglycan (PG) layer that coordinate to allow growth in diverse niches. The cell envelope is necessary for the maintenance and storage of essential molecules and provides a protective barrier against harsh environments. The genus *Acinetobacter* represents a diverse group of Gram-negative bacteria that inhabit several environmental niches (Baumann, 1968). Members of the genus are important opportunistic pathogens. Specifically, *A. baumannii* is a leading cause of ventilator-associated pneumonia and can cause wound and burn infections, urinary tract infections, and sepsis (Gaynes et al., 2005; Trouillet et al., 1998). The prevalence of multi-drug resistant strains prompted the World Health Organization to list *A. baumannii* as its most critical pathogen for the development of new therapeutics (WHO, 2017). Despite the global burden of *A. baumannii* infections, mechanistic studies of *A. baumannii* virulence and basic physiology are limited (Antunes et al., 2014; Harding et al., 2018).

Like other pathogens, *A. baumannii* must acquire nutrient metals from the host to replicate (Hood et al., 2012; Juttukonda et al., 2016). Metals are required for life and serve as protein structural components and enzymatic cofactors. For bacteria, these metals are essential for cell envelope maintenance, since key enzymatic steps are metal-dependent (Gattis et al., 2010; Rayman and MacLeod, 1975; Whittington et al., 2003). Vertebrates sequester metals from invading pathogens through a process termed nutritional immunity (Palmer and Skaar, 2016; Weinberg, 1975). One facet of nutritional immunity involves zinc (Zn) sequestration. Vertebrates withhold Zn from pathogens through the deployment of calprotectin (CP, calgranulin A/B, myeloid-related protein (MRP) 8/14). CP is the heterodimer of S100A8 and S100A9 (Hunter and Chazin, 1998). Two transition metal binding sites are formed at the dimer interface of CP that bind Zn and other nutrient metals (Baker et al., 2017; Corbin et al., 2008; Damo et al., 2013; Kehl-Fie et al., 2011; Nakashige et al., 2017). CP inhibits bacterial growth *in vitro*, and this inhibition is dependent on the metal-binding properties of the protein (Corbin et al., 2008; Hood et al., 2012; Kehl-Fie et al., 2011; Zackular et al., 2016). Furthermore, CP accumulates at infectious foci, underscoring the importance of CP and Zn withholding at the host-pathogen interface (Corbin et al., 2008; Hood et al., 2012; Juttukonda et al., 2017; Zackular et al., 2016).

Despite the evolution of host metal-sequestering strategies, *A. baumannii* and other bacteria have developed mechanisms to overcome Zn limitation (Ammendola et al., 2007; Desrosiers et al., 2010; Gaballa and Helmann, 1998; Hood et al., 2012; Liu et al., 2012; Patzer and Hantke, 1998; Stork et al., 2010). The response to Zn starvation in *A. baumannii* is primarily controlled by the Zn uptake repressor Zur (Hood et al., 2012; Mortensen et al., 2014). This response includes accessing a labile histidine-Zn pool within the cell and elaboration of high-affinity Zn acquisition systems (Hood et al., 2012; Mortensen et al., 2014; Nairn et al., 2016). However, the effects of Zn starvation on other aspects of *A. baumannii* physiology are unknown.

We previously identified genes differentially expressed in a strain lacking *zur* through the application of a transcriptomics-based approach (Mortensen et al., 2014). From this, we discovered a putative PG-modifying enzyme; based on sequence prediction and experimental evidence, we herein name the gene *zrlA* (Zur-regulated Lipoprotein A). The gene encoding ZrlA is regulated by Zur and is significantly upregulated in *A. baumannii* following exposure to CP (Mortensen et al., 2014). We hypothesized that ZrlA serves as an integral link between cell envelope and nutrient Zn homeostasis. ZrlA localizes to the inner membrane as a Zn-binding peptidase and is critical for the response of *A. baumannii* to Zn starvation. ZrlA also plays a pivotal role in maintaining robust cell envelope barrier function, and a strain lacking *zrlA* (Δ*zrlA*) is sensitive to envelope stresses. This barrier defect sensitizes the Δ*zrlA* strain to many classes of antibiotics *in vitro* and *in vivo*, establishing ZrlA as a viable target for small molecule drug development to combat *A. baumannii* infections.

Materials and Methods

Bacterial strains

Experiments were performed using *Acinetobacter baumannii* strain ATCC 17978 and its derivatives unless otherwise noted. Transposon mutants in the *A. baumannii* ABUW5075 background were purchased from the University of Washington *A. baumannii* mutant library, and transposon insertion was confirmed by PCR (Gallagher et al., 2015). Cloning was performed in *E. coli* DH5α, and protein expression was performed in *E. coli* BL21 (DE3). All experiments involving liquid cultures were performed in LB at 37 °C with aeration unless otherwise stated. Carbenicillin for plasmid maintenance was used at 50 μg/ml for *E. coli* or 75 μg/ml for *A. baumannii*. Kanamycin (Km) was used at 40 μg/ml. Relevant primers are listed in **Table 6**.

Animal models

Eight to ten-week-old male C57BL/6J mice were purchased from Jackson Laboratories. Mice were housed on standard VUMC facility chow and bedding with a 12 hour light-dark cycle. All animal experiments were approved by the Vanderbilt University Medical Center (VUMC) Institutional Care and Use Committee and conform to policies and guidelines established by VUMC, the Animal Welfare Act, the National Institutes of Health, and the American Veterinary Medical Association.

Bacterial mutant generation

To generate the *zrlA*::km strain, approximately 1000 base pairs of DNA in both the 5' and 3' flanking regions surrounding the open reading frame were amplified from *A. baumannii* genomic DNA, and the kanamycin resistance gene *aph* was amplified from pUC18K1 (Menard et al., 1993). The three PCR products were joined together using overlap extension PCR, and the construct was cloned into pFLP2 and sequence verified (Hoang et al., 1998). pFLP2 was then electroporated into *A. baumannii*, plated onto LB Km40 agar, and grown overnight at 37 °C. Transformants were patched to LB Km40 or LB agar with 10 % sucrose to isolate Km-resistant (Km^R) and sucrose-sensitive merodiploids. Merodiploid strains were grown in LB overnight at 37 °C to resolve the plasmid. Cultures were serially diluted, plated on LB agar with 10 % sucrose, and incubated at 37 °C overnight. The resulting Km^R sucrose-resistant strains were screened for loss of *zrlA* and replacement with *aph* by multiple PCR reactions and Southern blot using gene-specific probes. To generate the *zrlA* unmarked strain, recombineering was utilized as described previously (Tucker et al., 2014). Briefly, the pUC18K1 *aph* gene was amplified using primers that contained 120 bp regions of homology flanking the *zrlA* open reading frame. The resulting PCR product was purified, concentrated to > 1 μg/μl, and transformed via electroporation into WT *A. baumannii* containing pAT02 (Tucker et al., 2014). Rec_{Ab} recombinase expression was induced with 2 mM isopropyl β-D-1-thiogalactopyranoxide (IPTG). Cultures were grown for four hours and plated to LB agar supplemented with Km. Resulting colonies were screened using primers external to *zrlA* and restreaked to LB agar containing Km or carbenicillin to screen for loss of pAT02. Resulting Km^R $carbenicillin^S$ strains were transformed with PAT03 and plated to carbenicillin. From here, colonies were streaked to LB agar containing 1 mM IPTG to induce FLP recombinase expression and excision of the Km resistance cassette. Colonies were then screened for Km^S and $carbencillin^S$ and verified by PCR. Relevant primers are listed in **Table 6**.

Construction of *zrlA* expression and complementation vectors

To generate the *zrlA* complementation vector, the *zrlA* gene and its native promoter were amplified with a C-terminal cMyc tag and cloned into the digested pWH1266 vector using the BamHI/SalI restriction sites (Hunger et al., 1990). To generate the non-metal binding variant, a gene block with a C-terminal cMyc tag containing the following open reading frame nucleotide substitutions was synthesized: C448G, A449C, A470C, A617C (Integrated DNA Technologies, San Jose, CA) and cloned into pWH1266 under the native *zrlA* promoter. The integrity of the promoter and gene sequences were confirmed by sequencing. The empty vector and expression vectors were each transformed into *A. baumannii* by electroporation. All relevant primers are listed in **Table 6.**

Polyclonal antibody generation

ZrlA was purified as described below and submitted to the Vanderbilt Antibody and Protein Resource core for generation of two rabbit polyclonal antibodies against ZrlA through Cocalico Biologicals (Stevens, PA). The antisera were affinity purified for increased ZrlA specificity. All antibodies, reactive sera, and pre-immune sera collected from the rabbits were tested for reactivity and specificity in enzyme-linked immunosorbent assays with purified ZrlA protein as well as immunoblot analysis of WT and Δ*zrlA* whole cell lysates.

Quantitative RT-PCR

Overnight cultures of *A. baumannii* were diluted 1:50 in LB and grown for 1 h at 37 °C. Cultures were then diluted 1:100 into LB plus or minus 200 μg/ml calprotectin or 40 μM TPEN and grown to mid-log. Cultures were pelleted at 4 °C and resuspended in 1:1 acetone:ethanol prior to storage at -80 °C until processing. For RNA extraction, cells were pelleted and resuspended in LETS buffer (0.1 M LiCl, 0.01 M Na_2EDTA, 0.01 M Tris-HCl pH 7.4, 0.2 % SDS) and lysed using Lysis Matrix B tubes (MP Biologicals) and a FastPrep-24 (MP) bead beater. Samples were heated to 55 °C for 5 min and pelleted at 15,000 rpm for 10 min. The top phase was combined with TRIzol and incubated at room temperature for 5 min. Chloroform was mixed with each sample, incubated for 3 min, and centrifuged for 15 min at 4 °C at 15,000 rpm. Following centrifugation, the upper aqueous phase was transferred to a new tube and incubated with isopropyl alcohol for 10 min at room temperature to precipitate the RNA. Samples were centrifuged at 4 °C for 10 min at 15,000 rpm. Supernatant was removed, and the pellet was washed twice with 70 % ethanol and dissolved in water. DNA contamination was removed by adding RQ1 and RQ1 buffer (Promega), and RNAse inhibitor (Thermo Fisher Scientific), and the samples were incubated at 37

°C for 2 h. Following DNAse treatment, RNA was purified using RNease mini kit (Qiagen) following manufacturer's recommendation. RNA was quantified, and 2 μg of RNA was used for cDNA synthesis using M-MLV reverse transcriptase (Thermo Fisher Scientific). cDNA synthesis and qRT-PCR was performed as previously described using the $^{\Delta\Delta}$CT method with the iQ SYBR Green Supermix (BioRad) (Mortensen et al., 2014; Nairn et al., 2016). Data are combined from at least 3 biological replicates. Relevant primers were published previously or are listed in **Table 6** (Hood et al., 2012; Mortensen et al., 2014).

Membrane fractionation

Overnight cultures of *A. baumannii* were diluted 1:50 in LB and grown for 1 h at 37 °C. Cultures were then diluted 1:100 into LB plus or minus 200 μg/ml calprotectin or 40 μM TPEN and grown to mid log. Cells were pelleted, and whole cell lysates were generated by resuspending pellets in lysis buffer (150 mM NaCl, 50 mM Tris-HCl pH 7.5), transferring samples to Lysis Matrix B tubes (MP Biologicals), and lysing on a FastPrep-24 (MP) bead beater. Crude membrane fractions were separated from cytoplasmic fractions by ultracentrifugation at 100,000 x *g* for 90 min, with the cytoplasmic fraction being in the supernatant. The crude membrane fraction pellet was solubilized in lysis buffer containing 0.5 % sarkosyl and incubated at room temperature with shaking for 30 min. Insoluble outer membrane fractions were isolated from the cytoplasmic membrane fraction by centrifugation at 100,000 x *g* for 60 min. Protein concentrations for each fraction were determined by BCA assay (Thermo Scientific) using bovine serum albumin as a standard. Samples were analyzed by immunoblot using mouse anti-cMyc 9E10 or rabbit anti-ZrlA, along with goat anti-mouse or anti-rabbit Alexa Fluor 680. Presented immunoblots are representative of at least 3 biological replicates.

ZrlA purification

ZrlA was cloned into pMALc5x to produce recombinant ZrlA tagged with a maltose binding protein (MBP). *E. coli* BL21 (DE3) pREL containing the ZrlA expression vector was grown at 37 °C shaking to an OD_{600} of 0.5. Protein expression was induced with 0.5 mM IPTG and grown for an additional 6 h at 37 °C. Cells were harvested by centrifugation at 6000 x *g* and suspended in lysis buffer (150 mM NaCl, 50 mM Tris-HCl pH 7.5) supplemented with lysozyme (1 mg/ml) and bovine deoxyribonuclease (3 mg). Cells were lysed by five passes through an Emulsiflex homogenizer (Aventin, Inc.) at 20,000 psi. Lysates were centrifuged at 8,000 x *g* to remove intact cells, and insoluble debris was removed by ultracentrifugation at 100,000 x *g* for 1 h at 4 °C. Supernatants were applied to amylose resin pre-equilibrated with lysis buffer. The column was washed with 12 column volumes of wash buffer (500 mM NaCl, 20 mM Tris-HCl pH 7.5, 1 mM EDTA), and ZrlA was eluted in a single elution with 10 mM maltose. In some cases, the MBP tag was cleaved by incubation with Factor X_a (New England Biolabs) during an overnight dialysis at 4 °C into dialysis buffer (150 mM NaCl, 20 mM Tris-HCl pH 7.5, 2.5 mM $CaCl_2$) with a buffer change after 2 h. To separate the MBP tag from ZrlA, the cleaved proteins were applied to Ni-NTA resin pre-equilibrated with dialysis buffer, where ZrlA was retained on the resin and eluted with an imidazole gradient (50 – 250 mM). ZrlA-containing fractions and sample purity were assessed by SDS-PAGE, and protein concentrations were determined by BCA assay (Thermo Scientific). To assess metals bound to ZrlA-MBP, purified protein was diluted to 1 mg/ml into lysis buffer, and Millipore water was added to a final volume of 10 ml in 15 ml metal-free conical tubes. Element quantification was assessed by ICP-MS. ZrlA (42-end) ($ZrlA^{42C}$) was cloned into a pET22b(+) plasmid between NcoI and EcoRI sites and was expressed without the His-tag. This resulting plasmid was transformed into BL21 (DE3) for expression in LB with ampicillin (100 μg/ml) and grown to OD_{600} of 0.6, at which time 0.75 mM IPTG was added, and the cells allowed to grow at 16 ºC overnight. For each 1 L cell pellet, cells were suspended in 40 ml lysis buffer A (25 mM MES, 50 mM NaCl, pH 5.5) and sonicated at 60 % power (3 s on; 9 s off, on ice), for total 60 min/L cells. This solution was then subjected to low-speed centrifugation at 10,000 *x* g (20 min, 4 ºC). The supernatant was filtered with 0.22 μm and loaded onto a self-packed SP-Sepharose^{TM} FastFlow (GE Healthcare) column. The SP-column was run at 2 mL/min, and ZrlA^{42C} was eluted with a 0-50% buffer B (25 mM MES, 1 M NaCl, pH 5.5) gradient over 90 min. ZrlA^{42C}-containing fractions were pooled. EDTA to a final concentration of 2 mM was added. The protein sample were concentrated and dialyzed again G75 (Hi Load^{TM} 16/60 Superdex^{TM} 75 prep grade) running buffer (25 mM HEPES, 150 mM NaCl, pH 7.5). ZrlA^{42C} eluted at a flow-rate of 1 ml/min. ZrlA^{42C}-containing fractions were flash-frozen in liquid nitrogen and stored at –80 ºC, and buffer exchanged prior to use. Protein was judged to be 90 % pure by overloaded SDS-PAGE gels. The ZrlA^{42C} concentration was measured using λ_{280}= 36,690 $M^{-1}{\bullet}cm^{-1}$. An N-terminally deleted version of A1S_1248 lacking the 55 N-terminal residues, termed A1S_1248^{56C}, was purified essentially the same way, and concentration measured using λ_{280}= 40,910 $M^{-1}{\bullet}cm^{-1}$. Relevant primers are listed in **Table 6.**

Cobalt titration

These experiments were performed as described previously using a Hewlett-Packard model 8452A spectrophotometer (Ma et al., 2011). The experiments were carried out in chelated titration buffer (25 mM HEPES, 150 mM NaCl, pH 7.4) at ambient temperature. Apo ZrlA^{42C} or Apo A1S_1248^{56C} (1 ml of 100 μM) was titrated with stock solution of $CoCl_2$. The binding reaction was monitored using 1-cm path length. Five minutes of equilibration time was allowed before the UV-vis spectra were acquired. UV-vis spectra from 230–800 nm were recorded after each addition and baseline-corrected as previously described (Ma et al., 2011).

Quin-2 Zn competition assays

These chelator competition experiments were carried as described in previous work using a Hewlett-Packard model 8452A spectrophotometer (Reyes-Caballero et al., 2010). The experiments were carried out in chelated titration buffer (25 mM HEPES, 150 mM NaCl, pH 7.4) at ambient temperature. Apo ZrlA^{42C} or apo A1S_1248^{56C} (1 ml of 15~17 μM and 12~15 μM, respectively) in the presence of 12~15 μM (for ZrlA^{42C}) or 20~27 μM (for A1S_1248^{56C}) Quin-2 was titrated with a solution of $ZnSO_4$. Equilibrium time was 10 min between measurements. Peak intensities at 265 nm from two independent experiments were globally fit to a simple 1:1 binding competition model with $K_{Zn}^{quin\text{-}2} = 2.7 \times 10^{11}\ M^{-1}$ using Dynafit (Kuzmic, 1996).

PAR Zn binding assay

4-(2-pyridylazo)-resorcinol (PAR) Zn binding assays were performed as previously described (Hood et al., 2012; Mortensen et al., 2014; Nairn et al., 2016). Briefly, free PAR exhibits a peak absorbance of 410 nm that shifts to 500 nm upon Zn binding. To determine if ZrlA binds Zn, increasing concentrations of recombinant ZrlA-MBP (0 – 12.5 μM) were added to solutions containing 20 μM PAR and 10 μM $ZnCl_2$ in 20 mM Tris-HCl pH 7.5, 150 mM NaCl. Spectra were collected for free and Zn-bound PAR and compared to spectra obtained in the presence of ZrlA-MBP. Spectra are representative of at least 3 biological replicates.

^{70}Zn uptake assay

Cells were grown for 7 h ± calprotectin, and optical densities were normalized across strains. ^{70}ZnO was spiked into each sample for a final concentration of 25 μM, and samples were incubated at 37 °C for 15 min. A 1:1 mixture of acetone:ethanol was added to the cells and pelleted for 10 min at 6,000 rpm. Cells were then washed twice in PBS. Following the second wash, samples were transferred to metal-free 15 ml conical tubes (VWR). Samples were digested overnight in 50% Optima-grade nitric acid (Fisher Scientific) at 50 °C and diluted with Millipore water prior to inductively-coupled plasma mass spectrometry analysis. ^{70}Zn values were normalized to total ^{34}S.

Inductively-coupled plasma mass spectrometry

Element quantification analysis on acid-digested protein samples was performed using ELEMENT 2™ high resolution inductively coupled plasma mass spectrometry (HR-ICPMS, Thermo Fisher Scientific, Bremen, Germany) coupled with ESI auto sampler (Elemental Scientific, Omaha, NE). The ICPMS is equipped with a PFA microflow nebulizer (Elemental Scientific, Omaha, NE), a Scott double-pass spray chamber (at room temperature), a magnetic sector followed by an electric sector, and a second electron multiplier. Liquid sample was up-taken by self-aspiration via 0.50 mm ID sample probe and sample capillary. Interested metals were measured at medium resolution (R=4200). Elemental quantification on ^{70}Zn-labeled samples was performed using an Agilent 7700 inductively coupled plasma mass spectrometer (Agilent, Santa Clara, CA). The following settings were fixed for the analysis Cell Entrance = -40 V, Cell Exit = -60 V, Plate Bias = -60 V, OctP Bias = -18 V, and collison cell Helium Flow = 4.5 ml/min. Optimal voltages for Extract 2, Omega Bias, Omega Lens, OctP RF, and Deflect were determined empirically before each sample set was analyzed. Element calibration curves were generated using ARISTAR ICP Standard Mix (VWR, Radnor, PA). Samples were introduced by peristaltic pump with 0.5 mm internal diameter tubing through a MicroMist borosilicate glass nebulizer (Agilent). Samples were initially up taken at 0.5 rps for 30 s followed by 30 s at 0.1 rps to stabilize the signal. Samples were analyzed in Spectrum mode at 0.1 rps collecting three points across each peak and performing three replicates of 100 sweeps for each element analyzed. Data were acquired and analyzed using the Agilent Mass Hunter Workstation Software version A.01.02

Modified Cd-ninhydrin assay

The Cd-ninhydrin reagent was generated as previously described (Doi et al., 1981). Briefly, ninhydrin (Sigma) was dissolved in 99.5 % EtOH and acetic acid, and $CdCl_2$ was added to the mixture. Enzymatic assays were performed as described elsewhere (Wu et al., 1995). Briefly, recombinant MBP-ZrlA (1 mM) was combined with Nα,Nε-Diacetyl-Lys-D-Ala-D-Ala (10 mM; Sigma) in the reaction buffer (50 mM HEPES pH 8) and incubated for 15 min at 37 °C. Samples were mixed at a ratio of 1:2 with the Cd-ninhydrin reagent and heated for 5 min at 85 °C. Samples cooled briefly at room temperature, and the absorbance at 500 nm was determined using a Varian Cary 50 Bio UV-Visible Spectrophotometer. Data are combined from at least 3 independent experiments.

Fluorescent D-amino acid labeling

Overnight cultures of WT or Δ*zrlA A. baumannii* were diluted 1:50 into LB for 2 h and subsequently diluted 1:10 into M9 minimal media with 0.5 % sodium succinate and Vishniac's trace metal mix (Vishniac, 1955) ± 10 μM TPEN. HADA and DA-EDA were synthesized as described previously and added at a final concentration of 1 mM to each culture (Kuru et al., 2012; Liechti et al., 2014). Cells were incubated with shaking at 37 ˚C for 2 h and fixed in 70 % ethanol for 1 h at 0 ˚C. Cells were pelleted and washed twice with PBS. DA-EDA-labeled cells were conjugated with the Atto 488 azide label (Sigma) using the Click-iT cell reaction buffer kit (Thermo) to generate fluorescence signal. Cells were imaged using a Nikon Ti-E inverted microscope equipped with a 1.4NA Plan Apo 60X oil objective and Andor iXon ENCCD camera. NIS-Elements AR software was used for image acquisition. Quantitative analysis of fluorescence intensity was performed using the MicrobeJ plugin in FIJI (Ducret et al., 2016). Data are pooled from 100 cells per treatment.

Sacculi purification and UPLC-MS analysis

WT *A. baumannii* and Δ*zrlA* were grown for 12 h in LB ± 40 µM TPEN. Cells were collected, and sacculi were purified as described previously (Kuru et al., 2012; Litzinger et al., 2010). Briefly, cell pellets were resuspended in water, added dropwise to boiling 5 % sodium dodecyl sulfate (SDS, w/v), and incubated with stirring for 30 min. The SDS insoluble material was collected by ultracentrifugation at 39,000 *x* g at 30 ˚C. Insoluble material was resuspended in water and boiled for 30 min with stirring in 4 % SDS. Samples were collected again by ultracentrifugation, washed repeatedly with water, resuspended in a digestion buffer (10 mM Tris-HCl pH 7.0, 10 mM NaCl, 0.32 M imidazole, 1 mM $MgSO_4$) and digested with DNase I (Thermo Fisher Scientific) and α-amylase (Promega) for 2 h at 37 ˚C. Samples were pelleted and resuspended in 0.05 M Tris-pH 7.8 and pronase (type XXV from *Streptomyces griseus*) and incubated at 60 ˚C for 2 h. Following this digestion, samples were pelleted, resuspended in water, and added dropwise to boiling 1 % SDS with stirring for 30 min. Samples were collected by centrifugation and washed repeatedly in water before storage at -80 ˚C in a minimal amount of water. For UPLC-MS, the purified sacculi were thawed and digested with mutanolysin for 16 h at 37 °C. Before applying the sample to the UPLC-MS analysis, digested PG samples were reduced with 10 mg/ml sodium borohydrate in 0.5 M borax in miliQ water at pH 9.0. The reduction was stopped with 98 % phosphoric acid, with the resultant pH adjusted to 2~3. An Acquity UPLC coupled to a PDA detector and SynaptG2S mass spectrometer, using a Waters C_{18} CSH 130 Å, 1.7 μm, 2.1 mm × 100 mm column and associated guard column C_{18} CSH 130 Å, 1.7 mm, 2.1 mm × 35 mm were used for UPLC-MS analysis. Solvent A was 0.1 % TFA and solvent B was 0.1 % TFA in 30 % methanol and a linear gradient to 100 % B over 60 min at a flow rate of 0.176 ml/min was used at a column temperature of 52 °C. In a typical analytical run, 10 μl samples were injected and analyzed. PDA detects 210 nm. Muropeptides were identified with theoretical m/z ± 0.02 Da. Integration of peak areas were performed with Masslynx. Peak area for each muropeptide was normalized to the total peak area of all identified muropeptides (muropeptide peaks 1~10 in **Table 5** correspond to ≥ 95 % of the total peak area), and biological duplicates were grouped for statistical analyses.

Live cell microscopy

WT and mutant cells were grown to mid to late-exponential phase in LB ± 40 μM TPEN and immediately spotted onto agarose-PBS pads (0.05 % agarose). Cells were allowed to dry briefly before sealing and imaging using brightfield microscopy on an Olympus BX60 microscope at 100X magnification. Images are representative of at least 3 independent experiments.

Ethidium bromide uptake

WT and mutant cells were grown in LB, normalized to OD_{600} of 0.3, and washed once with PBS. Cell resuspensions were placed into black 96-well plates and spiked with ethidium bromide (1 μg/ml, Sigma) before immediately reading fluorescence at 2 s intervals (Ex: 530; Em: 600) using a BioTek Cytation 5 imaging reader. Data are combined from at least 3 independent experiments.

Bacterial growth in experimental conditions

Overnight cultures of WT or Δ*zrlA* were subcultured 1:50 in LB for 1 h. Back-diluted cultures were then inoculated 1:100 into LB containing various concentrations of SDS, ethylenediamine tetraacetic acid (EDTA) (Sigma), tetrakis-(2-pyridylmethyl)ethylenediamine (TPEN), calprotectin, carbenicillin (6.25 μg/ml), tetracycline (AlfaAesar, 78 ng/ml), polymyxin B (Alexis Biochemicals, 250 ng/ml), or vancomycin (Fisher Scientific, 100 μg/ml) and growth was monitored over time by monitoring OD_{600} using a BioTek Synergy 2 or Epoch 2 microplate reader. For growth in antibiotics with TPEN, cells were grown in carbenicillin (6.25 μg/ml) ± 20 μM TPEN or polymyxin B (1 μg/ml) ± 10 □M TPEN. For growth in calprotectin, back-diluted cultures were inoculated 1:100 into LB containing 40 % calprotectin buffer (20 mM Tris-HCl pH 7.5, 100 mM NaCl, 5 mM β-mercaptoethanol, 3 mM $CaCl_2$) supplemented with calprotectin. Recombinant human calprotectin was used for all *in vitro* experiments and was expressed and purified as described previously (Corbin et al., 2008; Kehl-Fie et al., 2011). Percent growth panels are combined from at least 3 biological replicates.

Mouse model for *A. baumannii* pneumonia

Eight to ten-week-old male mice were inoculated 1:1 with a mixture of *A. baumannii* (WT and Km-marked Δ*zrlA*, or unmarked Δ*zrlA* and Km-marked Δ*zrlA*) totaling 3 x 10^8 CFU in 40 μl PBS. For meropenem dosing experiments, mice were administered meropenem (Hospira, Inc.) dissolved in PBS (12.5 mg/kg) or vehicle via intraperitoneal injection at 0, 12, and 24 hours post-infection (hpi). At 36 hpi, mice were euthanized, and CFU were enumerated in the lungs and livers following tissue homogenization and dilution plating on LB and LB Km 40. The limit of detection of this assay is 100 CFU/ml.

Quantification and statistical analysis

Statistical analyses were performed using GraphPad Prism 7 and Microsoft Excel. Statistical significance was generally assessed using a two-tailed unpaired Student's *t* test, one-way ANOVA with Tukey multiple comparisons test, or Mann Whitney U test. Significance was defined as $p < 0.05$, and data were only excluded on the basis of technical errors associated with the experiment. Exact statistical tests used, significance values, group sizes, and dispersion and precision of measurements are defined in the figure legends

Table 5. Descriptions for muropeptide peak labeling depicted in Figure 23. The theoretical masses were reported previously (Kuhner et al., 2014; Brown et al., 2012). The first letter indicates whether the muropeptide is a monomer (M), or crosslinked dimer (D) or crosslinked trimer (T). The numbers indicate the number of amino acids of the peptide side chains from the donor to acceptor; G indicates glycine; (-GlcNAc) and (-Acetyl) indicates loss of GlcNAc or acetyl group. The difference column denotes the difference in experimental mass relative to the theoretical mass.

UPLC peak	**Muropeptide structure**	**Retention time in TIC (min)**	**Theoretical molecular mass**	**Theoretical m/z [M+H]+**	**Theoretical m/z [M+2H] 2+**	**Theoretical m/z [M+3H] 3+**	**Experimental m/z [M+xH]x +**	**Difference**
1	**M3**	**9.54**	**870.36**	**871.37**			**871.370**	**0.000**
1	**M3(-GlcNAc)**	**9.54**	**667.29**	**668.30**			**668.299**	**0.000**
2	**M3G**	**10.18**	**927.38**	**928.39**			**928.395**	**0.005**
2	**M3G(-GlcNAc)**	**10.20**	**724.31**	**725.32**			**725.316**	**-0.005**
3	**M4G(-GlcNAc)**	**12.34**	**795.35**	**796.36**			**796.349**	**-0.009**
3	**M4G**	**12.39**	**998.43**	**999.44**			**999.414**	**-0.023**
4	**M4**	**13.75**	**941.39**	**942.40**			**942.397**	**-0.003**
4	**M4(-GlcNAc)**	**13.76**	**738.33**	**739.34**			**739.335**	**-0.001**
5	**M43**	**17.45**	**1313.56**	**1314.57**	**657.79**		**657.791**	**0.002**
6	**M44**	**19.12**	**1384.59**	**1385.60**	**693.30**		**693.306**	**0.002**
7	**D34D and D43**	**25.34**	**1793.75**	**1794.76**	**897.88**		**897.877**	**-0.007**
8	**D44**	**26.72**	**1864.79**	**1865.80**	**933.40**		**933.401**	**-0.003**
9	**T444**	**32.8**	**2788.19**	**2789.20**		**930.41**	**930.390**	**-0.015**
10	**anhydroD44**	**35.97**	**1844.78**	**1845.79**	**923.40**		**923.388**	**-0.009**

Table 6. Oligonucleotides used in Chapter III.

Name	**Sequence (5’ to 3’)**	**Description**
***zrlA* mutant construction and confirmation**		
3412FL1For	CCCGGGAGAGTAAGTGCAATTG	Cloning into pFLP2, 5' flank, forward
3412FL1Rev	CTCCTAGTTAGTCACATATGACGCTT CATAAATATATTC	Cloning into pFLP2, 5' flank, reverse
3412FL2For	AGGGAATAATGACATATGGGACTAT AAAAGCAATTT	Cloning into pFLP2, 3' flank, forward
3412FL2Rev	CCCGGGTTGTGACCATGAATAAG	Cloning into pFLP2, 3' flank, reverse
3412KanFor	GAATATATTTATGAAGCGTCATATGT GACTAACTAGGAG	Cloning into pFLP2 for Km cassette from pUC18-k1, forward
3412KanRev	AAATTGCTTTTATAGTCCCATATGTC ATTATTCCCT	Cloning into pFLP2 for Km cassette from pUC18-k1, reverse
3412_KO_F	cgtcctttttttattttttaaaatttacaacagaaattaaaggattt aataattgttatattataacatttctgaaattaaatgattaaaggc ttccagatgtttagggaagatagaatatatttGTG TAG GCT GGA GCT GCT TC	To generate unmarked *zrlA* mutant, foward
3412_KO_R	tggccagatcacaggcgtaatctatttctaaaccacaataatg ttatgttataacataactattgatcaagtttttattctagttttatcta agccaaatcacttagtgtttgaaaaaattgcttCAT ATG AAT ATC CTC CTT AG	To generate unmarked *zrlA* mutant, foward
3412ExtR	GACCAGCTCTGCCAAACTTGC	External to *zrlA* for Tn insertion confirmation
Pgro-172	TGAGCTTTTTAGCTCGACTAATCCAT	T26 transposon-specific
***zrlA* complementation**		
3412mycFor	GGATTCATGGTGGCTTATCAATTTAA GCGCCG	Cloning into pWH1266, forward
3412mycRev	GGATTCTTATAGATCTTCTTCAGATA TCAG TTTCTGTTCTAGTCCCTGACAAAT	Cloning into pWH1266, reverse with cMyc tag
qRT-PCR		
r01RTf	CTGTAGCGGGTCTGAGAGGAT	*A1S_r01* (16S), forward
r01RTr	CCATAAGGCCTTCTTCACAC	*A1S_r01* (16S), reverse
3412RTf	CGCAACTGCAGATCACAGAC	*zrlA*, forward
3412RTr	GGAACTGCGTAAGGCTCAAC	*zrlA*, reverse
A1S_2479_RTFor	CAATGCCGGATCATTACACGACAG	*A1S_2479*, forward
A1S_2479_RTRev	AACCTGCTGCTTTGGTATAGCCAG	*A1S_2479*, reverse

A1S_2435_RTFor	ATGAACGAATCTGCTTGGTGTAAAGGC	*A1S_2435*, forward
A1S_2435_RTRev	CCTTCATTCCCAGCAATATGTTCAGCC	*A1S_2435*, reverse
A1S_1248_RTFor	CCACCTAAAGTTGAACCTGCTTCCTAT	*A1S_1248*, forward
A1S_1248_qRTRev	TCTGCCAATCACGAGCGGATCTTAATA	*A1S_1248*, reverse
Protein purification		
3412-sspMAL_fwd	gcggccgcgatatcgtcgacAGTACTCAAACACCCCAGC	Cloning into pMAL-c5X, forward
3412-sspMAL_rev	cctgcagggaattcggatccTTATAGTCCCTGACAAATTGAG	Cloning into pMAL-c5X, reverse
ZrlA^{42C}-F	CAACGACCGAAAACCTGTATTTTCAGGGCGCCATGGA TAAACAACAGCCT GAAGATTAT	Cloning into pET-22b, forward
ZrlA^{42C}-R	CACTAGTTGAGCTCGTCGACGTAGGCCTTTGAATTCTT ATAGTCCCTGACAAATTGAGGT	Cloning into pET-22b, reverse
A1S_1248^{56C}-F	GCCGGCGATGGCCATGGATAAAGTTGAACCTGCTTCCTAT	Cloning into pET-22b, forward
A1S_1248^{56C}-R	CGG CCG CAA GCT TGT CGA CGG AGC TCG AAT TCT TAG AAA TTA CAC ATT GAC GTA TTG C	Cloning into pET-22b, reverse

Results

ZrlA is a Zn binding peptidase critical for A. *baumannii* cellular envelope maintenance and morphology

To assess whether ZrlA contributes to the response of *A. baumannii* to Zn starvation, we monitored the transcriptional induction of *zrlA* during Zn limitation and generated a polyclonal antibody against ZrlA to monitor protein abundance in these conditions. *zrlA* and its gene product are both detectable in Zn-replete conditions but are induced during Zn starvation by the small molecule Zn chelator TPEN and the Zn-chelating host protein CP (**Figure 20A,B, Figure 21A,B,C**). Sequence predictions suggest that ZrlA has D-alanine-D-alanine carboxypeptidase (D,D-CPase) activity and is a member of the M15 metallopeptidase family (Rawlings and Barrett, 1993). Peptidase activity was confirmed using a modified cadmium ninhydrin assay (Wu et al., 1995) to detect release of free amino acids from a peptide substrate (**Figure 20C**). Additionally, subcellular fractionation experiments revealed that ZrlA localizes to the inner membrane (**Figure 20D, Figure 21D,E,F**). Finally, recombinant ZrlA coordinates Zn, and the binding of Zn is preferential over other divalent cations, which was validated by quantitative metal binding experiments with $\mathrm{Zn}^{\mathrm{II}}$, and $\mathrm{Co}^{\mathrm{II}}$ (**Figure 20E, F, Figure 21G,H**). Soluble ZrlA lacking the N-terminal 41 residue membrane anchoring domain (**Figure 21F**), denoted ZrlA^{42C}, binds a single molar equivalent of $\mathrm{Co}^{\mathrm{II}}$ or $\mathrm{Zn}^{\mathrm{II}}$ in a tetrahedral coordination geometry (**Figure 20E**) and is characterized by a high affinity for Zn, K_{Zn} of 3.6 (±0.5) $\times 10^{11}$ M^{-1} (Fig 1F). These results demonstrate that ZrlA is Zn-binding lipoprotein that is maximally induced during nutrient Zn starvation and exhibits peptidase activity.

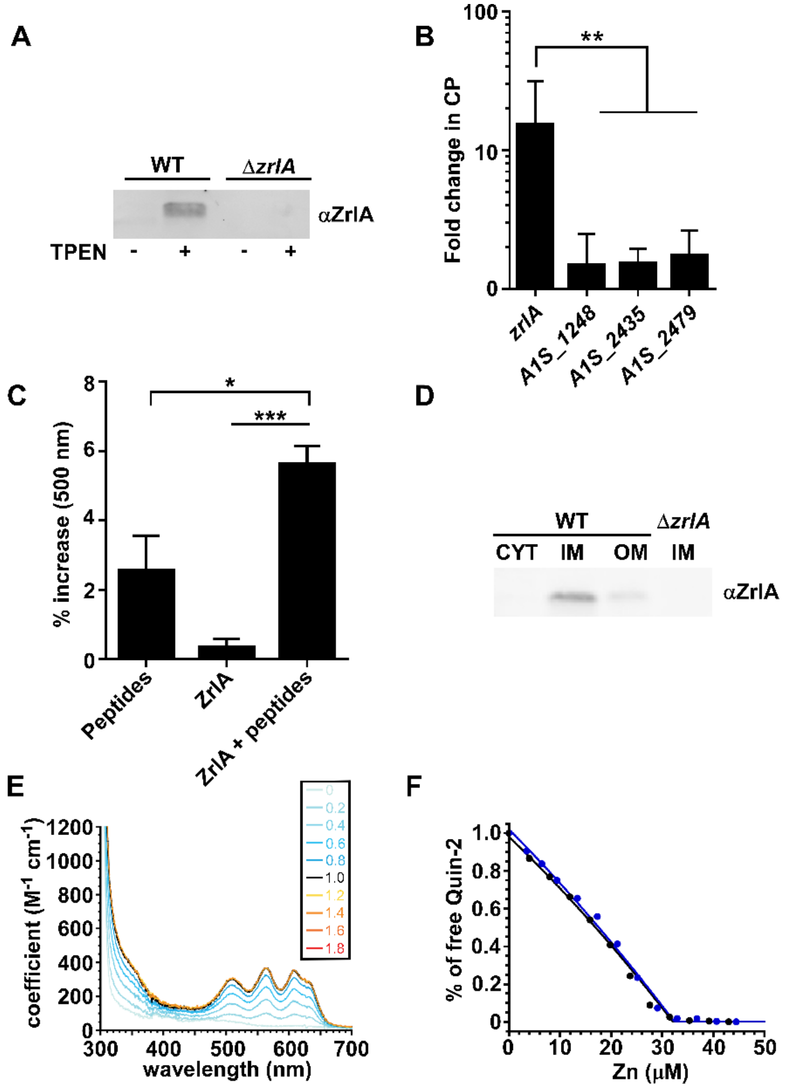

Figure 20. ZrlA is a peptidase induced during Zn starvation. A) ZrlA expression was assessed in WT and Δ*zrlA* (15 μg protein/lane) by immunoblot following growth in LB ± 40 μM TPEN. B) Transcriptional changes for *zrlA* and other predicted D,D-CPases *A1S_1248*, *A1S_2435*, and *A1S_2479* were assessed by qRT-PCR + 250 μg/ml CP. ** $p < 0.01$ as determined by one-way ANOVA with Tukey multiple comparisons test on three independent experiments, mean ± SD. C) Modified cadmium-ninhydrin assay was performed on recombinant MBP-ZrlA in the presence of a peptide substrate, * $p < 0.05$, *** $p < 0.001$ as determined by one-way ANOVA with Tukey multiple comparisons test on three independent experiments, mean ± SD. D) ZrlA protein localization was assessed in WT and Δ*zrlA* (7.5 μg protein/lane) by immunoblot of membrane fractions following growth in LB ± 40 μM TPEN. E) Co^{II} titration, where a tetrahedral or distorted tetrahedral coordination geometry is suggested with a d–d transition of 400 M^{-1}•cm^{-1} at 600 nm (Corwin, 1987). *Inset*, number of Co^{II}:ZrlA^{42C} mol•equivalents corresponding to each spectrum shown; note that all spectra acquired at Co^{II}:ZrlA^{42C} overlap, revealing a 1:1 metal binding stoichiometry. F) Normalized binding titration of a mixture of ZrlA^{42C} and competitor quin-2 with Zn in two independent experiments:17.0 μM ZrlA^{42C} with 15.2 μM quin-2 (blue filled circles) and

15.1 μM ZrlA^{42C} with 12.3 μM quin-2 (black filled circles). The continuous lines represent the results of a non-linear, least-squares fit to a Zn:ZrlA^{42C}=1:1 binding model. The global fitting results in $K_{Zn} = 3.6\ (\pm\ 0.4) \times 10^{11}\ M^{-1}$.

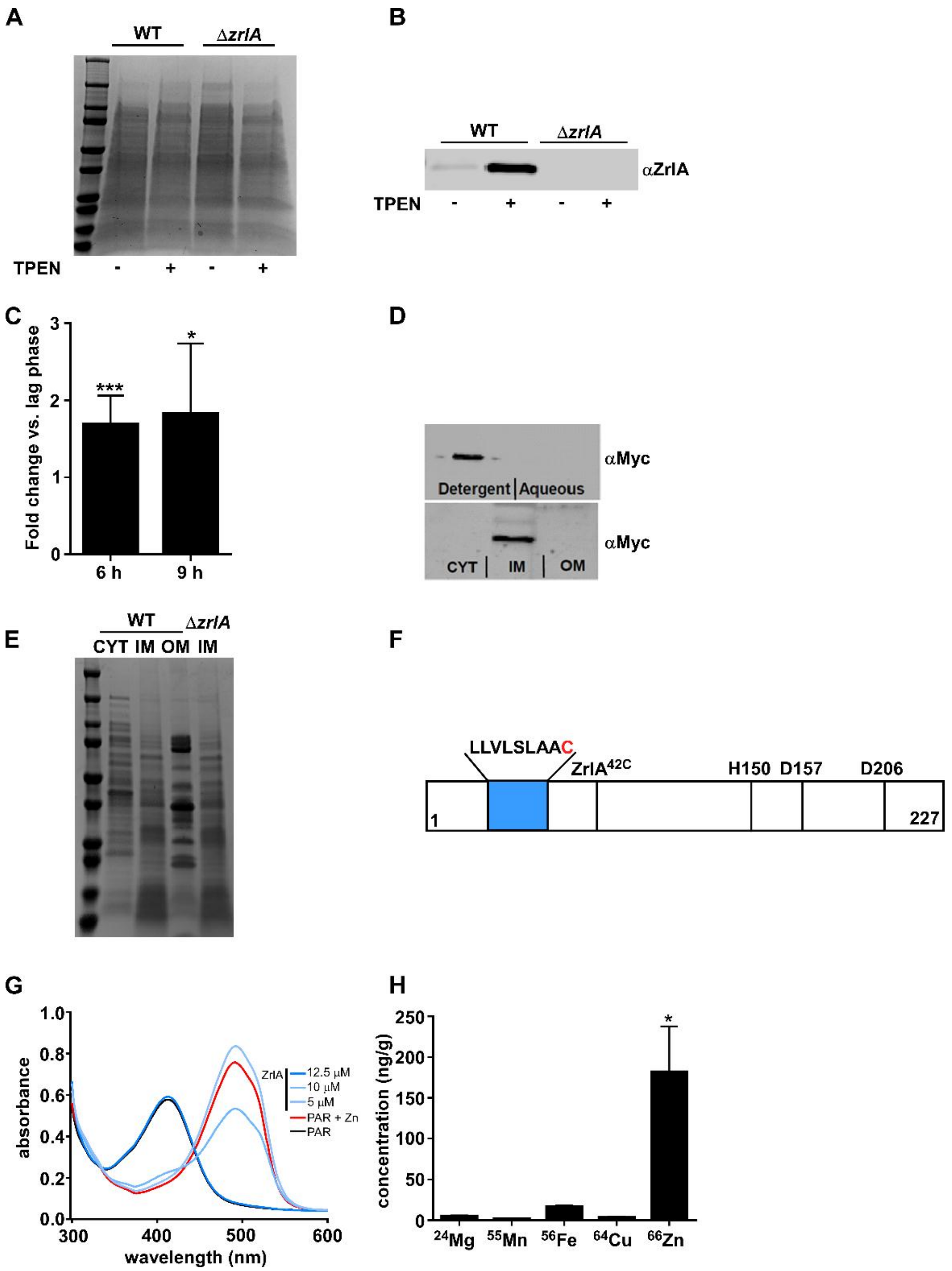

Figure 21. ZrlA is a zinc-binding inner membrane lipoprotein. A) SDS-PAGE analysis to assess total protein levels corresponding to the immunoblot in Fig 1A. B) Immunoblot on protein lysates from WT or Δ*zrlA* cells grown for 6 hours ± 40 μM TPEN (25 μg protein/lane). C) Relative expression of *zrlA* as determined by qRT-PCR on WT *A. baumannii* at 6 h and 9 h of growth compared to 2 h. * $p < 0.05$, *** $p < 0.001$ as determined by Student's *t* test from three independent experiments, mean ± SD. D) Immunoblot of membrane fractionations (15 μg protein/lane) reveals ZrlA^{myc} localizes to the detergent phase and localizes to the inner membrane. E) SDS-PAGE analysis to assess total protein levels corresponding to the immunoblot in Fig 1D. F) Schematic of

ZrlA, with the predicted lipobox denoted as a blue square and the conserved lipid-anchoring cysteine in red. The approximate N-terminus of the ZrlA^{42C} variant is indicated (residues 42-227). H150, D157, and D206 are the predicted metal-coordinating residues. G) Incubation of 20 μM 4-(2-pyridylazo)-resorcinol (PAR) with 10 μM Zn results in an absorbance shift of PAR from 410 nm to 500 nm; the addition of increasing concentrations of recombinant ZrlA from 5 μM to 12.5 μM results in return in absorbance to 410 nm. H) Recombinant ZrlA was analyzed by ICP-MS for associated Mg, Mn, Fe, Cu, and Zn concentrations. * $p < 0.05$ as determined by one-way ANOVA with Tukey multiple comparisons test from three independent experiments, mean ± SD.

We hypothesized that the absence of ZrlA may change PG architecture. To test this, we labeled PG with fluorescent D-amino acids and their dipeptide derivatives to monitor changes in PG during Zn starvation. For these experiments, we used conjugated fluorescent molecules designed to label either the fourth or fifth position of PG stem peptides using HADA and DA-EDA, respectively, and then monitored changes in fluorescence intensity during Zn limitation (Kuru et al., 2012; Liechti et al., 2014). Wild-type (WT) *A. baumannii* had increased fourth position labeling that corresponded with decreased fifth position labeling during Zn starvation that were diminished in the Δ*zrlA* strain (**Figure 22A,B**). This finding is consistent with ZrlA induction resulting in cleavage of terminal D-alanine residues and increased PG crosslinking. We next performed liquid chromatography-mass spectrometry (UPLC-MS) on PG purified from WT or Δ*zrlA A. baumannii* following growth in Zn-replete or Zn-deplete conditions and quantified the normalized abundances of major monomeric and dimeric (crosslinked) muropeptide species (**Figure 23A and Table 5**). Tripeptide monomers were more abundant in the Δ*zrlA* strain in Zn-replete conditions but significantly reduced during Zn starvation (**Figure 22C**). In contrast, tetrapeptide monomer species, while comparable in the WT and Δ*zrlA* strain in Zn-replete conditions, were increased in Δ*zrlA* strain in Zn-starved conditions relative to WT (**Figure 23B**). Conversely, dimeric tripeptide-tetrapeptide crosslinks were significantly reduced in the Δ*zrlA* strain in both Zn-replete and deplete conditions (**Figure 22D**), while dimeric tetrapeptides were slightly elevated in both strains in Zn-deplete conditions (**Figure 23C**). Taken collectively, these data demonstrate that *A. baumannii* increases major cell wall crosslinks during Zn starvation, and *zrlA* impacts both homeostatic muropeptide abundance and specific PG alterations that occur during Zn limitation.

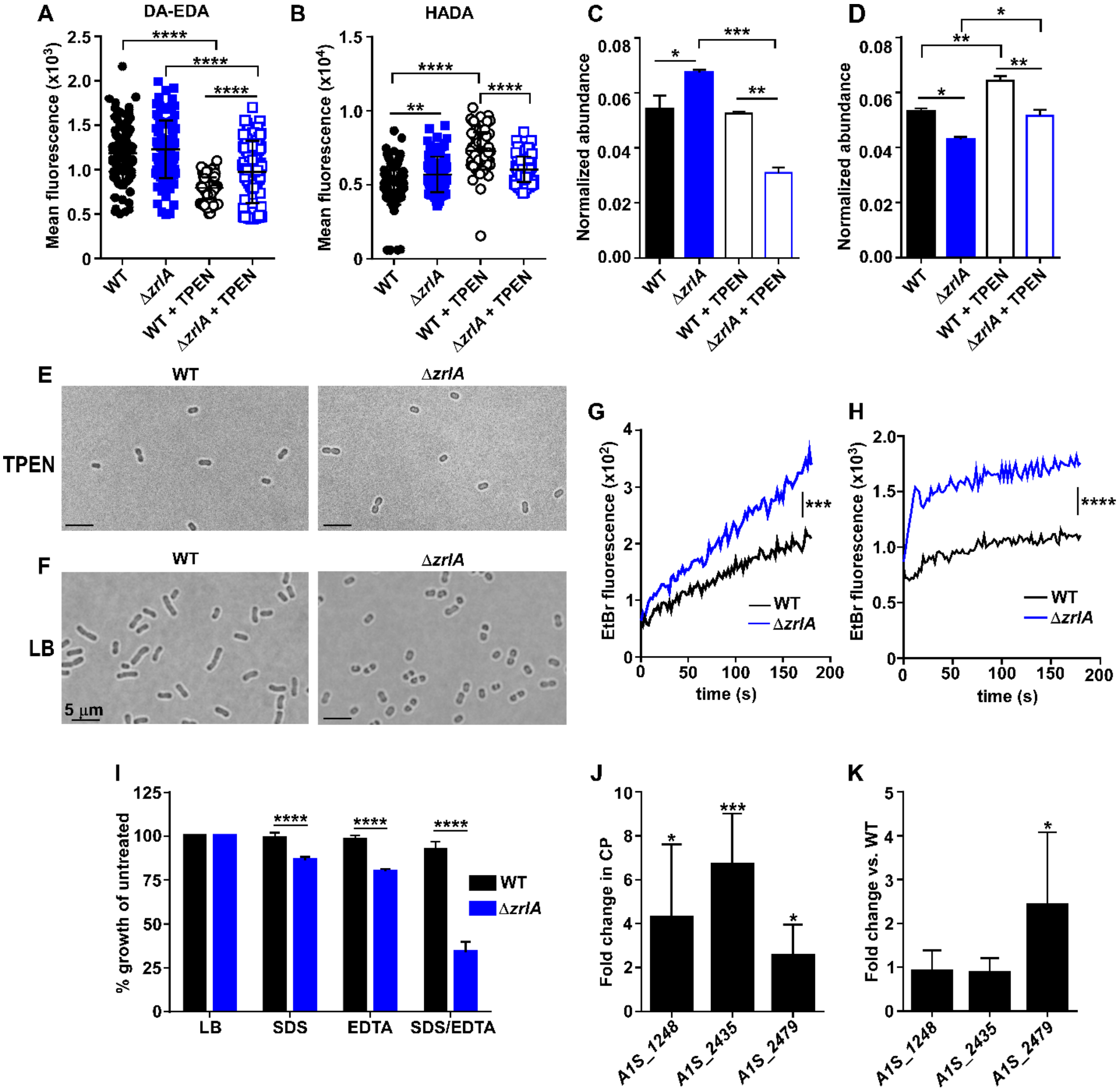

Figure 22. ZrlA contributes to cellular morphology and envelope integrity. A) Mean fluorescence of WT or Δ*zrlA* ± 10 µM TPEN following DA-EDA labeling of the fifth position of PG pentapeptides. **** $p < 0.0001$ as determined by one-way ANOVA with Tukey multiple comparisons test ($n = 100$ cells/group). B) Mean fluorescence of WT or Δ*zrlA* ± 10 µM TPEN following HADA labeling of the fourth position of PG pentapeptides ** $p < 0.01$, **** $p < 0.0001$ as determined by one-way ANOVA with Tukey multiple comparisons test ($n = 100$ cells/group). C) Normalized abundance of PG muropeptide tripeptide monomers [sum M3, M3(–GlcNAc); see Figure S2 for a representative LC-MS/MS chromatogram and Table S1 for muropeptide designations and expected and experimental masses) in WT or Δ*zrlA* ± 40 µM TPEN. D) Normalized abundance of muropeptide tetrapeptide monomers [sum M4,M4(–GlcNAc)] (Figure

S2, Table S1) in WT or Δ*zrlA* ± 40 μM TPEN. * $p < 0.05$, **, $p < 0.01$, *** $p < 0.001$ as determined by one-way ANOVA with Tukey multiple comparisons test on biological duplicates, mean ± SD. E) Microscopy of WT or Δ*zrlA A. baumannii* grown to mid-log in LB + 40 μM TPEN (100 x). F) Microscopy of WT or Δ*zrlA A. baumannii* grown to mid-log in LB (100 x). Scale bar is 5 μm. G) Ethidium bromide uptake following growth in LB. *** $p < 0.001$ as determined by Student's *t* test of mean line slopes from three independent experiments. H) Ethidium bromide uptake following growth in 40 μM TPEN, **** $p < 0.0001$ as determined by Student's *t* test of mean line slopes from three independent experiments. I) Percent growth as determined by OD_{600} at eight hours of growth in LB, 0.01 % SDS, or 0.01 mM EDTA for WT and Δ*zrlA* compared to untreated samples. **** $p < 0.05$ as determined by Student's *t* test from three independent experiments, mean ± SD. J) Δ*zrlA* was subjected to qRT-PCR analysis of putative D,D-CPases in 250 μg/ml CP. * $p < 0.05$, *** $p < 0.001$ as determined by Student's *t* test from three independent experiments, mean ± SD. K) Δ*zrlA* was subjected to qRT-PCR analysis of putative D,D-CPases in LB compared to expression in the WT strain. * $p < 0.05$ as determined by Student's *t* test from three independent experiments, mean ± SD.

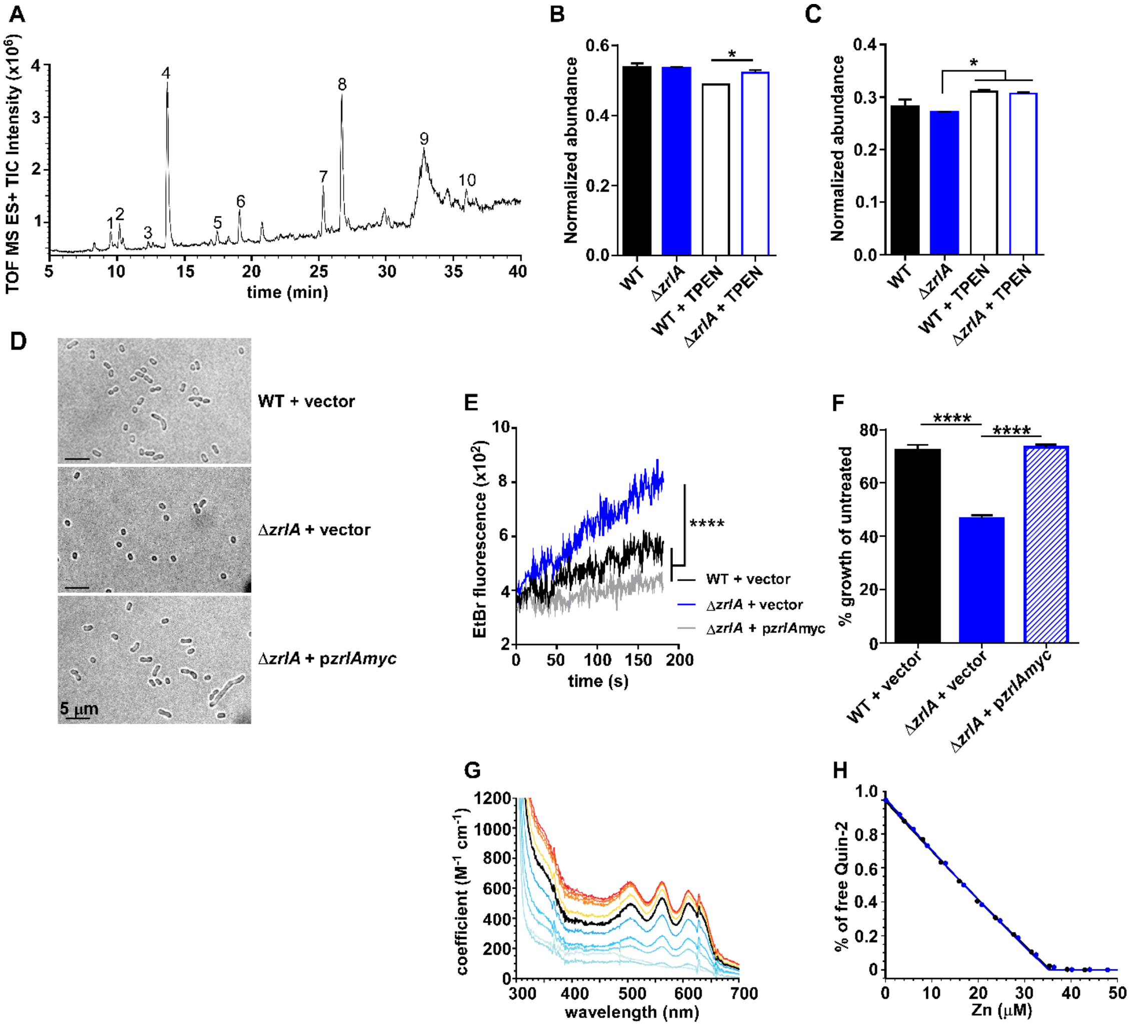

Figure 23. ZrlA contributes to PG homeostasis and cellular morphology. A) Representative total ion chromatogram (TIC) and accompanying UPLC-MS analysis of a muropeptide profile of *A. baumannii* ATCC 17978 Δ*zrlA* grown with 40 µM TPEN treatment. Other TICs were obtained for the WT strain grown with 40 µM TPEN. See **Table 5** for corresponding peak descriptions of peaks labeled 1-10 including molecular composition, retention time, theoretical *m/z*, experimental *m/z* and difference in *m/z*. Note that peaks 1-2 (monomeric trimers) and 3-4 (monomeric tetramers include muropeptides that harbor a disaccharide or monosacharaide (–GlcNAc) sugar moiety (see Table 5 for details). B) Normalized abundance of muropeptide tetrapeptide monomers [sum M4,M4(–GlcNAc)] (Figure 23, Table 5) in WT or Δ*zrlA* ± 40 µM TPEN. C) Normalized abundance of muropeptide dimeric tetrapeptides crosslinks (sum D44, M44; Figure 23, Table 5) in WT or Δ*zrlA* ± 40 µM TPEN. * $p < 0.05$ as determined by one-way ANOVA with Tukey multiple comparisons test on biological duplicates, mean ± SD. D) Live-cell imaging of WT + vector, Δ*zrlA* + vector, or Δ*zrlA* + p*zrlAmyc* following growth in LB Carb75 (100X). Scale bar is 5 µm. E) Ethidium bromide uptake assessed over time in WT + vector, Δ*zrlA*

+ vector, or Δ*zrlA* + p*zrlAmyc* following growth in LB Carb75. **** $p < 0.0001$ as determined by Student's *t* test on mean line slope from three independent experiments. F) WT + vector, Δ*zrlA* + vector, and Δ*zrlA* + p*zrlAmyc* were grown in 0.01 % SDS. Graph depicts percent growth relative to untreated strains at eight hours. *** $p < 0.001$ as determined by one-way ANOVA with Tukey multiple comparisons test from three indepdenent experiments, mean ± SD. G) Co(II) titration of apo A1S_1248^{56C} with the spectra colored as a function of the Co(II):protein ratio as in Fig 2E, main text: *cyan*, less than 1 mol•equivalent Co(II); *black*, 1:1 mol ratio; *tan to orange*, greater than 1:1 mol ratio. H) Replicate normalized titrations (*black*, *blue* filled symbols) of Zn(II) into a solution of the quin-2 and A1S_1248^{56C}, with the continuous lines individual fits to a 1:1 binding model. 12.4 μM A1S_1248^{56C} with 22.4 μM quin-2 (black filled circles) and 15.0 μM A1S_1248^{56C} with 20.2 μM quin-2 (blue filled circles). The average K_{Zn} of 2.2 (±0.1) x10^{11} M^{-1}.

To test whether the absence of *zrlA* leads to morphological changes, we performed live cell imaging on WT *A. baumannii* and a Δ*zrlA* strain following growth in Zn-replete and deplete conditions. WT *A. baumannii* and a Δ*zrlA* strain have a rounded morphology when grown in Zn-starved conditions (**Figure 22E**). When cultured in Zn-replete conditions, the WT strain displays morphological heterogeneity, with rounded cells and short and long rods detected, while the Δ*zrlA* strain remains rounded; this phenotype can be complemented by providing *zrlA in trans* (**Figure 22F, Figure 23D**). These results suggest that ZrlA contributes to morphological plasticity in *A. baumannii* and the ability of this organism to adapt to changing environmental conditions.

Given the altered PG structure and shape in the Δ*zrlA* mutant, we hypothesized that ZrlA may contribute to maintenance of overall cellular envelope integrity. To test this, the rate of ethidium bromide diffusion across the WT the Δ*zrlA* mutant envelope was assessed by monitoring fluorescence that occurs upon ethidium bromide-DNA interaction (Dalebroux et al., 2015). This assay revealed the Δ*zrlA* strain has increased fluorescence compared to the WT strain indicative of increased envelope permeability, and the rate of uptake is increased in the Δ*zrlA* strain during Zn starvation (**Figure 22G,H**). Furthermore, the Δ*zrlA* strain is more sensitive to the detergent SDS as well as EDTA, which chelates metals associated with the outer membrane (Malinverni and Silhavy, 2009) (**Fig 22I**). These envelope defects are complemented by expressing *zrlA in trans* (**Figure 23E,F**).

To determine if inactivation of *zrlA* imbalanced other cell wall-modifying enzymes, expression of predicted carboxypeptidases in *A. baumannii* was monitored in WT and Δ*zrlA* in Zn-replete and Zn-deplete conditions. These carboxypeptidases were identified based on sequence comparisons to defined D,D-CPases in *E. coli*, as well as through manual genome analysis (Ghosh et al., 2008). During Zn starvation, WT *A. baumannii* only induces expression of *zrlA* (Fig 20B).

However, the Δ*zrlA* strain has aberrant D,D-CPase expression in Zn-starved conditions as well as in Zn-replete conditions relative to the WT strain (**Figure 22J,K**). Protein sequence alignment revealed that one of these putative D,D-CPases, A1S_1248, is more closely related to ZrlA but not predicted to be regulated by Zur. This protein was purified as described for ZrlA, and found to possess a metal coordination geometry (**Figure 23G,H**) and K_{Zn} of 2.2 (±0.1) x10^{11} M^{-1} (**Figure 23G,H**) that is nearly indistinguishable from ZrlA. This finding effectively rules out a "zinc sparing" mechanism in which Zn-starved *A. baumannii* overexpresses a non-Zn requiring paralog (ZrlA) relative to constitutively expressed *A1S_1248* in WT cells (Blaby-Haas et al., 2011; Nanamiya et al., 2004). Taken together, these data establish ZrlA as a critical factor for maintaining cellular morphology and envelope integrity in *A. baumannii*.

ZrlA is required for *A. baumannii* to overcome nutrient Zn limitation

We next hypothesized that ZrlA has a role in the response of *A. baumannii* to Zn starvation. Upon growth of WT or Δ*zrlA* in the presence of CP or the Zn chelator TPEN, Δ*zrlA* exhibits a growth defect (**Figure 24A, 25A,B**) that can be fully rescued by Zn supplementation (**Figure 24B**) or expression of *zrlA in trans* (**Figure 25C**). Additionally, the predicted metal-coordinating residues of ZrlA (**Figure 21F**) are required for this complementation, as a mutant *zrlA* predicted to no longer bind Zn is unable to restore growth despite expression at levels comparable to WT ZrlA (**Figure 25D,E**). Furthermore, the requirement of *zrlA* for overcoming Zn limitation is conserved in a recently isolated multi-drug resistant strain of *A. baumannii* (**Figure 25F**). To determine if this growth defect was due to alterations in cytosolic Zn buffering or acquisition of extracellular Zn, Zn levels were monitored via inductively-coupled plasma mass spectrometry (ICP-MS). No differences were found in total cellular Zn of Δ*zrlA* relative to WT (**Figure 25G**).

However, qRT-PCR analysis of Zur-regulated Zn uptake genes revealed that the Δ*zrlA* strain has increased expression of *zur*, *znuA*, and *znuD1* relative to WT (Figure 24C), all of which are transcriptionally induced during Zn limitation (Mortensen et al., 2014). Since ZrlA affects cellular envelope integrity and homeostasis, we hypothesized that ZrlA specifically contributes to Zn uptake. Cultures were pulsed with a rare Zn isotope (^{70}Zn) and analyzed by ICP-MS to quantify cellular ^{70}Zn levels; this experiment revealed that WT *A. baumannii* is capable of competing with CP for Zn but that the Δ*zrlA* mutant is impaired in Zn uptake in conditions of Zn limitation (**Figure 24D**). To determine if aberrant expression of Zn uptake genes was the primary contributor to the envelope defects observed in the Δ*zrlA* mutant, a strain lacking *zur* (Δ*zur*), which overexpresses Zn uptake genes (Mortensen et al., 2014), was utilized to assess outer membrane envelope integrity following exposure to SDS/EDTA. This experiment revealed that the Δ*zur* strain has a modest growth defect in these conditions but grew significantly better than the Δ*zrlA* mutant (**Figure 24E**). This suggests that overexpression of the Zn uptake genes in the Δ*zrlA* mutant is not sufficient to cause cell envelope defects and that the direct impact of ZrlA on cell wall architecture is a major contributor for maintaining envelope integrity and overcoming Zn limitation.

Given that the vertebrate host is a harsh environment with limited metal availability, we investigated the contribution of ZrlA to *A. baumannii* pathogenesis. This experiment revealed that Δ*zrlA* is significantly attenuated in lung colonization (**Figure 24F**) and is defective at disseminating to the liver (**Figure 24G**). Taken together, these results suggest that *A. baumannii* uses ZrlA to coordinate nutrient Zn uptake and cellular envelope maintenance to persist within the vertebrate host.

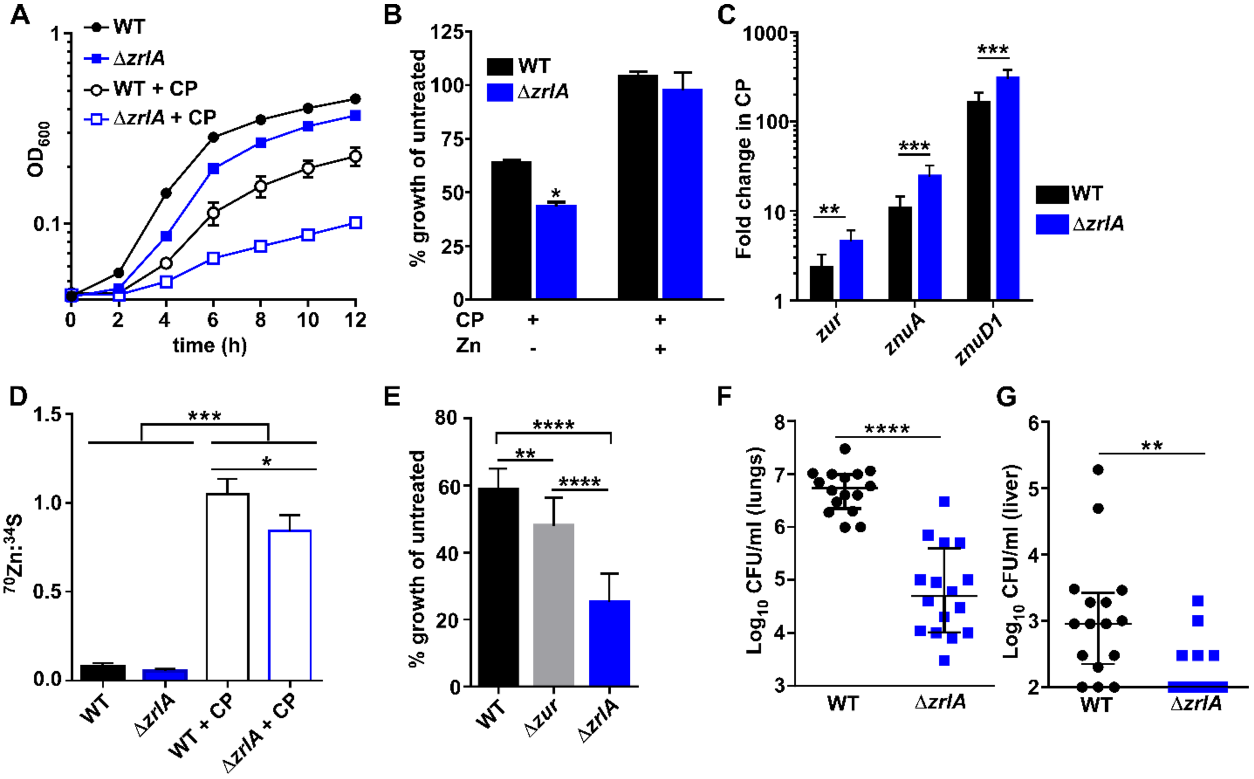

Figure 24. ZrlA is critical for full growth in low Zn and during infection. A) WT or Δ*zrlA* were grown ± 250 μg/ml CP with OD$_{600}$ monitored over time. B) Percent growth as determined by OD$_{600}$ at eight hours following growth in 250 μg/ml CP ± 50 μM ZnCl$_2$ compared to untreated strains. * $p < 0.05$ as determined by Student's *t* test from three independent experiments, mean ± SD. C) qRT-PCR analysis was performed on WT or Δ*zrlA* following growth in 250 μg/ml CP. ** $p < 0.01$, *** $p < 0.001$ as determined by Student's *t* test from three independent experiments, mean ± SD. D) Cellular ^{70}Zn was quantified by ICP-MS and normalized to ^{34}S for WT and Δ*zrlA*. * $p < 0.05$, *** $p < 0.001$ as determined by one-way ANOVA with Tukey multiple comparisons test from three independent experiments, mean ± SD. E) Percent growth as determined by OD$_{600}$ at six hours for WT, Δ*zur*, or Δ*zrlA* grown in 0.01 % SDS/0.1 mM EDTA relative to untreated strains. ** $p < 0.01$, **** $p < 0.0001$ as determined by one-way ANOVA with Tukey multiple comparisons test from three independent experiments, mean ± SD. F) Mice were intranasally infected with a 1:1 mixture of WT and Δ*zrlA*, and bacterial burdens were assessed at 36 hpi in the lungs. **** $p < 0.0001$ as determined by Mann-Whitney U test. G) WT and Δ*zrlA* bacterial burdens recovered from the liver at 36 hpi. ** $p < 0.01$ as determined by Mann-Whitney U test, error bars are median ± interquartile range ($n = 16$).

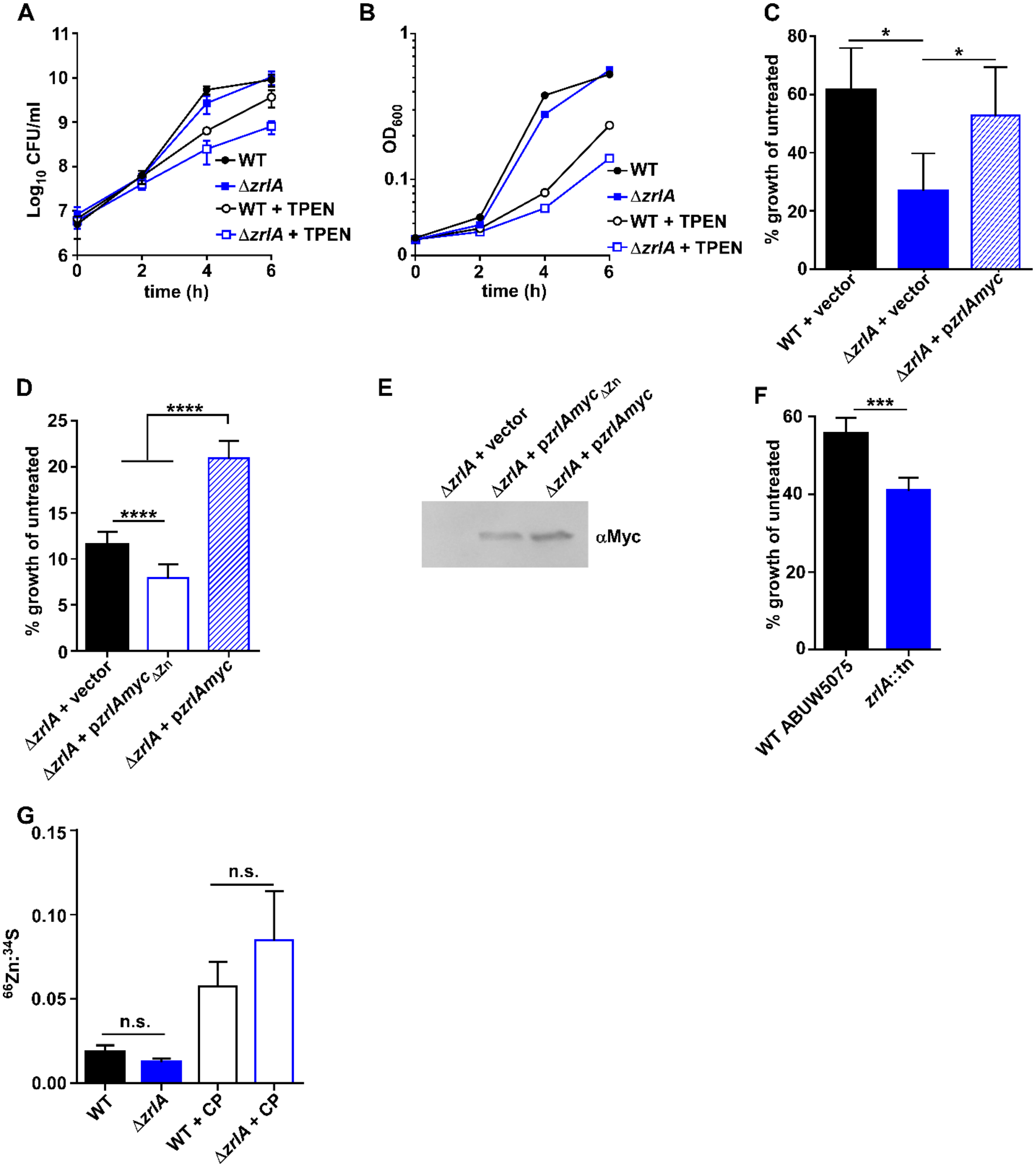

Figure 25. ZrlA is critical for full growth in low Zn. A) Colony forming units (CFU) were monitored over time for WT or Δ*zrlA* ± 40 μM TPEN. B) WT or Δ*zrlA* growth over time ± 40 μM TPEN as determined by OD_{600}. C) Growth of WT + vector, Δ*zrlA* + vector, or Δ*zrlA* + p*zrlAmyc* was monitored in the presence of 250 μg/ml calprotectin. Graph depicts percent growth at eight hours compared to untreated strains. * $p < 0.05$ as determined by Student's *t* test from three independent experiments, mean ± SD. D) Δ*zrlA* + vector, Δ*zrlA* + p*zrlAmyc*$_{\Delta Zn}$, or Δ*zrlA* + p*zrlAmyc* was monitored over time ± 40 μM TPEN. Graph depicts percent growth at eight hours

compared to untreated strains. **** $p < 0.0001$ as determined by Student's *t* test from three independent experiments, mean ± SD. E) Immunoblot on protein lysates from Δ*zrlA* + vector, Δ*zrlA* + p*zrlAmyc*$_{\Delta\mathrm{Zn}}$, or Δ*zrlA* + p*zrlAmyc* (20 μg protein/lane). F) *A. baumannii* strain ABUW5075 or a transposon mutant with an insertion in *zrlA* was grown ± 20 μM TPEN. Graph depicts percent growth at eight hours compared to untreated strains. *** $p < 0.001$ as determined by Student's *t* test from three independent experiments, mean ± SD. G) Total cellular ^{66}Zn was quantified in WT or Δ*zrlA* ± 250 μg/ml calprotectin by ICP-MS. n.s. = no significant difference as determined by one-way ANOVA with Tukey multiple comparisons test from three independent experiments, mean ± SD.

ZrlA is critical for surviving antibiotic exposure

To test if ZrlA provides a fitness advantage upon exposure to other cellular stressors such as antibiotics, WT and Δ*zrlA* *A. baumannii* were exposed to sub-inhibitory concentrations of several antibiotic classes. Incubation of these strains with antibiotics revealed that Δ*zrlA* exhibits increased sensitivity to several different antimicrobial molecules, including β-lactams, tetracyclines, polymyxins, and vancomycin (**Figure 26A-D**). WT and Δ*zrlA* *A. baumannii* were then subjected to low level Zn starvation and exposed to antibiotics. We found that the β-lactam antibiotic carbenicillin synergized with Zn restriction to inhibit *A. baumannii* growth, and the Δ*zrlA* strain remained more sensitive compared to the WT strain (**Figure 26E, Figure 27A**). Surprisingly, low level Zn starvation coupled with exposure to polymyxin B decreased antibiotic efficacy and permitted more *A. baumannii* growth compared to polymyxin B alone (**Figure 26F**). The Δ*zur* mutant is also sensitive to carbenicillin (**Figure 27B**), despite improved outer membrane barrier function compared to the Δ*zrlA* mutant (**Figure 24E**). These results illustrate that ZrlA contributes to antibiotic resistance in *A. baumannii* and that Zn availability alters antibiotic efficacy in a class-dependent manner.

We next evaluated whether inactivation of *zrlA* improves antibiotic efficacy during *A. baumannii* pneumonia. To test this, mice were intranasally inoculated with WT and Δ*zrlA* *A. baumannii* and administered either meropenem, a β-lactam antibiotic frequently used to treat *A. baumannii* infections, or a vehicle control at 0, 12, and 24 hpi. At 36 hpi, mice were humanely euthanized, and bacterial CFU were enumerated. Meropenem significantly reduced WT *A. baumannii* bacterial burdens in the lungs (**Figure 26G**). Strikingly, Δ*zrlA* burdens were further reduced with meropenem treatment (**Figure 26G,H**), and this reduction in burden was not due to the presence of the antibiotic marker in the mutant strain (**Figure 27C**). These results demonstrate that targeting ZrlA has the potential to increase the efficacy of existing antimicrobials against *A. baumannii*.

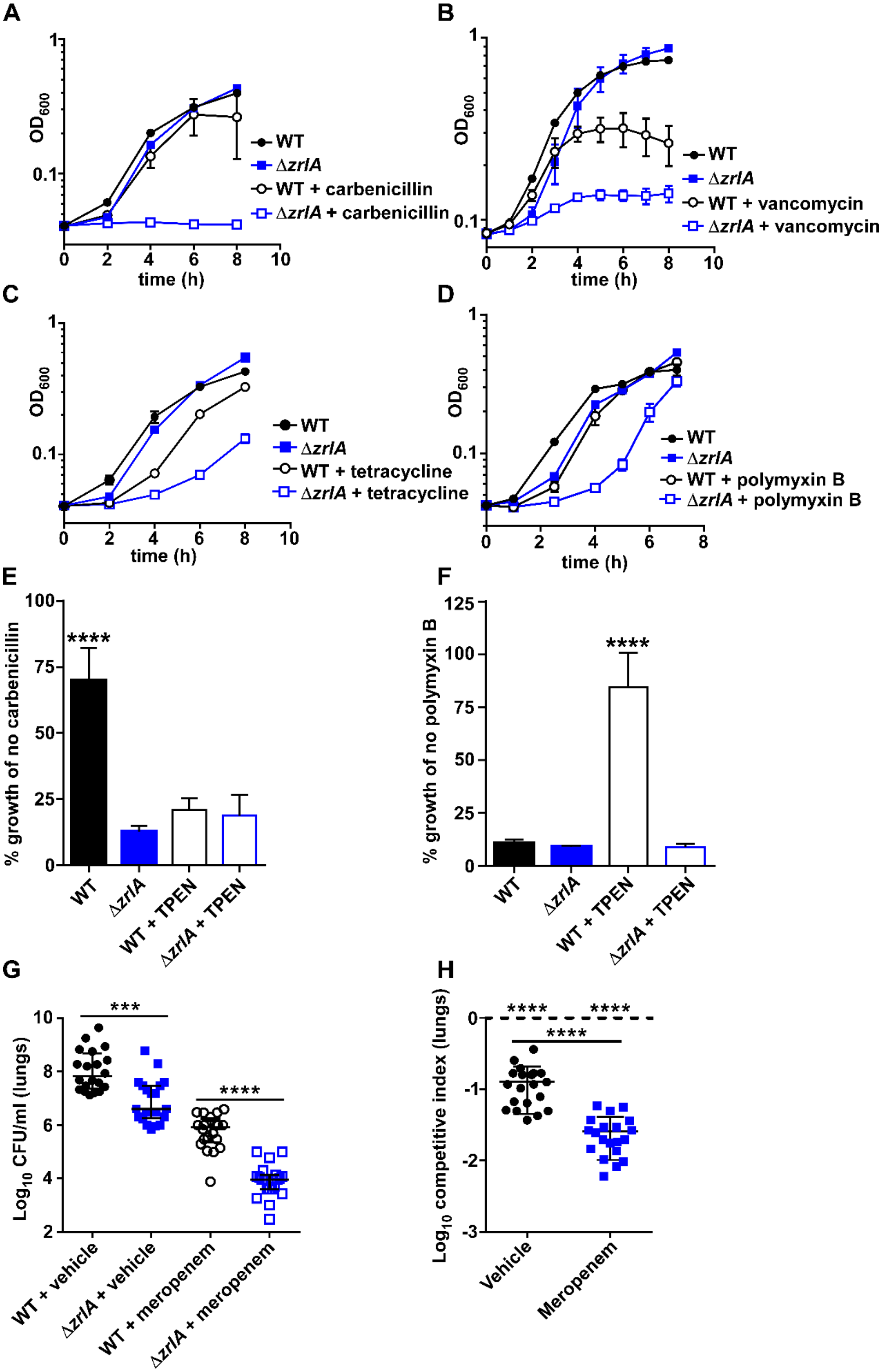

Figure 26. ZrlA is required for overcoming antibiotic exposure *in vitro* and *in vivo*. WT and Δ*zrlA* were grown A) ± carbenicillin, B) ± vancomycin, C) ± polymyxin B, D) ± tetracycline with OD_{600} monitored over time. E) WT and Δ*zrlA* were grown in the presence of carbenicillin ± TPEN with

OD_{600} monitored over time; data depict growth at eight hours relative to growth with no carbenicillin. **** $p < 0.0001$ as determined by one-way ANOVA with Tukey multiple comparison's test from three independent experiments, mean ± SD. F) WT and Δ*zrlA* were grown in the presence of polymyxin B ± TPEN with OD_{600} monitored over time; data depict growth at 24 hours relative to growth with no polymyxin B. **** $p < 0.0001$ as determined by one-way ANOVA with Tukey multiple comparisons test from three independent experiments, mean ± SD. G) WT or Δ*zrlA* bacterial burdens recovered from the lungs at 36 hpi. *** $p < 0.001$, **** $p < 0.0001$ as determined by Mann-Whitney U test, error bars are median ± interquartile range ($n = 20$). H) Competitive index ([input Δ*zrlA*/WT])[output Δ*zrlA*/WT]) in the lungs at 36 hpi. **** $p < 0.0001$ as determined by Student's *t* test with arbitrary value of 1 or between treatments, error bars are median ± interquartile range ($n = 20$).

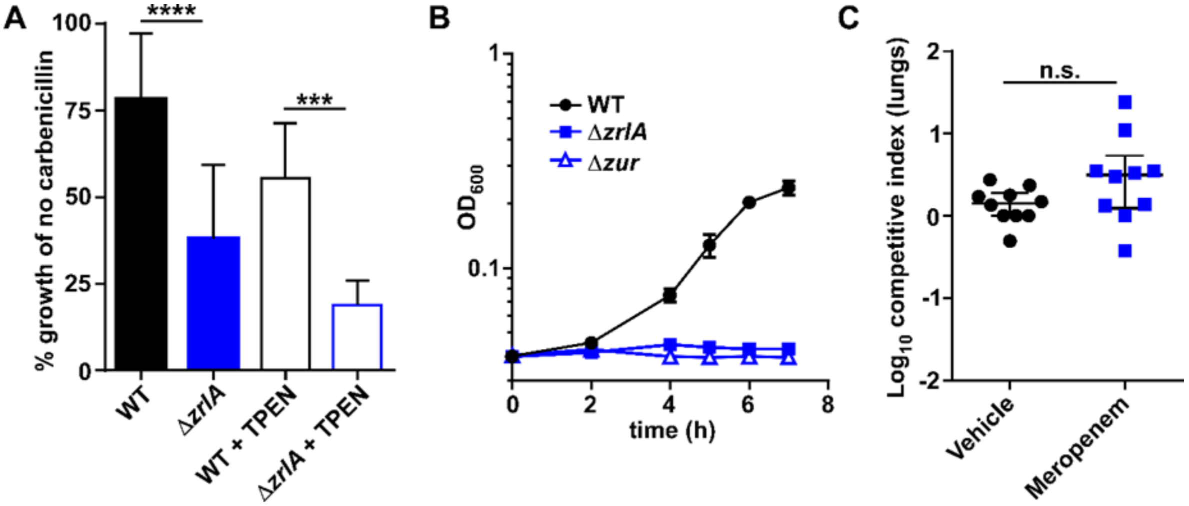

Figure 27. *zrlA* is required for overcoming antibiotic exposure. A) WT or Δ*zrlA* was grown with 3.125 μg/ml carbenicillin ± 20 μM TPEN with OD_{600} monitored over time. Data depict growth at eight hours relative to no carbenicillin treatment. *** $p < 0.001$, **** $p < 0.0001$ as determined by one-way ANOVA with Tukey multiple comparisons test from three independent experiments, mean ± SD. B) WT, Δ*zur*, or Δ*zrlA* was grown in the presence of 6.25 Δg/ml carbenicillin with OD_{600} monitored over time. C) Mice were intranasally infected with a 1:1 mixture of an unmarked and marked Δ*zrlA* strain and intraperitoneally administered meropenem (12.5 mg/kg) or vehicle at 12 hour intervals post-infection (t = 0, 12, 24 hpi). Data depict the competitive index of unmarked *zrlA* mutant: marked *zrlA* mutant in the lungs at 36 hpi. n.s. = no significant difference as determined by Student's *t* test (*n* = 10).

Discussion

Overcoming nutrient metal limitation is a requirement for bacterial pathogens to survive and cause disease. In *A. baumannii*, Zn starvation promotes upregulation of the *znuABCD* Zn uptake system and the predicted Zn metallochaperone *zigA* (Hood et al., 2012; Mortensen et al., 2014; Nairn et al., 2016). However, the capacity of *A. baumannii* to elaborate Zn acquisition systems while continuing cellular division requires the maintenance of the cell envelope. *A. baumannii* coordinates its response to Zn starvation with resistance to extracellular stressors through the action of ZrlA. ZrlA is required to maintain proper membrane barrier function and contributes to nutrient Zn acquisition. Antibiotics are more efficacious against a strain lacking *zrlA* both *in vitro* and in an animal model of *A. baumannii* pneumonia, suggesting that ZrlA inhibitors may improve therapeutic treatments during infection with *A. baumannii*.

Bacterial cell envelope maintenance is a dynamic process involving many enzymes and pathways, and the ability to modify the envelope promotes infection (Guo et al., 1997; Sycuro et al., 2010). Given the essentiality of the envelope for viability and pathogenesis, functional redundancy is common among envelope-modifying proteins, particularly among PG-modifying enzymes. While in-depth studies investigating PG biosynthesis and maintenance in *A. baumannii* are lacking, functional redundancy among D,D-CPases in *E. coli* is well-described (Peters et al., 2016). This redundancy may allow bacteria to utilize different subsets of D,D-CPases to adapt to unique environments (Ghosh et al., 2008). We identified four putative D,D-CPases in the *A. baumannii* genome; however, a large portion of *A. baumannii* genes remains unannotated, and therefore the existence of others cannot be excluded. Of these four putative D,D-CPases, *zrlA* is the only one that is induced during Zn starvation, and ZrlA is a Zn-binding peptidase. Some M15 family peptidases also have multiple enzymatic activities, including dipeptidase, transpeptidase, and endopeptidase activity, which suggests ZrlA may have additional enzymatic functions that contribute to muropeptide abundances detected in our analyses (Podmore and Reynolds, 2002; Stefanova et al., 2004). We predict that the other D,D-CPases in *A. baumannii* are induced in unique niches and that this likely contributes to the notable ability of pathogenic and nonpathogenic *Acinetobacter* species to persist in diverse environments.

Our observation the Δ*zrlA* strain accumulates ethidium bromide at a faster rate than WT *A. baumanniii* suggests that the Δ*zrlA* mutant has increased cellular permeability, although the contribution of bacterial efflux pumps to this phenotype was unexplored. We also discovered that the Δ*zrlA* strain is defective in Zn uptake despite overexpression of Zn acquisition genes. We suggest that the activity of ZrlA promotes more efficient Zn uptake through PG modification. While we have not shown a direct effect on membrane localization of the Zn acquisition machinery, other large membrane-anchored molecular structures such as secretion systems require PG modification for effective elaboration; this, in turn, suggests similar cell wall changes may be required to elaborate transition metal uptake systems (Dijkstra and Keck, 1996; Scheurwater and Burrows, 2011).

Zn availability modulates antibiotic efficacy, where the β-lactam antibiotic carbenicillin is more efficacious in low Zn environments. However, polymyxin B is less effective in Zn-limited conditions, which is consistent with previous observations that *Pseudomonas aeruginosa* is less susceptible to polymyxin B when other cations are restricted and also suggests Zn may be an important metal associated with the *A. baumannii* cell envelope (Nicas and Hancock, 1983) (Brown and Melling, 1969). These observations also suggest that changes in antibiotic efficacy may in part be driven by nutrient Zn availability and the capacity of pathogenic bacteria to alter local metal levels. We previously observed that during *A. baumannii* sepsis the host actively restricts ferrous iron, which is consistent with numerous reports that the host limits iron availability during infection (Aron et al., 2017; Schade and Caroline, 1946; Weinberg, 1974; Wright et al., 1981). Zn is also restricted from pathogens; only 0.1 % of total body Zn is located in the plasma, and this percentage is reduced during inflammation through sequestration by metal-binding proteins and through Zn transporters promoting tissue metal accumulation (Aydemir et al., 2012; Haase and Rink, 2014). However, this metal sequestration is not uniform, and bacteria may experience different metal levels within the host (Cassat et al., 2018). Therefore, microenvironments within the host can alter bacterial metabolic processes in a way that may change drug efficacy, so multifaceted approaches to target *A. baumannii* infections may be a long-term solution to combat multi-drug resistance.

This work demonstrates that ZrlA is induced during metal starvation, contributes to cell envelope maintenance, and it is critical for *A. baumannii* to survive exposure to antibiotics. Moreover, ZrlA contributes to the ability of *A. baumannii* to overcome Zn starvation and survive within the metal-restricted environment of a vertebrate host. Finally, we identified that antibiotics are more efficacious at treating *A. baumannii* infections in the absence of *zrlA*. These data highlight an exciting intersection between bacterial cell physiology, PG remodeling, and metal acquisition strategies, and they underscore the therapeutic potential of targeting bacterial metal acquisition systems to treat infections.

References

Ammendola, S., Pasquali, P., Pistoia, C., Petrucci, P., Petrarca, P., Rotilio, G., and Battistoni, A. (2007). High-affinity Zn2+ uptake system ZnuABC is required for bacterial zinc homeostasis in intracellular environments and contributes to the virulence of *Salmonella enterica*. *Infection and immunity 75*, 5867-5876.

Antunes, L.C., Visca, P., and Towner, K.J. (2014). *Acinetobacter baumannii*: evolution of a global pathogen. *Pathog Dis 71*, 292-301.

Aron, A.T., Heffern, M.C., Lonergan, Z.R., Vander Wal, M.N., Blank, B.R., Spangler, B., Zhang, Y., Park, H.M., Stahl, A., Renslo, A.R., *et al.* (2017). *In vivo* bioluminescence imaging of labile iron accumulation in a murine model of *Acinetobacter baumannii* infection. *Proceedings of the National Academy of Sciences of the United States of America 114*, 12669-12674.

Aydemir, T.B., Chang, S.M., Guthrie, G.J., Maki, A.B., Ryu, M.S., Karabiyik, A., and Cousins, R.J. (2012). Zinc transporter ZIP14 functions in hepatic zinc, iron and glucose homeostasis during the innate immune response (endotoxemia). *PloS one 7*, e48679.

Baker, T.M., Nakashige, T.G., Nolan, E.M., and Neidig, M.L. (2017). Magnetic circular dichroism studies of iron(ii) binding to human calprotectin. *Chem Sci 8*, 1369-1377.

Baumann, P. (1968). Isolation of *Acinetobacter* from soil and water. *Journal of bacteriology 96*, 39-42.

Blaby-Haas, C.E., Furman, R., Rodionov, D.A., Artsimovitch, I., and de Crecy-Lagard, V. (2011). Role of a Zn-independent DksA in Zn homeostasis and stringent response. *Molecular microbiology 79*, 700-715.

Boll, J.M., Crofts, A.A., Peters, K., Cattoir, V., Vollmer, W., Davies, B.W., and Trent, M.S. (2016). A penicillin-binding protein inhibits selection of colistin-resistant, lipooligosaccharide-deficient *Acinetobacter baumannii*. *Proceedings of the National Academy of Sciences of the United States of America.*

Brown, M.R., and Melling, J. (1969). Role of divalent cations in the action of polymyxin B and EDTA on *Pseudomonas aeruginosa*. *J Gen Microbiol 59*, 263-274.

Brown, P.J., de Pedro, M.A., Kysela, D.T., Van der Henst, C., Kim, J., De Bolle, X., Fuqua, C., and Brun, Y.V. (2012). Polar growth in the Alphaproteobacterial order Rhizobiales. *Proceedings of the National Academy of Sciences of the United States of America 109*, 1697-1701.

Cassat, J.E., Moore, J.L., Wilson, K.J., Stark, Z., Prentice, B.M., Van de Plas, R., Perry, W.J., Zhang, Y., Virostko, J., Colvin, D.C., *et al.* (2018). Integrated molecular imaging reveals tissue heterogeneity driving host-pathogen interactions. *Sci Transl Med 10*.

Corbin, B.D., Seeley, E.H., Raab, A., Feldmann, J., Miller, M.R., Torres, V.J., Anderson, K.L., Dattilo, B.M., Dunman, P.M., Gerads, R., *et al.* (2008). Metal chelation and inhibition of bacterial growth in tissue abscesses. *Science 319*, 962-965.

Corwin, D.F., R.; Koch, S. (1987). 4-Coordinate and 5-Coordinate Cobalt (II) Thiolate Complexes - Models for the Catalytic Site of Alcohol Dehydrogenase. *Inorganic Chemistry 26*, 3079-3080.

Dalebroux, Z.D., Edrozo, M.B., Pfuetzner, R.A., Ressl, S., Kulasekara, B.R., Blanc, M.P., and Miller, S.I. (2015). Delivery of cardiolipins to the *Salmonella* outer membrane is necessary for survival within host tissues and virulence. *Cell Host Microbe 17*, 441-451.

Damo, S.M., Kehl-Fie, T.E., Sugitani, N., Holt, M.E., Rathi, S., Murphy, W.J., Zhang, Y., Betz, C., Hench, L., Fritz, G., *et al.* (2013). Molecular basis for manganese sequestration by calprotectin and roles in the innate immune response to invading bacterial pathogens. *Proceedings of the National Academy of Sciences of the United States of America 110*, 3841-3846.

Desrosiers, D.C., Bearden, S.W., Mier, I., Jr., Abney, J., Paulley, J.T., Fetherston, J.D., Salazar, J.C., Radolf, J.D., and Perry, R.D. (2010). Znu is the predominant zinc importer in *Yersinia pestis* during in vitro growth but is not essential for virulence. *Infection and immunity 78*, 5163-5177.

Dijkstra, A.J., and Keck, W. (1996). Peptidoglycan as a barrier to transenvelope transport. *Journal of bacteriology 178*, 5555-5562.

Doi, E., Shibata, D., and Matoba, T. (1981). Modified colorimetric ninhydrin methods for peptidase assay. *Anal Biochem 118*, 173-184.

Ducret, A., Quardokus, E.M., and Brun, Y.V. (2016). MicrobeJ, a tool for high throughput bacterial cell detection and quantitative analysis. *Nat Microbiol 1*, 16077.

Gaballa, A., and Helmann, J.D. (1998). Identification of a zinc-specific metalloregulatory protein, Zur, controlling zinc transport operons in *Bacillus subtilis*. *Journal of bacteriology 180*, 5815-5821.

Gallagher, L.A., Ramage, E., Weiss, E.J., Radey, M., Hayden, H.S., Held, K.G., Huse, H.K., Zurawski, D.V., Brittnacher, M.J., and Manoil, C. (2015). Resources for Genetic and Genomic Analysis of Emerging Pathogen *Acinetobacter baumannii*. *Journal of bacteriology 197*, 2027-2035.

Gattis, S.G., Hernick, M., and Fierke, C.A. (2010). Active site metal ion in UDP-3-O-((R)-3-hydroxymyristoyl)-N-acetylglucosamine deacetylase (LpxC) switches between Fe(II) and Zn(II) depending on cellular conditions. *The Journal of biological chemistry 285*, 33788-33796.

Gaynes, R., Edwards, J.R., and National Nosocomial Infections Surveillance, S. (2005). Overview of nosocomial infections caused by gram-negative bacilli. *Clin Infect Dis 41*, 848-854.

Ghosh, A.S., Chowdhury, C., and Nelson, D.E. (2008). Physiological functions of D-alanine carboxypeptidases in *Escherichia coli*. *Trends Microbiol 16*, 309-317.

Guo, L., Lim, K.B., Gunn, J.S., Bainbridge, B., Darveau, R.P., Hackett, M., and Miller, S.I. (1997). Regulation of lipid A modifications by *Salmonella* Typhimurium virulence genes phoP-phoQ. *Science 276*, 250-253.

Haase, H., and Rink, L. (2014). Multiple impacts of zinc on immune function. *Metallomics : integrated biometal science 6*, 1175-1180.

Harding, C.M., Hennon, S.W., and Feldman, M.F. (2018). Uncovering the mechanisms of *Acinetobacter baumannii* virulence. *Nat Rev Microbiol 16*, 91-102.

Hoang, T.T., Karkhoff-Schweizer, R.R., Kutchma, A.J., and Schweizer, H.P. (1998). A broad-host-range Flp-FRT recombination system for site-specific excision of chromosomally-located DNA sequences: application for isolation of unmarked *Pseudomonas aeruginosa* mutants. *Gene 212*, 77-86.

Hood, M.I., Mortensen, B.L., Moore, J.L., Zhang, Y., Kehl-Fie, T.E., Sugitani, N., Chazin, W.J., Caprioli, R.M., and Skaar, E.P. (2012). Identification of an *Acinetobacter baumannii* zinc acquisition system that facilitates resistance to calprotectin-mediated zinc sequestration. *PLoS pathogens 8*, e1003068.

Hunger, M., Schmucker, R., Kishan, V., and Hillen, W. (1990). Analysis and nucleotide sequence of an origin of DNA replication in *Acinetobacter calcoaceticus* and its use for *Escherichia coli* shuttle plasmids. *Gene 87*, 45-51.

Hunter, M.J., and Chazin, W.J. (1998). High level expression and dimer characterization of the S100 EF-hand proteins, migration inhibitory factor-related proteins 8 and 14. *The Journal of biological chemistry 273*, 12427-12435.

Juttukonda, L.J., Berends, E.T.M., Zackular, J.P., Moore, J.L., Stier, M.T., Zhang, Y., Schmitz, J.E., Beavers, W.N., Wijers, C.D., Gilston, B.A., *et al.* (2017). Dietary Manganese Promotes Staphylococcal Infection of the Heart. *Cell Host Microbe 22*, 531-542 e538.

Juttukonda, L.J., Chazin, W.J., and Skaar, E.P. (2016). *Acinetobacter baumannii* Coordinates Urea Metabolism with Metal Import To Resist Host-Mediated Metal Limitation. *mBio 7*.

Kehl-Fie, T.E., Chitayat, S., Hood, M.I., Damo, S., Restrepo, N., Garcia, C., Munro, K.A., Chazin, W.J., and Skaar, E.P. (2011). Nutrient metal sequestration by calprotectin inhibits bacterial superoxide defense, enhancing neutrophil killing of *Staphylococcus aureus*. *Cell Host Microbe 10*, 158-164.

Kuru, E., Hughes, H.V., Brown, P.J., Hall, E., Tekkam, S., Cava, F., de Pedro, M.A., Brun, Y.V., and VanNieuwenhze, M.S. (2012). *In Situ* probing of newly synthesized peptidoglycan in live bacteria with fluorescent D-amino acids. *Angew Chem Int Ed Engl 51*, 12519-12523.

Kuzmic, P. (1996). Program DYNAFIT for the analysis of enzyme kinetic data: application to HIV proteinase. *Analytical biochemistry 237*, 260-273.

Liechti, G.W., Kuru, E., Hall, E., Kalinda, A., Brun, Y.V., VanNieuwenhze, M., and Maurelli, A.T. (2014). A new metabolic cell-wall labelling method reveals peptidoglycan in *Chlamydia trachomatis*. *Nature 506*, 507-510.

Litzinger, S., Duckworth, A., Nitzsche, K., Risinger, C., Wittmann, V., and Mayer, C. (2010). Muropeptide rescue in *Bacillus subtilis* involves sequential hydrolysis by beta-N-acetylglucosaminidase and N-acetylmuramyl-L-alanine amidase. *Journal of bacteriology 192*, 3132-3143.

Liu, J.Z., Jellbauer, S., Poe, A.J., Ton, V., Pesciaroli, M., Kehl-Fie, T.E., Restrepo, N.A., Hosking, M.P., Edwards, R.A., Battistoni, A., *et al.* (2012). Zinc sequestration by the neutrophil protein calprotectin enhances *Salmonella* growth in the inflamed gut. *Cell Host Microbe 11*, 227-239.

Ma, Z., Gabriel, S.E., and Helmann, J.D. (2011). Sequential binding and sensing of Zn(II) by *Bacillus subtilis* Zur. *Nucleic acids research 39*, 9130-9138.

Malinverni, J.C., and Silhavy, T.J. (2009). An ABC transport system that maintains lipid asymmetry in the Gram-negative outer membrane. *Proceedings of the National Academy of Sciences of the United States of America 106*, 8009-8014.

Menard, R., Sansonetti, P.J., and Parsot, C. (1993). Nonpolar mutagenesis of the ipa genes defines IpaB, IpaC, and IpaD as effectors of Shigella flexneri entry into epithelial cells. *Journal of bacteriology 175*, 5899-5906.

Moffatt, J.H., Harper, M., Harrison, P., Hale, J.D., Vinogradov, E., Seemann, T., Henry, R., Crane, B., St Michael, F., Cox, A.D., *et al.* (2010). Colistin resistance in *Acinetobacter baumannii* is mediated by complete loss of lipopolysaccharide production. *Antimicrobial agents and chemotherapy 54*, 4971-4977.

Mortensen, B.L., Rathi, S., Chazin, W.J., and Skaar, E.P. (2014). *Acinetobacter baumannii* response to host-mediated zinc limitation requires the transcriptional regulator Zur. *Journal of bacteriology 196*, 2616-2626.

Nairn, B.L., Lonergan, Z.R., Wang, J., Braymer, J.J., Zhang, Y., Calcutt, M.W., Lisher, J.P., Gilston, B.A., Chazin, W.J., de Crecy-Lagard, V., *et al.* (2016). The Response of *Acinetobacter baumannii* to Zinc Starvation. *Cell Host Microbe 19*, 826-836.

Nakashige, T.G., Zygiel, E.M., Drennan, C.L., and Nolan, E.M. (2017). Nickel Sequestration by the Host-Defense Protein Human Calprotectin. *Journal of the American Chemical Society 139*, 8828-8836.

Nanamiya, H., Akanuma, G., Natori, Y., Murayama, R., Kosono, S., Kudo, T., Kobayashi, K., Ogasawara, N., Park, S.M., Ochi, K., *et al.* (2004). Zinc is a key factor in controlling alternation of two types of L31 protein in the *Bacillus subtilis* ribosome. *Molecular microbiology 52*, 273-283.

Nicas, T.I., and Hancock, R.E. (1983). Alteration of susceptibility to EDTA, polymyxin B and gentamicin in *Pseudomonas aeruginosa* by divalent cation regulation of outer membrane protein H1. *J Gen Microbiol 129*, 509-517.

Palmer, L.D., and Skaar, E.P. (2016). Transition Metals and Virulence in Bacteria. *Annu Rev Genet 50*, 67-91.

Patzer, S.I., and Hantke, K. (1998). The ZnuABC high-affinity zinc uptake system and its regulator Zur in *Escherichia coli*. *Molecular microbiology 28*, 1199-1210.

Peters, K., Kannan, S., Rao, V.A., Biboy, J., Vollmer, D., Erickson, S.W., Lewis, R.J., Young, K.D., and Vollmer, W. (2016). The Redundancy of Peptidoglycan Carboxypeptidases Ensures Robust Cell Shape Maintenance in *Escherichia coli*. *mBio 7*.

Podmore, A.H., and Reynolds, P.E. (2002). Purification and characterization of VanXY(C), a D,D-dipeptidase/D,D-carboxypeptidase in vancomycin-resistant *Enterococcus gallinarum* BM4174. *Eur J Biochem 269*, 2740-2746.

Rawlings, N.D., and Barrett, A.J. (1993). Evolutionary families of peptidases. *Biochem J 290 (Pt 1)*, 205-218.

Rayman, M.K., and MacLeod, R.A. (1975). Interaction of Mg-2+ with peptidoglycan and its relation to the prevention of lysis of a marine pseudomonad. *Journal of bacteriology 122*, 650-659.

Reyes-Caballero, H., Guerra, A.J., Jacobsen, F.E., Kazmierczak, K.M., Cowart, D., Koppolu, U.M., Scott, R.A., Winkler, M.E., and Giedroc, D.P. (2010). The metalloregulatory zinc site in *Streptococcus pneumoniae* AdcR, a zinc-activated MarR family repressor. *Journal of molecular biology 403*, 197-216.

Schade, A.L., and Caroline, L. (1946). An iron-binding component in human blood plasma. *Science 104*, 340.

Scheurwater, E.M., and Burrows, L.L. (2011). Maintaining network security: how macromolecular structures cross the peptidoglycan layer. *FEMS Microbiol Lett 318*, 1-9.

Stefanova, M.E., Tomberg, J., Davies, C., Nicholas, R.A., and Gutheil, W.G. (2004). Overexpression and enzymatic characterization of *Neisseria gonorrhoeae* penicillin-binding protein 4. *Eur J Biochem 271*, 23-32.

Stork, M., Bos, M.P., Jongerius, I., de Kok, N., Schilders, I., Weynants, V.E., Poolman, J.T., and Tommassen, J. (2010). An outer membrane receptor of *Neisseria meningitidis* involved in zinc acquisition with vaccine potential. *PLoS pathogens 6*, e1000969.

Sycuro, L.K., Pincus, Z., Gutierrez, K.D., Biboy, J., Stern, C.A., Vollmer, W., and Salama, N.R. (2010). Peptidoglycan crosslinking relaxation promotes *Helicobacter pylori*'s helical shape and stomach colonization. *Cell 141*, 822-833.

Trouillet, J.L., Chastre, J., Vuagnat, A., Joly-Guillou, M.L., Combaux, D., Dombret, M.C., and Gibert, C. (1998). Ventilator-associated pneumonia caused by potentially drug-resistant bacteria. *Am J Respir Crit Care Med 157*, 531-539.

Tucker, A.T., Nowicki, E.M., Boll, J.M., Knauf, G.A., Burdis, N.C., Trent, M.S., and Davies, B.W. (2014). Defining gene-phenotype relationships in *Acinetobacter baumannii* through one-step chromosomal gene inactivation. *mBio 5*, e01313-01314.

Vishniac, H.S. (1955). The nutritional requirements of isolates of *Labyrinthula spp. J. Gen. Microbiol*. *12*, 455-463.

Wang, T., Si, M., Song, Y., Zhu, W., Gao, F., Wang, Y., Zhang, L., Zhang, W., Wei, G., Luo, Z.Q., *et al.* (2015). Type VI Secretion System Transports Zn2+ to Combat Multiple Stresses and Host Immunity. *PLoS pathogens 11*, e1005020.

Weinberg, E.D. (1974). Iron and susceptibility to infectious disease. *Science 184*, 952-956.

Weinberg, E.D. (1975). Nutritional immunity. Host's attempt to withold iron from microbial invaders. *JAMA 231*, 39-41.

Whittington, D.A., Rusche, K.M., Shin, H., Fierke, C.A., and Christianson, D.W. (2003). Crystal structure of LpxC, a zinc-dependent deacetylase essential for endotoxin biosynthesis. *Proceedings of the National Academy of Sciences of the United States of America 100*, 8146-8150.

WHO (2017). Guidelines for the prevention and control of carbapenem-resistant Enterobacteriaceae, *Acinetobacter baumannii* and *Pseudomonas aeruginosa* in health care facilities. World Health Organization.

Wright, A.C., Simpson, L.M., and Oliver, J.D. (1981). Role of iron in the pathogenesis of *Vibrio vulnificus* infections. *Infection and immunity 34*, 503-507.

Wu, Z., Wright, G.D., and Walsh, C.T. (1995). Overexpression, purification, and characterization of VanX, a D-, D-dipeptidase which is essential for vancomycin resistance in *Enterococcus faecium* BM4147. *Biochemistry 34*, 2455-2463.

Zackular, J.P., Moore, J.L., Jordan, A.T., Juttukonda, L.J., Noto, M.J., Nicholson, M.R., Crews, J.D., Semler, M.W., Zhang, Y., Ware, L.B., *et al.* (2016). Dietary zinc alters the microbiota and decreases resistance to *Clostridium difficile* infection. *Nat Med*.

CHAPTER IV

HISTIDINE UTILIZATION IS A CRITICAL DETERMINANT OF *ACINETOBACTER* VIRULENCE

Introduction

Amino acids are fundamental components of life, and as such, their concentrations in biological systems are tightly regulated. While humans require several amino acids from dietary sources, many bacterial species are capable of fully synthesizing all 20 genetically encoded amino acids. Among these, histidine (His) is the fourth most energetically expensive amino acid to synthesize (Akashi and Gojobori, 2002). His is derived from 5’-phosphoribosyl 1-pyrophosphate (PRPP), which also serves as a precursor for other critical pathways, including purine biosynthesis (Ingle, 2011). However, when His is in excess, many bacteria possess mechanisms to catabolize the amino acid for energy generation via the His utilization (Hut) system. The core enzymes are conserved across domains of life and results in ammonia, glutamate, and the one-carbon compound formate or formamide depending on the organism (Bender, 2012). Fundamental biological discoveries have been uncovered through investigations into the Hut system, including the discovery of catabolite repression and the identification of the master regulator CodY in *Bacillus subtilis* (Magasanik, 1961; Sonenshein, 2007). The system is controlled through a variety of transcriptional regulators, with the HutC repressor serving as one of the main regulators for the system (Allison and Phillips, 1990; Brill and Magasanik, 1969; Schwacha and Bender, 1990). Despite the widespread occurrence of the Hut system in bacteria, the contribution of His catabolism and the Hut system to bacterial pathogenesis is essentially undefined (Bender, 2012).

One organism that encodes a Hut system is the opportunistic Gram-negative bacterial pathogen *Acinetobacter baumannii*. *A. baumannii* is a frequent cause of nosocomial infections, including wound and burn infections, urinary tract infections, and ventilator-associated pneumonia (Peleg et al., 2008). The ability of *A. baumannii* to cause disease is partly driven by its metabolic and genetic plasticity (Harding et al., 2018). These features have led to the emergence of multi-drug resistant *A. baumannii* infections and prompted the World Health Organization (WHO) and the Centers for Disease Control and Prevention (CDC) to list *A. baumannii* as a top threat for which new therapeutics are needed (CDC, 2019; WHO, 2017).

We previously demonstrated that His is capable of forming complexes with nutrient metal zinc (Zn), and that *A. baumannii* uses the Hut system to degrade His, which liberates Zn for other biological processes (Nairn et al., 2016). However, the broader physiological role for the Hut system in *A. baumannii* is unexplored. Herein, we dissect aspects of the *A. baumannii* Hut system and discovered that the system is uniquely conserved in pathogenic *Acinetobacter* and no longer present in the environmental *Acinetobacter baylyi*. Additionally, we define HutC as a transcriptional repressor of *A. baumannii hut*, and we show that the first enzyme in the Hut system, HutH, serves as an important factor for His nitrogen source utilization. Finally, we determined that HutH is critical for *A. baumannii* lung colonization and dissemination to the liver, which suggests that His serves as a nitrogen source during *A. baumannii* pneumonia.

Materials and Methods

Bacterial strains and culture conditions

Experiments were performed using *Acinetobacter baumannii* strain ATCC 17978 and its derivatives unless otherwise noted. Transposon mutants in the *A. baumannii* ABUW5075 background were purchased from the University of Washington *A. baumannii* mutant library, and transposon insertion was confirmed by PCR. *Acinetobacter nosocomialis* M2 was kindly provided by Mario Feldman. *Acinetobacter baylyi* ADP1 was purchased from ATCC. Cloning was performed in *E. coli* DH5α, and protein expression was performed in *E. coli* BL21 (DE3). All experiments involving liquid cultures were performed in lysogeny broth (LB) at 37 ˚C with aeration unless otherwise stated.

Bacterial mutant generation

The Δ*hutH*, Δ*hutU*, Δ*hutT*, Δ*hutI*, and Δ*hutG* strains were generated previously (Nairn et al., 2016). To generate the *hutC*::km (*A1S_3409*) strain (Δ*hutC*), approximately 1000 base pairs of DNA in the 5' and 3' flanking regions surrounding the open reading frame were amplified from *A. baumannii* genomic DNA, and the kanamycin resistance gene *aph* was amplified from pUC18K1 (Menard et al., 1993). The three PCR products were joined together using Gibson assembly into pFLP2 and sequence-verified (Hoang et al., 1998). pFLP2 was then electroporated into *A. baumannii*, plated onto LB agar with kanamycin at 40 μg/ml (Km40), and grown overnight at 37 °C. Transformants were patched to LBKm40 or LB agar with 10 % sucrose to isolate Km-resistant (Km^R) and sucrose-sensitive merodiploids. Merodiploid strains were grown in LB overnight at 37 °C to resolve the plasmid. Cultures were serially diluted, plated on LB agar with 10 % sucrose, and incubated at 37 °C overnight. The resulting Km^R sucrose-resistant strains were screened for loss of *hutC* and replacement with *aph* by multiple PCR reactions. Relevant primers are listed in **Table 7**.

Growth in minimal media

Overnight bacterial cultures were diluted 1:50 into 1X M9 salts with no nitrogen source added (33.7 mM Na_2HPO_4, 22 mM KH_2PO_4, 8.55 mM NaCl) for 1.5 hours at 37 C, 180 rpm shaking. Cultures were then plated 1:100 in a 96 well plate into M9 minimal media (1X M9 salts, 1 mM $MgSO_4$, 0.3 mM $CaCl_2$, 1X Vishniac's trace metal mix +/- 9.35 mM NH_4Cl with L-Histidine and/or fumarate as the sole carbon and/or nitrogen source (0.5% w/v). Growth was monitored over time by monitoring the optical density at 600 nm (OD_{600}) on an EPOCH 2 microplate reader (Biotek).

HutC expression and purification

The HutC open reading frame was cloned into pET15b with an N-terminal His tag (pET15bHutC) transformed into *E. coli* BL21 DE3 pREL. Overnight cultures of pET15bHutC were inoculated into terrific broth supplemented with carbenicillin (50 μg/ml) and chloramphenicol (34 μg/ml) and grown to an OD of 0.5. Cells were induced with 0.5 mM IPTG and grown for an additional 5 hours. Cultures were pelleted, and pellets were frozen at -80 ˚C until processing. To purify protein, pellets were thawed on ice in lysis buffer (50 mM NaH_2PO_4, 300 mM NaCl, 20 mM imidazole, 1 mg/ml lysozyme) and lysed using an Emulsiflex with 5 passes at 20,000 psi. Insoluble material was removed by spinning lysates at 8,000 xg for 10 min followed by ultrcentrifugation at 100,000 xg for 1 hour at 4 ˚C. Supernatants were collected and applied to Ni-NTA columns (Qiagen) pre-equilibrated with lysis buffer. The protein loaded column was washed with wash buffer (50 mM NaH_2PO_4, 300 mM NaCl, 25 mM imidazole), and protein was eluted with an imidazole gradient ranging from 50 mM to 300 mM. Protein purity was confirmed by SDS-PAGE and Coomassie staining. Purified HutC was dialyzed overnight into buffer containing 20 mM Tris-HCl pH 8,150 mM NaCl. Following dialysis, protein samples were mixed with glycerol to 10 % and frozen at -80 ˚C.

Quantitative RT-PCR

Overnight cultures of *A. baumannii* were diluted 1:5000 in LB and grown to mid-exponential phase. Bacterial cultures were then mixed with an equal volume of acetone:ethanol (1:1) prior to storage at -80 ˚C until processing. For RNA extraction, cells were pelleted and resuspended in LETS buffer (0.1 M LiCl, 0.01 M Na_2EDTA, 0.01 M Tris-HCl pH 7.4, 0.2 % SDS) and lysed using Lysis Matrix B tubes (MP Biologicals) and a FastPrep-24 (MP) bead beater. Samples were heated to 55 °C for 5 min and pelleted at 15,000 rpm for 10 min. The top phase was combined with TRIzol and incubated at room temperature for 5 min. Chloroform was mixed with each sample, incubated for 3 min, and centrifuged for 15 min at 4 °C at 15,000 rpm. The top layer was collected, and RNA was precipitated with isopropyl alcohol for 10 min at room temperature. Samples were spun for 10 min at 15,000 rpm at 4 ˚C. Supernatant was removed, and pellets were washed with 70 % ethanol. Pellet was dissolved in water, and DNA contamination was removed by adding RQ1 and RQ1 buffer (Promega), and RNAse inhibitor (Thermo Fisher Scientific) for an incubation period of 2 h at 37 ˚C. After DNAse treatment, RNA was purified using the RNeasy Mini Kit (Qiagen) following the manufacturer's protocol. RNA was quantified, and 2 mg of RNA was used for cDNA synthesis using M-MLV reverse transcriptase and buffer (Thermo Fisher Scientific) and mixing in random hexamers (Thermo Fisher Scientific), and dNTP (Thermo Fisher Scientific). cDNA synthesis and purity was confirmed by PCR using 16s primers (*r01*) (Mortensen et al., 2014) with a "no RT" control. Synthesized cDNA was diluted 1:50 for quantitative RT-PCR using iQ SYBR Green Supermix (Biorad) on a Biorad CFX96 Real-Time thermocycler. Relative expression was determined using the $^{\Delta\Delta}$CT as previously described (Mortensen et al., 2014). Relevant primers were previously published (Nairn et al. 2016) or are listed in **Table 7**.

Electrophoretic mobility shift assays

EMSAs were performed generally as described previously (Juttukonda et al., 2019). Briefly, DNA probes were generated after amplification from genomic *A. baumannii* DNA using KAPA polymerase and appropriate primers (**Table** 7) and processed using a PCR Cleanup Kit (Thermo Fisher Scientific). Equimolar amounts of various DNA probes (300 fmol) were incubated with recombinant His-tagged HutC in binding buffer (20 mM Tris-HCl pH 7.5, 500 mM NaCl, 2.5 mM $MgCl_2$, 0.45 mM EDTA, 0.05 % Nonidet P-40, 10 % glycerol) for 30 min at 37 ˚C. Following incubation, samples were mixed with 6X EMSA loading dye (15 % glycerol, 0.25 % bromophenol blue, 0.25 % xylene cyanol in 1X TBE). Samples were loaded onto pre-run 5 % TBE gels (Biorad) and ran at 100 volts until dye front reached the gel bottom. Gels were stained with SYBR green (Invitrogen) in 0.5X TBE for 20 minutes, washed twice with Millipore water, and imaged on a Biorad ChemiDoc MP system with a SYBR green filter applied.

Mouse model of *A. baumannii* pneumonia

Eight to ten-week-old male (Δ*hutH* and Δ*hutU* infections) and female (Δ*hutI*, Δ*hutT*, and Δ*hutG* infections) C57BL6/J mice were purchased from Jackson Laboratories, and male *S100A9*$^{-/-}$ (CP$^{-/-}$) mice were bred in-house. Mice were housed with standard Vanderbilt University Medical Center (VUMC) facility chow and bedding with a 24-hour light-dark cycle. Mice were inoculated 1:1 with a mixture of WT and mutant *A. baumannii* strains totaling 3 x10^8 CFU in 40 μl PBS. At

36 hours post-infection, mice were euthanized, and CFU were enumerated in various organs following tissue homogenization and dilution plating on LB and LB Km 40. The limit of detection of this assay is 100 CFU/ml. All animal experiments were approved by the VUMC Institutional Care and Use Committee and conform to the policies and guidelines established by VUMC, the Animal Welfare Act, the National Institutes of Health, and the American Veterinary Medical Association.

Sequence analysis

A. baumannii ATCC 17978 protein sequences for components of the Hut system were obtained from the Kyoto Encyclopedia of Genes and Genomes (Skegg et al.) database. These sequences were used as the input for protein Basic Local Alignment Search Tool (BLAST) to find homologs in the following organisms: *Acinetobacter nosocomialis* M2, *Acinetobacter baylyi* ADP1, *Pseudomonas aeruginosa* PA14, and *Klebsiella pneumonia* ATCC 43816. These sequences were then aligned against *A. baumannii* ATCC 17978 using the EMBL pairwise sequence alignment tool, and percent protein identity was recorded.

Table 7. Oligonucleotides used in Chapter IV.

Name	**Sequence (5’ to 3’)**	**Description**
***hutC* mutant construction and confirmation**		
HutC FL1For	GGTTAAAAAGGATCGATCCTCTAG ACATCAAAACTTGAAAAATAGTG	Cloning into pFLP2, 5' flank, forward
HutC FL1 Rev	TAGTTAGTCACATATGAACAAATA CTCAAAAAGGCAG	Cloning into pFLP2, 5' flank, reverse
HutC Kan For	AGTATTTGTTCATATGTGACTAACT AGGAGGAATAAATG	Cloning into pFLP2, 3' flank, forward
HutC Kan Rev	ATCAATTCAACATATGTCATTATTC CCTCCAGGTAC	Cloning into pFLP2, 3' flank, reverse
HutC FL2 For	GGAATAATGACATATGTTGAATTG ATCAGGGCCG	Cloning into pFLP2 for Km cassette from pUC18-k1, forward
HutC FL2 Rev	AAGTTCCTATTCTCTAGGGGGATC CTTCTGCAACGTCCGGATC	Cloning into pFLP2 for Km cassette from pUC18-k1, reverse
EMSA probes		
hutC_EMSA_R	AAC AAA TAC TCA AAA AGG CAG CAG GCA	Upstream of *hutC*
hutC_EMSA_F1	GGC ACT GGC TTA GCA GAA ATA ACT	Upstream of *hutC*
hutU_EMSA_R	ACG CAA TGG GGC TTC AGT TAA	Upstream of *hutU*
hutU_EMSA_F1	TAC GAG CAA GCC TCT TCA CGC	Upstream of *hutU*
A1S_3412_F	CCA CGC GAG ATT TGG TCC AA	Internal to *A1S_3412*
A1S_3412_R	GCT TGG CCT TTA GTC GCC C	Internal to *A1S_3412*

Results

The Hut system is conserved in pathogenic *Acinetobacter*

The Hut system is comprised of four core enzymes, HutHUIG, that facilitate the conversion of His to glutamate that can be further modified to generate α-ketoglurate and enter the TCA cycle (**Figure 28A**). In bacteria, there are two general pathways defined for Hut systems, termed Pathway 1 and Pathway 2 (**Figure 28A**) (Bender, 2012). Both pathways yield glutamate and ammonia, but Pathway 1 generates formamide while Pathway 2 generates a second molecule of ammonia and formate. While many bacteria are able to utilize His as a carbon source, its occurrence is not universal, with *Escherichia coli* being a notable model organism unable to catabolize His (Bender, 2012). In order to determine the relative conservation of the Hut system in *Acinetobacter* relative to other Proteobacteria, genomic analyses and protein alignments were performed using EMBL Needle. *A. baumannii* ATCC 17978 was used as the basis for all alignments. Upon analyzing the genomes of pathogenic and non-pathogenic *Acinetobacter* species, it was identified that the closely related pathogenic species *Acinetobacter nosocomialis* possesses an intact Hut system, with the core enzymes and putative regulators having >90% amino acid identity to *A. baumannii* (**Figure 28B**). Conversely, the environmental species *Acinetobacter baylyi* does not possess a complete Hut system. Interestingly, though, the His transporter HutT appears to be conserved in *A. baylyi* with >88% amino acid identity (**Figure 28B**). Additionally, the *A. baylyi* genome possesses short (100 base pair) genomic remnants encoding the enzymes HutU, HutH, and HutG surrounding the gene encoding HutT (**Figure 28B**). These findings imply that *A. baylyi* specifically lost the ability to catabolize His, while pathogenic *Acinetobacter* maintained a functional Hut system, suggesting that unique environmental pressures selected for the loss and/or maintenance of the Hut system in these closely related organisms.

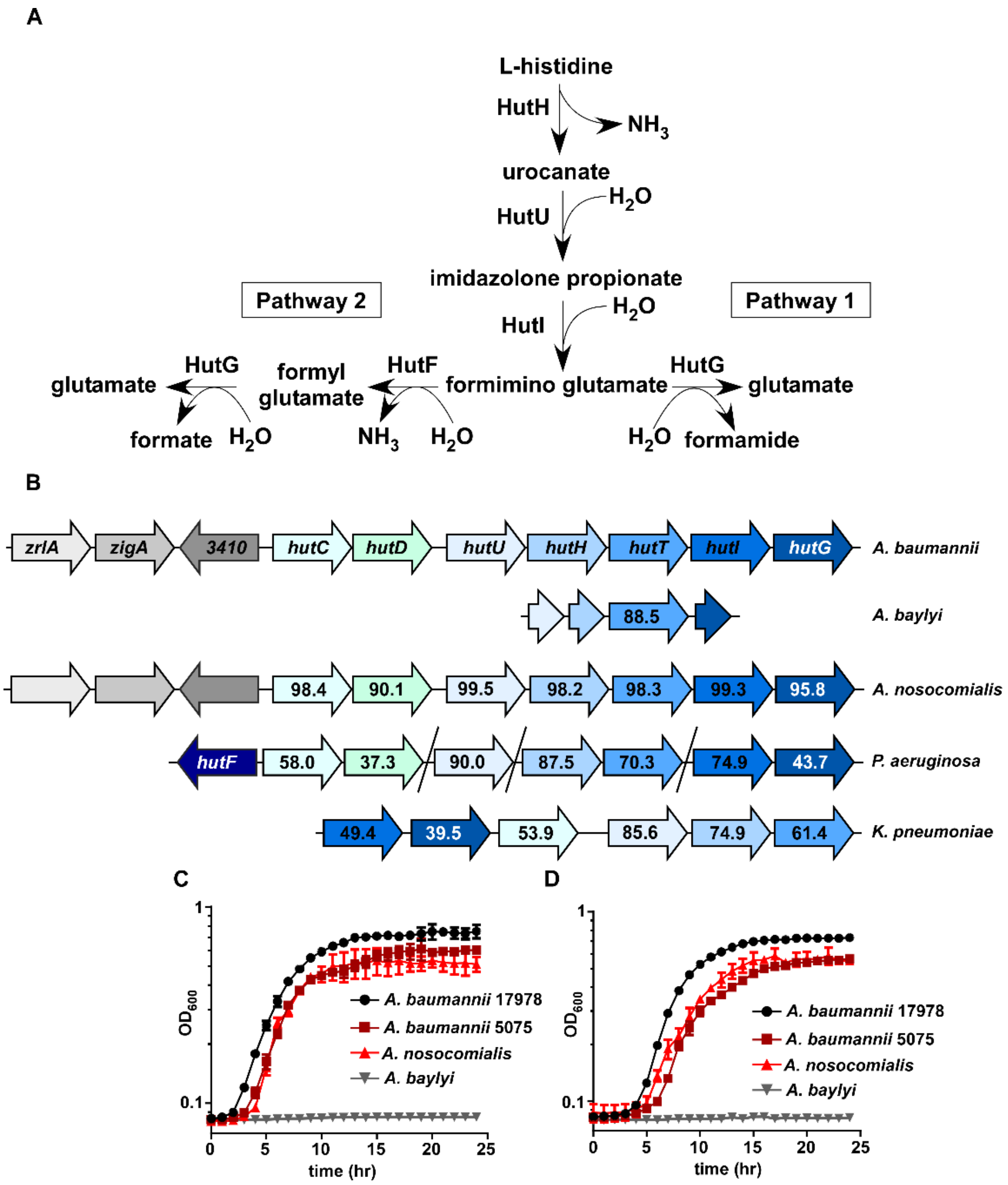

Figure 28. The histidine utilization system is broadly conserved. A) Model for the two defined pathways for Hut-mediated His catabolism, based on Bender, 2012. B) Genomic organization of *hut* systems in *A. baumannii* ATCC 17978, *A. baylyi* ADP1, *A. nosocomialis* M2, *Pseudomonas aeruginosa* PA14, and *Klebsiella pneumoniae* ATCC 43816. Numbers within arrows denote percent protein identity compared to *A. baumannii* ATCC 17978. C) Growth as monitored by OD_{600} over time of *A. baumannii* 17978, *A. baumannii* 5075, *A. nosocomialis* M2, and *A. baylyi* ADP1 in M9 minimal media with His as the sole carbon source. D) Growth as monitored by OD_{600} over time of *A. baumannii* 17978, *A. baumannii* 5075, *A. nosocomialis* M2, and *A. baylyi* ADP1 in M9 minimal media with His as the sole carbon and nitrogen source.

Our sequence analysis revealed that the *A. baumannii* four core enzymes have more similarity to *Pseudomonas* species, which possess Pathway 2 Hut systems, as opposed to *Klebsiella* that possesses Pathway 1. Pathway 2 Hut systems also encode *hutD*, which is a Hut-related gene that occurs downstream of the HutC repressor and whose function is not well-defined (**Figure 28B**) (Bender, 2012). We noted that *A. baumannii* encodes a *hutD* in the same positioning as in *Pseudomonas*. Intriguingly, *A. baumannii* lacks *hutF*, so it possesses the four enzyme system typical of Pathway 1 organisms. These findings suggest that *A. baumannii* possesses a hybrid Hut system that includes aspects of both Pathway 1 and Pathway 2.

In organisms containing an intact Hut system, His can be utilized as the sole carbon and nitrogen sources. To test functional outcomes from sequence predictions, wildtype strains of the pathogens *A. baumannii* and *A. nosocomialis* and the environmental species *A. baylyi* were grown in minimal media with L-His supplemented as the sole carbon or sole carbon and nitrogen source. As predicted, multiple strains of *A. baumannii* and *A. nosocomialis* utilize His as the sole energy source, and *A. baylyi* is unable to grow in these conditions (**Figure 28C,D**). Additionally, *A. baumannii* requires an intact Hut system to support growth on His, as genetic inactivation of the first enzyme in the catabolic pathway *hutH*, the first enzyme in the catabolic pathway, or the histidine transporter *hutT*, prevents growth (**Figure 29A,B**). Taken together, these results establish Hut-mediated His catabolism as a unique feature of *A. baumannii* physiology.

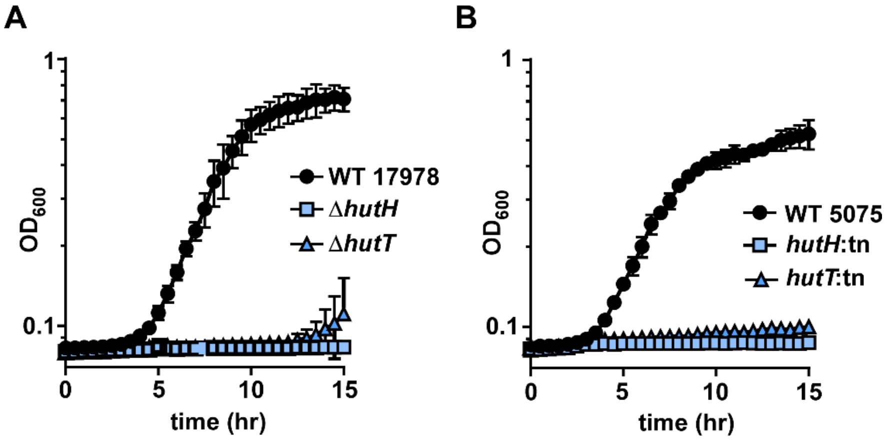

Figure 29. The Hut system requires His transporter and enzymatic activity. A) Growth monitored by OD_{600} of WT *A. baumannii* 17978, Δ*hutH*, and Δ*hutT* in M9 minimal media with His as the sole carbon source. B) Growth monitored by OD_{600} of WT *A. baumannii* 5075, *hutH*:tn, and *hutT*:tn in M9 minimal media with His as the sole carbon source.

HutC transcriptionally regulates the Hut system

In both types of previously defined Hut systems, the primary transcriptional regulation occurs via HutC-mediated repression of the core enzymes, although other regulators for the Hut system have been defined (Allison and Phillips, 1990; Hu et al., 1989; Schwacha and Bender, 1990). Despite earlier noted differences between the *A. baumannii* and *P. aeruginosa* Hut systems, the overall organization of the *A. baumannii* Hut system is similar to that of Pseudomonads (**Figure 28B**) (Bender, 2012). In *P. putida*, HutC binding sites were identified upstream of both the *hutCD* genes and upstream of the genes encoding the Hut enzymes (Allison and Phillips, 1990). Based on these observations, we predicted that *A. baumannii* HutC binds the promoter region upstream of *hutCD* and *hutUHTIG* (**Figure 30A**). In order to test this prediction, recombinant HutC was purified (**Figure 31A**) and subjected to electrophoretic mobility shift assays. Incubation of recombinant HutC with DNA containing the promoter region of *hutC* (**Figure 30B**) or *hutU* (**Figure 30C**) resulted in visible DNA-protein complexes that were absent with a nonspecific DNA probe (**Figure 31B**). In order to determine the nature of HutC-mediated regulation of the core Hut enzymes, *hutC* was genetically inactivated, and expression of the Hut enzymes was monitored using quantitative RT-PCR. This analysis demonstrated that inactivation of *hutC* resulted in significant upregulation of the genes encoding the Hut enzymes relative to wildtype (WT) *A. baumannii* (**Figure 30D**), which demonstrates that HutC likely functions as a transcriptional repressor in this organism. Collectively, these data define HutC as a transcriptional regulator of the Hut system in *A. baumannii*.

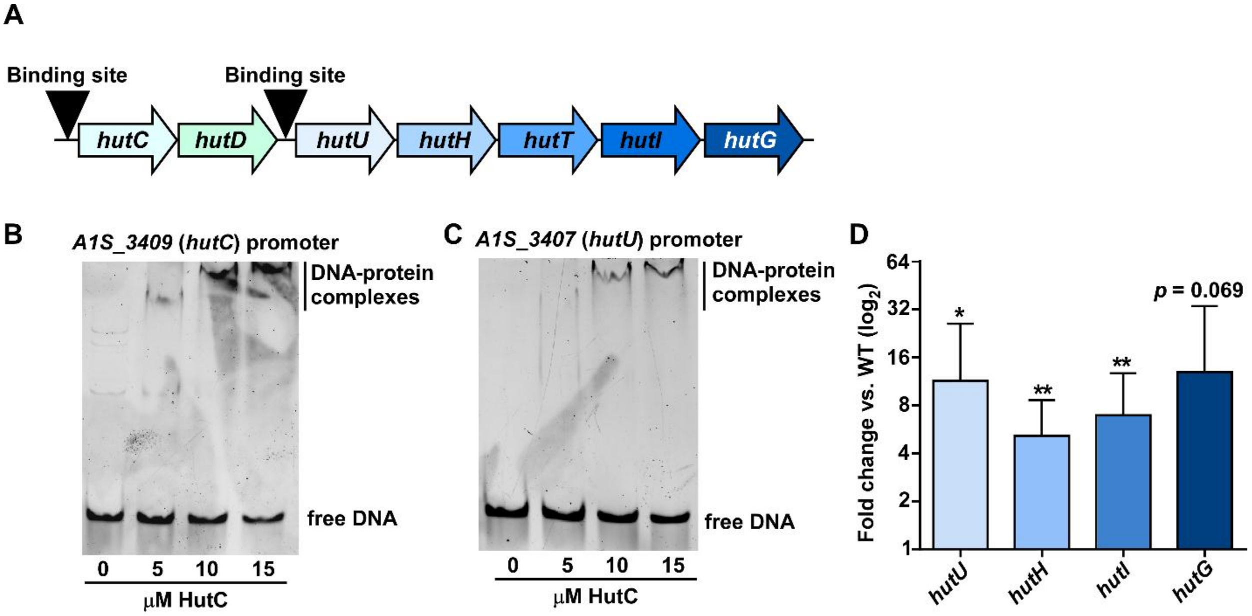

Figure 30. HutC transcriptionally regulates *A. baumannii hut*. A) Model detailing predicted *hutC* binding locations upstream of *hutC* and *hutU*. B) Electrophoretic mobility shift assay (EMSA) performed with recombinant HutC and a DNA probe containing the *hutC* promoter region. C) EMSA performed with recombinant HutC and a DNA probe containing the *hutU* promoter region. D) Quantiative RT-PCR analysis of Δ*hutC hut* enzymes grown to mid-log and compared to expression in WT *A. baumannii*. * $p < 0.05$, ** $p < 0.01$ as determined by Student's *t* test with a value of 1.

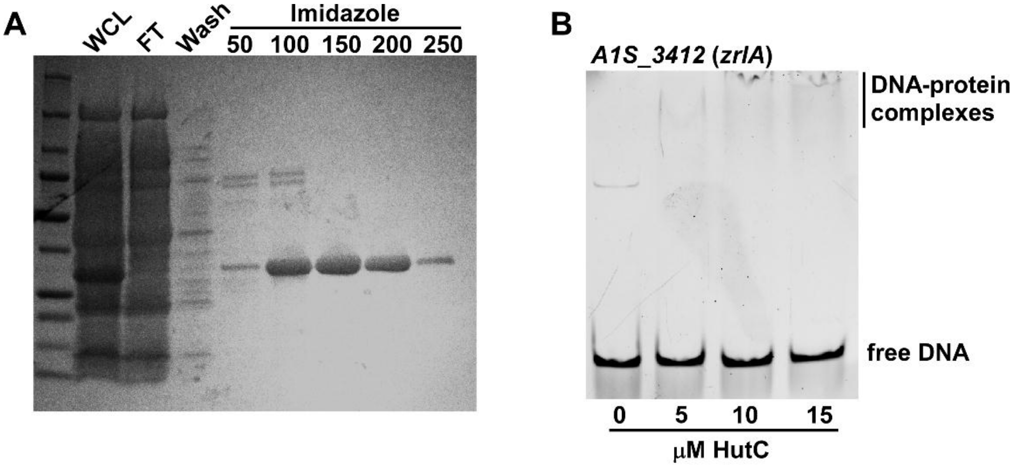

Figure 31. HutC regulates the *hut* system. A) Purification scheme for recombinant HutC from *E. coli*. B) EMSA performed with recombinant HutC and a DNA probe targeting the intergenic region of *A1S_3412* (*zrlA*).

HutH permits histidine nitrogen source utilization

Hut-mediated histidine catabolism proceeds from L-His to the first intermediate urocanate via the histidine ammonia lyase HutH (**Figure 28A**). We have previously confirmed the enzymatic activity of HutH and its requirement for His carbon source utilization (Nairn et al., 2016). However, whether *A. baumannii* can utilize His as a sole nitrogen source is undefined. To assess the contribution of HutH-mediated ammonium release to nitrogen source utilization, WT *A. baumannii* and strains genetically inactivated for *hutH* or *hutU*, which encodes the second enzyme in the Hut system, were grown in minimal media in the presence or absence of ammonium chloride. When fumarate is provided as the sole carbon source, ammonium chloride is required for growth of all three strains, since fumarate metabolism does not provide any nitrogen sources (**Figure 32A**). When His is provided as the sole carbon source, the WT strain is proficient for growth regardless of ammonium chloride supplementation, while the *hutH* and *hutU* mutants are both unable to grow (**Figure 32B**). If fumarate is provided as the carbon source and supplemented with His as the sole nitrogen source, WT *A. baumannii* has normal growth kinetics, while the *hutH* mutant growth is inhibited (**Figure 32C**). However, the *hutU* mutant is partially restored in its ability to grow in these conditions, and grows significantly better than the *hutH* mutant (**Figure 32C,D**). These results are consistent with a model whereby *A. baumannii* utilizes His as a nitrogen source in combination with other, more energetically efficient carbon sources, such as fumarate, through the action of HutH.

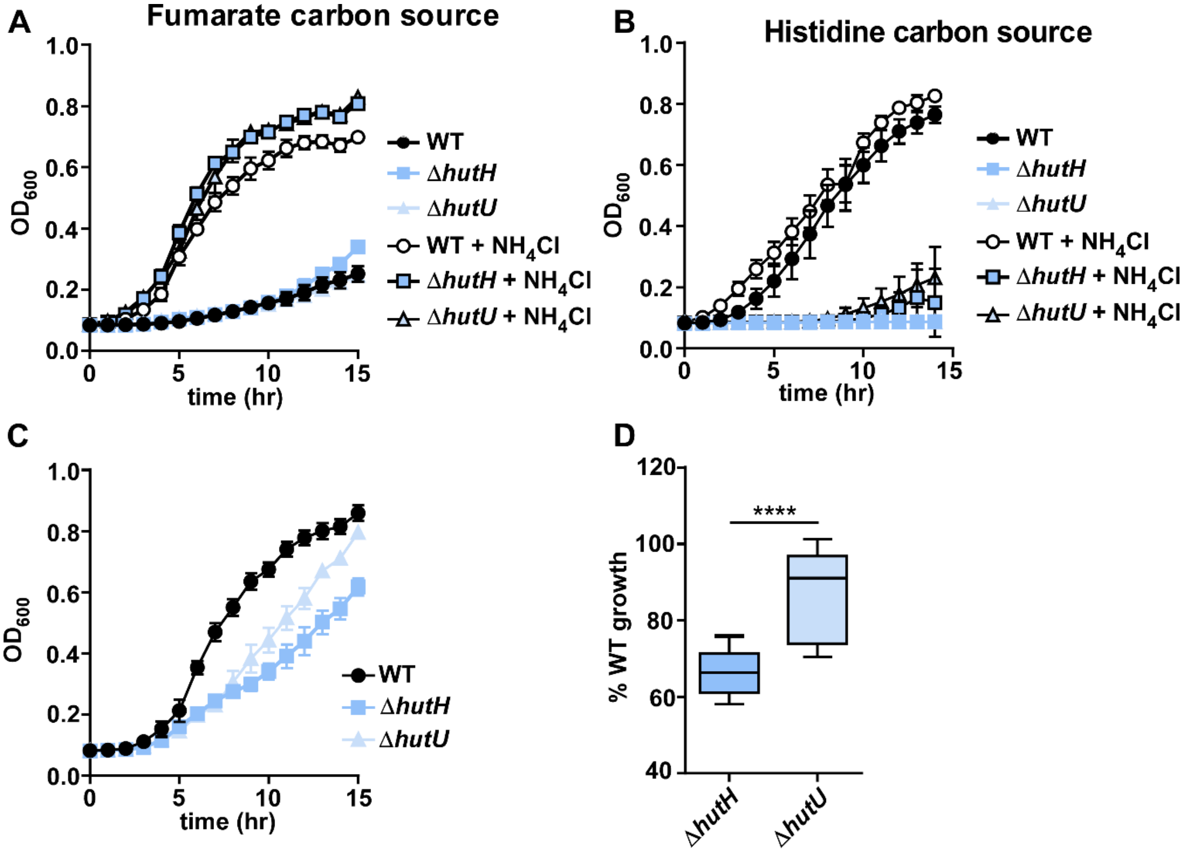

Figure 32. HutH promotes *A. baumannii* His nitrogen source utilization. A) Growth monitored by OD_{600} of WT *A. baumannii* 17978, Δ*hutH*, and Δ*hutU* in M9 minimal media with fumarate as the sole carbon source +/- NH_4Cl. B) Growth monitored by OD_{600} of WT *A. baumannii* 17978, Δ*hutH*, and Δ*hutU* in M9 minimal media with His as the sole carbon source +/- NH_4Cl. C) Growth monitored by OD_{600} of WT *A. baumannii* 17978, Δ*hutH*, and Δ*hutU* in M9 minimal media with fumarate as the sole carbon source and His as the sole nitrogen source. D) Percent growth relative to WT at 15 h for Δ*hutH* and Δ*hutU* with fumarate as the sole carbon source and His as the sole nitrogen source. **** $p < 0.0001$ as determined by Student's *t* test.

Histidine nitrogen source utilization contributes to *Acinetobacter* pathogenesis

Given the conservation of the Hut system in pathogenic *Acinetobacter*, we wondered whether components of this system are important for surviving within the vertebrate host. To determine this, 8-10 week old C57BL6/J mice were intranasally infected with WT *A. baumannii* in pairwise combinations with each of the components of the Hut system genetically inactivated. These experiments revealed that the *hutH* mutant was severely attenuated within the lungs and defective in dissemination to the liver (**Figure 33A, Figure 34A**), with a ~100 fold decrease in its ability to compete against the WT strain (**Figure 33F**). Additionally, the *hutT* His transport mutant was also displayed a colonization defect in the lungs and liver (**Figure 33B,F, Figure 344B**). However, no other *hut* mutants displayed any significant defect in the lungs or in the liver (**Figures 33C-33F, Figures 34C-E**). Additionally, we previously demonstrated that HutH-mediated His catabolism may release zinc (Zn) from His-Zn complexes to promote survival in low Zn environments generated by the metal-binding properties of the host protein calprotectin (CP) (Nairn et al., 2016). However, the *hutH* mutant remains defective in the lungs of CP$^{-/-}$ mice, while the *hutU* mutant is unaffected (**Figure 34F-H**). Collectively, these results esteablish that HutH-mediated His catabolism as a key determinant of *A. baumannnii* virulence.

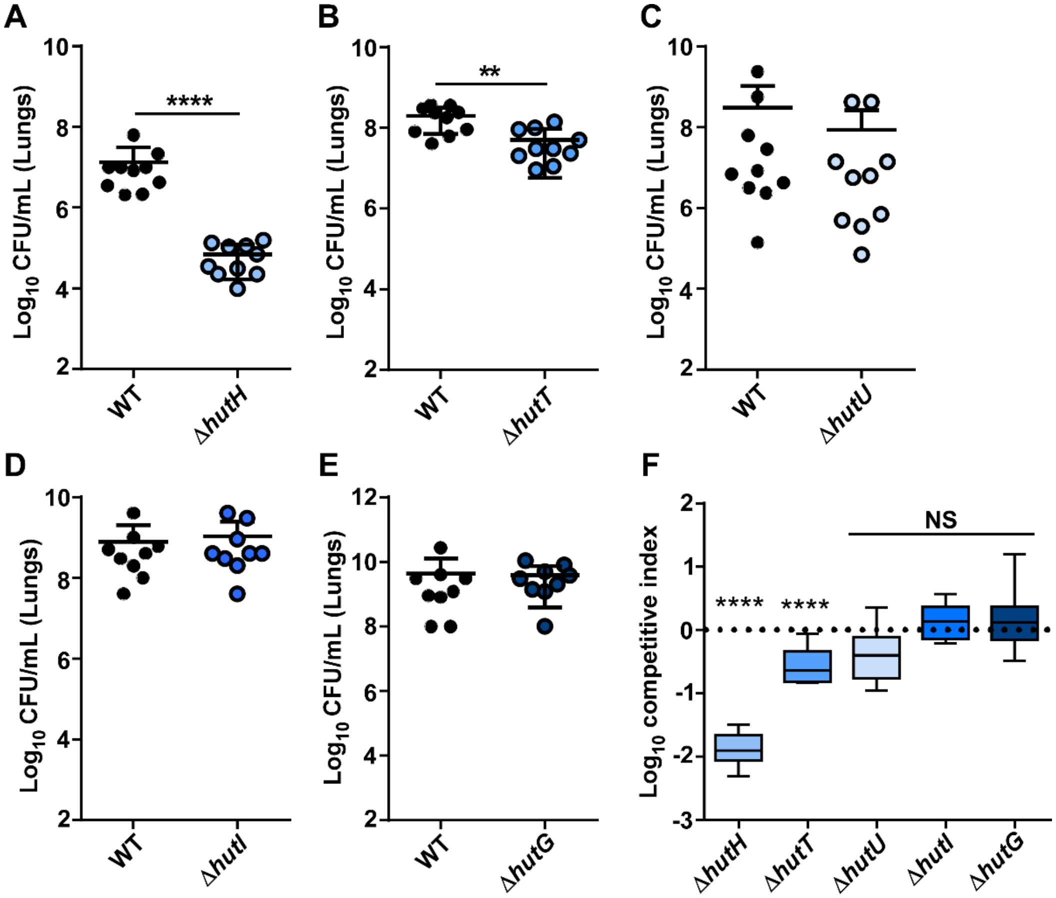

Figure 33. Components of the Hut system are important for *A. baumannii* pathogenesis. Eight to 10 week old mice were intranasally infected with a 1:1 mixture of WT and mutant *A. baumannii*. A) Bacterial burdens recovered at 36 hours post infection (hpi) in the lungs of WT and Δ*hutH* strains. B) Bacterial burdens recovered at 36 hpi in the lungs of WT and Δ*hutT* strains. C) Bacterial burdens recovered at 36 hpi in the lungs of WT and Δ*hutU* strains. D) Bacterial burdens recovered at 36 hpi in the lungs of WT and Δ*hutI* strains. E) Bacterial burdens recovered at 36 hpi in the lungs of WT and Δ*hutG* strains. ** $p < 0.01$, **** $p < 0.0001$, as determined by Mann Whitney U-test with Dunnett's multiple comparisons. F) Competitive index ([input mutant/WT]/[output mutant/WT]) for the various mutants in the lungs. **** $p < 0.0001$ as determined by Student's *t* test against value of 1.

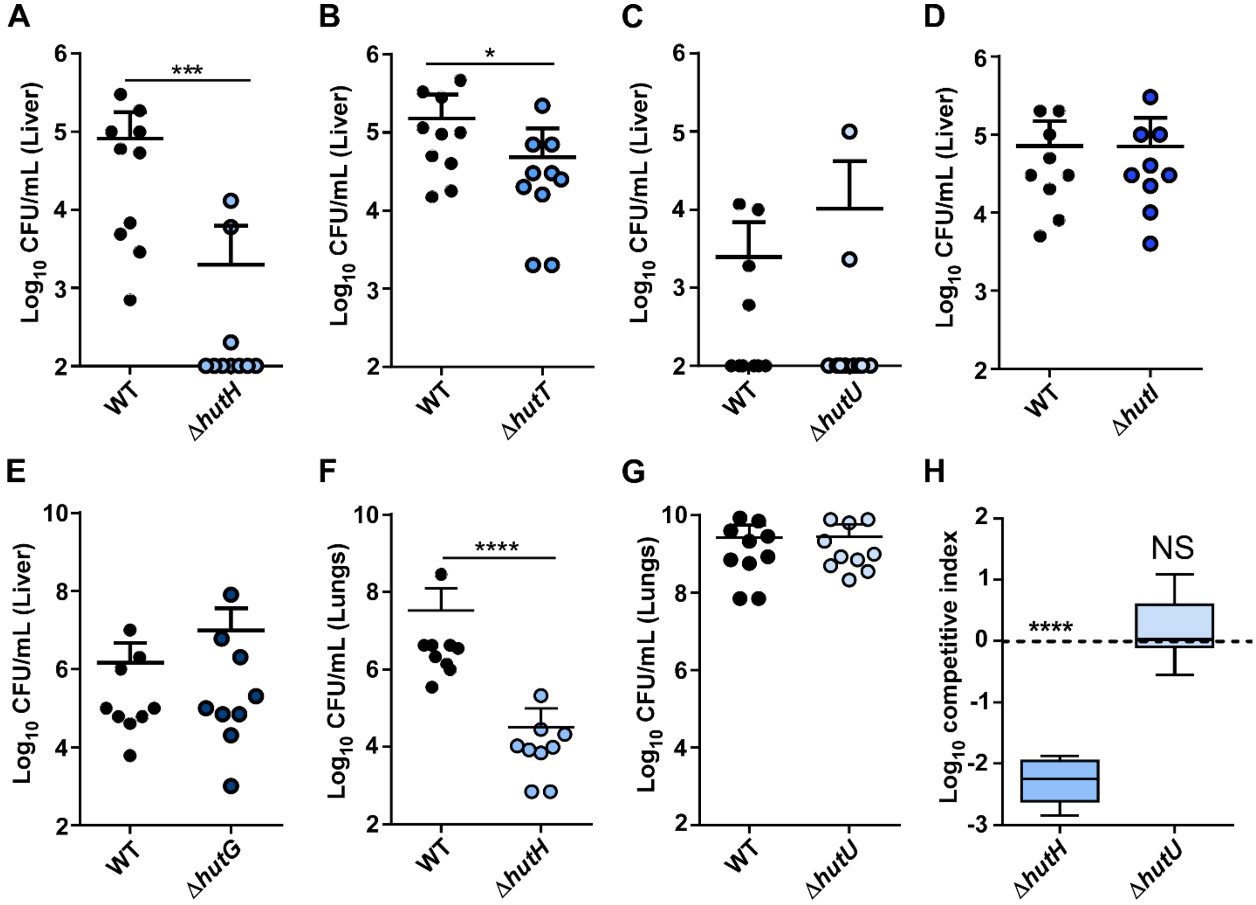

Figure 34. Components of the Hut system are important for *A. baumannii* pathogenesis. Eight to 10 week old mice were intranasally infected with a 1:1 mixture of WT and mutant *A. baumannii*. A) Bacterial burdens recovered at 36 hours post infection (hpi) in the liver of WT and Δ*hutH* strains. B) Bacterial burdens recovered at 36 hpi in the liver of WT and Δ*hutT* strains. C) Bacterial burdens recovered at 36 hpi in the liver of WT and Δ*hutU* strains. D) Bacterial burdens recovered at 36 hpi in the liver of WT and Δ*hutI* strains. E) Bacterial burdens recovered at 36 hpi in the liver of WT and Δ*hutG* strains. F) Bacterial burdens recovered in the lungs at 36 hpi from $CP^{-/-}$ mice of WT and Δ*hutH* strains. G) Bacterial burdens recovered in the lungs at 36 hpi from $CP^{-/-}$ mice of WT and Δ*hutU* strains. * $p < 0.05$, *** $p < 0.001$, **** $p < 0.0001$ as determined by Mann Whitney U-test with Dunnett's multiple comparisons. H) Competitive index ([input mutant/WT]/[output mutant/WT]) for the various mutants in the lungs of $CP^{-/-}$ mice. **** $p < 0.0001$ as determined by Student's *t* test against a value of 1.

Discussion

The ability of opportunistic bacterial pathogens to persist in diverse environments is likely a major contributor to their disease-causing potential. *A. baumannii* is capable of producing all required biological cofactors from simple starting materials, including biosynthesis of the full suite of amino acids. While amino acids serve as the building blocks of proteins, many bacteria can further metabolize these as nutrient sources. His is one of the most energetically expensive amino acids to synthesize, so acquiring it from the environment is preferential over biosynthesis. As such, both the import of His and its degradation are tightly regulated to maintain a cellular supply for protein synthesis (Bender, 2012). Here, we describe the sole pathway for His nutrient utilization in *A. baumannii* and demonstrate that the catabolic enzymes are conserved among pathogenic *Acinetobacter* but lost in environmental *Acinetobacter*. Additionally, HutC serves as a transcriptional repressor of *hut*. The Hut system is required for *A. baumannii* to utilize His as a carbon source, but it also permits His degradation for nitrogen source utilization. This nitrogen source utilization requires the HutH enzyme, which produces ammonia as a byproduct. A strain lacking *hutH* is defective at His nitrogen source utilization, and it is attenuated in a mouse model of *A. baumannii* pneumonia. These findings suggest that His serves as an important nitrogen source for *A. baumannii* within the lung and that inhibiting *A. baumannii* HutH may be a viable strategy for limiting *A. baumannii* pathogenesis.

While HutC is a major regulator of the Hut system, other transcriptional regulators may influence expression of *hut* gene expression in *A. baumannii*. In *Pseudomonas* additional regulators include the CbrAB and NtrBC two-component systems (Bender, 2012). In carbon-limiting conditions, CbrAB serves as a transcriptional activator of *hut* genes, and nitrogen-limiting conditions are sensed by NtrBC to activate *hut* (Zhang and Rainey, 2008). These two-component systems do have functional overlap and are independently sufficient to activate *hut* genes (Zhang and Rainey, 2008). Additionally, the function of HutD, which is encoded directly downstream of HutC in *A. baumannii* and in *Pseudomonas* species, is not well-defined, but may alter expression of *hut* genes (Zhang et al., 2006). Given the importance of fine-tuning His levels within the bacterial cell, *A. baumannii* Hut system regulation is likely multi-faceted and is an exciting area of future investigation.

Our demonstration for the first time that HutH is critical for survival within the vertebrate host suggests that the Hut system and His utilization have broader impacts outside of simple energy generation. We have previously demonstrated that HutH-mediated His catabolism also plays a role in liberating Zn from His-Zn complexes during nutrient limitation (Nairn et al., 2016). Further, *A. baumannii* grown in L-His as the sole carbon source has enhanced biofilm formation that is dependent on an intact Hut system (Cabral et al., 2011). Additionally, His stimulates the production of extracellular proteases in the marine opportunistic bacterial pathogen *Vibrio alginolyticus*, and this production is dependent on *hutH* (Bowden et al., 1982). In *Brucella abortus*, the causative agent of brucellosis, the HutC repressor regulates not only *hut* expression, but it also serves as a coactivator of the Type IV secretion system that is responsible for effector translocation to host cells (Sieira R., 2010). Collectively, these findings illustrate the diversity in which Hut-mediated His metabolism and sensing may impact bacterial pathogenesis and physiology more broadly. Our observation that only pathogenic *Acinetobacter* maintain the Hut system supports a model whereby niche differences between pathogenic and nonpathogenic *Acinetobacter* selected for maintenance of Hut system enzymes.

This work demonstrates that the Hut system, and specifically HutH, is important for the pathogenesis of *A. baumannii*, where His may serve as a nitrogen source alongside more energetically favorable carbon sources to promote *A. baumannii* lung colonization. These data highlight an exciting intersection between bacterial amino acid metabolism and host-pathogen interactions that may be targeted for therapeutic potential.

References

Akashi, H., and Gojobori, T. (2002). Metabolic efficiency and amino acid composition in the proteomes of *Escherichia coli* and *Bacillus subtilis*. *Proceedings of the National Academy of Sciences of the United States of America 99*, 3695-3700.

Allison, S.L., and Phillips, A.T. (1990). Nucleotide sequence of the gene encoding the repressor for the histidine utilization genes of *Pseudomonas putida*. *Journal of bacteriology 172*, 5470-5476.

Bender, R.A. (2012). Regulation of the histidine utilization (hut) system in bacteria. *Microbiol Mol Biol Rev 76*, 565-584.

Bowden, G., Mothibeli, M.A., Robb, F.T., and Woods, D.R. (1982). Regulation of hut enzymes and intracellular protease activities in *Vibrio alginolyticus* hut mutants. *J Gen Microbiol 128*, 2041-2045.

Brill, W.J., and Magasanik, B. (1969). Genetic and metabolic control of histidase and urocanase in *Salmonella* Typhimurium, strain 15-59. *The Journal of biological chemistry 244*, 5392-5402.

Cabral, M.P., Soares, N.C., Aranda, J., Parreira, J.R., Rumbo, C., Poza, M., Valle, J., Calamia, V., Lasa, I., and Bou, G. (2011). Proteomic and functional analyses reveal a unique lifestyle for *Acinetobacter baumannii* biofilms and a key role for histidine metabolism. *Journal of proteome research 10*, 3399-3417.

CDC (2019). Antibiotic resistance threats in the United States.

Harding, C.M., Hennon, S.W., and Feldman, M.F. (2018). Uncovering the mechanisms of *Acinetobacter baumannii* virulence. *Nat Rev Microbiol 16*, 91-102.

Hoang, T.T., Karkhoff-Schweizer, R.R., Kutchma, A.J., and Schweizer, H.P. (1998). A broad-host-range Flp-FRT recombination system for site-specific excision of chromosomally-located DNA sequences: application for isolation of unmarked *Pseudomonas aeruginosa* mutants. *Gene 212*, 77-86.

Hu, L., Allison, S.L., and Phillips, A.T. (1989). Identification of multiple repressor recognition sites in the hut system of *Pseudomonas putida*. Journal of bacteriology *171*, 4189-4195.
Ingle, R.A. (2011). Histidine biosynthesis. Arabidopsis Book *9*, e0141.

Juttukonda, L.J., Green, E.R., Lonergan, Z.R., Heffern, M.C., Chang, C.J., and Skaar, E.P. (2019). *Acinetobacter baumannii* OxyR Regulates the Transcriptional Response to Hydrogen Peroxide. *Infection and immunity 87*.

Magasanik, B. (1961). Catabolite repression. Cold Spring Harb Symp Quant Biol *26*, 249-256.
Menard, R., Sansonetti, P.J., and Parsot, C. (1993). Nonpolar mutagenesis of the ipa genes defines IpaB, IpaC, and IpaD as effectors of *Shigella flexneri* entry into epithelial cells. *Journal of bacteriology 175*, 5899-5906.

Mortensen, B.L., Rathi, S., Chazin, W.J., and Skaar, E.P. (2014). *Acinetobacter baumannii* response to host-mediated zinc limitation requires the transcriptional regulator Zur. *Journal of bacteriology 196*, 2616-2626.

Nairn, B.L., Lonergan, Z.R., Wang, J., Braymer, J.J., Zhang, Y., Calcutt, M.W., Lisher, J.P., Gilston, B.A., Chazin, W.J., de Crecy-Lagard, V., *et al.* (2016). The Response of *Acinetobacter baumannii* to Zinc Starvation. *Cell Host Microbe 19*, 826-836.

Peleg, A.Y., Seifert, H., and Paterson, D.L. (2008). *Acinetobacter baumannii*: emergence of a successful pathogen. *Clin Microbiol Rev 21*, 538-582.

Schwacha, A., and Bender, R.A. (1990). Nucleotide sequence of the gene encoding the repressor for the histidine utilization genes of *Klebsiella aerogenes*. *Journal of bacteriology 172*, 5477-5481.

Sieira R., A.G.M., Bukata L., Comerci D.J., Ugalde R. A. (2010). Metabolic control of virulence genes in *Brucella abortus*: HutC coordinates virB expression and the histidine utilization pathway by direct binding to both promoters. *Journal of bacteriology 192*, 217-224

Skegg, D.C., Corwin, P.A., Craven, R.S., Malloch, J.A., and Pollock, M. (1987). Occurrence of multiple sclerosis in the north and south of New Zealand. *J Neurol Neurosurg Psychiatry 50*, 134-139.

Sonenshein, A.L. (2007). Control of key metabolic intersections in *Bacillus subtilis*. *Nat Rev Microbiol 5*, 917-927.

WHO (2017). Guidelines for the prevention and control of carbapenem-resistant Enterobacteriaceae, *Acinetobacter baumannii* and *Pseudomonas aeruginosa* in health care facilities. World Health Organization.

Zhang, X.X., George, A., Bailey, M.J., and Rainey, P.B. (2006). The histidine utilization (hut) genes of *Pseudomonas fluorescens* SBW25 are active on plant surfaces, but are not required for competitive colonization of sugar beet seedlings. *Microbiology 152*, 1867-1875.

Zhang, X.X., and Rainey, P.B. (2008). Dual involvement of CbrAB and NtrBC in the regulation of histidine utilization in *Pseudomonas fluorescens* SBW25. *Genetics 178*, 185-195.

CHAPTER V

IN VIVO BIOLUMINESCENCE IMAGING OF LABILE IRON ACCUMULATION IN A MURINE MODEL OF *ACINETOBACTER BAUMANNII* INFECTION

A version of the following section was previously published in *Proceedings of the National Academy of Sciences of the United States of America* 114(48) 12669-12674 (November 2017)

doi: 10.1073/pnas.1708747114

Introduction

Iron is an essential mineral for every form of life, owing in large part to its ability to cycle between different oxidation states for processes such as nucleotide synthesis, oxygen transport, and respiration (Andrews, 2000; Cammack et al., 1989; Johnson et al., 2005; Xu et al., 2013). At the same time, the potent redox activity of iron is potentially toxic, particularly in unregulated labile forms that can trigger aberrant production of reactive oxygen species (ROS) via Fenton chemistry (Winterbourn, 1995). Indeed, iron deficiency remains one of the most common nutritional deficiencies in the world (Miller, 2013), and aberrant iron levels have been linked to various ailments, including cancer (Pinnix et al., 2010; Torti and Torti, 2013; Toyokuni, 2009; Wu et al., 1999), cardiovascular (von Haehling et al., 2015) and neurodegenerative (Gerlach et al., 1994, ; Hare et al., 2013, 5, 34) disorders, as well as aging (James et al., 2015). The situation is even more complex in infectious diseases, where the requirement for iron by both host organism and invading pathogen leads to an intricate chemical tug-of-war for this metal nutrient during various stages of the immune response (Nairz et al., 2014; Skaar, 2010).

The foregoing examples provide motivation for developing technologies to monitor biological iron status, with particular interest in methods to achieve *in vivo* iron imaging in live animal models that go beyond current state-of-the-art assays that are limited primarily to cell culture specimens. In this regard, detection of iron with both metal and oxidation state specificity is of central importance, because while iron is stored primarily in the ferric oxidation state, a ferrous iron pool loosely bound to cellular ligands, defined as the labile iron pool (Zastrow et al.), exists at the center of highly regulated networks that control iron acquisition, trafficking, and excretion. Indeed, as a weak binder on the Irving-Williams stability series (Irving and Williams, 1953), Fe^{2+} provides a challenge for detection by traditional recognition-based approaches (Carter et al., 2014), and as such we (Aron et al., 2016; Au-Yeung et al., 2013; Spangler et al., 2016b) and others (Hirayama et al., 2013; Hirayama et al., 2017; Niwa et al., 2014; Zastrow et al., 2016) have pursued activity-based approaches to sense labile Fe^{2+} stores in cells (Aron et al., 2015; Chan et al., 2012; Chen et al., 2011; Cho and Sessler, 2009; Yang et al., 2013). These tools have already provided insights into iron biology, as illustrated by the direct identification of elevations in LIPs during ferroptosis (Dixon et al., 2012; Dixon and Stockwell, 2014), an emerging form of cell death, using the ratiometric iron indicator FIP-1(Aron et al., 2016).

We now report the design, synthesis, and molecular imaging applications of Iron-Caged Luciferin-1 (ICL-1), a first-generation caged luciferin probe that enables *in vivo* iron imaging in living animals. Work from our lab and others has demonstrated the utility of caged luciferins *in vivo* (Adams and Miller, 2014; Li et al., 2013; Xu et al., 2016) for measuring transient small molecules (Chen et al., 2017; Takakura et al., 2015; Van de Bittner et al., 2010; Van de Bittner et al., 2013), enzyme and transporter activities (Chang et al., 2011; Dragulescu-Andrasi et al., 2009; Eiriksdottir et al., 2010; Godinat et al., 2013; Henkin et al., 2012; Jones et al., 2006; Mofford et al., 2015; Porterfield et al., 2015; Rush et al., 2010; Van de Bittner et al., 2013; Vorobyeva et al., 2015; Yao et al., 2007; Zhou et al., 2008), protein-protein and cell-cell interactions (Cohen et al., 2010; Porterfield et al., 2015; Sellmyer et al., 2013), and copper (Heffern et al., 2016). Indeed, previous work from our laboratory utilized a Cu-dependent oxidation reaction to uncage luciferin for *in vivo* copper imaging (Spangler et al., 2016a), a first demonstration of a general activity-based sensing strategy which we envisioned expanding to other essential metals in biology by changing the reaction trigger. In ICL-1, we caged D-aminoluciferin with an Fe^{2+} reactive endoperoxide trigger (Aron et al., 2016; Fontaine et al.; Spangler et al., 2016b) inspired by antimalarial agents that exhibit Fe^{2+}-dependent pharmacology (Borstnik et al., 2002; Creek et al., 2007; Tang et al., 2005). ICL-1 was designed to undergo metal- and redox-specific Fe^{2+}-dependent cleavage to generate D-aminoluciferin, which can interact with the firefly luciferase enzyme to produce red light output through a catalytic bioluminescent reaction. ICL-1 is capable of monitoring changes in LIPs in live cells and mice under situations of iron overload and/or deficiency. Application of this technology to a mouse model of systemic *Acinetobacter baumannii* infection, a Gram-negative bacterial pathogen that infects susceptible intensive care unit (ICU) populations, reveals an elevation of LIPs by in vivo imaging that co-registers with increases in total iron as monitored by *ex vivo* imaging using laser ablation inductively coupled plasma mass spectrometry (LA-ICPMS). This unique tool for imaging iron in living animals provides a platform for probing its contributions to physiology, aging, and disease.

Materials and Methods

General methods

Reactions using air- or moisture-sensitive reagents were conducted in flame-dried glassware under an inert atmosphere of N_2. When dry solvent was required, solvent was passed over activated alumina and was stored over activated 3Å molecular sieves before use. All other commercially purchased chemicals were used as received (without further purification). 2-Adamantanone and hydroxylamine methyl ester hydrochloride were purchased from AK Scientific (Union City, CA); 6-amino 2-cyanobenzothiazole was purchased from Abblis Chemicals (Houston, TX); all other reagents were purchased from Sigma-Aldrich (St. Louis, MO). 3-Hydroxycyclohexan-1-one was synthesized as described previously (*). 3-[(tert-butyldiphenylsilyl)oxy]cyclohexan-1-one was synthesized according to published procedures.(D. et al., 2015) Silica gel P60 (SiliCycle) was used for column chromatography and SiliCycle 60 F254 silica gel (pre-coated sheets, 0.25 mm thick) were used for analytical thin layer chromatography and visualized by fluorescence quenching under UV light. ^{1}H and ^{13}C NMR NMR spectra were collected at 298 K in $CDCl_3$ or CD_3OD (Cambridge Isotope Laboratories, Cambridge, MA) at 25 °C on Bruker AVQ-400, AVB-400, AV-500, or AV-600 at the College of Chemistry NMR Facility at the University of California, Berkeley or on Bruker 900 at the QB3 Central California 900 MHz NMR Facility. All chemical shifts are reported in the standard notation of δ parts per million relative to residual solvent peak at 7.26 ($CDCl_3$) or 3.31 (CD_3OD) for ^{1}H and 77.16 ($CDCl_3$) or 49.00 (CD_3OD) for ^{13}C as an internal reference. Splitting patterns are indicated as follows: br, broad; s, singlet; d, doublet; t, triplet; m, multiplet; dd, doublet of doublets. Low-resolution electrospray mass spectral analyses were carried out using a LC-MS (Agilent Technology 6130, Quadrupole LC/MS and Advion expression-L Compact Mass Spectrometer). High-resolution mass spectral analyses (ESI-MS) were carried out at the College of Chemistry Mass Spectrometry Facility at the University of California, Berkeley.

Synthesis of endoperoxide (1)

The endoperoxide **1** was synthesized following procedures in the literature.(D. et al., 2015)

Synthesis of benzothiazole (2)

To 2-cyano-6-aminobenzothiazole (0.0616 g, 0.352 mmol), bis(trichloromethyl) carbonate (0.1045 g, 0.352 mmol) and 4-dimethylaminopyridine (0.086 g, 0.7032 mmol) was added 25 mL dry toluene. This mixture was heated to reflux for 3 hours then was cooled to 35 ºC, at which point N_2 was bubbled through the solution for 15 minutes and collected in a KOH trap. At this point, endoperoxide 1 (0.1223 g, 0.44 mmol) was added in 5 mL of dry toluene followed by addition of sodium hydride (0.025 g, 1.09 mmol). The reaction mixture was stirred overnight at 35 ºC under N_2. The reaction was quenched with water then was diluted with ethyl acetate. The aqueous phase was extracted two more times with ethyl acetate and the combined organic layers were washed with a saturated NaCl solution, dried over Na_2SO_4, and concentrated under reduced pressure to afford a brown powder. Purification by silica chromatography (0 → 15 % ethyl acetate in hexanes) yielded **2** as a pale yellow foam. Yield = 135.34 mg, 80 %. ^{1}H NMR (400 MHz, $CDCl_3$, 298 K) δ (ppm): 8.44 (s, 1 H), 8.12 – 8.09 (d, 1 H), 7.34 – 7.30 (dd, 1 H), 6.87 (s, 1 H), 4.95 – 4.86 (m, 1 H), 2.37 – 2.31 (m,1 H), 2.06 – 1.64 (m, 21 H). ^{13}C NMR (101 MHz, $CDCl_3$, 298 K) δ (ppm): 152.5, 148.3, 138.9, 137.3, 134.9, 125.5, 119.8, 113.2, 111.9, 109.7, 108.6, 72.4, 45.5, 40.1, 36.8, 36.4, 36.4, 36.2, 34.9, 34.8, 33.8, 30.8, 30.6, 26.9, 26.5, 24.8, 21.2, 19.8. LRMS calcd. for $C_{25}H_{27}N_3O_5S$ $[M-H]^-$ *m/z* 480.2; found: 480.3.

Synthesis of ICL-1

To a Schlenk tube charged with D-cysteine hydrochloride monohydrate (0.022 g, 0.125 mmol) and K_2CO_3 (0.020 g, 0.15 mmol) in N_2 was added deoxygenated water (0.2 ml), followed by a solution of 3 (0.040 g, 0.0832 mmol) in deoxygenated MeOH (0.6 ml) and dichloromethane (0.6 ml). The solution was stirred under N_2 at room temperature overnight. At this point, the reaction mixture was filtered and the filtrate was neutralized by addition of one equivalent of 1 M HCl. The filtrate was diluted with ethyl acetate and water. The aqueous phase was separated and extracted with three portions of ethyl acetate. The combined organic phases were washed with saturated aq NaCl solution, dried over Na_2SO_4, filtered, and concentrated to afford a yellow oil. The crude material was purified by HPLC on an Agilent Life Sciences SB-C18 Semi-Prep HPLC Column 9.4 x 250 mm (flow rate = 1.5 ml/min, H_2O/MeCN with 0.05% formic acid gradient: 0-50 min, 35% → 100% MeCN in water, 50-65 min, 100% MeCN in water). Yield = 11.43 mg, 24%. ^1H NMR (600 MHz, CD_3OD, 298 K) δ (ppm): 8.27 (s, 1 H), 7.95 – 7.94 (d, 1 H), 7.51 – 7.49 (dd, 1 H), 5.41 – 5.38 (s, 1 H), 4.97 (m, 1 H), 3.79 – 3.73 (q, 1 H), 2.36 – 2.33 (m,1 H), 1.99 – 1.65 (m, 22 H). ^{13}C NMR (151 MHz, CD_3OD, 298 K) δ (ppm): 173.3, 167.5, 164.5, 160.3, 155, 150.0, 140.2, 138.4, 125.2, 120.1, 118.1, 112.7, 111.3, 109.9, 79.6, 72.7, 49.9, 49.6, 40.9, 37.8, 35.9, 35.8, 35.7, 34.8, 31.5, 28.3, 27.9, 20.8. HRMS (ESI) calcd. for $C_{28}H_{31}N_3O_7S_2$ $[M-H]^-$ *m/z* = 584.1603; found: 584.1528.

***In Vitro* luminescence assays**

Millipore water was used to prepare all aqueous solutions. Incubation of 5 µM of ICL-1 (100x dilution of a 500 µM stock in DMSO) with different metal ions ($MgCl_2$, $CaCl_2$, $MnCl_2$,

$FeCl_2$, $FeCl_3$, $CoCl_2$, $NiCl_2$, $Cu(MeCN)_4(PF_6)$, $CuCl_2$ and $ZnCl_2$) was performed in 50 mM HEPES buffer at pH 7.4. Similar experiments were performed with D-aminoluciferin (termed here aminoluciferin; 100 nM, 100x dilution of a 10 µM stock in DMSO) to determine any effects of the metal ion treatments on luciferase activity. At the end of the incubation, 40 µl each of the solution was transferred to a well of a white, opaque half-area 96-well plate (Corning). An equal volume (40 µl) of a solution of luciferase (100 µg/ml, Promega) in 50 mM Tris buffer at pH 7.4, with 10 mM Mg^{2+} ($MgCl_2$), 0.1 mM Zn^{2+} ($ZnCl_2$) and 2 mM ATP was added and mixed well. Bioluminescent signals were measured using a Synergy Mx plate reader at 37°C for 30 min. To determine the reactivity of ICL-1 with iron-containing species, similar experiments were performed as with the metal selectivity assays, but with iron-bound transferrin (holo-transferrin, holoTf), ferritin, hemin, and hemoglobin. For holoTf, hemin, and hemoglobin, stoichiometric binding of iron was assumed and the species were measured by weight. For ferritin, total iron per mg of ferritin was approximated with the ferrozine assay. ICL-1 or aminoluciferin was incubated with the appropriate amounts of the iron-containing species to achieve 100 µM total iron in the incubation solution with subsequent bioluminescent assays as described.

Cellular assays

A Xenogen IVIS Spectrum instrument (Caliper Life Sciences) was used for bioluminescence imaging in all cellular experiments. PC3M-Luc, HEK293-Luc, MDA-MB-293-Luc, and LNCaP-Luc cells were each cultured in DMEM containing 10% FBS. Cells were passaged and plated in black 96-well plate with clear bottoms (Becton, Dickson and Company) to achieve 75% confluence 1 day after plating (or 90% confluence 2 days after plating), and were treated, assayed, and imaged 2 days after plating. For iron treatments, stock solutions of FAS were prepared in millipore water at 20x the final concentration of the treatment. Ninety minutes prior to imaging, the serum-containing DMEM was aspirated from the cells and replaced with 95 µL serum-free DMEM followed by 5 µL of the aqueous solution of FAS and the cells were incubated at 37 ºC.

Chelator treatments were performed as follows. For treatments with BPY, concentrated stocks of BPY (2000x the final concentration of treatment) were prepared in DMSO with brief heating to solubilize the agent. The DMSO stock was diluted 100-fold with millipore water. Ninety minutes prior to imaging, the serum-containing DMEM was aspirated from the cells and replaced with either 100 µL serum-free DMEM (or with FAS-containing DMEM as described) and the cells were incubated at 37 ºC. Thirty minutes prior to imaging, 5 µL of the DMEM (or the FAS-containing DMEM) was removed from the wells and 5 µL of the BPY solutions were added to the wells and the cells were further incubated at 37 ºC. For treatments with DFO and BPS, 20 mM and 50 mM stock solutions were prepared in millipore water and diluted 80-fold and 20-fold with DMEM containing 10% FBS to obtain 250 µM and 1 mM solutions, respectively. The solutions were sterilized by filtration through a 0.2 µm filter. Nine hours prior to imaging, the serum-containing media was aspirated from the cells and replaced with the chelator-containing media and the treated cells were incubated at 37 ºC. Ninety minutes before imaging, the serum-containing chelator treatments were aspirated from the cells and replaced with equivalent concentrations of chelator in serum-free DMEM, and the cells were further incubated at 37 ºC.

To prepare the solutions of ICL-1 for imaging, 0.5 mM (PC3M-Luc, HEK293-luc, and LNCaP-Luc) or 0.25 mM (MDA-MB-231-Luc) solutions of the probe were prepared in DMSO and diluted 40-fold in HBSS (20 and 10 µM final concentrations, respectively). At the end of the treatment times, the cells were aspirated of the chelator- and/or iron-containing media and replaced with the probe-containing HBSS. The plates were immediately imaged for 1 h (for PC3M-Luc and HEK293-Luc) or 30 min (LNCaP-Luc and MDA-MB-231-Luc) with 1 min exposure times and segments with delay times of 1 - 3 min between segments. For control experiments, cells were treated under the same conditions and imaged with 1 µM aminoluciferin.

Animals

FVB-luc$^+$ (FVB-Tg(CAG-luc,-GFP)L2G85Chco/J) mice were obtained from our in-house breeding colony. Mice were group-housed on a 12∶12 light–dark cycle at 22 °C with free access to food and water. All animal studies were approved by and performed according to the guidelines of the Animal Care and Use Committee of the University of California, Berkeley or the Vanderbilt University Medical Center Institutional Animal Care and Use Committee.

General animal imaging methods and data analysis

A Xenogen IVIS Spectrum instrument (Caliper Life Sciences) was used for bioluminescence imaging in all animal experiments, and image analysis was performed using the Living Image software. The total photon flux for each animal was determined by drawing a region of interest around the entire animal and integrating the photon flux over the total imaging period. Mice were anesthetized prior to injection and during imaging via inhalation of isoflurane. Isoflurane was purchased from Phoenix Pharmaceuticals, Inc. DMSO, BPY, and pharmaceutical grade ferric ammonium citrate (FAC) were purchased from Sigma-Aldrich, and medical-grade oxygen was purchased from Praxair.

In vivo imaging with ICL-1

Six to ten-week old FVB-luc$^+$ were given intraperitoneal (i.p.) injections of the following sets of compounds and/or vehicles under anesthesia (isoflurane inhalation 2-3%). To measure basal signals from ICL-1 or D-luciferin, FVB-luc$^+$ mice were injected with either ICL-1 (10 - 50 nmol in 25 µL DMSO, 75 µL DPBS; 100 - 200 nmol in 25 µL DMSO, 25 µL DPBS) or D-luciferin (25 nmol in 100 µL DPBS) prior to any treatment. To visualize changes in bioluminescence from various treatments, the same doses and volumes of the imaging agents were administered after i.p. injection of vehicle (50 µL DPBS), FAC (20 mg/kg in 50 µL PBS)), BPY (8mg/kg; 0.4mg/uL stock in absolute ethanol, diluted 200-fold with DPBS, 100uL injected for a 25 g mouse) or both FAC and BPY (5 mg/kg in 50 µL PBS). Injections of vehicle and FAC were performed 1 h prior to imaging and BPY was injected 20 min prior to imaging. Following the treatment period, ICL-1 was injected and mice were immediately transferred to a Xenogen IVIS Spectrum (Caliper Life Sciences) and imaged for 50 min under isoflurane anesthesia (2%). For the treatment conditions, the data are depicted as a ratio of the imaging signal prior to treatment to the imaging signal after treatment.

To determine the clearance kinetics of the imaging agents, male FVB-luc$^+$ were given i.p. injections of 25 nmol ICL-1 or D-luciferin as described above, and images were acquired at 5 and 20 min, as well as 1, 3, 6, 9, 12, and 24 hours post-injection. For each time point, mice were anesthetized under isoflurane (2%) for 3 min prior to imaging, then transferred to a Xenogen IVIS Spectrum (Caliper Life Sciences) for image acquisition.

To investigate different methods of ICL-1 administration, male FVP-luc+ were anesthetized with 2,2,2-tribromoethanol diluted in PBS and administered 25 nmol ICL-1 or D-luciferin by either i.p. or retro-orbital injection. Mice were immediately transferred to a Xenoven IVIS Spectrum (Caliper Life Sciences) and imaged for 50 min.

Murine model of *A. baumannii* systemic infection

Mice were infected retro-orbitally with *A. baumannii* strain ATCC 17978 grown to mid-exponential phase in Luria broth (LB), washed, and resuspended in 100 μL ice-cold PBS totaling 2-4 x 10^8 colony forming units (CFU) of bacteria. At 24 hours post-infection, mice were imaged as described. For ex vivo imaging, mice were euthanized, and organs were collected and immediately imaged using a Xenogen IVIS Spectrum (Caliper Life Sciences). To determine bacterial burdens, mice were euthanized and CFU enumerated for hearts, lungs, livers, and kidneys following tissue homogenization in sterile PBS and spot-plating of serial dilutions onto solid medium. For elemental and imaging analyses, organs were flash-frozen in liquid nitrogen and stored at -80˚C.

Tissue sectioning

Livers were sectioned at -20˚C using a Thermo Fisher Scientific CryoStar NX70 Cryostat (Thermo Fisher Scientific, Waltham, MA). Sections for LA-ICP-MS were sectioned at 30 μm thickness and thaw-mounted onto nitric-acid washed poly(L)lysine-coated vinyl slides (Electron Microscopy Sciences, Hatfield, PA). Regions of interest were selected across animals by gallbladder localization. Serial sections for histological analysis were sectioned at 10 μm thickness, collected onto microscope slides, hematoxylin and eosin stained, and scanned at 20x magnification using a Leica SCN400 Brightfield Slide Scanner (Leica Microsystems, Buffalo Grove, IL).

Inductively coupled plasma mass spectrometry

Whole organs were homogenized in 1 mL PBS and digested in 2 mL HNO_3 (Optima grade metal-free; Thermo Fisher Scientific, Waltham, MA) and 500 uL H_2O_2 (EMD Chemicals, Gibbstown, NJ) at 85˚C overnight in metal-free Teflon jars. Digested samples were diluted in millipore water and submitted for inductively coupled plasma mass spectrometry (ICP-MS) analysis at the Vanderbilt Mass Spectrometry Research Center. Element quantification analysis on acid-digested liquid samples was performed using ELEMENT 2™ high resolution inductively coupled plasma mass spectrometry (HR-ICP-MS, Thermo Fisher Scientific, Bremen, Germany) coupled with ESI auto sampler (Elemental Scientific, Omaha, NE). The ICP-MS is equipped with a PFA microflow nebulizer (Elemental Scientific, Omaha, NE), a Scott double-pass spray chamber (at room temperature), a magnetic sector followed by an electric sector, and a second electron multiplier. Liquid sample was up-taken by self-aspiration via 0.50 mm ID sample probe and sample capillary. Interested metals were measured at medium resolution (R=4200).

Laser ablation inductively coupled plasma mass spectrometry

Elemental imaging were performed using LSX-213 laser ablation system (LA, CETAC, Omaha, USA) online coupled with ELEMENT 2™ inductively coupled plasma mass spectrometry (HR-ICP-MS, Thermo Fisher Scientific, Bremen, Germany). Slices of mouse liver were mounted on polylysine coated slides, then placed in sealed ablation cell and ablated in multi-parallel-line mode at a rate of 30 µm/s using a focused Nd:YAG laser beam (213 nm) at a round-shaped spot size of 100 µm diameter. The ablated sample particles were then transferred to ICP-MS for the detection at medium resolution (R=4200).

qRT-PCR of liver tissues

For analysis of mRNA by qRT-PCR, tissues were immediately placed in RNAlater (Thermo Fisher) after harvesting. mouse livers were minced into 5-10 mg samples and RNA was isolated from homogenized samples using the RNeasy Mini Kit (Qiagen) according to manufacturer's protocols. From the isolated RNA, cDNA was synthesized from 1 μg of RNA using the iScript Reverse Transcription Supermix for qRT-PCR kit (Bio-Rad) and the resulting cDNAwas amplified by quantitative real-time PCR using the 2x iQ SYBR Green Supermix (Bio-Rad) and the BioRad iCycler iQ Multicolor qRT-PCR Detection System. The cDNA levels were normalized to GAPDH and the fold-change in gene expression between mock-infected and infected mice were determined through the comparative Cq method ($2^{-\Delta\Delta Cq}$) and plotted the $\log_2$(fold change). The primers used for the analysis are shown in **Table 8**.

Serum protein analyses

Serum was collected 24 hours post infection from male FVB-luc$^+$ mice either mock-infected or infected with *A. baumannii*. Serum transferrin and ferritin levels were processed through the Vanderbilt Translational Pathology Shared Resource facility using the Vet Axcel Chemistry Analyzer (Alfa Wassermann Diagnostic Techologies, West Caldell, NJ).

Table 8. Oligonucleotides used in Chapter V.

Gene		**Primer Sequence**
GAPDH	fwd	5'-ATGGTGAAGGTCGGTGTGAA-3'
GAPDH	rev	5'-AGTGGAGTCATACTGGAACA-3'
HMBS	fwd	5'-ACTCTGCTTCGCTGCATTG-3'
HMBS	rev	5'-AGTTGCCCATCTTTCATCACTG-3'
RPLP0	fwd	5'-AGATTCGGGATATGCTGTTGGC-3'
RPLP0	rev	5'-TCGGGTCCTAGACCAGTGTTC-3'
FPN	fwd	5'-GGGTGGATAAGAATGCCAGACTT-3'
FPN	rev	5'-GTCAGGAGCTCATTCTTGTGTAGGA-3'
TfR	fwd	5'-CGCTTTGGGTGCTGGTG-3'
TfR	rev	5'-GGGCAAGTTTCAACAGAAGACC-3'
DMT1	fwd	5'-AGGTGACACTATAGAATAGCCAGCCAGTAAGTTCAAGG-3'
DMT1	rev	5'-GTACGACTCACTATAGGGAGCTGTCCAGGAAGACCTGAG-3'
Hepcidin	fwd	5'-GGCAGACATTGCGATACCAAT-3'
Hepcidin	rev	5'-TGCAACAGATACCACACTGGGAA-3'
LCN2	fwd	5'-CCATCTATGAGCTACAAGAGAACAAT-3'
LCN2	rev	5'-TCTGATCCAGTAGCGACAGC-3'
FHC	fwd	5'-TGGAACTGCACAAACTGGCTACT-3'
FHC	rev	5'-ATGGATTTCACCTGTTCACTCAGATAA-3'
FLC	fwd	5'-CGTGGATCTGTGTCTTGCTTCA-3'
FLC	rev	5'-GCGAAGAGACGGTGCAGACT-3'
IRP1	fwd	5'-GCGGATCCTACTGGGCCATCTTTCGGAT-3'
IRP1	rev	5'-GCTCTAGAGGCAGAGAGCTATGAGCGCATTCAC-3'
IRP2	fwd	5'-AGGTGACACTATAGAATATGAAGAAACGGACCTGCTCT-3'
IRP2	rev	5'-GTACGACTCACTATAGGGAGCTCACATCCAACCACCTCT-3'

Results and Discussion

Design and synthesis of Iron-Caged Luciferin-1 (ICL-1)

Our design of ICL-1 involved caging D-luciferin with a 1,2,4-trioxolane scaffold (Fontaine et al.) used previously for *in vivo* delivery of therapeutic payloads in an Fe^{2+}-dependent manner (Lauterwasser et al., 2015; Spangler et al., 2016a). The excellent pharmacokinetic properties of these therapeutic conjugates suggested that ICL-1 would have suitable *in vivo* properties for the desired imaging applications. In the conjugate form, ICL-1 is an incompetent substrate for the luciferase enzyme. Upon Fe^{2+}-promoted reduction of the peroxide, however, a cyclohexanone intermediate is formed that spontaneously releases free D-aminoluciferin, which luciferase can transform to produce a bioluminescent signal (**Figure 35**). D-aminoluciferin imaging can be used as a control for changes in enzyme activity and can be used in parallel for signal normalization. **Figure 36** depicts the synthetic route to ICL-1. Briefly, commercially available 6-amino-2-cyanobenzothiazole is activated using triphosgene, which is subsequently reacted with (±)-*trans*-**1** (Fontaine et al.) to yield carbamate **2**. Cyclization of **2** with D-cysteine-HCl affords ICL-1 after high-performance liquid chromatography (HPLC) purification.

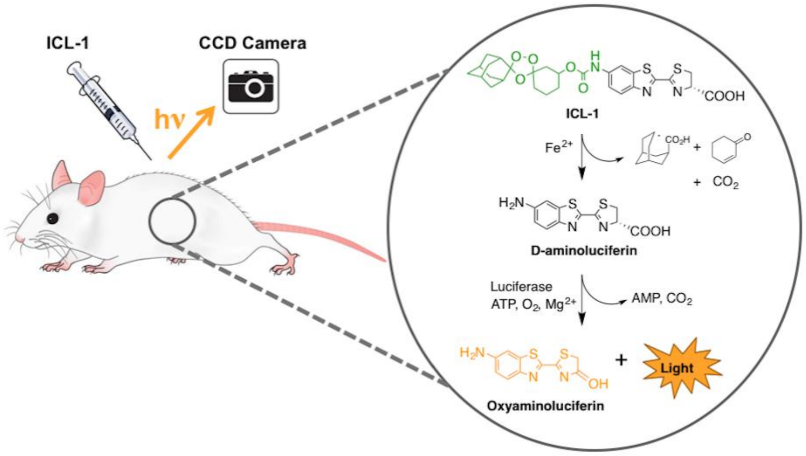

Figure 35. Mechanism of Fe^{2+}-dependent cleavage of Iron-Caged Luciferin-1 (ICL-1), an endoperoxide-luciferin conjugate and in vivo probe of Fe^{2+}.

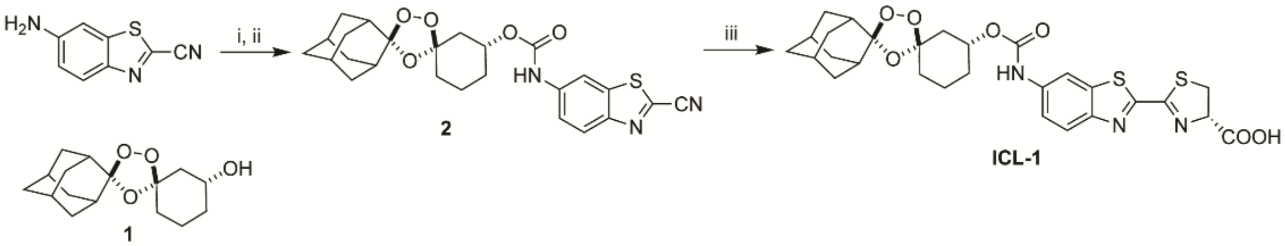

Figure 36. Synthesis of ICL-1[a]**;** [a]Reagents and conditions: (i) triphosgene, 4-DMAP, toluene, 125 °C to 35 °C, 3 h; (ii) **1**, NaH, toluene, 35 °C, 12 h, 80% over two steps; (iii) D-cysteine, K_2CO_3, CH_2Cl_2, MeOH, H_2O, 0 °C, 12 h, 24%.

Reactivity and selectivity of ICL-1

Fe^{2+}-dependent reactivity of ICL-1 was assessed in aqueous solution buffered to physiological pH (50 mM HEPES, pH 7.4). Treatment of 5 μM ICL-1 with ferrous ammonium sulfate (FAS) as an Fe^{2+} source at concentrations spanning 25 to 100 μM shows a dose-dependent increase in bioluminescent signal in the presence of luciferase (**Figure 37A**, gray bars), saturating at a ca. 7-fold bioluminescent signal enhancement at highest Fe^{2+} concentrations, when incubation is performed aerobically, versus a ca. 30-fold bioluminescent signal enhancement at the same Fe^{2+} concentration, when incubation is performed anaerobically (**Figure 38**). The observed signal increase is Fe^{2+}-dependent, as co-incubation of ICL-1/luciferase solutions with the Fe^{2+} chelator bipyridine results in a decrease in bioluminescence intensity (**Figure 37A**, gray patterned bars). Further control experiments establish that iron-dependent responses are not observed with the parent D-aminoluciferin substrate (**Figure 39**), aside from a slight decrease in signal observed with hemoglobin. ICL-1 exhibits high selectivity for Fe^{2+} over other biologically relevant d-block and s-block metals, including redox-active copper and cobalt transition metals (**Figure 37B**). A modest response is observed with free copper salts, as is similarly observed for the related fluorescence probe FIP-1 (Aron et al., 2016). However, as a typical eukaryotic cell exhibits a ca. 10-fold higher level of iron over copper coupled with the high buffering capacity of copper with glutathione and metallochaperones (pM-fM K_d values) (Ackerman et al., 2017; Cerchiaro et al., 2013; Cotruvo et al., 2015; Epsztejn et al., 1997; Ramos-Torres et al., 2016; Rubino and Franz, 2012), the modest response to free copper salts suggests that ICL-1 should have sufficient selectivity to detect alterations in biological ferrous iron levels. ICL-1 is also selective for labile Fe^{2+} over other biologically-relevant forms of iron that are tightly bound to proteins and cofactors, such as transferrin, ferritin, hemin, and hemoglobin, as well as Fe^{3+}, along with reductants glutathione, N-acetyl cysteine, β-mercaptoethanol, and ascorbic acid (**Figure 37C**).

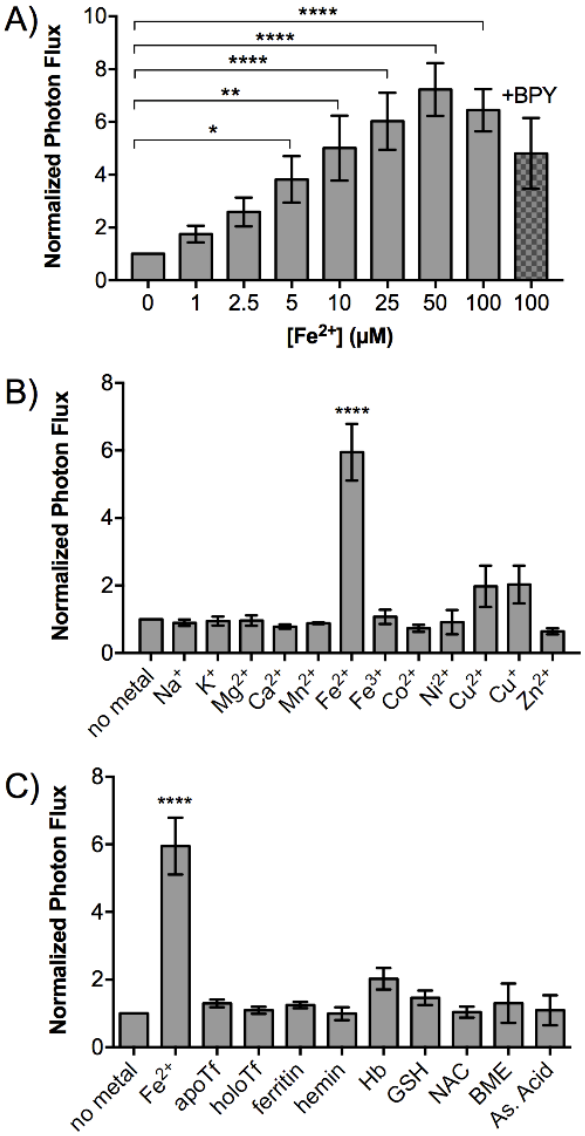

Figure 37. ICL-1 selectively responds to Fe^{2+} over other metals and tightly-bound biological iron species with metal and redox specificity. Bioluminescence response of ICL-1 incubated with A) varying concentrations of Fe^{2+} as the ferrous ammonium sulfate salt (FAS) (gray bars) or 100 µM FAS with 100 µM of the iron chelator bipyridine (BPY, gray patterned bars), B) various biologically relevant s-block (1 mM) and d-block (100 µM) metal ions, and C) tightly-bound iron-species of biological relevance, such as transferrin (without iron, apoTf; with iron, holoTf), ferritin, hemin, and hemoglobin (Jones et al.), and reductants, such as glutathione (GSH), N-acetyl cysteine (NAC), β-mercaptoethanol (BME), and ascorbic acid (as. acid). Signals are integrated over 30 min and expressed as photon fluxes normalized to ICL-1 bioluminescence with no treatment (buffer alone). Statistical analyses were performed with one-way analysis of variance (ANOVA) with multiple comparisons to the control with no metal treatment, where $*p \le 0.05$, $**p \le 0.01$ and $****p \le 0.0001$. Error bars are ± SEM (n = 3).

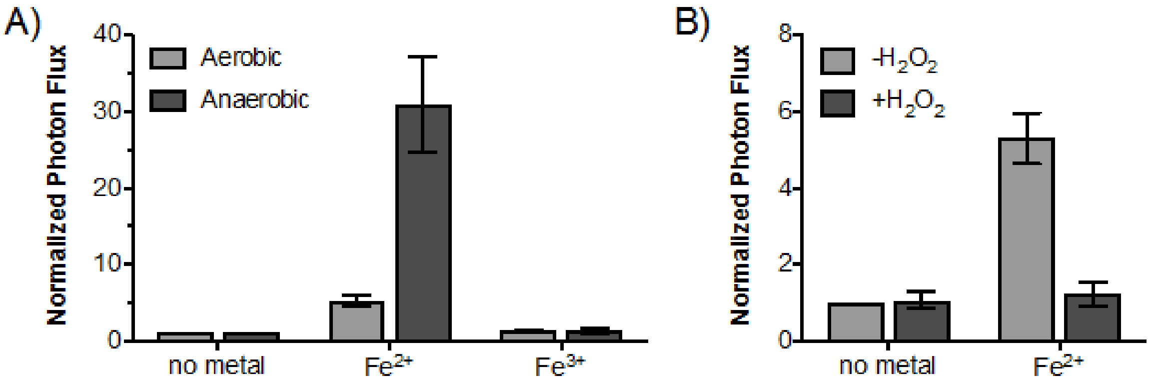

Figure 38. ICL-1 selectively responds to Fe^{2+} over other metals and biologically-relevant oxidants. Bioluminescence response of ICL-1 incubated with A) 100 µM Fe^{2+} or Fe^{3+} in aerobic versus anaerobic incubation conditions, or B) hydrogen peroxide in the absence and presence of Fe^{2}. Signals are integrated over 30 min and expressed as photon fluxes normalized to ICL-1 bioluminescence with no treatment (buffer alone). Error bars are ± SEM (n = 3).

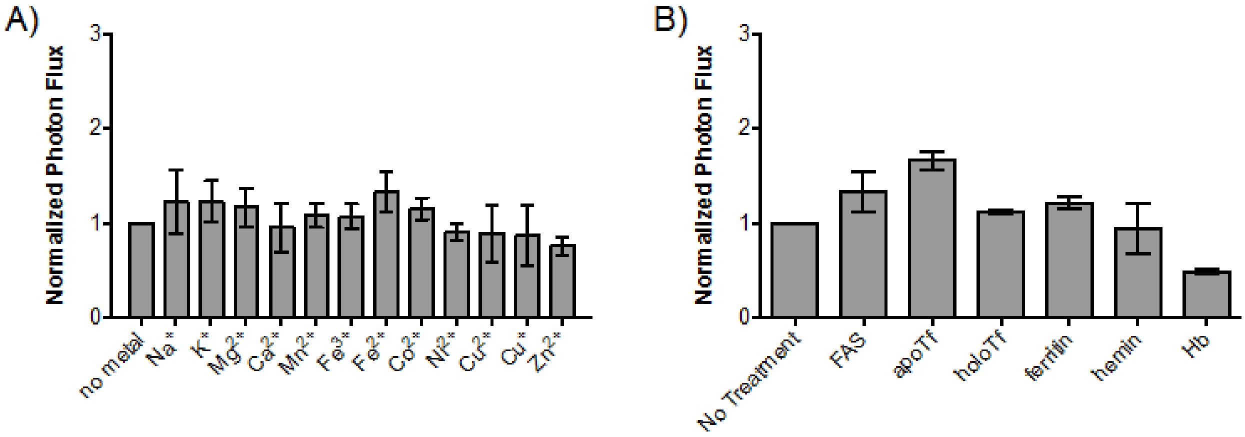

Figure 39. The selective response of ICL-1 to ferrous iron is not observed when the same treatments are performed with aminoluciferin. Bioluminescence response of aminoluciferin incubated with A) various biologically relevant s-block (1 mM) and d-block (100 µM) metal ions and B) biologically-relevant non-labile iron-containing species, namely transferrin (without iron, apoTf; with iron, holoTf), ferritin, hemin, and hemoglobin (Jones et al.). Signals are integrated over 30 m and expressed as photon fluxes normalized to aminoluciferin bioluminescence with no treatment (buffer alone). Statistical analyses were performed with one-way analysis of variance (ANOVA) with multiple comparisons to the control with no metal treatment, and no statistically significant differences were observed. Error bars are ± SD (n = 3).

ICL-1 detects changes in labile iron levels in living cells

We next sought to evaluate the ability of the ICL-1 probe to detect changes in Fe^{2+} levels in live cells. Initial experiments employed a luciferase-expressing prostate cancer cell line, PC3M-luc, that has been shown previously to respond to TRX-PURO (Spangler et al., 2016b), a cellular Fe^{2+} probe based on the same caging moiety used in ICL-1. Cells were supplemented with various concentrations of an iron salt (FAS), iron chelator (BPY), or FAS followed by BPY, then treated with ICL-1 and imaged using an IVIS bioluminescence imaging system (**Figure 40**). Iron supplementation results in an increase in ICL-1-dependent bioluminescence that can be attenuated by addition of BPY. Additionally, iron deficiency induced by treatment with BPY alone results in a decrease in ICL-1 signal relative to basal levels. Notably, ICL-1 exhibits excellent stability in media (**Figure 41**). Additionally, ICL-1 signal is unaffected by short-term treatment with a cell-impermeable, extracellular iron chelator, bathophenanthrolinedisulfonic acid (BPS), suggesting that observed ICL-1 reactivity is due to intracellular, as opposed to extracellular, iron (**Figure 42**). Control experiments with the parent D-aminoluciferin substrate show no sensitivity to iron status.

The probe was further evaluated in a broader set of luciferase-expressing cell lines and with additional iron chelators. In addition to PC3M-luc, a second prostate cancer cell line (LNCaP-luc), breast cancer cell line (MDA-MB-231-luc), and embryonic kidney cell line (HEK293-luc) were each treated with FAS, the iron chelators desferroxamine (Zastrow et al.), BPS, or BPY, or a combination of FAS and BPY for ICL-1 imaging (**Figure 43**). Consistent with what is observed using PC3M-luc cells, LNCaP-luc, MDA-MB-231-luc, and HEK-293-luc cells supplemented with 100 µM FAS exhibit increased light production relative to untreated control cells, and these increases are attenuated by co-incubation with the iron chelator BPY. Likewise, iron depletion induced by chelator addition results in decreases in ICL-1-dependent bioluminescence in all cell lines tested. Again, control experiments confirm that D-aminoluciferin signal is not affected by either iron supplementation and/or depletion (**Figure 44**). The data establish that ICL-1 can assess labile Fe^{2+} status across many cell types.

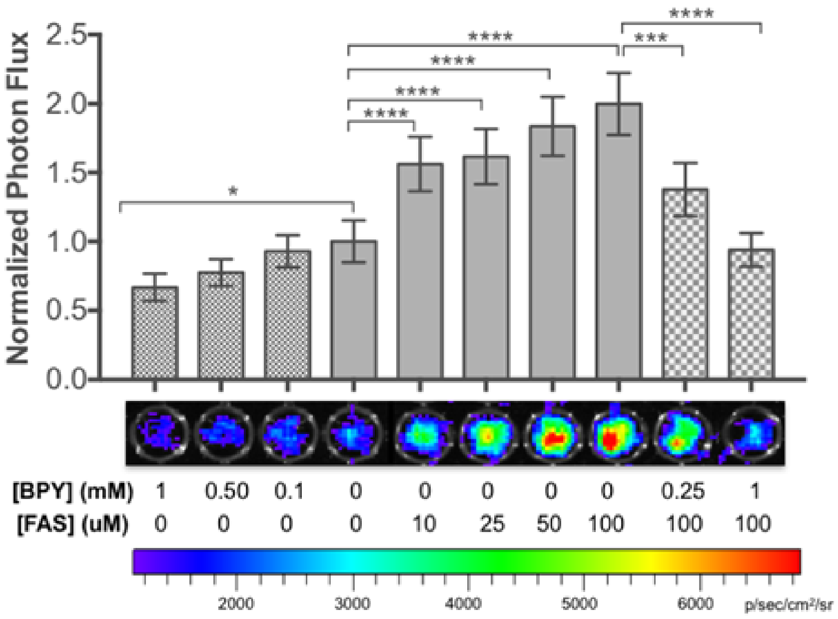

Figure 40. Bioluminescent signals from PC3M-luc cells probed with ICL-1. Cells were supplemented with varying concentrations of FAS for 90 min, BPY for 30 min, or a combination the two chemicals followed by addition of ICL-1 (20 µM). Total photon flux was integrated over 1 hr and normalized to cells treated with buffer alone. Representative bioluminescence images of PC3M-luc cells with each treatment are shown below the corresponding data bar in the graph. Statistical analyses were performed with one-way analysis of variance (ANOVA) with multiple comparisons to the control with no metal treatment, where $*p \leq 0.05$, $***p \leq 0.001$ and $****p \leq 0.0001$. Error bars are ± SD (n = 3 - 5).

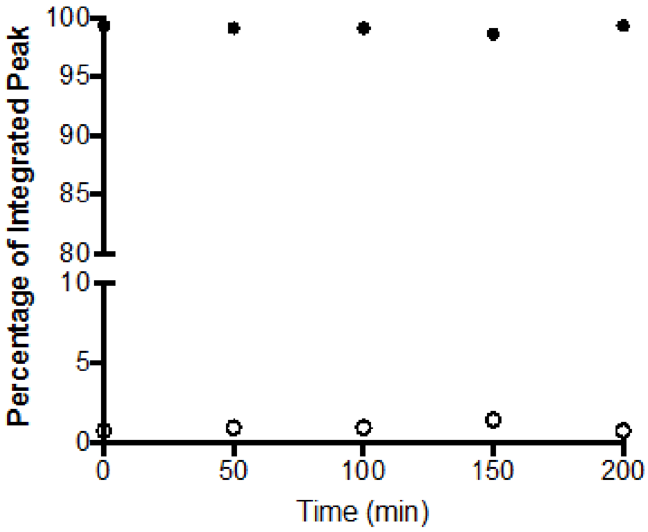

Figure 41. ICL-1 exhibits stability of over 200 minutes assayed, as followed by an LCMS assay. ICL-1 dissolved in DMSO was added to HBSS and aliquots were assessed at various time points (t=0, 50, 100, 150, 200 minutes). Over the 200 minutes assayed, no significant uncaging of ICL-1 (solid circles) to D-aminoluciferin (hollow circles) is observed.

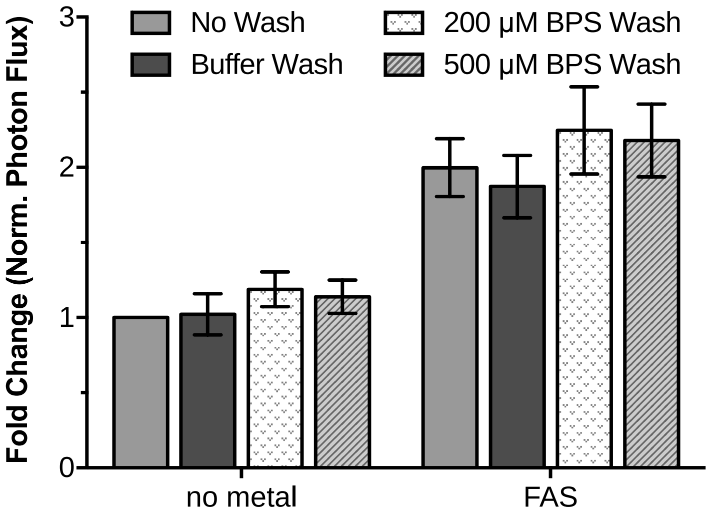

Figure 42. Bioluminescent signals from PC3M-Luc cells probed with ICL-1. Cells were supplemented with 50 µM FAS (90 min), then were either unwashed, washed with HBSS buffer, or washed with 200 or 500 µM bathophenanthrolinedisulfonic acid (BPS, an extracellular iron chelator), then imaged with 20 µM ICL-1 or 1 µM D-aminoluciferin. Total photon flux was integrated over 1 h; this signal was divided by D-aminoluciferin signal then normalized to cells treated with buffer alone. Signal is unaffected by short treatment with an extracellular iron chelator, suggesting that ICL-1 releases intracellularly.

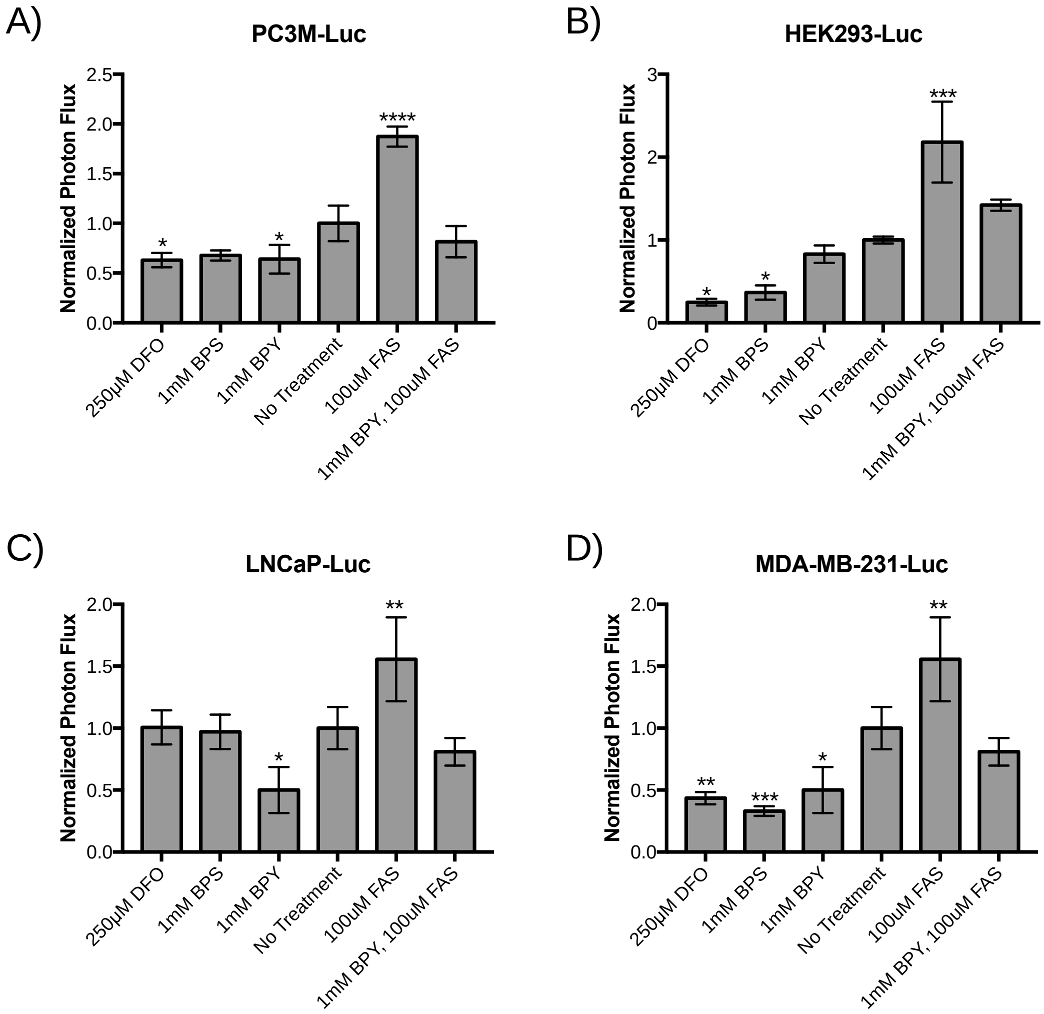

Figure 43. Bioluminescent signals from A) PC3M-Luc, B) HEK293-Luc, C) LNCaP-Luc, and D) MDA-MB-231-Luc cells probed with ICL-1. Cells were supplemented with 250 µM DFO (9 hours), 1 mM BPS (9 hours), 1 mM BPY (30 min), 100 µM FAS (90 min) or both BPY and FAS and imaged with either 20 µM (PC3M-Luc, HEK293-Luc, LNCaP-Luc) or 10 µM (MDA-MB-231-Luc) of ICL-1. Total photon flux was integrated over 1 h (PC3M-Luc and HEK293-Luc) or 30 min (LNCaP-Luc or MDA-MB-231-Luc) and normalized to cells treated with buffer alone. Statistical analyses were performed with one-way analysis of variance (ANOVA) with multiple comparisons to the control with no metal treatment, where $^{*}p \leq 0.05$, $^{**}p \leq 0.01$, $^{***}p \leq 0.001$ and $^{****}p \leq 0.0001$. Error bars are ± SD (n = 3 - 5).

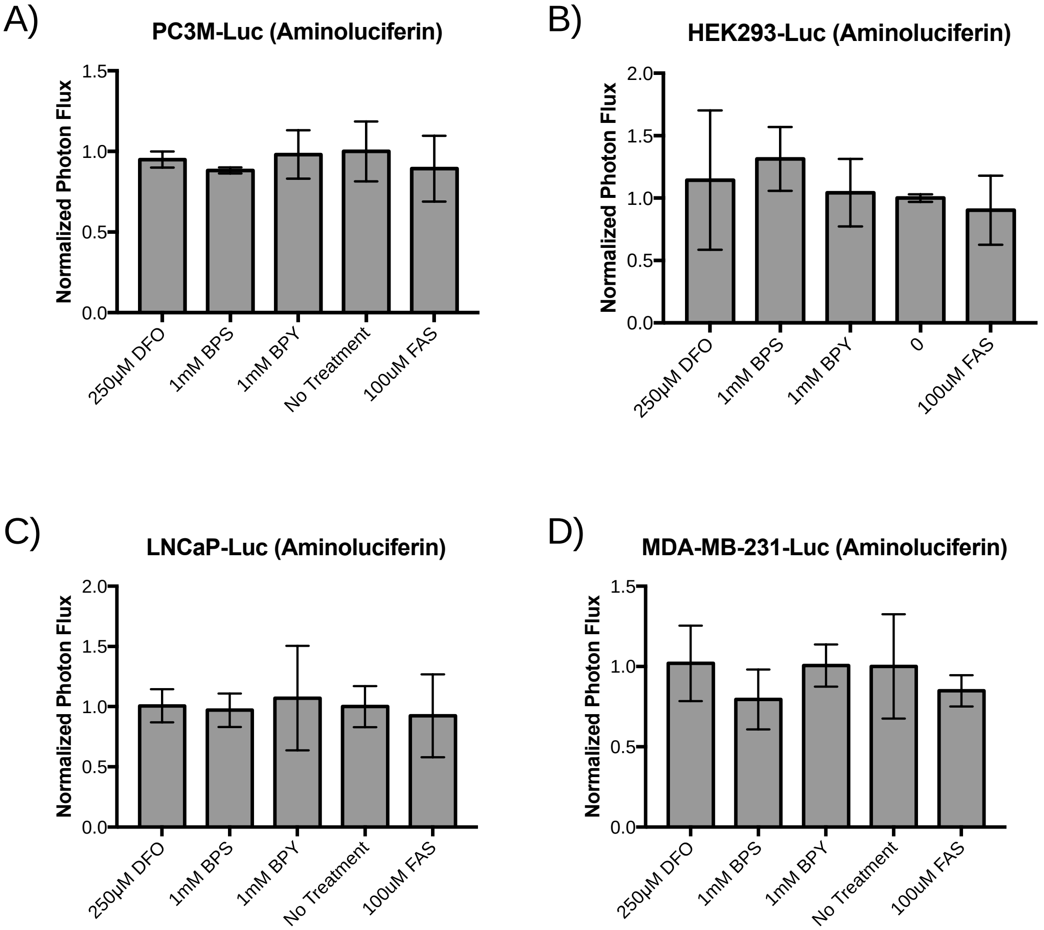

Figure 44. Bioluminescent signals from A) PC3M-Luc, B) HEK293-Luc, C) LNCaP-Luc, and D) MDA-MB-231-Luc cells probed with aminoluciferin. Cells were supplemented with 250 µM DFO (9 hours), 1 mM BPS (9 hours), 1 mM BPY (30 min), 100 µM FAS (90 min) or both BPY and FAS and imaged with either 1 µM amionluciferin. Total photon flux was integrated over 1 h (PC3M-Luc and HEK293-Luc) or 30 min (LNCaP-Luc or MDA-MB-231-Luc) and normalized to cells treated with buffer alone. Statistical analyses were performed with one-way analysis of variance (ANOVA) with multiple comparisons to the control with no metal treatment, and no statistically significant differences were observed. Error bars are ± SD (n = 3 - 5).

ICL-1 detects changes in labile iron levels in living mice

Having established the ability of ICL-1 to assess labile iron levels in living cells, we next utilized this chemical tool to visualize labile iron stores in living mice. For these studies, we employed FVB-luc$^+$ mice strains using the actin-promoter to induce expression of this enzyme in virtually all organs. Intraperitoneal (i.p.) injection of varying amounts of ICL-1 (10, 25, 50, 100, and 200 nmol; **Figure 45**) into age- and weight-matched male FVB-luc$^+$ mice was performed with subsequent IVIS imaging of the live mice. The ICL-1-dependent bioluminescent signal rises with increasing probe dose in the range of 10 to 50 nmol, with saturation at ≥100 nmol of injected probe. The signal shows the most intense localization in the peritoneal region, and is consistent with the expected high levels of iron in the intestines (**Figure 46A**). Administration of ICL-1 into the bloodstream via retro-orbital injection mirrors the signal visualized in animals with D-luciferin injected through the same route (**Figure 47**). The long-term clearance kinetics in male FVB-Luc$^+$ mice were evaluated at a dose of 25 nmol ICL-1; the bioluminescent signal sharply increases from 0-20 minutes post-injection of the probe and slowly clears by 6 h (**Figure 48A, C**). The clearance kinetics differ from D-luciferin, the native substrate of firefly luciferase, which peaks in bioluminescence at 5 min and rapidly clears by 3 h (**Figure 48B, D**). The observed differences between the metabolic clearances of ICL-1 and D-luciferin are consistent with the slow kinetics of the trioxolane-based trigger to release the parent luciferin from ICL-1 upon reaction with Fe^{2+}, relative to bioluminescence generation from enzymatic recognition and clearance from the system. Interestingly, the ICL-1 probe response is different between male and female mice, with the females exhibiting a >2-fold increase in signal over males (**Figure 49A**). In contrast, injection of both male and female mice with equivalent doses of D-luciferin results in similar bioluminescent signal (**Figure 49B**). The results suggest that females may have higher resting levels of LIPs compared to males, an interesting but complex observation that merits further investigation (Hahn et al., 2009; Kong et al., 2014).

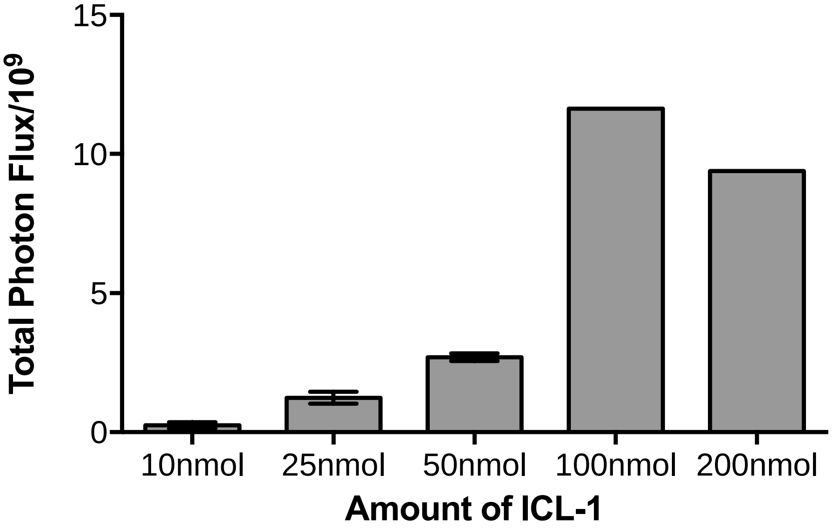

Figure 45. Basal levels of iron can be detected in FVB-luc$^+$ with a dose-dependence on ICL-1 concentration. Mice were injected with 10, 25 nmol, 50 nmol, 0.1 µmol, and 0.2 µmol ICL-1 and total photon flux was acquired 0-50 min post-injection; n = 3 - 5 and error bars are ± SEM.

To determine the responses of ICL-1 to elevations in iron levels, male FVB-luc$^+$ mice were treated with a sub-lethal dose of an iron supplement, ferric ammonium citrate (FAC), 1 hr prior to probe injection (**Figure 46**). The data are plotted as a ratio of signals from treated animals over animals under basal conditions, determined from a 25-nmol i.p. injection of ICL-1 for each corresponding animal 2 to 4 days prior to treatment with FAC. Treatment of FAC-supplemented mice with 20 mg/kg ICL-1 introduced by i.p. injection resulted in a ca. 77% increase in signal over mice treated with Dulbecco's Phosphate-Buffered Saline (DPBS) vehicle alone. In contrast, FAC-supplemented mice that were subsequently treated with the ferrous iron chelator BPY for 20 min prior to probe injection (8 mg/kg, i.p.) showed a ca. 47% reduction in signal compared to mice treated with vehicle alone. Further experiments establish that ICL-1 can also respond to depletion of basal levels of LIPs, with a ca. 86% decrease in signal observed in mice treated with BPY (8 mg/kg, i.p.) compared to vehicle control. In line with what was observed in cell-based assays, mice treated with the same doses of either FAC or BPY and imaged with parent D-luciferin do not exhibit differences in bioluminescent signal (**Figure 50**). Taken together, the data establish the ability of ICL-1 to monitor fluctuations in the labile ferrous iron levels in living animals.

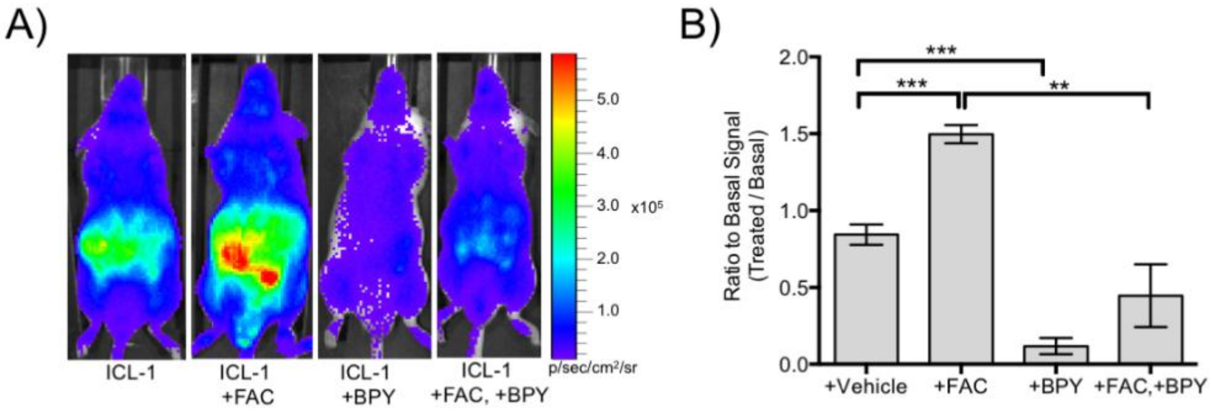

Figure 46. ICL-1 monitors labile iron dynamics in luciferase-expressing mice. FVB-luc$^+$ mice were injected (i.p.) with ICL-1 (25 nmol) after i.p. injection of vehicle (DPBS), FAC (20 mg/kg), BPY (8 mg/kg), or both FAC and BPY. Mice were injected with vehicle or FAC 1 h prior to injection of ICL-1 and with BPY 20 min prior to injection of ICL-1. A) Representative images of FVB-luc$^+$ mice treated with vehicle, FAC, and/or BPY and imaged with ICL-1. B) Ratios of the total photon fluxes from ICL-1 of treated animals to their basal signals. Basal bioluminescence of each animal was acquired 2-4 days prior to treatment. Bioluminescent photon fluxes were acquired 0-50 min post-injection of the ICL-1 (i.p. injection, 25 nmol). Statistical analyses were performed with a two-tailed Student's *t*-test where $**p \leq 0.01$ and $***p \leq 0.001$ (n = 3 - 7), and error bars are ± SEM.

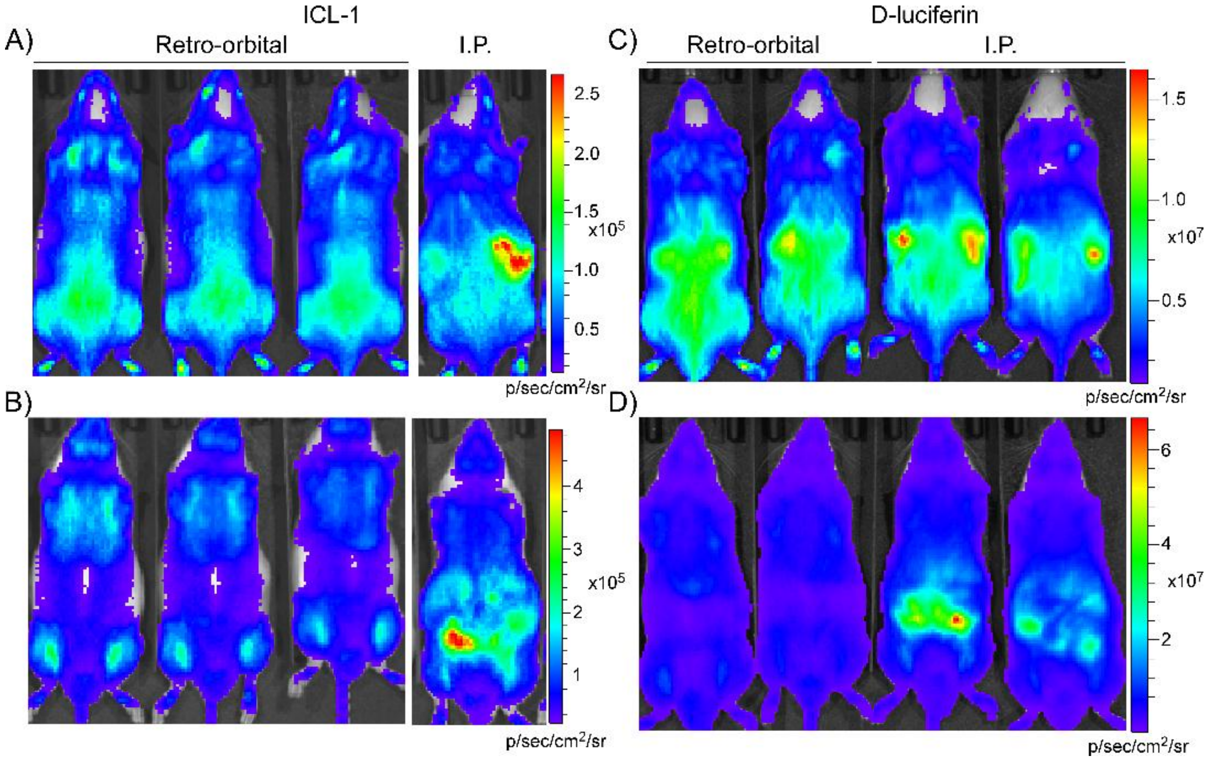

Figure 47. Representative images of Male FVB-luc$^+$ mice administered ICL-1 or D-luciferin either retro-orbitally or i.p. A) Dorsal view 27 min after ICL-1 administration displays slight changes in signal distribution similar to the signal intensity of C) the dorsal view of D-luciferin administration by the two different routes 12 min after D-luciferin injection. B) Ventral view 30 min after ICL-1 administration has similar signal localization patterns as the D) the ventral view of D-luciferin administration at 15 min after D-luciferin injection.

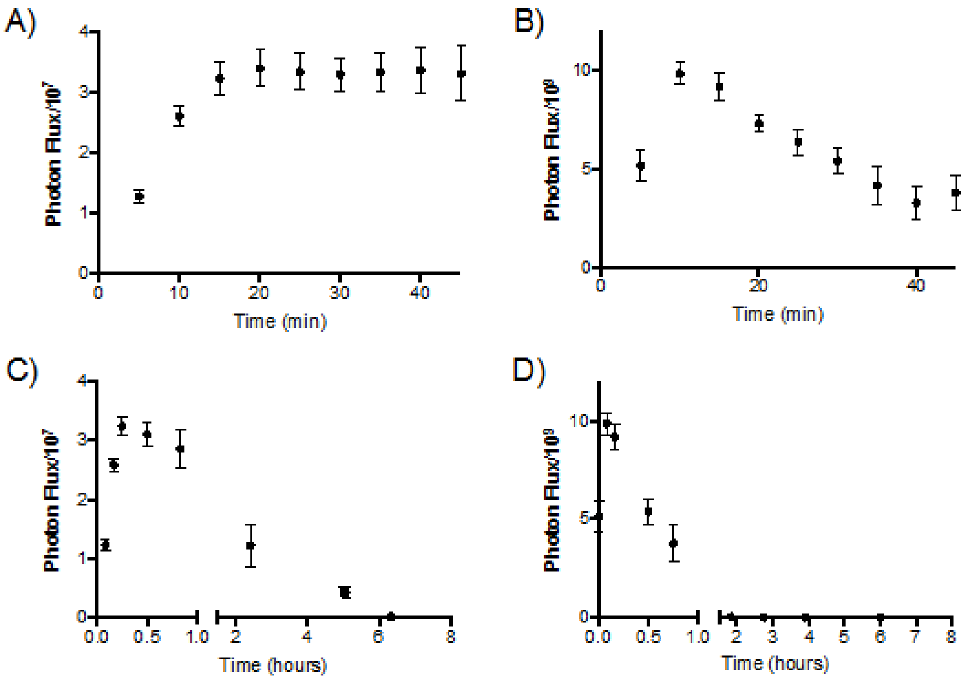

Figure 48. Kinetics of bioluminescence in male FVB-luc$^+$ mice injected with A) 25 nmol ICL-1 or B) 25 nmol D-luciferin over a short (45 min post-injection) time period as well as metabolic clearances of mice injected with C) 25 nmol ICL-1 or D) 25 nmol D-luciferin over a long (6 hours post-injection) time period; n = 3 - 6 and error bars are ± SEM.

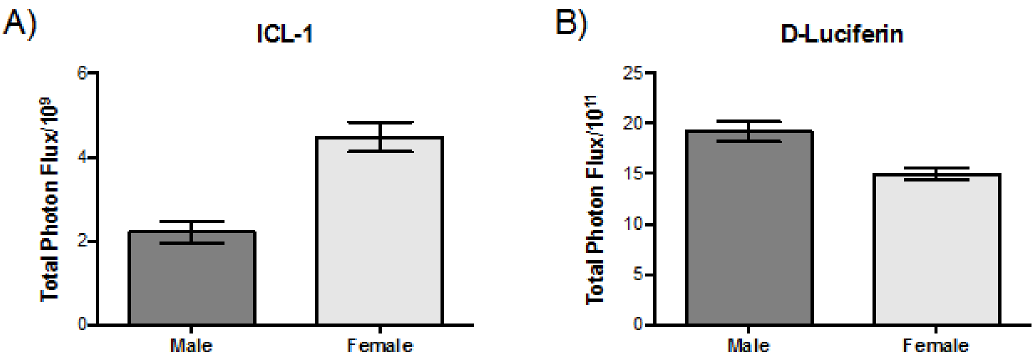

Figure 49. Variations between sexes are observed in FVB-luc$^+$ mice imaged with ICL-1. A) Male and female mice injected and imaged with 25 nmol ICL-1 at 6 - 8 weeks of age and photon fluxes were acquired 0-50 min post-injection.. B) Male and female mice injected and imaged with 25 nmol D-luciferin at 6 - 8 weeks of age and photon fluxes were acquired 0-30 min post-injection. Bio can be detected in FVB-luc$^+$ with a dose-dependence on ICL-1 concentration. Total photon flux was acquired 0-50 min post-injection; n = 4 - 15 and error bars are ± SEM.

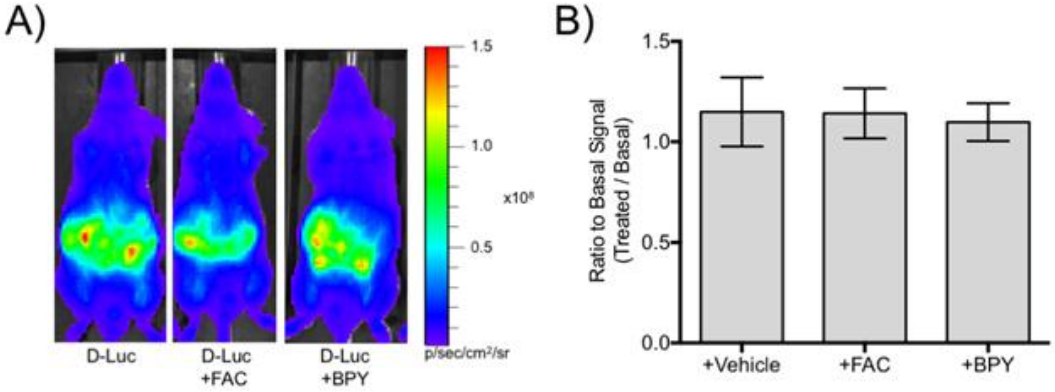

Figure 50. FVB-luc$^+$ with altered levels of iron exhibit no detectable change in bioluminescence signal from imaging with D-luciferin. FVB-luc$^+$ mice were injected (i.p.) with D-luciferin (25 nmol) after i.p. injection of vehicle (DPBS), FAC (20 mg/kg), or BPY (8 mg/kg). Mice were injected with Vehicle or FAC 1 h prior to injection of ICL-1 and with BPY 20 min prior to injection of D-luciferin. A) Representative images of FVB-luc$^+$ mice treated with vehicle, FAC, or BPY and imaged with D-luciferin. B) The data are shown as the ratio of the total photon fluxes from D-luciferin of treated animals to their basal signals. Basal bioluminescence from D-luciferin of each animal was acquired 2 – 4 days prior to treatment. Bioluminescent photon fluxes were acquired 0-30 min post-injection of D-luciferin (i.p. injection, 25 nmol); n = 3 - 7 and error bars are ± SEM. Statistical analyses were performed with a two-tailed Student's *t*-test, and no statistically significant differences were observed.

ICL-1 visualizes changes in labile iron pools in an *A. baumannii* model of systemic infection

To showcase how ICL-1 can enable *in vivo* studies of iron biology, we next utilized this reagent in a live mouse model of bacterial infection. Indeed, host-pathogen interactions involve a competition for iron as a central resource that is essential to both host organisms and microbial pathogens (Palmer and Skaar, 2016). The vertebrate host employs immune defense mechanisms to regulate iron pools against invading pathogens, which in turn have counterstrategies to evade such defenses. As a starting point, we turned our attention to *A. baumannii*, a Gram-negative bacterium that frequently infects patients with impaired immune systems, such as those found in hospitals (ICUs) (Howard et al., 2012), making it a significant health care risk with rises in antibiotic resistance. In this regard, although the precise mechanisms that govern metal nutrient starvation by the host during *A. baumannii* infection remain elusive, previous work has established the importance of iron for its growth in vertebrates. Moreover, adaptations have been identified in the pathogen pointing to the development of iron-dependent survival responses, including upregulation of the ferric uptake regulator (Fur) and its regulon during nutrient iron starvation (Eijkelkamp et al., 2011).

Given the importance of iron regulation to *A. baumannii*, we utilized ICL-1 to assess alterations in iron status in living mice infected with this pathogen. Male FVB-luc$^+$ mice were systemically infected with wild-type *A. baumannii* ($2.0 \times 10^8 - 4.0 \times 10^8$ CFUs) or with mock treatments (PBS, termed “mock-infected”) through retro-orbital injection and imaged with ICL-1 with an IVIS imager 24 h post-inoculation (**Figure 51A**). Following the *in vivo* imaging experiments, the lungs, hearts, kidneys, and livers of the mice were harvested and homogenized, and the bacterial burdens were enumerated. The inoculated mice confirmed detectable levels of infection in all organs tested, consistent with sepsis (**Figure 51B**). Compared to mock-infected mice, the *A. baumannii*-infected mice displayed notable elevations in total bioluminescence signal from ICL-1 (**Figure 51A, Figure 52A**). Importantly, such differences between mock and infected cohorts were not evident in mice that were imaged with the D-luciferin control probe that is not responsive to iron (**Figure 52B**). Moreover, we observed a patent difference in the iron-dependent localization of ICL-1 bioluminescence signal in infected versus mock-infected mice. The highest signal intensities in the mock-infected mice are localized to peritoneal region, whereas the ICL-1 bioluminescent signal in the infected mice is localized to the upper dorsal regions of the animals, which contain the heart, lung, and liver (**Figure 51A**). This infection-dependent signal increase was further validated with *ex vivo* bioluminescent imaging after ICL-1 administration (**Figure 53A,B**). Furthermore, the degree of bacterial burden in the lungs, hearts, and livers of the individual mice largely track with the observed localization of ICL-1 signal in each corresponding mouse (**Figure 54**). In contrast, while some slight relocalization in signal was observed in infected mice imaged with D-luciferin (**Figure 55**), possibly due to ATP release or altered respiration in infected tissues, the changes were to a far lesser degree than in the infected mice imaged with ICL-1.

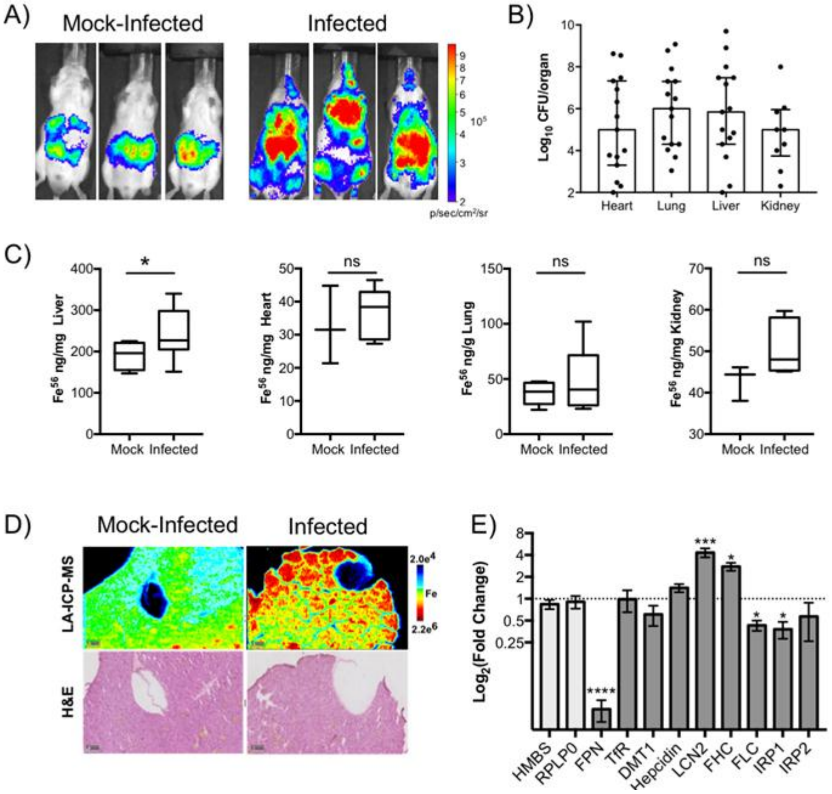

Figure 51. ICL-1 imaging visualizes changes in tissue labile iron levels and distributions in systemic infection with *A. baumannii*. A) Representative images of FVB-Luc$^+$ mice mock-infected with PBS or infected with 2.0 x 10^8 – 4.0 x 10^8 CFUs of *A. baumannii* through retro-orbital injection. Mice were imaged with 25 nmol of ICL-1 at 24 hr post-infection and the dorsal bioluminescent images at 30 min post-injection of the probe are shown. B) Bacterial burdens in the liver, heart, lung, and kidney of infected mice represented as scatter plots with bars representing the medians, with each organ being significantly colonized (n = 9 - 15, $P \leq 0.005$, Wilcoxon Signed Rank Test). Error bars are interquartile ranges. C) Liquid ICP-MS analysis of total iron in the liver, lung, heart, and kidney of mock-infected and infected mice. Tissues were harvested and homogenized 24 hr post-infection. Data are represented as box and whiskers plots (n = 3 - 9) and statistical analyses were performed with a two-tailed Student's *t*-test where $^*P \leq 0.05$. D) LA-ICP-MS analysis of iron in liver tissue slices from a mock-infected and an infected mouse (top) and H&E stains of the corresponding slices (bottom). (E) Gene expression analysis of iron proteins in homogenized liver tissues by real-time PCR. The mRNA levels of each protein were normalized to GAPDH mRNA levels. Data are plotted as the $\log_2$ fold change of the mean gene expression in the livers of infected mice from mean gene expression of the livers of mock-infected mice. The mRNA levels were quantified for the iron transporters ferroportin (FPN), transferrin receptor (TfR) and divalent metal transporter-1 (DMT-1); the secreted factors hepcidin and lipocalin-2 (LCN2); the iron storage proteins ferritin heavy chain (FHC) and ferritin light chain (FLC), and the iron regulatory proteins IRP1 and IRP2 (dark gray bars). The fold-change in gene expression of additional housekeeping genes HMBS and RLPL0 are included as controls (light gray bars). Statistical analyses were performed on $\Delta\Delta C_t$ values with one-way analysis of variance (ANOVA) with multiple comparisons to the GAPDH control, where $^*p \leq 0.05$, $^{***}p \leq 0.001$ and $^{****}p \leq 0.0001$. Error bars are ± SEM (n = 4 - 6).

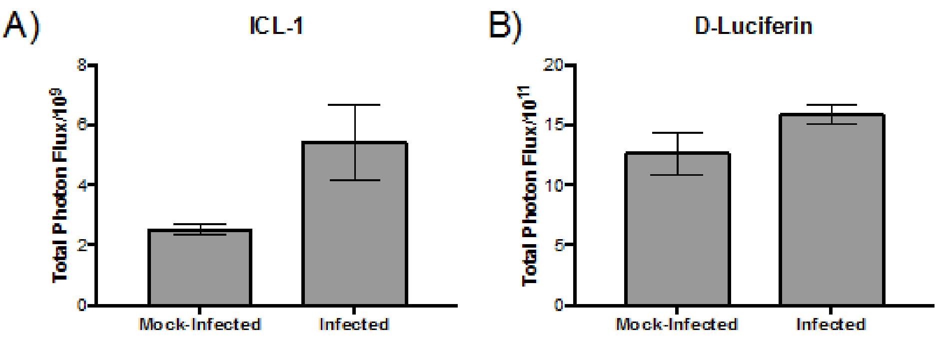

Figure 52. Global bioluminescence signal of FVB-Luc$^+$ mock-infected with PBS or infected with 2.0 x 10^8 – 4.0 x 10^8 CFUs of *A. baumannii* and imaged with 25 nmol A) ICL-1 or B) D-luciferin. Bioluminescent photon fluxes were acquired 0-45 min post-injection of ICL-1 or 0-30 min post-injection of D-luciferin; n = 3 – 6 and error bars are ± SEM.

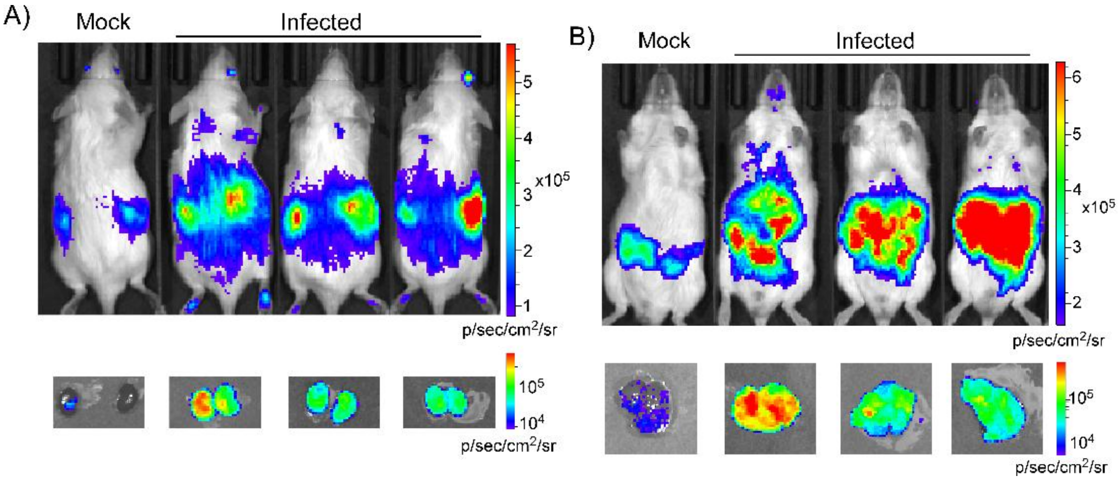

Figure 53. Representative *ex vivo* imaging of organs following ICL-1 probe administration. Male FVB-luc$^+$ mice were administered ICL-1 and imaged for 30 min prior to euthanasia and organ extraction. A) Dorsal view of mice mock-infected or infected with *A. baumannii* at 27 min after ICL-1 administration and corresponding kidney images 40 min after ICL-1 administration. B) Ventral view of mice mock-infected or infected with *A. baumannii* at 30 min after ICL-1 administration and corresponding liver images 35 min after ICL-1 administration.

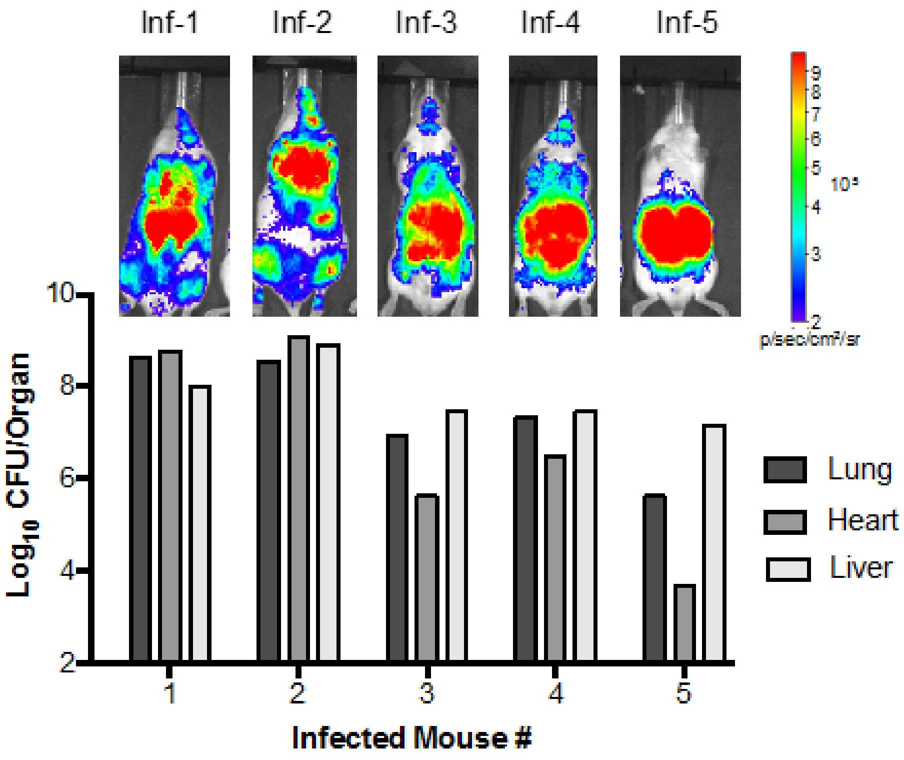

Figure 54. FVB-luc$^+$ mice exhibit a redistribution of signal from ICL-1 upon infection with *A. baumannii*. Representative dorsal images are shown at 30 min post-injection of ICL-1 and 24 hours after infection through retro-orbital injection. The individual bacterial burdens in the heart, liver, and lung of each mice are shown below the corresponding image.

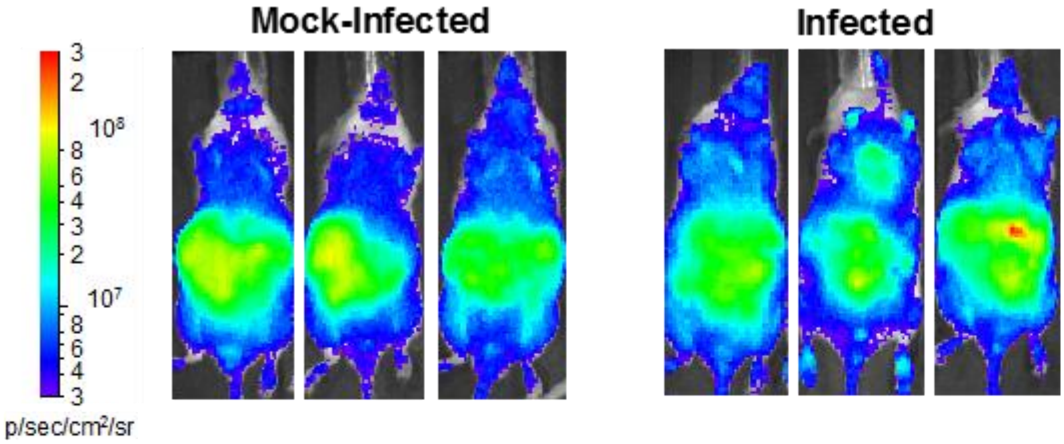

Figure 55. Representative images of FVB-Luc$^+$ mock-infected with PBS or infected with 2.0 x 10^8 – 4.0 x 10^8 CFUs of *A. baumannii* through retro-orbital injection and imaged with D-luciferin. Mice were imaged with 25 nmol of ICL-1 24-hour post-infection and the dorsal bioluminescent images at 25 min post-injection of D-luciferin are shown.

Having observed the differences in labile iron stores between mice infected with *A. baumannii* compared to mock controls, we next performed *ex vivo* metal analyses on the tissues of the infected mice to directly measure and co-register total iron status. First, to assess whether the changes in ICL-1 signal could be attributed to changes in total iron in the tissues, we performed bulk inductively coupled plasma mass spectrometry (ICP-MS) on the lung, liver, heart and kidney. Whereas no statistically significant differences in total iron levels were observed in the heart, lung, and kidney, a statistically significant elevation of total iron levels were observed specifically in livers of infected mice (**Figure 51C**). Such elevations were further corroborated by elemental analysis of iron distributions in liver sections by laser ablation ICP-MS (LA-ICP-MS). As shown in Figure 51D, regions of elevated iron were observed in the peripheries of the liver slices of infected mice compared to those of mock-infected counterparts.

With metal analysis data obtained using multiple complementary techniques, we further probed aspects of how *A. baumannii* infection altered iron metabolism in the host liver by analyzing the changes in gene expression of a selected panel of iron proteins in homogenized liver tissues. Specifically, we measured the mRNA levels of post-transcriptional regulators of iron proteins, IRP1 and IRP2; iron transporters, ferroportin-1 (FPN), transferrin receptor (TfR) and divalent metal transporter-1 (DMT1); the two subunits of the iron storage protein ferritin, ferritin heavy chain (FHC) and ferritin light chain (FLC); and two secreted factors associated with iron, hepcidin and lipocalin-2 (LCN2). Gene expression levels were normalized to the housekeeping gene, GAPDH, and additional housekeeping genes, HPRT1 and RLPL0, were measured to validate the use of GAPDH as the reference gene (**Figure 51E**). Interestingly, a notable decrease in the mRNA of the iron exporter FPN was observed, consistent with a response to increased iron retention in this tissue. In contrast, the mRNA levels of hepcidin, a peptide hormone that regulates iron levels by degrading FPN, shows only moderate elevation at 24 h post-infection. Previous studies with infection models have shown hepcidin induction occurring during the first 12 h of infection (Arezes et al., 2015), and the moderate change we observe is after the time window at which the hepcidin transcripts increase. The notable decrease in FPN mRNA suggests that hepatic iron regulation at this time point may also involve additional hepcidin-independent pathways that involve transcriptional regulation of FPN (Enculescu et al., 2017; Guida et al., 2015). The mRNA levels of TfR appear unchanged while DMT1 mRNA levels are reduced in the infected mice compared to the mock-infected mice. We also found a significant reduction in serum transferrin during infection (**Figure 56A**). Transferrin has previously been shown to decrease during inflammation (Neves et al., 2009; Ritchie et al., 1999). Both transferrin and DMT1 proteins are associated with the uptake of transferrin-bound iron (Nam et al., 2013). We also observe an increase in the mRNA levels of LCN2, a secreted glycoprotein that sequesters bacterial iron-binding siderophores to limit the bacterial growth (Flo et al., 2004; Goetz et al., 2002) and has been implicated as an importer of both non-transferrin bound iron (NTBI) and transferrin-bound iron (Bao et al., 2010; Correnti and Strong, 2012; Srinivasan et al., 2012). Finally, we observe alteration in the gene expression of ferritin subunits, with upregulation of FHC and downregulation of FLC, which is consistent with modulation of the intracellular iron storage machinery (Fan et al., 2014; Pham et al., 2004). In particular, FHC has been shown to facilitate rapid iron uptake (Pham et al., 2004; Rucker et al., 1996; Torti and Torti, 1994). Significant elevation in serum ferritin levels was also detected, with approximately ten-fold increase in ferritin abundance during infection (**Figure 56B**). This elevation corroborates previous studies that identified increased ferritin associated with LPS challenge and bacterial infections (Carraway et al., 1998; Neves et al., 2009). Consistent with alterations of ferritin levels is the decrease in the gene expression of the

IRP proteins, IRP1 and IRP2, which have been shown to repress translation through binding to the iron responsive element on the ferritin mRNAs (Muckenthaler et al., 2008; Rouault, 2006). These qPCR data, combined with bioluminescence imaging of labile iron stores with ICL-1 and measurement of total iron levels by bulk and laser ablation ICP-MS, indicate that systemic *A. baumannii* infection alters the iron homeostasis of the host, manifested as elevated iron levels in the liver 24 h post-infection.

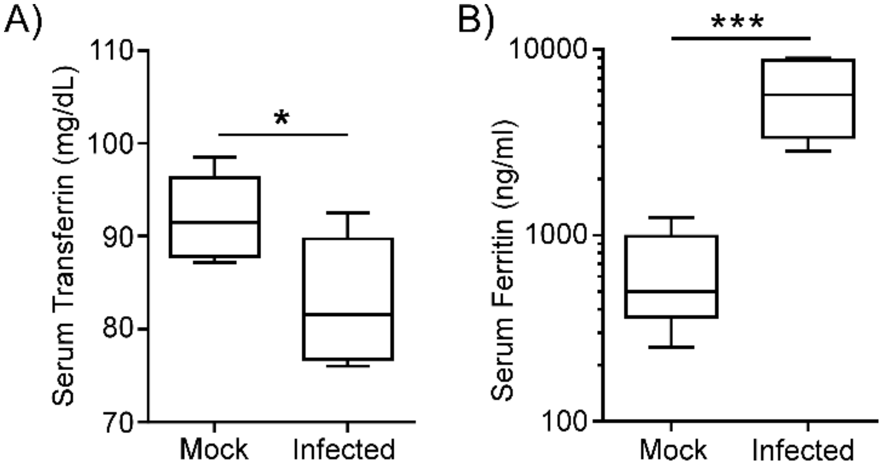

Figure 56. Serum levels of A) transferrin and B) ferritin are altered with *A. baumannii* systemic infection. Male FVB-Luc$^+$ mice were retro-orbitally injected with PBS or 2 x 10^8 – 4 x 10^8 CFUs of *A. baumannii*. At 24 hours post-infection, mice were euthanized, and serum was collected. Statistical analyses were performed using a two-tailed Student's *t*-test where $^*p \leq 0.05$ and $^{***} p \leq 0.001$ (n = 6), and error bars are ± SD.

In summary, we have presented the design, synthesis, and characterization of ICL-1, a first-generation bioluminescence probe for *in vivo* imaging of labile iron stores in living animals, and its application to an *A. baumannii* infection model. ICL-1 utilizes a bioinspired Fe^{2+}-dependent endoperoxide cleavage reaction to release D-aminoluciferin and generate an increase in bioluminescent signal with high metal and oxidation-state specificity. This probe is capable of monitoring changes in LIPs upon iron supplementation and/or depletion in live cells and animals, enabling the detection of dynamic alterations in Fe^{2+} under physiological and pathological situations. Application of ICL-1 to an *A. baumannii* model of systemic infection showcases the utility of this probe for interrogating alterations in iron status in vivo, as we observe an increase in liver iron by direct ICP-MS and LA-ICP-MS data that is supported by complementary *in vivo* and *ex vivo* bioluminescent imaging using this probe. The combination of ICL-1 and related chemical probes with tissue-specific luciferase-expressing mice can increase spatial resolution. Consistent with the observed redistributions of hepatic iron and elevations in total hepatic iron, qPCR analyses of isolated liver tissues after infection reveal concomitant decreases in mRNA levels of the iron export protein ferroportin, increased mRNA levels of the secreted factor LCN2, and modulation in the mRNA levels of key iron storage machinery – namely increased FHC and decreased FLC. These transcriptional changes are supported by significant alterations in serum transferrin and ferritin during infection. We hypothesize that such transcriptional alterations can serve as important contributors to changes in labile and total hepatic iron stores. By expanding our ability to monitor iron dynamics from cell culture to living animals, ICL-1 provides a unique chemical tool to study biological contributions of this essential metal nutrient and a starting point for developing next-generation probes for advancing our understanding of metals in biology *in vivo.*

References

Ackerman, C.M., Lee, S., and Chang, C.J. (2017). Analytical Methods for Imaging Metals in Biology: From Transition Metal Metabolism to Transition Metal Signaling. *Analytical Chemistry 89*, 22-41.

Adams, S.T., Jr., and Miller, S.C. (2014). Beyond D-luciferin: expanding the scope of bioluminescence imaging *in vivo*. *Curr Opin Chem Biol 21*, 112-120.

Andrews, N.C. (2000). Iron homeostasis: insights from genetics and animal models. *Nat Rev Genet 1*, 208-217.

Arezes, J., Jung, G., Gabayan, V., Valore, E., Ruchala, P., Gulig, P.A., Ganz, T., Nemeth, E., and Bulut, Y. (2015). Hepcidin-induced hypoferremia is a critical host defense mechanism against the siderophilic bacterium *Vibrio vulnificus*. *Cell Host Microbe 17*, 47-57.

Aron, A.T., Loehr, M.O., Bogena, J., and Chang, C.J. (2016). An Endoperoxide Reactivity-Based FRET Probe for Ratiometric Fluorescence Imaging of Labile Iron Pools in Living Cells. *J Am Chem Soc 138*, 14338-14346.

Aron, A.T., Ramos-Torres, K.M., Cotruvo, J., J. A., and Chang, C.J. (2015). Recognition- and Reactivity-Based Fluorescent Probes for Studying Transition Metal Signaling in Living Systems. *Acc Chem Res 48*, 2434-2442.

Au-Yeung, H.Y., Chan, J., Chantarojsiri, T., and Chang, C.J. (2013). Molecular Imaging of Labile Iron(II) Pools in Living Cells with a Turn-On Fluorescent Probe. *J Am Chem Soc 135*, 15165-15173.

Bao, G., Clifton, M., Hoette, T.M., Mori, K., Deng, S.X., Qiu, A., Viltard, M., Williams, D., Paragas, N., Leete, T., *et al.* (2010). Iron traffics in circulation bound to a siderocalin (Ngal)-catechol complex. *Nat Chem Biol 6*, 602-609.

Borstnik, K., Paik, I.H., Shapiro, T.A., and Posner, G.H. (2002). Antimalarial chemotherapeutic peroxides: artemisinin, yingzhaosu A and related compounds. *Int J Parasitol 32*, 1661-1667.

Cammack, R., Wrigglesworth, J.M., and Baum, H. (1989). *Transport and Storage* (CRC Press).

Carraway, M.S., Ghio, A.J., Taylor, J.L., and Piantadosi, C.A. (1998). Induction of ferritin and heme oxygenase-1 by endotoxin in the lung. *Am J Physiol 275*, L583-592.

Carter, K.P., Young, A.M., and Palmer, A.E. (2014). Fluorescent Sensors for Measuring Metal Ions in Living Systems Chem Rev *114*, 4564–4601.

Cerchiaro, G., Manieri, T.M., and Bertuchi, F.R. (2013). Analytical methods for copper, zinc and iron quantification in mammalian cells. *Metallomics 5*, 1336-1345.

Chan, J., Dodani, S.C., and Chang, C.J. (2012). Reaction-based small-molecule fluorescent probes for chemoselective bioimaging. *Nat Chem 4*, 973-984.

Chang, Y.C., Chao, P.W., and Tung, C.H. (2011). Sensitive luciferin derived probes for selective carboxypeptidase activity. *Bioorg Med Chem Lett 21*, 3931-3934.

Chen, P., Zheng, Z., Zhu, Y., Dong, Y., Wang, F., and Liang, G. (2017). Bioluminescent Turn-On Probe for Sensing Hypochlorite in Vitro and in Tumors. *Anal Chem*.

Chen, X., Tian, X., Shin, I., and Yoon, J. (2011). Fluorescent and luminescent probes for detection of reactive oxygen and nitrogen species. *Chem Soc Rev 40*, 4783-4804.

Cho, D.G., and Sessler, J.L. (2009). Modern reaction-based indicator systems. *Chem Soc Rev 38*, 1647-1662.

Cohen, A.S., Dubikovskaya, E.A., Rush, J.S., and Bertozzi, C.R. (2010). Real-time bioluminescence imaging of glycans on live cells. *J Am Chem Soc 132*, 8563-8565.

Correnti, C., and Strong, R.K. (2012). Mammalian siderophores, siderophore-binding lipocalins, and the labile iron pool. *J Biol Chem 287*, 13524-13531.

Cotruvo, J.A., Aron, A.T., Ramos-Torres, K.M., and Chang, C.J. (2015). Synthetic fluorescent probes for studying copper in biological systems. *Chemical Society Reviews 44*, 4400-4414.

Creek, D.J., Charman, W.N., Chiu, F.C., Prankerd, R.J., McCullough, K.J., Dong, Y., Vennerstrom, J.L., and Charman, S.A. (2007). Iron-mediated degradation kinetics of substituted dispiro-1,2,4-trioxolane antimalarials. *J Pharm Sci 96*, 2945-2956.

D., F.S., B., S., J., G., M., L.E., J., R.P., and R., R.A. (2015). Drug delivery to the malaria parasite using an arterolane-like scaffold. *ChemMedChem 2015*, 47-51.

Dixon, S.J., Lemberg, K.M., Lamprecht, M.R., Skouta, R., Zaitsev, E.M., Gleason, C.E., Patel, D.N., Bauer, A.J., Cantley, A.M., Yang, W.S., *et al.* (2012). Ferroptosis: an iron-dependent form of nonapoptotic cell death. *Cell 149*.

Dixon, S.J., and Stockwell, B.R. (2014). The role of iron and reactive oxygen species in cell death. *Nat Chem Biol 10*, 9-17.

Dragulescu-Andrasi, A., Liang, G., and Rao, J. (2009). *In Vivo* Bioluminescence Imaging of Furin Activity in Breast Cancer Cells Using Bioluminogenic Substrates. *Bioconjugate Chem 20*, 1660-1666.

Eijkelkamp, B.A., Hassan, K.A., Paulsen, I.T., and Brown, M.H. (2011). Investigation of the human pathogen *Acinetobacter baumannii* under iron limiting conditions. *BMC Genomics 12*, 126.

Eiriksdottir, E., Mager, I., Lehto, T., El Andaloussi, S., and Langel, U. (2010). Cellular internalization kinetics of (luciferin-)cell-penetrating peptide conjugates. *Bioconjug Chem 21*, 1662-1672.

Enculescu, M., Metzendorf, C., Sparla, R., Hahnel, M., Bode, J., Muckenthaler, M.U., and Legewie, S. (2017). Modelling Systemic Iron Regulation during Dietary Iron Overload and Acute Inflammation: Role of Hepcidin-Independent Mechanisms. *PLoS Comput Biol 13*, e1005322.

Epsztejn, S., Kakhlon, O., Glickstein, H., Breuer, W., and Cabantchik, I. (1997). Fluorescence analysis of the labile iron pool of mammalian cells. *Anal Biochem 248*, 31-40.

Fan, Y., Zhang, J., Cai, L., Wang, S., Liu, C., Zhang, Y., You, L., Fu, Y., Shi, Z., Yin, Z., *et al.* (2014). The effect of anti-inflammatory properties of ferritin light chain on lipopolysaccharide-induced inflammatory response in murine macrophages. *Biochim Biophys Acta 1843*, 2775-2783.

Flo, T.H., Smith, K.D., Sato, S., Rodriguez, D.J., Holmes, M.A., Strong, R.K., Akira, S., and Aderem, A. (2004). Lipocalin 2 mediates an innate immune response to bacterial infection by sequestrating iron. *Nature 432*, 917-921.

Fontaine, S.D., DiPasquale, A.G., and Renslo, A.R. Efficient and Stereocontrolled Synthesis of 1,2,4-Trioxolanes Useful for Ferrous Iron-Dependent Drug Delivery. *Org Lett 16*, 5776-5779.

Gerlach, M., Ben-Shachar, D.B., Riedere, P., and Youdim, M.B.H. (1994,). Altered brain metabolism of iron as a cause of neurodegenerative diseases? *J Neurochem 63*, 793-807.

Godinat, A., Park, H.M., Miller, S.C., Cheng, K.H., D. , Sanman, L.E., Bogyo, M., Yu, A., Nikitin, G.F., Stahl, A., and Dubikovskaya, E.A. (2013). A biocompatible *in vivo* ligation reaction and its application for noninvasive bioluminescent imaging of protease activity in living mice. *ACS Chem Biol 8*, 987–999.

Goetz, D.H., Holmes, M.A., Borregaard, N., Bluhm, M.E., Raymond, K.N., and Strong, R.K. (2002). The neutrophil lipocalin NGAL is a bacteriostatic agent that interferes with siderophore-mediated iron acquisition. *Mol Cell 10*, 1033-1043.

Guida, C., Altamura, S., Klein, F.A., Galy, B., Boutros, M., Ulmer, A.J., Hentze, M.W., and Muckenthaler, M.U. (2015). A novel inflammatory pathway mediating rapid hepcidin-independent hypoferremia. *Blood 125*, 2265-2275.

Hahn, P., Song, Y., Ying, G.S., He, X., Beard, J., and Dunaief, J.L. (2009). Age-dependent and gender-specific changes in mouse tissue iron by strain. *Exp Gerontol 44*, 594-600.

Hare, D., Ayton, S., Bush, A., and Lei, P. (2013, 5, 34). A delicate balance: Iron metabolism and diseases of the brain. *Front Aging Neurosci 5*, 34.

Heffern, M.C., Park, H.M., Au-Yeung, H.Y., Van de Bittner, G.C., Ackerman, C.M., Stahl, A., and Chang, C.J. (2016). *In vivo* bioluminescence imaging reveals copper deficiency in a murine model of nonalcoholic fatty liver disease *Proc Natl Acad Sci USA 113*, 14219-14224.

Henkin, A.H., Cohen, A.S., Dubikovskaya, E.A., Park, H.M., Nikitin, G.F., Auzias, M.G., Kazantzis, M., Bertozzi, C.R., and Stahl, A. (2012). Real-time noninvasive imaging of fatty acid uptake *in vivo*. *ACS Chem Biol 7*, 1884-1891.

Hirayama, T., Okuda, K., and Nagasawa, H. (2013). A highly selective turn-on fluorescent probe for iron(II) to visualize labile iron in living cells. *Chem Sci 4*, 1250-1256.

Hirayama, T., Tsuboi, H., Niwa, M., Miki, A., Kadota, S., Ikeshita, Y., Okuda, K., and Nagasawa, H. (2017). A universal fluorogenic switch for Fe(II) ion based on N-oxide chemistry permits the visualization of intracellular redox equilibrium shift towards labile iron in hypoxic tumor cells. *Chem Sci Advance Article*.

Howard, A., O'Donoghue, M., Feeney, A., and Sleator, R.D. (2012). *Acinetobacter baumannii*: an emerging opportunistic pathogen. *Virulence 3*, 243-250.

Irving, H., and Williams, R.J.P. (1953). The stability of transition-metal complexes. *J Chem Soc*, 3192-3210.

James, S.A., Robert, B.R., Hare, D.J., de Jonge, M.D., Birchall, I.E., Jenkin, N.L., Cherny, R.A., Bush, A.I., and McColl, G. (2015). Direct *in vivo* imaging of ferrous iron dyshomeostasis in ageing *Caenorhabditis elegans*. *Chem Sci 6*, 2952-2962.

Johnson, D.C., Dean, D.R., Smith, A.D., and Johnson, M.K. (2005). Structure, function, and formation of biological iron-sulfur clusters. *Annu Rev Biochem 74*, 247-281.

Jones, L.R., Goun, E.A., Shinde, R., Rothbard, J.B., Contag, C.H., and Wender, P.A. (2006). Releasable luciferin-transporter conjugates: tools for the real-time analysis of cellular uptake and release. *J Am Chem Soc 128*, 6526-6527.

Kong, W.N., Niu, Q.M., Ge, L., Zhang, N., Yan, S.F., Chen, W.B., Chang, Y.Z., and Zhao, S.E. (2014). Sex differences in iron status and hepcidin expression in rats. *Biol Trace Elem Res 160*, 258-267.

Lauterwasser, E.M., Fontaine, S.D., Li, H., Gut, J., Katneni, K., Charman, S.A., Rosenthal, P.J., Bogyo, M., and Renslo, A.R. (2015). Trioxolane-Mediated Delivery of Mefloquine Limits Brain Exposure in a Mouse Model of Malaria. *ACS Med Chem Lett 6*, 1145-1149.

Li, J., Chen, L., Du, L., and Li, M. (2013). Cage the firefly luciferin! - a strategy for developing bioluminescent probes. *Chem Soc Rev 42*, 662-676.

Miller, J.L. (2013). Iron deficiency anemia: a common and curable disease. *Cold Spring Harb Perspect Med 3*.

Mofford, D.M., Adams, S.T.J., Reddy, G.S., Reddy, G.R., and Miller, S.C. (2015). Luciferin Amides Enable *in Vivo* Bioluminescence Detection of Endogenous Fatty Acid Amide Hydrolase Activity. *J Am Chem Soc 137*, 8684-8687.

Muckenthaler, M.U., Galy, B., and Hentze, M.W. (2008). Systemic iron homeostasis and the iron-responsive element/iron-regulatory protein (IRE/IRP) regulatory network. *Annu Rev Nutr 28*, 197-213.

Nairz, M., Haschka, D., Demetz, E., and Weiss, G. (2014). Iron at the interface of immunity and infection. *Front Pharmacol 5*, 152.

Nam, H., Wang, C.Y., Zhang, L., Zhang, W., Hojyo, S., Fukada, T., and Knutson, M.D. (2013). ZIP14 and DMT1 in the liver, pancreas, and heart are differentially regulated by iron deficiency and overload: implications for tissue iron uptake in iron-related disorders. *Haematologica 98*, 1049-1057.

Neves, J.V., Wilson, J.M., and Rodrigues, P.N. (2009). Transferrin and ferritin response to bacterial infection: the role of the liver and brain in fish. *Dev Comp Immunol 33*, 848-857.

Niwa, M., Hirayama, T., Okuda, K., and Nagasawa, H. (2014). A new class of high-contrast Fe(II) selective fluorescent probes based on spirocyclized scaffolds for visualization of intracellular labile iron delivered by transferrin. *Org Biomol Chem 12*, 6590-6597.

Palmer, L.D., and Skaar, E.P. (2016). Transition Metals and Virulence in Bacteria. *Annu Rev Genet 50*, 67-91.

Pham, C.G., Bubici, C., Zazzeroni, F., Papa, S., Jones, J., Alvarez, K., Jayawardena, S., De Smaele, E., Cong, R., Beaumont, C., *et al.* (2004). Ferritin heavy chain upregulation by NF-kappaB inhibits TNFalpha-induced apoptosis by suppressing reactive oxygen species. *Cell 119*, 529-542.

Pinnix, Z.K., Miller, L.D., Wang, W., D'Agostino, R.J., Kute, T., Willingham, M.C., Hatcher, H., Tesfay, L., Sui, G., Di, X., *et al.* (2010). Ferroportin and Iron Regulation in Breast Cancer Progression and Prognosis. *Sci Transl Med 2* 43ra56.

Porterfield, W.B., Jones, K.A., McCutcheon, D.C., and Prescher, J.A. (2015). A “Caged” Luciferin for Imaging Cell–Cell Contacts. *J Am Chem Soc 137*, 8656–8659.

Ramos-Torres, K.M., Kolemen, S., and Chang, C.J. (2016). Thioether Coordination Chemistry for Molecular Imaging of Copper in Biological Systems. *Isr J Chem 56*, 724-737.

Ritchie, R.F., Palomaki, G.E., Neveux, L.M., Navolotskaia, O., Ledue, T.B., and Craig, W.Y. (1999). Reference distributions for the negative acute-phase serum proteins, albumin, transferrin and transthyretin: a practical, simple and clinically relevant approach in a large cohort. *J Clin Lab Anal 13*, 273-279.

Rouault, T.A. (2006). The role of iron regulatory proteins in mammalian iron homeostasis and disease. *Nat Chem Biol 2*, 406-414.

Rubino, J.T., and Franz, K.J. (2012). Coordination chemistry of copper proteins: How nature handles a toxic cargo for essential function. *J Inorg Biochem 107*, 129-143.

Rucker, P., Torti, F.M., and Torti, S.V. (1996). Role of H and L subunits in mouse ferritin. *J Biol Chem 271*, 33352-33357.

Rush, J.S., Beatty, K.E., and Bertozzi, C.R. (2010). Bioluminescent Probes of Sulfatase Activity. *ChemBioChem 11*, 2096-2099.

Sellmyer, M.A., Bronsart, L., Imoto, H., Contag, C.H., Wandless, T.J., and Prescher, J.A. (2013). Visualizing cellular interactions with a generalized proximity reporter. *Proc Natl Acad Sci USA 110*, 8567-8572.

Skaar, E.P. (2010). The battle for iron between bacterial pathogens and their vertebrate hosts. *PLoS Pathog 6*, e1000949.

Spangler, B., Fontaine, S.D., Shi, Y., Sambucetti, L., Mattis, A.N., Hann, B., Wells, J.A., and Renslo, A.R. (2016a). A Novel Tumor-Activated Prodrug Strategy Targeting Ferrous Iron Is Effective in Multiple Preclinical Cancer Models. *J Med Chem 59*, 11161-11170.

Spangler, B., Morgan, C.W., Fontaine, S.D., Vander Wal, M.N., Chang, C.J., Wells, J.A., and Renslo, A.R. (2016b). A reactivity-based probe of the intracellular labile ferrous iron pool. *Nat Chem Biol 12*, 680-685.

Srinivasan, G., Aitken, J.D., Zhang, B., Carvalho, F.A., Chassaing, B., Shashidharamurthy, R., Borregaard, N., Jones, D.P., Gewirtz, A.T., and Vijay-Kumar, M. (2012). Lipocalin 2 deficiency dysregulates iron homeostasis and exacerbates endotoxin-induced sepsis. *J Immunol 189*, 1911-1919.

Takakura, H., Kojima, R., Kamiya, M., Kobayashi, E., Komatsu, T., Ueno, T., Terai, T., Hanaoka, K., Nagano, T., and Urano, Y. (2015). New class of bioluminogenic probe based on bioluminescent enzyme-induced electron transfer: BioLeT. *J Am Chem Soc 137*, 4010-4013.

Tang, Y., Dong, Y., Wang, X., Sriraghavan, K., Wood, J.K., and Vennerstrom, J.L. (2005). Dispiro-1,2,4-trioxane Analogues of a Prototype Dispiro-1,2,4-trioxolane: Mechanistic Comparators for Artemisinin in the Context of Reaction Pathways with Iron(II). *J Org Chem 70*, 5103–5110.

Torti, S.V., and Torti, F.M. (1994). Iron and ferritin in inflammation and cancer. *Adv Inorg Biochem 10*, 119-137.

Torti, S.V., and Torti, F.M. (2013). Iron and cancer: more ore to be mined. *Nat Rev Cancer 13*, 342-355.

Toyokuni, S. (2009). Role of iron in carcinogenesis: cancer as a ferrotoxic disease. *Cancer Sci 100*, 9-16.

Van de Bittner, G.C., A., D.E., Bertozzi, C.R., and Chang, C.J. (2010). *In vivo* imaging of hydrogen peroxide production in a murine tumor model with a chemoselective bioluminescent reporter. *Proc Natl Acad Sci USA 107*, 21316-21321.

Van de Bittner, G.C., Bertozzi, C.R., and Chang, C.J. (2013). Strategy for Dual-Analyte Luciferin Imaging: *In Vivo* Bioluminescence Detection of Hydrogen Peroxide and Caspase Activity in a Murine Model of Acute Inflammation. *J Am Chem* Soc *135*.

von Haehling, S., Jankowska, E.A., van Veldhuisen, D.J., Ponikowski, P., and Anker, S.D. (2015). Iron deficiency and cardiovascular disease. *Nat Rev Cardiol 12*, 659-669.

Vorobyeva, A.G., Stanton, M., Godinat, A., Lund, K.B., Karateev, G.G., Francis, K.P., Allen, E., Gelovani, J.G., McCormack, E., Tangney, M., *et al.* (2015). Development of a Bioluminescent Nitroreductase Probe for Preclinical Imaging. *PLoS One 10*, e0131037.

Winterbourn, C.C. (1995). Toxicity of iron and hydrogen peroxide: the Fenton reaction. *Toxicol Lett 82/83*, 969-974.

Wu, K.J., Polack, A., and Dala-Favera, R. (1999). Coordinated regulation of iron-controlling genes, H-ferritin and IRP2, by c-MYC. *Science 283*, 676-679.

Xu, T., Close, D., Handagama, W., Marr, E., Sayler, G., and Ripp, S. (2016). The Expanding Toolbox of In Vivo Bioluminescent Imaging. *Front Oncol 6*, 150.

Xu, W., Barrientos, T., and Andrews, N.C. (2013). Iron and copper in mitochondrial diseases. *Cell Metab 17*, 319-328.

Yang, Y., Zhao, Q., Feng, W., and Li, F. (2013). Luminescent chemodosimeters for bioimaging. *Chem Rev 113*, 192-270.

Yao, H., So, M.K., and Rao, J. (2007). A bioluminogenic substrate for *in vivo* imaging of beta-lactamase activity. *Angew Chem Int Ed Engl 46*, 7031-7034.

Zastrow, M.L., Radford, R.J., Chyan, W., Anderson, C.T., Zhang, D.Y., Loas, A., Tzounopoulos, T., and Lippard, S.J. (2016). Reaction-Based Probes for Imaging Mobile Zinc in Live Cells and Tissues. *ACS Sensors 1*, 32-39.

Zhou, W., Andrews, C., Liu, J., Shultz, J.W., Valley, M.P., Cali, J.J., Hawkins, E.M., Dieter H. Klaubert Dr., Robert F. Bulleit Dr., and Dr., K.V.W. (2008). Self-Cleavable Bioluminogenic Luciferin Phosphates as Alkaline Phosphatase Reporters. *ChemBioChem 9*, 714-718.

CHAPTER VI

SUMMARY & FUTURE DIRECTIONS

Conclusions

The struggle for nutrients at the host-pathogen interface represents an area where bacterial physiology must provide protection against the host immune response. *Acinetobacter baumannii* utilizes its metabolic flexibility to persist in many niches, including abiotic surfaces, hospital ventilators, and even within the lungs of immunocompromised individuals. This ability of *A. baumannii* to cause disease coupled with its alarming rate of antibiotic resistance acquisition led both the CDC and the WHO to list *A. baumannii* as a top-level threat for which new therapeutics are needed (CDC, 2019; WHO, 2017). In this thesis, I investigated strategies used by *A. baumannii* to respond to nutrient fluctuations that occur within the vertebrate host and identified potential new targets for antimicrobial therapeutic development.

Zinc (Zn) is one of the key nutrients that *A. baumannii* requires to grow and cause disease, and this bacterial pathogen possesses unique strategies for acquiring this metal in Zn-limited environments. The host restricts nutrient Zn through a number of processes, one of which relies on the deployment of the metal-binding protein calprotectin (CP). CP is a major component of neutrophils and is readily detected at infectious lesions in vertebrates (Cassat et al., 2018; Corbin et al., 2008). However, as reviewed in Chapter I, bacteria possess a myriad of Zn acquisition systems capable of competing with the host and CP for metals. We previously identified that Zn uptake in *A. baumannii* is regulated by the Zn uptake repressor Zur and found that Zur-regulated genes are derepressed when *A. baumannii* is grown in the presence of CP (Mortensen et al., 2014).

However, the broader role that CP played in changing metal availability and *A. baumannii* physiology was unclear and encompassed a major research area for this Thesis.

Defining the response of *A. baumannii* to calprotectin

While CP was known to induce manganese (Mn) and Zn starvation in *A. baumannii* (Hood et al., 2012; Juttukonda et al., 2016), the broader impacts of this metal starvation on the bacterium were not clear. To uncover these processes, Chapter II details how transcriptomics and proteomics-based analyses were performed on *A. baumannii* following growth in the presence of CP (Wang et al., 2019). One of the most striking findings from these experiments was that CP not only induces a strong Zn starvation response, but also promotes iron (Fe) starvation responses (Nakashige et al., 2015), where *A. baumannii* displays robust siderophore production when grown in the presence of CP. This siderophore production was likely driven by the Fe-binding properties recently attributed to CP, and we found that CP readily reduces Fe concentrations when incubated in a variety of laboratory growth media (Wang et al., 2019). However, whether *A. baumannii* experiences this multi-metal starvation during infection remains to be explored.

The proteomics analysis was performed not only in WT *A. baumannii*, but also in a strain lacking the predicted Zn metallochaperone ZigA (Nairn et al., 2016). ZigA is a member of a GTPase superfamily involved in the delivery of metal cofactors to metal-containing enzymes (Chapter I). Since no direct interaction partners are known for ZigA, we postulated that analyzing the proteome of this strain during Zn starved conditions may identify pathways affected by the absence of ZigA-mediated metal cofactor delivery, which may lead to protein instability. From this analysis, enzymes involved in the biosynthesis of the essential cofactor riboflavin were enriched in the presence of CP, and one of these was more abundant in the *zigA* mutant. These findings suggest that flavins may play an important role in the response of *A. baumannii* to CP. By quantifying cellular flavin levels in the presence and absence of CP, I discovered that metal starvation stresses the riboflavin biosynthesis pathway in a ZigA-dependent manner, which implies that ZigA may be directly involved in flavin biosynthesis. So far, no direct protein-protein interactions were identified between ZigA and flavin biosynthetic enzymes, so the possibility remains that ZigA's activity may occur upstream of flavin biosynthesis and limit precursor availability for the biosynthetic pathway. These findings also established a new parameter for flavin synthesis regulation in bacteria by assigning function to a previously undescribed flavin biosynthetic enzyme, which we named RibBX. RibBX possesses the same enzymatic activity as a well-defined flavin biosynthesis enzyme named RibB, which *A. baumannii* also possesses. However, RibBX is regulated by flavin abundance at the protein-level, as opposed to the transcriptional level regulation that occurs for RibB. There is a concentration-dependent regulation as well, where RibBX and RibB may become active at different flavin concentrations. However, more research is required to dissect how RibBX is translationally regulated and if it is truly functionally redundant with RibB in *A. baumannii* and what sort of transcriptional regulation may exist for RibBX. However, studies from other organisms have shown that *ribBX* is upregulated in low Fe environments (Worst et al., 1998). Consistent with this, I found that the Δ*ribBX A. baumannii* strain is sensitive to growth in Fe-starved conditions, which suggests that low Fe environments may be the condition where RibBX is maximally active. These findings represent an exciting area of future research into how flavin abundance is linked to nutrient status.

Bacterial cell wall dynamics during Zn starvation

Calprotectin-mediated metal starvation not only stresses riboflavin biosynthesis, but it also produces other changes in *A. baumannii* physiology. The transcriptomics analysis described in Chapter I identified a gene of unknown function as being highly upregulated in the presence of CP (Wang et al., 2019). Previous transcriptomic analyses in the *A. baumannii* Δ*zur* strain identified this gene as being within the Zur regulon as well, suggesting that it is involved in Zn homeostasis. Chapter III provides a functional characterization of this gene with the locus tag *A1S_3412,* which I named ZrlA (Zur-regulated Lipoprotein A). ZrlA is specifically induced during Zn limitation, and assessments of the cell wall found that ZrlA contributes to both homeostatic cell wall peptides and modifications in the cell wall that occur during nutrient restriction (Lonergan et al., 2019). These cell wall defects cause the *A. baumannii* envelope to become more permeable, which renders *A. baumannii* more susceptible to antibiotics and the host immune response. Importantly, the efficacy of meropenem, a clinically relevant antibiotic, was improved against a *zrlA* mutant in a murine model of *A. baumannii* pneumonia. These findings suggest that developing a small molecule inhibitor of ZrlA may improve antibiotic efficacy in difficult-to-treat *A. baumannii* infections. On a more fundamental level, these discoveries identified that bacteria possess mechanisms to induce specific cell wall differences when nutrient availability shifts.

One model for the importance of ZrlA during Zn starvation is that ZrlA's action on the peptidoglycan layer aids in the localization of Zn uptake machinery to the cellular envelope. Consistent with this concept, a *zrlA* mutant has a defect in acquiring Zn from the environment, even though the strain has heightened expression of Zn uptake genes. However, more experiments are needed to validate whether this increased expression of Zn uptake machinery correlates with heightened abundance in the cell envelope. Additionally, it remains to be determined if ZrlA directly interacts with Zn uptake machinery, or even other cell wall division machinery, to aid in cell wall homeostasis in *A. baumannii*.

A. baumannii **histidine utilization at the host-pathogen interface**

Many metabolic processes require nutrient metals for function. One of these that we found plays a role in the adaptation of *A. baumannii* to a low Zn environment is the histidine utilization (Hut) system. We identified histidine (His) as being a component of an intracellular metal-binding pool that, through its degradation, may liberate Zn for other biological processes (Chapter 1). However, it was unclear what function the Hut system may have under basal conditions in *A. baumannii* and whether this system had an impact on bacterial virulence. Additionally, to our knowledge, no one had assessed the contribution of Hut enzymes to bacterial pathogenesis in any organism. As outlined in Chapter IV, I found that the Hut system is conserved in pathogenic *Acinetobacter* while absent in environmental species, such as *Acinetobacter baylyi*. The Hut system is functional in *A. baumannii* and permits His utilization as the sole carbon source, nitrogen source, or both. Additionally, His nitrogen source utilization is dependent on HutH, which is the first enzyme in His catabolism that releaseas ammonia as part of its reaction mechanism. Upon assessing the fitness of various *hut* mutants in a murine model of *A. baumannii* pneumonia, it was revealed that the *hutH* and *hutT* His transporter mutant were significantly impaired at lung colonization and in dissemination to the liver. These results suggest that His is not primarily serving as a carbon source for *A. baumannii*, but it may be serving as a nitrogen source *in vivo*.

Identifying His as a possible nitrogen source for *A. baumannii* is intriguing, since it suggests that another, more energetically favorable carbon source is likely present within the lung. In *Pseudmonoas*, TCA cycle intermediates are preferred over sugar substrates (Bender, 2012), so it would be interesting to determine if these substrates are available for energy generation during *A. baumannii* infections. Our *in vitro* growth assessments have determined *A. baumannii* readily uses succinate and fumarate as carbon sources (Wang et al., 2019), and we experimentally validated that fumarate and His in combination supports robust bacterial growth. More broadly, understanding bacterial nutritional options for bacterial pathogens in the context of an infection represents an interesting avenue of future investigation.

While the Hut system is broadly conserved in bacterial species, including several species of *Acinetobacter*, the system is notably absent from the environmental species *A. baylyi*. However, closeinspection of the *A. baylyi* genome reveals that remnants of the genes encoding the Hut enzymes are present, which suggests that an ancestral *Acinetobacter* may have possessed an intact Hut system that was lost in *A. baylyi*. Conversely, the pathogenic species *A. baumannii* and *A. nosocomialis* have maintained a complete Hut system. These observations suggest that unique environmental pressures affected the maintenance of the Hut system in these closely related species, but requires further research to resolve. Collectively, Chapter IV demonstrates the importance of bacterial nutrient homeostasis systems in surviving within the host niche.

Nutrient iron fluctuations during *A. baumannii* infections

Both bacterial pathogens and the hosts they infect have complex buffering and regulatory systems to modify metal levels when needed, which is described for nutrient Zn in Chapter I. Fe levels are also extensively buffered within living systems, since its requirement for life must be balanced against its redox potential and inherent toxicity. Decades of research have uncovered mechanisms that vertebrates employ to balance Fe levels (Wallander et al., 2006), but the ability to dynamically monitor these changes, particularly during cases of infection or inflammation, were understudied. In Chapter V, a bioluminescent probe named ICL-1 is described, and its utility to monitor changes in ferrous iron (Fe^{2+}) during *A. baumannii* infection is reported. By utilizing ICL-1, high levels of ferrous iron were detected during normal conditions radiating from the intestines, which is consistent with the intestines being the major source of Fe^{2+} uptake. Upon challenge with *A. baumannii*, there was a significant increase in signal intensity as well as a dramatic change in localization. These changes in bioluminescence were confirmed using a variety of techniques to assess changes in Fe levels. These strategies included bulk measurement of total iron using inductively-coupled plasma mass spectrometry (ICP-MS) as well as performing elemental imaging by coupling a laser ablation system to ICP-MS (LA-ICP-MS). Additionally, quantitative RT-PCR was performed on infected tissues, and the expression of genes related to iron homeostasis and inflammation were assessed, all of which showed a consistent expression pattern with iron withholding and redistribution during infection and inflammation.

As an opportunistic pathogen, *A. baumannii* does not possess a suite of virulence factors that may dampen the host immune response, and as such, infection with *A. baumannii* induces maximum inflammatory responses. However, how professional pathogens like *Yersinia pestis* or *Staphylococcus aureus* dynamically modulate host iron withholding during infection would be an interesting area to explore. Indeed, investigations into infections with *Vibrio vulnificus* revealed iron withholding by the host (Arezes et al., 2015), but the kinetics of iron withholding may vary dramatically over the course of days or weeks of infection instead of hours. Additionally, these experiments were only performed in male mice, since we observed sex-based differences in ICL-1 response. Therefore, monitoring both long-term changes in Fe distribution in each sex as well as short-term changes during inflammation may provide valuable information as to how sex differences modulate metal homeostasis and inflammatory processes.

Future Directions

Determine other physiological changes occurring during CP-mediated metal starvation

Chapter II explores how both Zn and Fe starvation occur simultaneously when *A. baumannii* is grown in the presence of CP, with flavin biosynthesis being one of the metabolic processes stressed by this multi-metal starvation. However, many other changes were detected through transcriptomics and proteomics that suggest other metabolic processes are affected when *A. baumannii* is metal-starved.

One of the observations in Chapter II is that genes and proteins involved in copper (Cu) uptake and storage were changed in a way that suggested Cu toxicity may be occurring, despite the fact that no changes in Cu levels occurred in media incubated with CP. These findings suggest that alterations in abundant nutrient metals like Fe and Zn may have downstream effects on less abundant metals, such as Cu. Indeed, a previous study found that *A. baumannii* has a functional link between Zn toxicity inducing Cu depletion (Hassan et al., 2017), but how Zn starvation affects Cu levels is unexplored. Strategies to further define the relationship between Zn and/or Fe and Cu are ongoing. These experiments include specifically assessing the relationship between Zn starvation and Cu toxicity, quantifying bacterial Cu levels during Zn starvation, and generating a genetic mutant in a newly identified putative copper storage protein that may be involved in buffering intracellular copper levels. Additionally, bacterial reporter strains could be made that respond to various metal starvation or toxicity conditions, which could define what kind of metal stresses are experienced within a macrophage; this would be an important area of investigation, since there are inconsistencies reported in the literature as to what metal stresses may be experienced within macrophages (Chapter I).

Other changes that occurred following CP-mediated metal sequestration included increased transcriptional upregulation of the gene encoding the *A. baumannii* leucine-responsive regulatory protein (Lrp). While not characterized in *A. baumannii*, Lrp is well-defined in *Escherichia coli*, and it serves as a global regulator of *E. coli* transcription and either directly or indirectly controls expression of one third of the *E. coli* genome (Kroner et al., 2019). Lrp's regulon includes many types of genes, such as those that are involved in the bacterium's transition between growth phases. Additionally, nutrient composition and growth phase both alter the types of genes regulated by Lrp (Kroner et al., 2019). However, the relationship between Lrp and nutrient metal availability is undefined, but results presented in Chapter II suggest that Lrp may be particularly responsive to metal starvation and have broad effects on *A. baumannii* physiology in these growth conditions. Experiments to define the relationship between Lrp and metal starvation include, first, to validate that *lrp* is transcriptionally upregulated in the presence of CP using quantitative RT-PCR (qRT-PCR). This experiment could also be performed in *E. coli* to determine if the metal-responsiveness of *lrp* is specific to *A. baumannii*. Additionally, the promoter region of *lrp* could be assessed for possible metal-responsive transcriptional regulator binding sites, such as Zur and Fur and coupled with electrophoretic mobility shift assays (EMSAs) to determine if metalloregulator proteins are able to diretly regulat *lrp*. A key experiment would be to genetically inactivate *lrp* and determine how the absence of this transcriptional regulator affects *A. baumannii* growth *in vitro* in metal-restricted growth conditions as well as the ability of *A. baumannii* to cause disease in a murine model of bacterial pneumonia. These experiments would define an exciting new area of how metal starvation globally alters *A. baumannii* physiology outside of the traditional metalloregulator regulon.

Define ZigA protein-protein interactions

We have extensively characterized phenotypes associated with the Δ*zigA* strain that implicate the protein in being critical for some core metabolic process that must be maintained during nutrient restriction and has wide-reaching effects on *A. baumannii* physiology (Nairn et al., 2016; Wang et al., 2019). However, despite several attempts, no direct protein-protein interacts have been reported for ZigA, which may be complicated by the fact that such interactions are likely transient. However, there are additional strategies that, when coupled with existing datasets, may provide insight into specific processes impacted by ZigA.

Given that the *zigA* mutant is severely defective but is capable of growing in low Zn environments, identifying additional genes required for this growth may identify important genetic interactions. To identify potential genetic interactions, a saturated transposon mutant library was generated in WT *A. baumannii* and a Δ*zigA* strain, and these cells will be grown in Zn-replete and deplete conditions. Following this growth, transposon junctions will be mapped to identify mutants that displayed altered abundance relative to the input pool. These experiments are ongoing and will define both new genes required for overcoming Zn starvation in the WT strain, but also have the potential to discover new targets for ZigA protein interactions.

A second strategy to define the broader impact of ZigA during Zn starvation is based on the observations that the *zigA* mutant has specific metabolic defects in low Zn environments, where the Δ*zigA* strain is defective at using certain carbon sources and has a deficiency in synthesizing flavins (Nairn et al., 2016; Wang et al., 2019). Given the multitude of ways metabolic networks may be interconnected, an efficient strategy to track differences in metabolism during metal starvation would be to perform a labeled metabolomics analysis. In this experiment, WT *A. baumannii* and the Δ*zigA* strain would be pulsed with a labeled carbon source, and the isotopic label can be tracked using mass spectrometry-based approaches in order to monitor metabolic flux through various pathways. Traditionally, labeled glucose would be the preferred carbon source since it can enter central metabolism through a single point; however, *A. baumannii* is unable to utilize glucose as a carbon source (data not shown), so a different label such as pyruvate would be required, but this may lead to complications in analysis that must be considered beforehand. This experiment would provide crucial information as to 1) how *A. baumannii* alters its metabolism during metal starvation and 2) what precise metabolic blockades occur in the absence of ZigA.

Identify how ZrlA promotes large-scale changes in cell wall composition

Chapter III describes how ZrlA aids in maintaining *A. baumannii* cell envelope integrity by potentially acting on specific types of crosslinks during nutrient starvation. While this Chapter provides a foundation for ZrlA's role, more experiments are needed to define its broader contribution to the bacterial envelope. One interesting observation from investigating ZrlA was that *A. baumannii* displays morphological plasticity that is driven by metal availability, where the bacterial cells are round during Zn restriction. This observation has been documented for other *Acinetobacter* species as well (James et al., 1995), which demonstrates this is an adaptation that occurs outside of *A. baumannii*. However, how the activity of ZrlA relates to this shape phenotype is unknown. To assess this, a fluorescently-tagged version of ZrlA has been generated that could be employed to monitor the protein's expression and localization in real-time by microscopy in Zn-replete and deplete conditions. Additionally, bacterial samples could be collected over a time course for peptidoglycan purification in order to correlate morphological changes with cell wall composition, which would provide valuable insight into *A. baumannii* cell wall dynamics. Additionally, high levels of functional redundancy exist within cell wall modifying enzymes, and these proteins have been known to act in close proximity to other cell wall synthesis proteins (Scheffers and Pinho, 2005). Therefore, defining possible ZrlA protein-protein interactions is paramount to understanding the relationship between ZrlA and other cell-wall synthesis enzymes. As detailed in Chapter III, a ZrlA polyclonal antibody has been generated that could be employed for immunoprecipitation experiments that would define stable protein interactions.

Determine *A. baumannii* carbon and nitrogen sources during infection

In Chapter IV, the importance of HutH-mediated His nitrogen source utilization is defined for *A. baumannii*. Importantly, only a Δ*hutH* mutant is defective at colonizing the lungs of mice during acute pneumonia, which suggests that His is serving as a nitrogen source during infection. However, the carbon source that would be used alongside His as a nitrogen source is unknown. To begin assessing this question, experiments are ongoing to quantify metabolites and amino acids in the lung extracellular space. To perform this quantification, bronchial alveolar lavage (BAL) fluid was collected from uninfected and *A. baumannii* infected mice; immune cells were removed by centrifugation, and the BAL was sterile-filtered to remove bacterial contamination. The samples will be processed using high performance liquid chromatography-based methods to quantify amino acids and other stable metabolites within the BAL. One important caveat of this experiment is that not all simple carbon sources will be detectable, and since the closely related opportunistic pathogen *Pseudomonas aeruginosa* prefers TCA intermediates such as succinate, these metabolites may be missed from this analysis. To capture more transient metabolites, the BAL could be preserved in organic solvents like methanol, which has previously been performed following *Klebsiella* infections (Silver et al., 2019). Additionally, genetic approaches could be performed, where mutants in specific carbon source-utilization pathway could be assessed for their fitness individually and in combinatorial mutations in our murine pneumonia model.

Work in Chapter IV demonstrates that *hutH* from the Hut system is necessary for *A. baumannii* lung colonization. However, it would be interesting to determine if *hutH* alone is sufficient to promote infection. This could be achieved by expressing *hutH* alone in *A. baumannii* lacking all other Hut enzymes, or by expressing *hutH* and/or other *hut* genes in organisms like *E. coli* and *A. baylyi* that do not encode *hut* and, in the case of *A. baylyi*, are not typically pathogenic. Additionally, a broader investigation of the presence or absence of Hut systems in closely related species could provide insight into how niche occupation drives maintenance of the pathway.

Investigate host iron homeostasis in diverse contexts

Chapter V focuses on the development and implementation of an Fe^{2+}-responsive probe (ICL-1) and its utility in monitoring host-mediated iron withholding during *A. baumannii* infection. These experiments established that after a 24-hour infection, Fe^{2+} accumulates within infected tissues and is consistent with what is known about models of host nutritional immunity. However, the time scale of this infection is not necessarily representative of the diversity of pathogens that cause disease, so expanding ICL-1 studies to other infection models is an important next step in understanding host Fe withholding. Additionally, with our *A. baumannii* infection models, the pathogen will eventually be cleared from the animal, which provides an opportunity to understand how the resolution of infection alters Fe dynamics. This area of investigation would be particularly interesting since the animal likely needs to access nutrients that are being withheld from bacterial pathogens in order to resolve infections and promote healing. This experiment could also be coupled with a time course of Fe redistribution in order to gauge how the metals change in a more dynamic manner. Collectively, ICL-1 provides a unique tool for understanding host Fe homeostasis changes during inflammatory processes.

In summary, this Dissertation highlights the complex interplay between *A. baumannii* metabolism and virulence driven by changes in nutrient availability. These findings provide the foundation for exciting research into mechanisms of nutrient acquisition by pathogens and withholding by vertebrate hosts that will hopefully inform therapeutic design to improve human health.

References

Arezes, J., Jung, G., Gabayan, V., Valore, E., Ruchala, P., Gulig, P.A., Ganz, T., Nemeth, E., and Bulut, Y. (2015). Hepcidin-induced hypoferremia is a critical host defense mechanism against the siderophilic bacterium *Vibrio vulnificus*. *Cell Host Microbe 17*, 47-57.

Bender, R.A. (2012). Regulation of the histidine utilization (hut) system in bacteria. *Microbiol Mol Biol Rev 76*, 565-584.

Cassat, J.E., Moore, J.L., Wilson, K.J., Stark, Z., Prentice, B.M., Van de Plas, R., Perry, W.J., Zhang, Y., Virostko, J., Colvin, D.C., *et al.* (2018). Integrated molecular imaging reveals tissue heterogeneity driving host-pathogen interactions. *Sci Transl Med 10*.

CDC (2019). Antibiotic resistance threats in the United States.

Corbin, B.D., Seeley, E.H., Raab, A., Feldmann, J., Miller, M.R., Torres, V.J., Anderson, K.L., Dattilo, B.M., Dunman, P.M., Gerads, R., *et al.* (2008). Metal chelation and inhibition of bacterial growth in tissue abscesses. *Science 319*, 962-965.

Hassan, K.A., Pederick, V.G., Elbourne, L.D., Paulsen, I.T., Paton, J.C., McDevitt, C.A., and Eijkelkamp, B.A. (2017). Zinc stress induces copper depletion in *Acinetobacter baumannii*. *BMC microbiology 17*, 59.

Hood, M.I., Mortensen, B.L., Moore, J.L., Zhang, Y., Kehl-Fie, T.E., Sugitani, N., Chazin, W.J., Caprioli, R.M., and Skaar, E.P. (2012). Identification of an *Acinetobacter baumannii* zinc acquisition system that facilitates resistance to calprotectin-mediated zinc sequestration. *PLoS pathogens 8*, e1003068.

James, G.A., Korber, D.R., Caldwell, D.E., and Costerton, J.W. (1995). Digital image analysis of growth and starvation responses of a surface-colonizing *Acinetobacter* sp. *Journal of bacteriology 177*, 907-915.

Juttukonda, L.J., Chazin, W.J., and Skaar, E.P. (2016). *Acinetobacter baumannii* Coordinates Urea Metabolism with Metal Import To Resist Host-Mediated Metal Limitation. *mBio 7*.

Kroner, G.M., Wolfe, M.B., and Freddolino, P.L. (2019). *Escherichia coli* Lrp Regulates One-Third of the Genome via Direct, Cooperative, and Indirect Routes. *Journal of bacteriology 201*.

Lonergan, Z.R., Nairn, B.L., Wang, J., Hsu, Y.P., Hesse, L.E., Beavers, W.N., Chazin, W.J., Trinidad, J.C., VanNieuwenhze, M.S., Giedroc, D.P., *et al.* (2019). An *Acinetobacter baumannii*, Zinc-Regulated Peptidase Maintains Cell Wall Integrity during Immune-Mediated Nutrient Sequestration. *Cell Rep 26*, 2009-2018 e2006.

Mortensen, B.L., Rathi, S., Chazin, W.J., and Skaar, E.P. (2014). *Acinetobacter baumannii* response to host-mediated zinc limitation requires the transcriptional regulator Zur. *Journal of bacteriology 196*, 2616-2626.

Nairn, B.L., Lonergan, Z.R., Wang, J., Braymer, J.J., Zhang, Y., Calcutt, M.W., Lisher, J.P., Gilston, B.A., Chazin, W.J., de Crecy-Lagard, V., *et al.* (2016). The Response of *Acinetobacter baumannii* to Zinc Starvation. *Cell Host Microbe 19*, 826-836.

Nakashige, T.G., Zhang, B., Krebs, C., and Nolan, E.M. (2015). Human calprotectin is an iron-sequestering host-defense protein. *Nature chemical biology 11*, 765-771.

Scheffers, D.J., and Pinho, M.G. (2005). Bacterial cell wall synthesis: new insights from localization studies. *Microbiol Mol Biol Rev 69*, 585-607.

Silver, R.J., Paczosa, M.K., McCabe, A.L., Balada-Llasat, J.M., Baleja, J.D., and Mecsas, J. (2019). Amino Acid Biosynthetic Pathways Are Required for *Klebsiella pneumoniae* Growth in Immunocompromised Lungs and Are Druggable Targets during Infection. *Antimicrobial agents and chemotherapy 63*.

Wallander, M.L., Leibold, E.A., and Eisenstein, R.S. (2006). Molecular control of vertebrate iron homeostasis by iron regulatory proteins. *Biochim Biophys Acta 1763*, 668-689.

Wang, J., Lonergan, Z.R., Gonzalez-Gutierrez, G., Nairn, B.L., Maxwell, C.N., Zhang, Y., Andreini, C., Karty, J.A., Chazin, W.J., Trinidad, J.C., *et al.* (2019). Multi-metal Restriction by Calprotectin Impacts De Novo Flavin Biosynthesis in *Acinetobacter baumannii*. *Cell Chem Biol*.

WHO (2017). Guidelines for the prevention and control of carbapenem-resistant Enterobacteriaceae, *Acinetobacter baumannii* and *Pseudomonas aeruginosa* in health care facilities. World Health Organization.

Worst, D.J., Gerrits, M.M., Vandenbroucke-Grauls, C.M., and Kusters, J.G. (1998). Helicobacter pylori ribBA-mediated riboflavin production is involved in iron acquisition. *Journal of bacteriology 180*, 1473-1479.

APPENDIX A

Supplementary Tables associated with Chapter II

Table 2. Significant ($p < 0.01$) changes following RNA-seq analysis of WT *A. baumannii* grown in the presence of CP compared to untreated cells.

id	**foldChange**	**pval**	**padj**
Up-regulated-significant and >2-fold change			
A1S_3411	184.94	2.20E-59	4.26E-56
A1S_0094	5.68	1.16E-15	2.82E-13
A1S_0146	5.82	7.15E-09	7.93E-07
A1S_0242	5.27	3.22E-08	3.28E-06
A1S_0244	3.24	1.40E-05	8.64E-04
A1S_0391	106.38	7.93E-69	3.08E-65
A1S_0655	4.00	5.06E-06	3.65E-04
A1S_0666	2.19	5.37E-04	1.96E-02
A1S_1063	6.42	2.98E-09	3.51E-07
A1S_1504	13.35	3.78E-08	3.76E-06
A1S_1647	95.87	8.38E-05	4.11E-03
A1S_1648	104.74	7.71E-06	5.12E-04
A1S_1650	51.03	4.06E-05	2.19E-03
A1S_1652	43.34	3.78E-06	2.99E-04
A1S_1654	16.62	1.97E-04	8.22E-03
A1S_1656	8.65	9.04E-10	1.21E-07
A1S_1666	16.40	9.38E-06	5.90E-04
A1S_1667	8.90	9.63E-04	3.17E-02
A1S_1921	4.11	5.08E-06	3.65E-04
A1S_2076	8.00	9.40E-06	5.90E-04

A1S_2080	4.47	7.52E-07	6.64E-05
A1S_2081	4.32	3.83E-09	4.37E-07
A1S_2385	36.43	1.26E-03	3.97E-02
A1S_2387	91.13	8.89E-04	2.99E-02
A1S_2559	4.03	5.95E-06	4.20E-04
A1S_2892	45.37	6.19E-49	8.01E-46
A1S_3174	13.20	4.94E-06	3.65E-04
A1S_3324	9.52	7.48E-11	1.12E-08
A1S_3402	6.70	7.96E-04	2.76E-02
A1S_3403	6.31	7.21E-04	2.52E-02
A1S_3406	6.16	1.58E-04	6.82E-03
A1S_3407	6.34	5.48E-05	2.80E-03
A1S_3409	5.76	5.29E-10	7.33E-08
A1S_3412	20.49	5.33E-21	2.30E-18
A1S_3476	7.17	6.34E-11	9.84E-09
A1S_3816	18.36	1.51E-18	5.87E-16
Down-regulated, significant and >2-fold change	**1/Fold Change**	**log2FoldChange**	**padj**
A1S_0169	7.85	-2.97	1.12E-08
A1S_0170	10.38	-3.38	1.99E-14
A1S_0171	9.18	-3.20	5.13E-10
A1S_0371	5.52	-2.46	7.91E-06
A1S_0372	2.62	-1.39	1.77E-03
A1S_0463	2.56	-1.35	2.72E-03
A1S_0464	3.01	-1.59	5.90E-04
A1S_0465	3.60	-1.85	5.51E-03
A1S_0466	3.48	-1.80	2.72E-03
A1S_0800	6.28	-2.65	4.33E-09
A1S_0889	2.16	-1.11	5.50E-03
A1S_1155	2.50	-1.32	1.27E-02
A1S_1156	2.59	-1.37	1.67E-02

A1S_1159	2.17	-1.12	6.04E-03
A1S_1161	2.20	-1.14	5.82E-03
A1S_1385	2.37	-1.25	2.99E-02
A1S_2016	2.64	-1.40	1.48E-02
A1S_2022	2.34	-1.23	3.96E-02
A1S_2025	2.24	-1.16	2.86E-02
A1S_2027	2.65	-1.41	6.36E-03
A1S_2028	2.02	-1.01	2.86E-02
A1S_2294	2.62	-1.39	2.01E-03
A1S_3219	5.40	-2.43	4.65E-13
A1S_3415	2.85	-1.51	1.55E-02
A1S_3758	2.92	-1.54	1.24E-02
A1S_3764	2.63	-1.39	5.12E-04
A1S_3765	2.27	-1.18	1.86E-02
A1S_3771	2.18	-1.12	5.44E-03